level events in the Paleozoic range from a few tens of meters to ~250 m (*22*). A recent synthesis of the Carboniferous-Permian yielded fluctuations of a few tens of meters in the nonglacial intervals and changes of up to 120 m in the glacially dominated periods (*23*). Many of these regional estimates will be subject to refinement in the future, once the sections in question are rigorously backstripped.

Although we deem the long-term trends to be real, the difficulties in estimating meaningful measures of the magnitude of eustatic changes discussed above imply that the absolute global amplitude of both the long-term envelope and the short-term changes remain elusive. All such measures must be currently considered as approximate. These observations also caution us about the futility of generalizing the magnitude of individual sea-level events from one continental margin to represent worldwide eustatic values.

The concept of RDs [first proposed by M. E. Johnson (*24*)] implies that we consider the sections therein to be currently the best available representation of the modal mean for the time segment under consideration. Our criteria for inclusion of an area as a RD are as follows: (i) the time segment in question is represented by a period of tectonic quiescence locally (or is correctable for tectonic influences) and has suffered relatively little postdepositional deformation and is thus interpretable with sequence-stratigraphic methodologies; (ii) sections are relatively well-dated, preferably with multiple biostratigraphies (to enhance the chronostratigraphic signal-to-noise ratio); (iii) outcrops in the area have open public access; and (iv) the area will easily lend itself to geohistory analysis so that the relevant sections can be eventually backstripped (as well as corrected for local dynamic topographic changes over time) for more-refined estimates of the magnitude of changes in sea level. We list the selected RDs and ancillary sections in the SOM, along with background literature and ages assigned by us to the interpreted sequence boundaries.

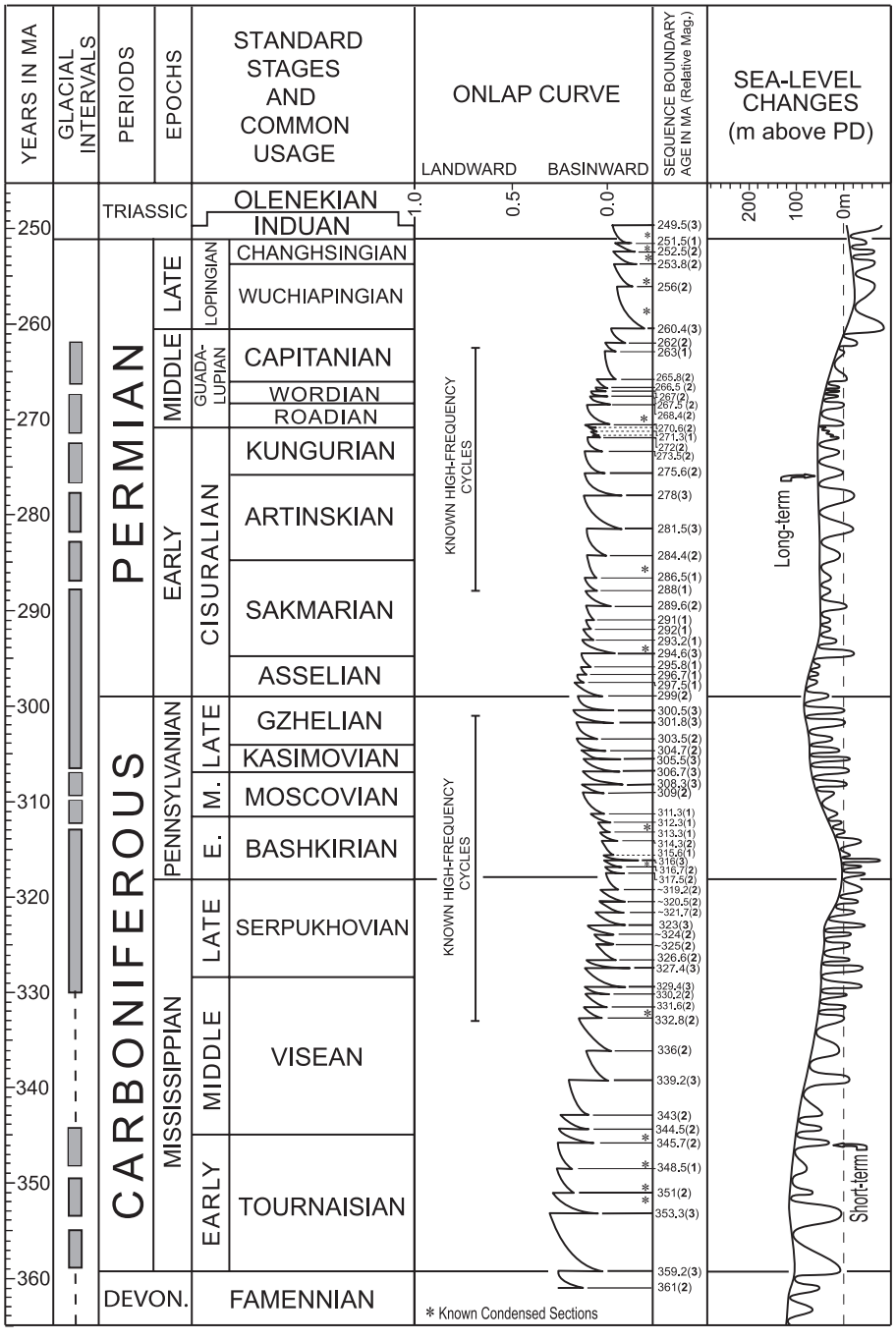

Fig. 3. Carboniferous-Permian sea-level changes. See the caption of Fig. 1 for details.

Results and conclusions. Here we offer (in our view) a robust working model of the history of the Paleozoic sea level that is, nevertheless, subject to refinement with better chonostratigraphies and when the sections are subjected to backstripping analyses. Our results show a long-term sea level curve, including a rising sea level during the Cambrian–through–Early Ordovician interval [see fig. S1 and explanation in (*25*)], a marked dip during the Middle Ordovician (the Dapingian to early Darriwilian) preceding a substantial rise entering the early Late Ordovician, and the highest sea levels of the Paleozoic during the early Katian (when the sea level is estimated to be ~225 m higher than at the PD). This was followed by a sharp fall during the latest Ordovician (late Katian to the Hirnantian) that continued into the earliest Silurian. The remainder of the Early Silurian saw the beginning of another long-term rise that culminated in a mid-Silurian (mid-Wenlock) high, followed by a decline that lasted from Late Silurian (Ludlow) through Early Devonian (Emsian). The Middle Devonian saw the beginning of yet another long-term rise, which reached its acme in the early Late Devonian (Frasnian). After a slight dip at the Frasnian/Famennian boundary and a recovery in the early Famennian, the long-term curve shows a gradual sea-level decline in the later Devonian (late Famennian) with a punctuated fall near the Devonian/Carboniferous boundary. After a short recovery, subsequent long-term decline began in the mid-Mississippian (mid Visean), reaching a low in the late Mississippian (near the Mississippian/Pennsylvanian boundary). The next long-term rise (though less pronounced than all previous rises) began in the mid-Pennsylvanian (Moscovian) and lasted only until the end of the Pennsylvanian (Gzhelian), followed by a slight fall thereafter in the earliest Permian (Asselian). The sea level stabilized at that level for the remainder

Downloaded from www.sciencemag.org on October 2, 2008

of the Early Permian. A sharp trend toward a declining sea level started in the mid-Permian (Roadian), culminating in the nadir of the sea level for the Paleozoic in the early Late Permian (Wuchiapingian). It began to recover in the latest Permian (Changhsingian), but the general low extended into the Early Triassic.

The shorter-term (third-order) base-level changes generally vary in duration from ~0.5 to 3.0 My (with the exception of Early-to-Middle Mississippian). One hundred seventy-two discrete third-order events (cycles) have been identified, with an average duration of ~1.7 My per cycle. In some intervals, the sections preferentially preserve fourth-order cycles, indicating a possible long-period orbital eccentricity control. Four such intervals have been identified so far: in the middle Cambrian (Toyonian to Mayan), middle Devonian (late Eifelian to Givetian), middle to late Carboniferous (late Visean to Kasimovian), and early to Middle Permian (Artinskian to Capitanian); however, fourth-order cycles may exist more widely. Whether this higher frequency is entirely due to higher sedimentation (a preservational effect) or the underlying signal (that is, long-term orbital forcing) is not always clear. The two younger intervals of higher-frequency cycles (in the Carboniferous and Permian) also coincide with periods of known glaciation, but for the two older intervals (the middle Cambrian and middle Devonian) no glaciation has been documented (*26*–*28*).

It should be noted that for the Early to middle Mississippian, the duration of most of the third-order cycles seem inordinately long (up to ~6.0 My). Although occasional long cycles (3 to 5 My) also occur at other times (for example, in the Cambrian through early Silurian), the consistent occurrence of long cycles in the Early to middle Mississippian may point to time-scale problems for this interval (the Tournaisian and Visean stages are also inordinately long, probably for the same reason).

We are unable to comment on all of the causes for shorter-term (third-order and fourth-order) eustatic changes in the Paleozoic. Although glaciation has been attributed to ~28% of the Paleozoic time (and suspected for another 10%), it has not been documented for the remainder of this era (*26*–*28*). Thus, waxing and waning ice sheets cannot be considered to be the only underlying cause for fluctuations in the Paleozoic sea level. Nevertheless, because the Paleozoic glacial record remains fragmentary, the question remains open. Conversely, there may be other, nonclimatic, causal mechanisms for short-term changes in sea level that still remain to be discovered.

References and Notes

1. J. Hardenbol *et al.*, *Soc. Econ. Paleontol. Mineral. Spec. Publ.* **60**, 3 (1998).
2. K. G. Miller *et al.*, *Science* **310**, 1293 (2005).
3. J. C. Van Wagoner, R. M. Mitchum, K. M. Campion, V. D. Rahmanian, *Am. Assoc. Petrol. Geol. Methods Explor. Ser.* **7**, 55 (1990).
4. *A Geologic Time Scale, 2004*, F. M. Gradstein, J. G. Ogg, A. G. Smith, Eds. (Cambridge Univ. Press, Cambridge, 2004), pp. 1–589.
5. J. G. Ogg, G. M. Ogg, F. M. Gradstein, *The Concise Geologic Time Scale* (Cambridge Univ. Press, Cambridge, 2008), pp. 1–178.
6. K. F. Kuiper *et al.*, *Science* **320**, 500 (2008).
7. Common Paleozoic biostratigraphic indicators include brachiopods, graptolites, chitinozoans, ammonoids, fusulinids, and conodonts. Brachiopods appear in the Early Cambrian and are common throughout the Paleozoic but tend to be provincial and facies-dependent, preferring shallow-water environments. Planktonic graptolites appear in the late Cambrian and persist through the early Devonian. They are particularly useful as index fossils in the Ordovician and Silurian, but they are more likely to occur in the basinal facies. Chitinozoa occur from Ordovician through Devonian and have been used successfully for the subdivision of this interval. Paleozoic ammonoids in general are common from the Devonian through the Permian and, although relatively widespread, they also show a considerable degree of provincialism or facies-dependence for some intervals. For example, the ammonoid *Goniatites,* preserved in Devonian-to-Permian strata, are strongly facies-controlled, preferring mostly the basinal environments of inland seas. Fusulinids have been used for biochronologic subdivision with varying degrees of success from the Late Mississippian through the Permian. Conodonts first appeared in the Cambrian and range through the Triassic. Their shallowest-water biofacies tend to be eurytopic, opportunistic, and long-ranging and thus only marginally useful for biostratigraphic resolution. But toward deeper waters they become more cosmopolitan and biostratigraphically meaningful. When deeper-water biofacies are present, conodonts are well suited for higher-resolution correlations from the Ordovician through the Permian interval.
8. W. A. van Sickel, M. A. Kominz, K. G. Miller, J. V. Browning, *Basin Res.* **16**, 451 (2004).
9. M. A. Kominz *et al.*, *Basin Res.* **20**, 211 (2008).
10. P. R. Vail, R. M. Mitchum, S. Thompson III, *Am. Assoc. Pet. Geol. Mem.* **26**, 63 (1977).
11. A. Hallam, in *Phanerozoic Sea-Level Changes* (Columbia Univ. Press, New York, 1992), p. 266.
12. B. U. Haq, A. M. Al-Qahtani, *GeoArabia* **10**, 127 (2005).
13. B. U. Haq, J. Hardenbol, P. R. Vail, *Soc. Econ. Paleontol. Mineral Spec. Publ.* **42**, 71 (1988).
14. D. U. Wise, in *The Geology of Continental Margin,* C. A. Burke, C. L. Drake, Eds. (Springer Verlag, New York, 1974), pp. 45–58.
15. *Phanerozoic History of Australia*, J. J. Veevers, Ed. (Clarendon Press, Oxford, 1984), pp. 1–418.
16. A. B. Ronov, *Am. J. Sci.* **294**, 777 (1994).
17. T. J. Algeo, K. B. Seslavinsky, in *Sequence Stratigraphy and Depositional Response to Eustatic, Tectonic and Climatic Forcing*, B. U. Haq, Ed. (Kluwer Academic, Dordrecht, The Netherlands, 1995), pp. 209–246.
18. M. Gurnis, *Nature* **344**, 754 (1990).
19. J. P. Cogné, E. Humler, V. Courtillot, *Earth Planet. Sci. Lett.* **245**, 115 (2006).
20. J. P. Cogné, E. Humler, *Earth Planet. Sci. Lett.* **273**, 251 (2008).
21. D. Müller, M. Sdrollias, C. Gaina, B. Steinberger, C. Heine, *Science* **319**, 1357 (2008).
22. For example, in the Middle and Late Cambrian, backstripped estimates from the Canadian Rockies yielded values of up to 250 m of change, whereas in Utah for strata of the same age, only ~100 m of change was estimated (*29*). In Iowa, nonbackstripped measurements from the Ordovician through Mississippian sequences provided estimates of a few tens of meters to ~100 m of change (*30*). Estimates from topographic relief of incised valleys in the Silurian yielded values of ~30 to >70 m of change worldwide (*24, 31, 32*). In the British Isles, a cumulative rise of 227 m in the Early Carboniferous and ~200 m in the mid-Carboniferous was indicated after partial backstripping, with the magnitude of individual third-order events ranging between 5 and 56 m (*33*). Estimates from the Late Mississippian yield magnitudes of 30 to 100 m of change in the Illinois Basin (*34*). Other estimates from North America in this glacially dominated interval imply minimum amplitudes of 80 m, reaching >100 m of change from preserved relief on subaerial exposure surfaces of large algal bioherms (*35*).
23. M. Rygel, C. R. Fielding, T. D. Frank, L. P. Birgenheier, *J. Sed. Res.* **78**, 500 (2008).
24. M. E. Johnson, J. Y. Rong, S. Kershaw, *N.Y. State Mus. Bull.* **491**, 3 (1998).
25. Because of scalar limitations, the Paleozoic cycle chart of sea level fluctuations is presented in three separate figures, each comprising two of the periods of the Paleozoic Era (Figs. 1 to 3). The SOM also includes a complete downloadable color PDF version (fig. S1) of the cycle chart with more details [for example, major orogenic and anoxic events, regional stratigraphic subdivisions and biozonations, and sequence nomenclature (*36*) and known carbonate megabreccias as they have been synthesized from the worldwide data. The latter tend to occur in the carbonate systems at major drawdowns of sea level].
26. M. V. Caputo, J. C. Crowell, *Geol. Soc. Am. Bull.* **96**, 1020 (1985).
27. N. Eyles, G. M. Young, in *Earth's Glacial Record,* M. Deynoux *et al.*, Eds. (Cambridge Univ. Press, Cambridge, 1994), p. 1.
28. J. L. Isbell, M. F. Miller, K. L. Wolfe, P. A. Lenaker, *Geol. Soc. Am. Spec. Pap.* **370**, 5 (2003).
29. G. C. Bond, M. A. Kominz, *Geol. Soc. Am. Bull.* **95**, 155 (1984).
30. B. J. Witzke, B. J. Bunker, *Geol. Soc. Am. Spec. Pap.* **306**, 307 (1996).
31. H. A. McClure, *Palaeogeogr. Palaeoclimatol. Palaeoecol.* **25**, 315 (1978).
32. D. Vaslet, *Episodes* **13**, 147 (1990).
33. W. H. C. Ramsbottom, *Proc. Yorkshire Geol. Soc.* **43**, 473 (1981).
34. L. A. Smith Jr., J. F. Read, *J. Sed. Res.* **71**, 985 (2001).
35. G. S. Soreghan, K. A. Giles, *Geology* **27**, 255 (1999).
36. L. L. Sloss, *Geol. Soc. Am. Bull.* **74**, 93 (1963).

37. Many regional experts, too numerous to name, both in the United States and abroad discussed the Paleozoic stratigraphic issues with us. Their insights were indispensable for our synthesis. B.U.H. acknowledges his release by NSF for a sabbatical during 2007 to complete this work. Much of that time was spent at the Institut Français de Recherche pour l'exploitation de la Mer, Brest, France. Their Marine Geosciences Department's (particularly S. Berne's) help in organizing the stay is gratefully acknowledged. S.R.S. in particular acknowledges P. Heckel for many valuable leads into Paleozoic eustasy and the state of Iowa for its amazing Paleozoic record. The authors also thank T. Algeo, A. Hallam, W. Hay, J. Ogg, and another anonymous reviewer for their comments and suggestions. We dedicate this work to our friends and colleagues Peter Vail, Jan Hardenbol, and Tony Hallam, pioneers in the study of sea-level changes of the past.

Supporting Online Material

www.sciencemag.org/cgi/content/full/322/5898/64/DC1
SOM Text
Fig. S1
References

11 June 2008; accepted 29 August 2008
10.1126/science.1161648

Downloaded from www.sciencemag.org on October 2, 2008

EXTENDED PDF FORMAT
SPONSORED BY
usb
Products from Affymetrix
www.usbweb.com

Ultrafast X-ray Thomson Scattering of Shock-Compressed Matter

Andrea L. Kritcher, *et al.*

Science **322**, 69 (2008);
DOI: 10.1126/science.1161466

The following resources related to this article are available online at www.sciencemag.org (this information is current as of October 2, 2008):

Updated information and services, including high-resolution figures, can be found in the online version of this article at:
http://www.sciencemag.org/cgi/content/full/322/5898/69

Supporting Online Material can be found at:
http://www.sciencemag.org/cgi/content/full/322/5898/69/DC1

This article **cites 23 articles**, 4 of which can be accessed for free:
http://www.sciencemag.org/cgi/content/full/322/5898/69#otherarticles

This article appears in the following **subject collections**:
Physics
http://www.sciencemag.org/cgi/collection/physics

Information about obtaining **reprints** of this article or about obtaining **permission to reproduce this article** in whole or in part can be found at:
http://www.sciencemag.org/about/permissions.dtl

Downloaded from www.sciencemag.org on October 2, 2008

Science (print ISSN 0036-8075; online ISSN 1095-9203) is published weekly, except the last week in December, by the American Association for the Advancement of Science, 1200 New York Avenue NW, Washington, DC 20005. Copyright 2008 by the American Association for the Advancement of Science; all rights reserved. The title *Science* is a registered trademark of AAAS.

Ultrafast X-ray Thomson Scattering of Shock-Compressed Matter

Andrea L. Kritcher,[1,2]* Paul Neumayer,[2] John Castor,[2] Tilo Döppner,[2] Roger W. Falcone,[3] Otto L. Landen,[2] Hae Ja Lee,[3] Richard W. Lee,[2,3] Edward C. Morse,[1] Andrew Ng,[2] Steve Pollaine,[2] Dwight Price,[2] Siegfried H. Glenzer[2]

Spectrally resolved scattering of ultrafast K-α x-rays has provided experimental validation of the modeling of the compression and heating of shocked matter. The elastic scattering component has characterized the evolution and coalescence of two shocks launched by a nanosecond laser pulse into lithium hydride with an unprecedented temporal resolution of 10 picoseconds. At shock coalescence, we observed rapid heating to temperatures of 25,000 kelvin when the scattering spectra show the collective plasmon oscillations that indicate the transition to the dense metallic plasma state. The plasmon frequency determines the material compression, which is found to be a factor of 3, thereby reaching conditions in the laboratory relevant for studying the physics of planetary formation.

Shock wave heating is a key technique to produce matter at extreme conditions in the laboratory in which the physics of planetary formation (*1*) and modeling of planetary composition (*2*) can be tested. Contemporary experiments are designed to determine the equation of state (EOS) of light elements (*3*–*5*) or to measure effects of shock waves on matter, for example, to investigate effects by solar nebula shocks (*6*). In addition, the inertial confinement approach to controlled nuclear fusion (*7*) uses a deuterium-tritium–filled capsule that will be compressed to 1000 times solid density and heated to temperatures larger than the interior of the Sun by using a sequence of coalescing shock waves.

Previous shock wave experiments have been restricted to measuring particle and shock velocities (*4*). The experiments reported here directly measured the thermodynamic properties and dynamic structure factors of shocked matter. These experiments have become possible with the advent of penetrating powerful x-ray probes (*8*) produced by high-energy (300 J) petawatt-class ultrashort pulse lasers.

We shock-compressed lithium-hydride, LiH, with an energetic nanosecond laser and measured the conditions with spectrally resolved x-ray Thomson scattering (*9*). These pump-probe experiments show that efficient compression and heating occur at temperature and density conditions previously not accessible to quantitative in situ characterization. The experimental data show a factor of 3 compression with concomitant heating to T = 25,000 K = 2.2 eV, in broad agreement with radiation-hydrodynamic modeling. Although the range of temperatures traversed in phase space by shock compression agrees with calculations that use a quotidian (*10*) equation of state (QEOS), calculations with the Sesame (*11*) EOS tables provide a better match of the coalescence time.

In the schematic of the experiment shown together with a data record from the x-ray spectrometer (Fig. 1A), a 450-J laser beam (*12*) irradiates 300-μm-thick LiH (initial density of ρ_0 = 0.78 g cm^{-3}). The laser pulse was shaped in time (Fig. 1B) with a 4-ns-long foot at a laser intensity of 10^{13} W cm^{-2} followed by a 2-ns-long peak at 3 × 10^{13} W cm^{-2}. Radiation-hydrodynamic simulations (*13*) indicate that the two shock waves launched into the target compress the target to 2.2 g cm^{-3} and coalesce about 7 ns after the beginning of the laser drive (Fig. 1C).

An ultrashort pulse laser delayed from the nanosecond laser illuminates a titanium foil, producing a 10-ps-long K-α x-ray pulse (*14*) at an x-ray energy of E_0 = 4.51 keV that penetrates through the dense compressed LiH. By varying the delay between the nanosecond heater beam and the short pulse probe beam, we probed conditions before and during shock coalescence. The short pulse laser energy of 300 J is converted to Ti K-α with an efficiency of 5 × 10^{-5}, providing 10^{12} x-ray photons on target, sufficient for measurements of elastic and inelastic scattering components in a single shot.

The data record at shock coalescence shows features in the scattering spectrum resulting from interactions with the delocalized, that is, metallic, and bound electrons. The former undergo plasma (Langmuir wave) (*15*) oscillations at the plasma frequency that give rise to the inelastic plasmon scattering feature (*9*), whereas the latter give rise to elastic Rayleigh scattering.

The plasmon feature is downshifted from the incident 4.51-keV x-rays as determined by the Bohm Gross dispersion relation (*16*), with the leading term being the plasma frequency, ω_p =

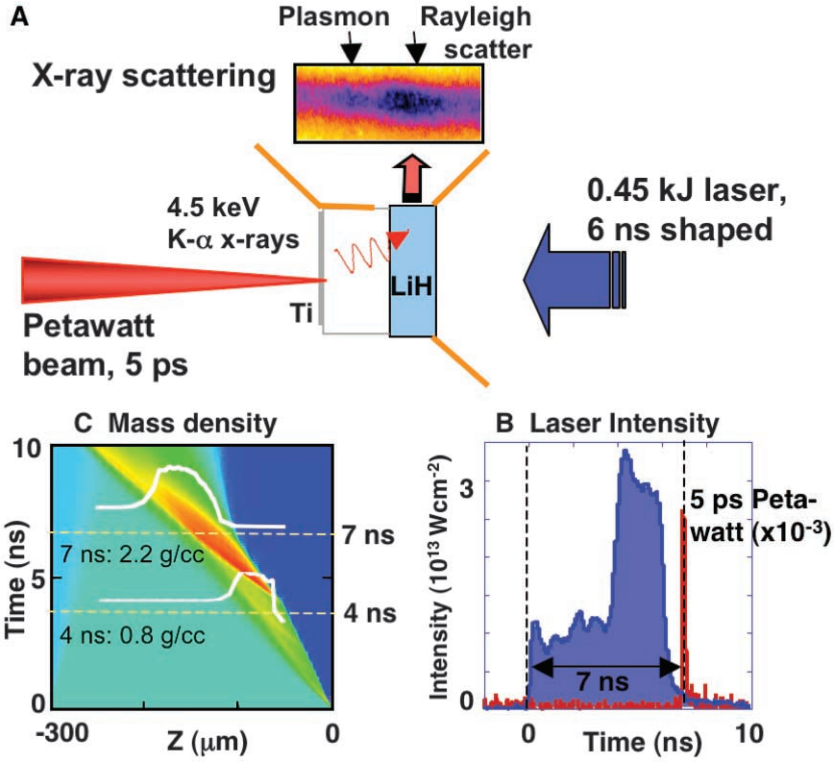

Fig. 1. (**A**) Schematic of the experimental setup. A short (10-ps), monoenergetic ($\Delta E/E$ < 0.5%), K-α x-ray probe is generated by ultrashort pulse laser irradiation of a titanium foil. The x-rays interact with matter compressed by a 6-ns-long shaped laser pulse. The x-ray Thomson scattering spectrum shows inelastic scattering on plasmons and elastic Rayleigh scattering features. (**B**) The evolution of the shocks is measured at various times by changing the delay between the ultrashort pulse laser and the long-pulse pump beam. (**C**) Radiation hydrodynamic modeling indicates coalescence of the shock waves at t = 7 ns.

[1]Nuclear Engineering Department, University of California Berkeley, Berkeley, CA 94709, USA. [2]Lawrence Livermore National Laboratory, Post Office Box 808, Livermore, CA 94551, USA. [3]Physics Department, University of California Berkeley, Berkeley, CA 94709, USA.

*To whom correspondence should be addressed. E-mail: kritcher@berkeley.edu

Downloaded from www.sciencemag.org on October 2, 2008

$(n_e e^2/\varepsilon_o m_e)^{1/2}$. Here, n_e is the electron density, ε_o the permittivity of free space, and e and m_e the electron charge and mass, respectively. Thermal corrections to the dispersion relation resulting from the propagation of the oscillations are small, whereas quantum diffraction is calculated from the Compton energy, $E_C = (h/2\pi)^2 k^2/2m_e$ = 9.3 eV. h is Planck's constant, and the magnitude of scattering vector k determines the scale length of electron density fluctuations probed in this experiment. The scattering vector depends only on the probe energy and scattering angle, $k = 4\pi(E_0/hc)\sin(\theta/2) = 1.6$ Å^{-1}. Thus, the downshift of the plasmon provides the electron density from its main dependence on the plasma frequency.

The strongly bound K-shell electrons of Li and H that interact with x-ray photons are not excited by the scattering process because their ionization potential is greater than the Compton energy, and therefore those electrons scatter elastically. The intensity of the elastic scattering feature is sensitive to the number of strongly bound electrons and the ion-ion structure factor; the latter is sensitive to the ion temperature. Hence, the temperature can be inferred from the elastic scattering strength.

The experimental scattering spectrum at shock coalescence, t = 7 ns, and at t = 4 ns, just before the second strong shock wave was launched, are shown in Fig. 2. These spectra are fit with calculated scattering profiles by using the theoretical dynamic form factor of (*17*). Also shown is a spectral profile of the Ti K-α source measured with the same spectrometer. In addition to the short probe pulse duration required to time-resolve the shock wave coalescence, this x-ray source exhibits no spectral features on the red wing of the K-α doublet, allowing accurate observations of inelastic scattering on plasmons.

The scattering signal at t = 4 ns shows only elastic scattering, indicating a lack of free electrons. The theoretical fit that takes into account contributions from bound and free electrons limits the degree of ionization to $Z^* < 0.1$. However, the intensity of the elastic scattering peak alone has increased by 40% ± 10% compared with scattering from cold samples, indicating a $T < 0.4$ eV.

In contrast, when the shock waves coalesce at t = 7 ns, strong plasmon oscillations give rise to inelastic scattering downshifted from the elastic peak by ΔE_{pl} = 24 eV. In this case, the elastic scattering signal has increased by 100% ± 10% compared with scattering from cold samples, indicating T = 2.2 eV. Compression and heating results in ionized material with Z^* = 1 for $Li^{(+)}H$ as determined from the shape of the scattering spectrum. An error bar of +2% and –10% is inferred from the minimum of the root mean square difference between the experimental data and the theoretical spectrum (*18*).

For the degenerate systems encountered here, the plasma screening length, λ_S = 0.57 Å, at which local electric fields are shielded by mobile charge carriers, approaches the Thomas-Fermi length (*17*). Therefore, scattering is collective with a scattering parameter (*19*) $\alpha = 1/k\lambda_S$ = 1.1, where the scattering scale length is on the order of the screening length required for the observation of plasmon oscillations.

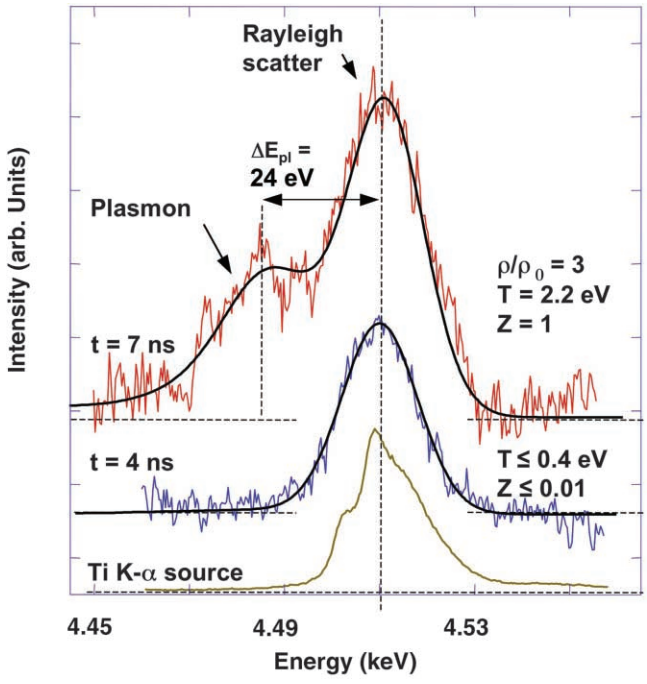

Fig. 2. X-ray scattering spectrum from shocked LiH, showing elastic Rayleigh scattering and inelastic plasmon scattering features. At t = 7 ns (top), the plasmon energy shift of 24 eV indicates 3× compression, whereas the intensity of the elastic scattering feature shows heating to temperatures of 2.2 eV. Earlier in time only elastic scattering is observed (middle) as demonstrated when compared with the K-α source spectrum (bottom). The observation of plasmons at t = 7 ns indicates the transition to the metallic free electron plasma in the solid phase.

The plasmon shift determined by the calculated spectra provides the electron density, $n_e = 1.7 \times 10^{23}$ cm^{-3}. The density is obtained with an error of 10% because of noise in these single-shot data. Accurate knowledge of the electron density further determines the absolute electron-electron structure factor (*20*). In the long-wavelength limit

$$S_{aa}(k) = k^2/[k^2 + (1/\lambda_S)^2] \quad (1)$$

with a indicating e or i for electron or ion, respectively. With λ_S for a partly degenerate electron fluid, we find $S_{ee}(k = 1.6$ Å$^{-1}) = 0.46$. This value, combined with the measured elastic and inelastic scattering amplitude, determines the absolute ion-ion structure factor, which yields the ion temperature from the ion Debye screening length. The spectral calculations and parameters of Fig. 2 include multiple-species ion-ion structure factors from one-component electron-ion interaction potentials (*17*) that have been shown to be consistent with previous experiments (*9*).

The evolution of the measured temperature as a function of time is shown (Fig. 3) along with results from radiation-hydrodynamic calculations using the code LASNEX (*18*). The strong rise at t = 7 ns indicates coalescence of the shock waves. The temperature has been inferred with an error of 10 to 20% because of noise. Partial scattering from uncompressed material has been accounted for, resulting in a correction of about 10%.

The simulation results shown in Fig. 3 are mainly dependent on the choice of the EOS and rather insensitive to details in radiation transport and heat conduction. The ranges of temperatures arise from variations in the amount of impurities and oxide layers consistent with target characterization. The QEOS, being the simpler model, includes a modified electronic Thomas-Fermi statistical model with ion thermal motion calculated beyond the Grüneisen EOS by including temperature-dependent corrections to the pressure. This model is consistent with the wide range of temperatures accessed in this experiment.

The Sesame EOS includes atomic structure based on solutions of the single-particle quantum levels in the self-consistent field of an atom (*21*). The peak temperature and the experimentally observed coalescence time are in excellent agreement with modeling that uses the Sesame EOS. However, early in time the agreement is less satisfactory, indicating that a future comparison with first-principle statistical models (*22*) will be of interest to understand these weakly shocked systems.

At peak temperature, the calculations indicate pressures in the range of P = 300 to 420 GPa. With Z^* = 1 and the electron density from the plasmon data, we find a density of $\rho = 2.25$ g cm^{-3}, corresponding to three times compressed LiH. This value is consistent with the EOS data obtained from density functional perturbation theory (*23*) and approaches conditions where a pressure-induced insulator-metal transition is predicted (*24*).

Our results demonstrate the capability to measure temperature and density in dense matter during shock compression with 10-ps temporal resolution. The experiments have shown the transition to a metallic plasma state in the solid phase, resulting in the observation of plas-

Downloaded from www.sciencemag.org on October 2, 2008

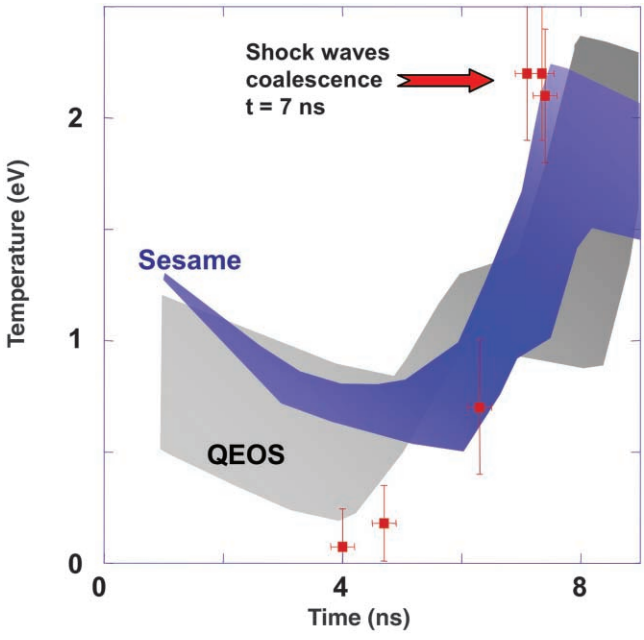

Fig. 3. The temperature of the shocked LiH as a function of time from x-ray Thomson scattering measurements and from radiation-hydrodynamic modeling using different EOS models. The range of temperatures for each model accounts for LiOH surface impurities (lower bounds) to no impurities (upper bounds). The experiments and calculations demonstrate efficient heating by shock coalescence, with small differences in shock timing resolved by the short K-α x-ray pulses. Error bars result mainly from noise in the experimental data.

mons. This feature has further allowed testing of radiation-hydrodynamic calculations with different EOS models for shock-compressed matter. This technique is opportune for inertial confinement fusion experiments that will achieve extreme densities, for example, on the National Ignition Facility (*25*).

Lastly, the K-α x-ray source used in this study provides the same number of x-ray photons on target as projected for future x-ray free electron laser facilities (*26*, *27*). This indicates that x-ray Thomson scattering experiments on dense matter will soon be accessible for high-repetition measurements of thermodynamic properties with 20- to 200-fs temporal resolution.

References and Notes

1. H. C. Connolly Jr., S. G. Love, *Science* **280**, 62 (1998).
2. T. Guillot, *Science* **286**, 72 (1999).
3. N. C. Holmes, M. Ross, W. J. Nellis, *Phys. Rev. B* **52**, 15835 (1995).
4. G. W. Collins *et al.*, *Science* **281**, 1178 (1998).
5. M. D. Knudson, D. L. Hanson, J. E. Bailey, C. A. Hall, J. R. Asay, *Phys. Rev. Lett.* **87**, 225501 (2001).
6. C. P. McKay, W. J. Borucki, *Science* **276**, 390 (1997).
7. J. D. Lindl *et al.*, *Phys. Plasmas* **11**, 339 (2004).
8. O. L. Landen *et al.*, *Rev. Sci. Instrum.* **72**, 627 (2001).
9. S. H. Glenzer *et al.*, *Phys. Rev. Lett.* **98**, 065002 (2007).
10. R. M. More, K. H. Warren, D. A. Young, G. B. Zimmerman, *Phys. Fluids* **31**, 3059 (1988).
11. S. Crockett, *Los Alamos National Laboratory Report No. LA-UR-06-8403* (Los Alamos National Laboratory, Los Alamos, NM, 2006).
12. B. C. Stuart *et al.*, in report no. UCRL-CONF-221530 (Conference on Lasers and Electro-Optics, IEEE/LEOS, Lasers and Electro-Optics Society and the Optical Society, Long Beach, CA, 21 to 26 May 2006), pp. 56–68.
13. J. J. MacFarlane, I. E. Golovkin, P. R. Woodruff, *J. Quant. Spectrosc. Radiat. Transfer* **99**, 381 (2006).
14. H. Chen *et al.*, *Phys. Rev. E* **76**, 056402 (2007).
15. L. Tonks, I. Langmuir, *Phys. Rev.* **33**, 195 (1929).
16. D. Bohm, E. P. Gross, *Phys. Rev.* **75**, 1851 (1949).
17. G. Gregori, A. Ravasio, A. Höll, S. H. Glenzer, S. J. Rose, *High Energy Density Phys.* **3**, 99 (2007).
18. Materials and methods are available as supporting material on *Science* Online.
19. J. Sheffield, *Plasma Scattering of Electromagnetic Radiation* (Academic Press, New York, 1975).
20. S. Ichimaru, *Rev. Mod. Phys.* **54**, 1017 (1982).
21. D. A. Lieberman, *Phys. Rev. B* **20**, 4798 (1979).
22. T. Ogitsu, E. Schwegler, F. Gygi, G. Galli, *Phys. Rev. Lett.* **91**, 175502 (2003).
23. W. Yu, C. Jin, A. Kohlmeyer, *J. Phys. Condens. Matter* **19**, 086209 (2007).
24. Y. Wang, R. Ahuja, B. Johansson, *Phys. Status Solidi* **235**, 470 (2003).
25. E. Moses, C. R. Wuest, *Fusion Sci. Tech. (Paris)* **47**, 314 (2005).
26. R. Akre *et al.*, *Phys. Rev. Spec. Top. Accelerators Beams* **11**, 030703 (2008).
27. W. Ackermann *et al.*, *Nat. Photonics* **1**, 336 (2007).

28. This work was performed under the auspices of the U.S. Department of Energy (DOE) by Lawrence Livermore National Laboratory under contract DE-AC52-07NA27344. This work was further supported by a DOE grant, the NA-16 Intermediate Facility Initiative, grant 08-ERI-002, grant 08-LW-004, and the Lawrence Scholar Program fellowship.

Supporting Online Material

www.sciencemag.org/cgi/content/full/322/5898/69/DC1
Materials and Methods
Figs. S1 to S4
References

6 June 2008; accepted 27 August 2008
10.1126/science.1161466

Time Reversal and Negative Refraction

J. B. Pendry

Time reversal and negative refraction have been shown to be intimately linked processes. We propose a scheme that exploits transitions between positive and negative frequencies to mimic negative refraction at an interface and hence to make a negatively refracting lens. The theory applies equally to electromagnetic and acoustic waves. We also propose an experimental realization, and under ideal circumstances this lens can exhibit subwavelength resolution, limited only by the strength of the time-reversed signal.

In a time-reversal experiment, a wave might strike a surface where it is reflected into a new state such that its phase evolves backward in time (*1*, *2*). As a result, a wave originally diverging from a source now converges back onto that source. In contrast, a wave striking a negatively refracting medium (*3*, *4*) is transmitted into the medium, where its phase evolves backward in space (Fig. 1), and the wave converges to a focus inside the medium. There is an appealing symmetry between the two processes, provoking a deeper inquiry into their relationship.

Let us examine the similarities between the two processes. Negative refraction implies that, as a pulse of waves moves forward, the phase evolves in the opposite direction. In other words, the group and phase velocities are oppositely directed

$$\frac{\omega}{k}\frac{d\omega}{dk} < 0 \qquad (1)$$

and hence moving into the negatively refracting medium begins the process of phase reversal (here, ω is the frequency and k is the wave vector). Sometimes the same medium can host both positively and negatively refracting states. This may happen in certain chiral media (*5*), where the spin of the photon dictates positive or negative refraction, or in graphene (*6*, *7*), where the pseudospin of an electron close to the Fermi energy controls the phase evolution. Such media are designated as "self-conjugate."

Self conjugation forges the link between time reversal and negative refraction. Consider a wave of the form

$$\mathbf{E} = E_0\,\hat{\mathbf{e}}_0 \exp(i\mathbf{k}\cdot\mathbf{r} - i\omega t) \qquad (2)$$

where $\mathbf{E}$ is the electric component of the field, E_0 is a constant, $\hat{\mathbf{e}}_0$ is a unit vector defining the polarization, $\boldsymbol{r}$ is a position vector, and t is time. Now shift the frequency down by an amount $\delta\omega = 2\omega$ (here, $\mathbf{E}'$ is the shifted electric field)

$$\mathbf{E}' = E_0\,\hat{\mathbf{e}}_0 \exp(i\mathbf{k}\cdot\mathbf{r} + i\omega t) \qquad (3)$$

Reversing frequency has the same effect as reversing time (Fig. 2). The same figure shows that, if negative frequencies are included, any linearly dispersing medium can be regarded as self-

Department of Physics, The Blackett Laboratory, Imperial College London, London SW7 2AZ, UK. E-mail: j.pendry@imperial.ac.uk

Downloaded from www.sciencemag.org on October 2, 2008

EXTENDED PDF FORMAT
SPONSORED BY
usb
Products from Affymetrix
www.usbweb.com

Time Reversal and Negative Refraction
J. B. Pendry, *et al.*
Science **322**, 71 (2008);
DOI: 10.1126/science.1162087

The following resources related to this article are available online at www.sciencemag.org (this information is current as of October 2, 2008):

Updated information and services, including high-resolution figures, can be found in the online version of this article at:
http://www.sciencemag.org/cgi/content/full/322/5898/71

Supporting Online Material can be found at:
http://www.sciencemag.org/cgi/content/full/1162087/DC1

This article **cites 16 articles**, 3 of which can be accessed for free:
http://www.sciencemag.org/cgi/content/full/322/5898/71#otherarticles

This article appears in the following **subject collections**:
Physics
http://www.sciencemag.org/cgi/collection/physics

Information about obtaining **reprints** of this article or about obtaining **permission to reproduce this article** in whole or in part can be found at:
http://www.sciencemag.org/about/permissions.dtl

Downloaded from www.sciencemag.org on October 2, 2008

Science (print ISSN 0036-8075; online ISSN 1095-9203) is published weekly, except the last week in December, by the American Association for the Advancement of Science, 1200 New York Avenue NW, Washington, DC 20005. Copyright 2008 by the American Association for the Advancement of Science; all rights reserved. The title *Science* is a registered trademark of AAAS.

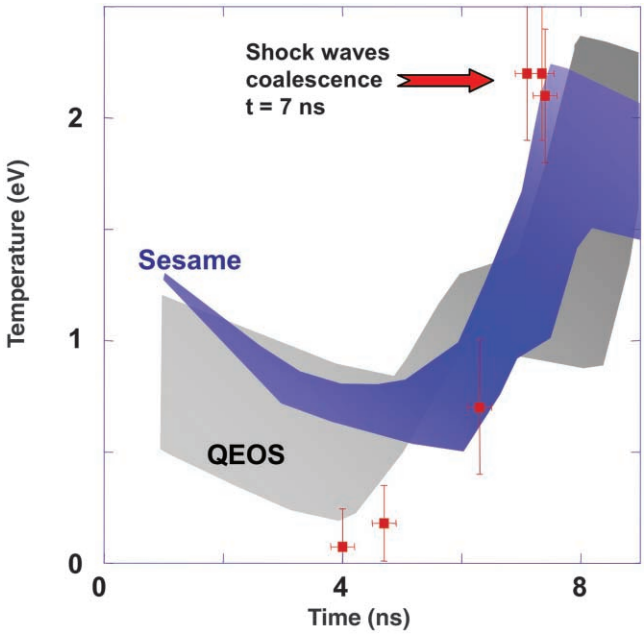

Fig. 3. The temperature of the shocked LiH as a function of time from x-ray Thomson scattering measurements and from radiation-hydrodynamic modeling using different EOS models. The range of temperatures for each model accounts for LiOH surface impurities (lower bounds) to no impurities (upper bounds). The experiments and calculations demonstrate efficient heating by shock coalescence, with small differences in shock timing resolved by the short K-α x-ray pulses. Error bars result mainly from noise in the experimental data.

mons. This feature has further allowed testing of radiation-hydrodynamic calculations with different EOS models for shock-compressed matter. This technique is opportune for inertial confinement fusion experiments that will achieve extreme densities, for example, on the National Ignition Facility (*25*).

Lastly, the K-α x-ray source used in this study provides the same number of x-ray photons on target as projected for future x-ray free electron laser facilities (*26*, *27*). This indicates that x-ray Thomson scattering experiments on dense matter will soon be accessible for high-repetition measurements of thermodynamic properties with 20- to 200-fs temporal resolution.

References and Notes

1. H. C. Connolly Jr., S. G. Love, *Science* **280**, 62 (1998).
2. T. Guillot, *Science* **286**, 72 (1999).
3. N. C. Holmes, M. Ross, W. J. Nellis, *Phys. Rev. B* **52**, 15835 (1995).
4. G. W. Collins *et al.*, *Science* **281**, 1178 (1998).
5. M. D. Knudson, D. L. Hanson, J. E. Bailey, C. A. Hall, J. R. Asay, *Phys. Rev. Lett.* **87**, 225501 (2001).
6. C. P. McKay, W. J. Borucki, *Science* **276**, 390 (1997).
7. J. D. Lindl *et al.*, *Phys. Plasmas* **11**, 339 (2004).
8. O. L. Landen *et al.*, *Rev. Sci. Instrum.* **72**, 627 (2001).
9. S. H. Glenzer *et al.*, *Phys. Rev. Lett.* **98**, 065002 (2007).
10. R. M. More, K. H. Warren, D. A. Young, G. B. Zimmerman, *Phys. Fluids* **31**, 3059 (1988).
11. S. Crockett, *Los Alamos National Laboratory Report No. LA-UR-06-8403* (Los Alamos National Laboratory, Los Alamos, NM, 2006).
12. B. C. Stuart *et al.*, in report no. UCRL-CONF-221530 (Conference on Lasers and Electro-Optics, IEEE/LEOS, Lasers and Electro-Optics Society and the Optical Society, Long Beach, CA, 21 to 26 May 2006), pp. 56–68.
13. J. J. MacFarlane, I. E. Golovkin, P. R. Woodruff, *J. Quant. Spectrosc. Radiat. Transfer* **99**, 381 (2006).
14. H. Chen *et al.*, *Phys. Rev. E* **76**, 056402 (2007).
15. L. Tonks, I. Langmuir, *Phys. Rev.* **33**, 195 (1929).
16. D. Bohm, E. P. Gross, *Phys. Rev.* **75**, 1851 (1949).
17. G. Gregori, A. Ravasio, A. Höll, S. H. Glenzer, S. J. Rose, *High Energy Density Phys.* **3**, 99 (2007).
18. Materials and methods are available as supporting material on *Science* Online.
19. J. Sheffield, *Plasma Scattering of Electromagnetic Radiation* (Academic Press, New York, 1975).
20. S. Ichimaru, *Rev. Mod. Phys.* **54**, 1017 (1982).
21. D. A. Lieberman, *Phys. Rev. B* **20**, 4798 (1979).
22. T. Ogitsu, E. Schwegler, F. Gygi, G. Galli, *Phys. Rev. Lett.* **91**, 175502 (2003).
23. W. Yu, C. Jin, A. Kohlmeyer, *J. Phys. Condens. Matter* **19**, 086209 (2007).
24. Y. Wang, R. Ahuja, B. Johansson, *Phys. Status Solidi* **235**, 470 (2003).
25. E. Moses, C. R. Wuest, *Fusion Sci. Tech. (Paris)* **47**, 314 (2005).
26. R. Akre *et al.*, *Phys. Rev. Spec. Top. Accelerators Beams* **11**, 030703 (2008).
27. W. Ackermann *et al.*, *Nat. Photonics* **1**, 336 (2007).

28. This work was performed under the auspices of the U.S. Department of Energy (DOE) by Lawrence Livermore National Laboratory under contract DE-AC52-07NA27344. This work was further supported by a DOE grant, the NA-16 Intermediate Facility Initiative, grant 08-ERI-002, grant 08-LW-004, and the Lawrence Scholar Program fellowship.

Supporting Online Material

www.sciencemag.org/cgi/content/full/322/5898/69/DC1
Materials and Methods
Figs. S1 to S4
References

6 June 2008; accepted 27 August 2008
10.1126/science.1161466

Time Reversal and Negative Refraction

J. B. Pendry

Time reversal and negative refraction have been shown to be intimately linked processes. We propose a scheme that exploits transitions between positive and negative frequencies to mimic negative refraction at an interface and hence to make a negatively refracting lens. The theory applies equally to electromagnetic and acoustic waves. We also propose an experimental realization, and under ideal circumstances this lens can exhibit subwavelength resolution, limited only by the strength of the time-reversed signal.

In a time-reversal experiment, a wave might strike a surface where it is reflected into a new state such that its phase evolves backward in time (*1*, *2*). As a result, a wave originally diverging from a source now converges back onto that source. In contrast, a wave striking a negatively refracting medium (*3*, *4*) is transmitted into the medium, where its phase evolves backward in space (Fig. 1), and the wave converges to a focus inside the medium. There is an appealing symmetry between the two processes, provoking a deeper inquiry into their relationship.

Let us examine the similarities between the two processes. Negative refraction implies that, as a pulse of waves moves forward, the phase evolves in the opposite direction. In other words, the group and phase velocities are oppositely directed

$$\frac{\omega}{k}\frac{d\omega}{dk} < 0 \qquad (1)$$

and hence moving into the negatively refracting medium begins the process of phase reversal (here, ω is the frequency and k is the wave vector). Sometimes the same medium can host both positively and negatively refracting states. This may happen in certain chiral media (*5*), where the spin of the photon dictates positive or negative refraction, or in graphene (*6*, *7*), where the pseudospin of an electron close to the Fermi energy controls the phase evolution. Such media are designated as "self-conjugate."

Self conjugation forges the link between time reversal and negative refraction. Consider a wave of the form

$$\mathbf{E} = E_0\,\hat{\mathbf{e}}_0 \exp(i\mathbf{k}\cdot\mathbf{r} - i\omega t) \qquad (2)$$

where $\mathbf{E}$ is the electric component of the field, E_0 is a constant, $\hat{\mathbf{e}}_0$ is a unit vector defining the polarization, $\boldsymbol{r}$ is a position vector, and t is time. Now shift the frequency down by an amount $\delta\omega = 2\omega$ (here, $\mathbf{E}'$ is the shifted electric field)

$$\mathbf{E}' = E_0\,\hat{\mathbf{e}}_0 \exp(i\mathbf{k}\cdot\mathbf{r} + i\omega t) \qquad (3)$$

Reversing frequency has the same effect as reversing time (Fig. 2). The same figure shows that, if negative frequencies are included, any linearly dispersing medium can be regarded as self-

Department of Physics, The Blackett Laboratory, Imperial College London, London SW7 2AZ, UK. E-mail: j.pendry@imperial.ac.uk

Downloaded from www.sciencemag.org on October 2, 2008

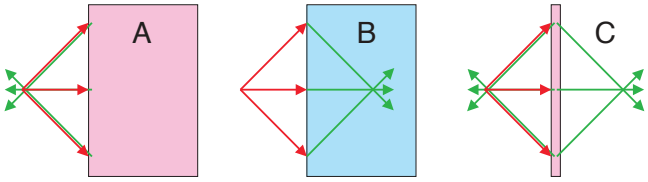

Fig. 1. **(A)** Medium (A) time-reverses a wave winding the phase backward in time to refocus on the source. **(B)** Medium (B) is negatively refracting and reverses the spatial evolution of the phase refocusing at some point inside the medium. **(C)** A thin sheet, (C), of time-reversing material produces negative frequency waves on both sides of the sheet: It both time-reverses and negatively refracts.

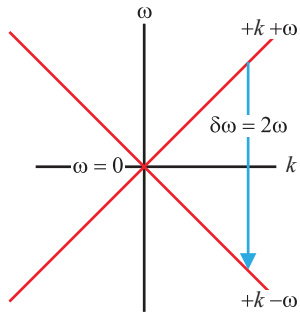

Fig. 2. Dispersion of a wave in a medium with constant velocity $\omega = ck$ (where c is the velocity of light). Both positive and negative frequencies are displayed. Time reversal can be understood as a vertical transition between positive and negative frequencies.

conjugate and contains a negatively dispersing band. Of course, negative refraction is never seen at an interface between ordinary media, because a positive frequency band has to refract into another positive frequency band or a negative frequency into another negative frequency. Both cases imply a positive angle of refraction. This is always true of passive systems.

The link between negative refraction and time reversal has been remarked on before in (*8*), where a phase-conjugating interface between two regions of space was postulated as a particular mathematical construction—one of many possible. Apparently independently of the earlier work, the analogy was carried further in (*9*), where it was pointed out that this particular interface supported surface resonances of the same character as those appearing at interfaces with negatively refracting materials. Somewhat later in (*10*), a practical realization of this mathematical scheme was proposed, but only a partial realization. Whereas the scheme is effective for the far field, it does not reproduce the same boundary conditions for evanescent states and therefore supports no surface modes. In fact, a realization of the boundary condition had already been implemented in (*11*), but again only effective for the far field.

Now consider a possible physical realization of the present approach. By making the interface time-dependent, more interesting things can happen. Consider the simplest case where a thin sheet of dielectric separates two regions of otherwise empty space, and let the permittivity uniformly pulsate at a frequency of 2ω. This parametric oscillation will induce transitions between positive and negative frequencies in a manner familiar to four-wave mixing experiments. There is an important difference in our configuration: If the dielectric sheet is much thinner than the wavelength, there is no momentum conservation normal to the sheet; only parallel momentum is conserved [scattering from a thin sheet has also been considered (*12*)]. Thus, the pulsating sheet generates two waves that are shown in Fig. 1C: (i) a conventional time-reversed wave that returns to the source on the same side of the sheet and (ii) another with opposite momentum normal to the sheet exiting on the far side to form an image in the manner of a medium with a refractive index $n = -1$.

Our configuration is an alternative to the Veselago lens, except that this version focuses only the far field and, like other schemes (*8*–*11*), is subject to wavelength limitations on resolution. It lacks the extraordinary property of a true $n = -1$ material of subwavelength resolution. This limitation can be overcome by the addition of further components to the system.

Figure 3 shows a system containing two time-reversing sheets separated by a distance d. Waves are reversed by the first sheet and again by the second, returning to "positive frequency" on emerging from the system.

More formally, transmission and reflection coefficients (T and R) are defined for the sheets that are assumed to be identical. Furthermore, if the sheets are very thin

$$T = R \tag{4}$$

This result can easily be understood by noting that transmitted and reflected waves are sourced on the same set of currents and charges. Because the sources are two-dimensional (2D), they are mirror symmetrical about the plane and hence give rise to the same transmitted and reflected fields.

The component of the wave vector perpendicular to the sheets is given by

$$k_z = +\sqrt{\omega^2/c_0^2 - k_x^2 - k_y^2} \tag{5}$$

when k_z is real, and by

$$k_z = +i\sqrt{k_x^2 + k_y^2 - \omega^2/c_0^2} \tag{6}$$

when k_z is imaginary.

The transmitted wave between the two sheets can be written in the case of real k_z (where R is a constant, $\|$ denotes the component of a vector parallel to the plane of the sheet, and d is defined in Fig. 3

$$\mathbf{E} = E_0\hat{\mathbf{e}}\, Re^{i\mathbf{k}_\parallel\cdot\mathbf{r}_\parallel} \times \begin{bmatrix} +(1 + R^2 + \cdots)e^{(-ik_z z + i\omega t)} \\ +(R + R^3 + \cdots)e^{(-ik_z z - i\omega t)} \end{bmatrix} = E_0\hat{\mathbf{e}}Re^{i\mathbf{k}_\parallel\cdot\mathbf{r}_\parallel} \times \begin{bmatrix} +(1-R^2)^{-1}e^{(-ik_z z + i\omega t)} \\ +R(1-R^2)^{-1}e^{(-ik_z z - i\omega t)} \end{bmatrix}, 0 < z < d \tag{7}$$

Note the careful choice of signs in the exponents dictated by the requirement that each set of waves must carry flux away from the last surface of interaction. At each reflection and transmission, the frequency is reversed. See the supporting online material (SOM) for further discussion of this point.

A slightly different result follows when k_z is imaginary

$$\mathbf{E} = E_0\hat{\mathbf{e}}\, Re^{i\mathbf{k}_\parallel\cdot\mathbf{r}_\parallel} \times \begin{bmatrix} +(1 + R^2e^{2ik_z d} + \cdots)e^{(+ik_z z + i\omega t)} \\ +(R + R^3e^{2ik_z d} + \cdots)e^{(-ik_z(z-2d) - i\omega t)} \end{bmatrix} = E_0\hat{\mathbf{e}}Re^{i\mathbf{k}_\parallel\cdot\mathbf{r}_\parallel} \times \begin{bmatrix} +(1 - R^2e^{2ik_z d})^{-1}e^{(+ik_z z + i\omega t)} \\ +R(1 - R^2e^{2ik_z d})^{-1}e^{(-ik_z(z-2d) - i\omega t)} \end{bmatrix}, 0 < z < d \tag{8}$$

Finally, the waves are allowed to emerge from the end of the cavity. For real k_z

$$\mathbf{E} = E_0\hat{\mathbf{e}}\,\frac{R^2e^{i\mathbf{k}_\parallel\cdot\mathbf{r}_\parallel + ik_z(z-2d) - i\omega t}}{1 - R^2}, d < z \tag{9}$$

For imaginary k_z

$$\mathbf{E} = E_0\hat{\mathbf{e}}\,\frac{R^2e^{i\mathbf{k}_\parallel\cdot\mathbf{r}_\parallel + ik_z z - i\omega t}}{1 - R^2e^{2ik_z d}}, d < z \tag{10}$$

Because the sheets are connected to a source of power, there is no longer a requirement that energy is conserved, so (at least in theory) the limit of very large transmission and reflection coefficients could be envisaged

$$\lim_{R\to\infty}\mathbf{E} = -E_0\hat{\mathbf{e}}e^{i\mathbf{k}_\parallel\cdot\mathbf{r}_\parallel + ik_z(z-2d) - i\omega t}, d < z \tag{11}$$

It is assumed that Eq. 4 is true, and the limit is independent of whether k_z is real or imaginary. In the same limit, it can be shown that the sheets do not scatter waves back into the region $z < 0$.

The interpretation of Eq. 11 is that fields are translated along the axis normal to the sheets by a distance $2d$. In other words, objects between $-d < z < 0$ appear as images between $d < z < 2d$. Furthermore, according to Eq. 11, all Fourier components of the image that satisfy

$$|R| >> \left|e^{ik_z d}\right| \tag{12}$$

contribute their due weight to the image, and in the limit $R \to \infty$ the image tends to perfection.

Downloaded from www.sciencemag.org on October 2, 2008

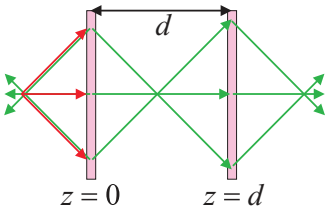

Fig. 3. Two thin sheets of time-reversing material produce a focusing effect very similar to a negatively refracting lens. The system is capable of subwavelength resolution.

Unlike the perfect lens based on negative refraction (*13*), loss is not an issue in this instance because the fields are translated through loss-less vacuum. The issue here is whether a time-reversing sheet can be found sufficiently powerful to give the resolution, Δ, required

$$\Delta \approx 1/k_{\parallel \max} \approx d/\ln R \qquad (13)$$

A scheme for subwavelength resolution was also proposed in (*9*) but, as noted above, this scheme depended on the existence of surface states derived from a mathematically postulated boundary for which no physical realization has so far been suggested.

Although our discussion has been in terms of electromagnetic waves, the same principles apply to any waves and particularly to acoustic waves, where time-reversal studies are also well developed (*14*).

Our original discussion (illustrated in Fig. 2) assumes a single-step transition from +ω to –ω. Such processes occur but are very weak. At optical frequencies, perhaps the best system for the realization of these ideas is a four-wave mixing experiment: One of two counterpropagating pump beams of the same frequency as the signal writes a hologram. The second pump beam then reads the hologram to produce a time-reversed signal. In other words, there is a two-step process in which there first occurs a transition $+\omega \rightarrow 0$ and then a second transition $0 \rightarrow -\omega$. This process has much in common with the recent proposal for a subwavelength focusing device (*15*), except that in our scheme the system writes its own hologram.

As a generalization of the analogy, any positively refracting medium can have the sign of its refraction reversed by coating the surface with a phase-reversing sheet. This leads to the possibility of curved lenses that can magnify an object (*16*).

In principle, our new lens can be realized if the hologram is written in a thin sheet of nonlinear material. In practice, such a hologram would be very weak, and instead, 3D holograms are written if a strong output is desired. As a consequence of the 3D nature of the hologram, the second phase-reversed beam (shown on the right of Fig. 1C) is not seen, but if the left-hand surface of the medium is half silver (Fig. 4), reflection of the phase-reversed beam will generate an image

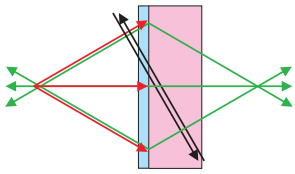

Fig. 4. In a four-wave mixing experiment, two counterpropagating waves first create a hologram and then diffract off the hologram to form a phase-reversed beam. A half-silvered mirror reflects the reversed beam to form an image on the far side of the system.

to the right of the system reproducing the effect predicted in Fig. 1C and mimicking the Veselago negatively refracting lens. However, the 3D nature of the hologram precludes any subwavelength resolution.

Creating a 2D hologram and attaining the ideal shown in Fig. 3 will be a challenge. Enhancing the nonlinearity of existing media—possibly through the use of plasmonic or metamaterial layers to enhance the local fields (*17*)—may offer a route to realizing a 2D version and hence subwavelength resolution. Further discussion of the practicalities of a four-wave mixing scheme can be found in the SOM.

References and Notes

1. J. P. Woerdman, *Opt. Commun.* **2**, 212 (1970).
2. P. Yeh, *Introduction to Photorefractive Nonlinear Optics* (Wiley, New York, 1993).
3. V. G. Veselago, *Sov. Phys. Usp.* **10**, 509 (1968).
4. J. B. Pendry, *Contemp. Phys.* **45**, 191 (2004).
5. J. B. Pendry, *Science* **306**, 1353 (2004).
6. K. Kobayashi, *J. Phys. Condens. Matter* **18**, 3703 (2006).
7. V. V. Cheianov, V. Fal'ko, B. L. Altshuler, *Science* **315**, 1252 (2007).
8. M. Nieto-Vesperinas, E. Wolf, *J. Opt. Soc. Am. A* **2**, 1429 (1985).
9. S. Maslovski, S. Tretyakov, *J. Appl. Phys.* **94**, 4241 (2003).
10. O. Malyuskin, V. Fusco, A. G. Schuchinsky, *IEEE Trans. Antenn. Propag.* **54**, 1399 (2006).
11. C. A. Allen, K. M. K. H. Leong, T. Itoh, *IEEE Int. Microwave Theory Tech. Symp. Dig.* **3**, 1875 (2003).
12. M. Wubs, A. Lagendijk, *Phys. Rev. E Stat. Nonlin. Soft Matter Phys.* **65**, 046612 (2002).
13. J. B. Pendry, *Phys. Rev. Lett.* **85**, 3966 (2000).
14. S. Yon, M. Tanter, M. Fink, *J. Acoust. Soc. Am.* **113**, 1533 (2003).
15. R. Merlin, *Science* **317**, 927 (2007); published online 11 July 2007 (10.1126/science.1143884).
16. J. B. Pendry, S. A. Ramakrishna, *J. Phys. Condens. Matter* **15**, 6345 (2003).
17. J. B. Pendry, A. J. Holden, D. J. Robbins, W. J. Stewart, *IEEE Trans. Microwave Theory Tech.* **47**, 2075 (1999).

18. I thank the Engineering and Physical Sciences Research Council for a Senior Fellowship, M. Damsen for educating me in various aspects of four-wave mixing, S. Maier for discussions on plasmonic enhancements of fields, and A. Lagendijk for comments on the manuscript.

Supporting Online Material

www.sciencemag.org/cgi/content/full/1162087/DC1
SOM Text
Figs. S1 to S6

20 June 2008; accepted 20 August 2008
Published online 28 August 2008;
10.1126/science.1162087
Include this information when citing this paper.

Surface-Modified Carbon Nanotubes Catalyze Oxidative Dehydrogenation of *n*-Butane

Jian Zhang, Xi Liu, Raoul Blume, Aihua Zhang, Robert Schlögl, Dang Sheng Su*

Butenes and butadiene, which are useful intermediates for the synthesis of polymers and other compounds, are synthesized traditionally by oxidative dehydrogenation (ODH) of *n*-butane over complex metal oxides. Such catalysts require high O_2/butane ratios to maintain the activity, which leads to unwanted product oxidation. We show that carbon nanotubes with modified surface functionality efficiently catalyze the oxidative dehydrogenation of *n*-butane to butenes, especially butadiene. For low O_2/butane ratios, a high selectivity to alkenes was achieved for periods as long as 100 hours. This process is mildly catalyzed by ketonic C=O groups and occurs via a combination of parallel and sequential oxidation steps. A small amount of phosphorus greatly improved the selectivity by suppressing the combustion of hydrocarbons.

Transition metal oxides have been widely used as catalysts for the conversion of butane to C_4 alkenes, important industrial precursors for producing synthetic rubbers, plastics, and a number of industrially important chemicals. Despite a great deal of research, alkene selectivity in the current butane-to-butadiene process is severely limited (*1*). One important reason is that the unsaturated products are much more readily oxidized to CO_2 than is the starting alkane. The chemical complexity of polyvalent metal oxides, although found to be necessary for catalytic activity, impedes satisfactory selectivity through isolation of active sites (*2*–*6*). For this reason, the origin of the catalytic activity is debated, and there is as yet no generally accepted picture of the reaction mechanism (*7*, *8*).

Carbon materials have been reported to catalyze the oxidative dehydrogenation (ODH) of an aromatic molecule, ethylbenzene. However, conventional carbons, in particular activated carbon, underwent unavoidable deactivations

Downloaded from www.sciencemag.org on October 2, 2008

EXTENDED PDF FORMAT
SPONSORED BY
usb
Products from Affymetrix
www.usbweb.com

Surface-Modified Carbon Nanotubes Catalyze Oxidative Dehydrogenation of n-Butane

Jian Zhang, *et al.*

Science **322**, 73 (2008);
DOI: 10.1126/science.1161916

The following resources related to this article are available online at www.sciencemag.org (this information is current as of October 2, 2008):

Updated information and services, including high-resolution figures, can be found in the online version of this article at:
http://www.sciencemag.org/cgi/content/full/322/5898/73

Supporting Online Material can be found at:
http://www.sciencemag.org/cgi/content/full/322/5898/73/DC1

This article appears in the following **subject collections**:
Chemistry
http://www.sciencemag.org/cgi/collection/chemistry

Information about obtaining **reprints** of this article or about obtaining **permission to reproduce this article** in whole or in part can be found at:
http://www.sciencemag.org/about/permissions.dtl

Downloaded from www.sciencemag.org on October 2, 2008

Science (print ISSN 0036-8075; online ISSN 1095-9203) is published weekly, except the last week in December, by the American Association for the Advancement of Science, 1200 New York Avenue NW, Washington, DC 20005. Copyright 2008 by the American Association for the Advancement of Science; all rights reserved. The title *Science* is a registered trademark of AAAS.

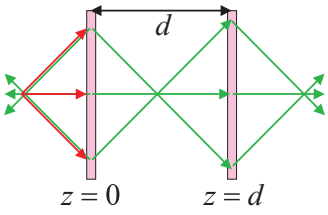

Fig. 3. Two thin sheets of time-reversing material produce a focusing effect very similar to a negatively refracting lens. The system is capable of subwavelength resolution.

Unlike the perfect lens based on negative refraction (*13*), loss is not an issue in this instance because the fields are translated through loss-less vacuum. The issue here is whether a time-reversing sheet can be found sufficiently powerful to give the resolution, Δ, required

$$\Delta \approx 1/k_{\parallel \max} \approx d/\ln R \qquad (13)$$

A scheme for subwavelength resolution was also proposed in (*9*) but, as noted above, this scheme depended on the existence of surface states derived from a mathematically postulated boundary for which no physical realization has so far been suggested.

Although our discussion has been in terms of electromagnetic waves, the same principles apply to any waves and particularly to acoustic waves, where time-reversal studies are also well developed (*14*).

Our original discussion (illustrated in Fig. 2) assumes a single-step transition from +ω to –ω. Such processes occur but are very weak. At optical frequencies, perhaps the best system for the realization of these ideas is a four-wave mixing experiment: One of two counterpropagating pump beams of the same frequency as the signal writes a hologram. The second pump beam then reads the hologram to produce a time-reversed signal. In other words, there is a two-step process in which there first occurs a transition $+\omega \rightarrow 0$ and then a second transition $0 \rightarrow -\omega$. This process has much in common with the recent proposal for a subwavelength focusing device (*15*), except that in our scheme the system writes its own hologram.

As a generalization of the analogy, any positively refracting medium can have the sign of its refraction reversed by coating the surface with a phase-reversing sheet. This leads to the possibility of curved lenses that can magnify an object (*16*).

In principle, our new lens can be realized if the hologram is written in a thin sheet of nonlinear material. In practice, such a hologram would be very weak, and instead, 3D holograms are written if a strong output is desired. As a consequence of the 3D nature of the hologram, the second phase-reversed beam (shown on the right of Fig. 1C) is not seen, but if the left-hand surface of the medium is half silver (Fig. 4), reflection of the phase-reversed beam will generate an image

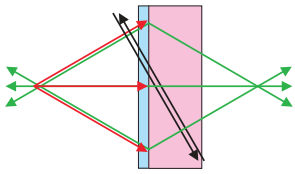

Fig. 4. In a four-wave mixing experiment, two counterpropagating waves first create a hologram and then diffract off the hologram to form a phase-reversed beam. A half-silvered mirror reflects the reversed beam to form an image on the far side of the system.

to the right of the system reproducing the effect predicted in Fig. 1C and mimicking the Veselago negatively refracting lens. However, the 3D nature of the hologram precludes any subwavelength resolution.

Creating a 2D hologram and attaining the ideal shown in Fig. 3 will be a challenge. Enhancing the nonlinearity of existing media—possibly through the use of plasmonic or metamaterial layers to enhance the local fields (*17*)—may offer a route to realizing a 2D version and hence subwavelength resolution. Further discussion of the practicalities of a four-wave mixing scheme can be found in the SOM.

References and Notes

1. J. P. Woerdman, *Opt. Commun.* **2**, 212 (1970).
2. P. Yeh, *Introduction to Photorefractive Nonlinear Optics* (Wiley, New York, 1993).
3. V. G. Veselago, *Sov. Phys. Usp.* **10**, 509 (1968).
4. J. B. Pendry, *Contemp. Phys.* **45**, 191 (2004).
5. J. B. Pendry, *Science* **306**, 1353 (2004).
6. K. Kobayashi, *J. Phys. Condens. Matter* **18**, 3703 (2006).
7. V. V. Cheianov, V. Fal'ko, B. L. Altshuler, *Science* **315**, 1252 (2007).
8. M. Nieto-Vesperinas, E. Wolf, *J. Opt. Soc. Am. A* **2**, 1429 (1985).
9. S. Maslovski, S. Tretyakov, *J. Appl. Phys.* **94**, 4241 (2003).
10. O. Malyuskin, V. Fusco, A. G. Schuchinsky, *IEEE Trans. Antenn. Propag.* **54**, 1399 (2006).
11. C. A. Allen, K. M. K. H. Leong, T. Itoh, *IEEE Int. Microwave Theory Tech. Symp. Dig.* **3**, 1875 (2003).
12. M. Wubs, A. Lagendijk, *Phys. Rev. E Stat. Nonlin. Soft Matter Phys.* **65**, 046612 (2002).
13. J. B. Pendry, *Phys. Rev. Lett.* **85**, 3966 (2000).
14. S. Yon, M. Tanter, M. Fink, *J. Acoust. Soc. Am.* **113**, 1533 (2003).
15. R. Merlin, *Science* **317**, 927 (2007); published online 11 July 2007 (10.1126/science.1143884).
16. J. B. Pendry, S. A. Ramakrishna, *J. Phys. Condens. Matter* **15**, 6345 (2003).
17. J. B. Pendry, A. J. Holden, D. J. Robbins, W. J. Stewart, *IEEE Trans. Microwave Theory Tech.* **47**, 2075 (1999).

18. I thank the Engineering and Physical Sciences Research Council for a Senior Fellowship, M. Damsen for educating me in various aspects of four-wave mixing, S. Maier for discussions on plasmonic enhancements of fields, and A. Lagendijk for comments on the manuscript.

Supporting Online Material

www.sciencemag.org/cgi/content/full/1162087/DC1
SOM Text
Figs. S1 to S6

20 June 2008; accepted 20 August 2008
Published online 28 August 2008;
10.1126/science.1162087
Include this information when citing this paper.

Surface-Modified Carbon Nanotubes Catalyze Oxidative Dehydrogenation of *n*-Butane

Jian Zhang, Xi Liu, Raoul Blume, Aihua Zhang, Robert Schlögl, Dang Sheng Su*

Butenes and butadiene, which are useful intermediates for the synthesis of polymers and other compounds, are synthesized traditionally by oxidative dehydrogenation (ODH) of *n*-butane over complex metal oxides. Such catalysts require high O_2/butane ratios to maintain the activity, which leads to unwanted product oxidation. We show that carbon nanotubes with modified surface functionality efficiently catalyze the oxidative dehydrogenation of *n*-butane to butenes, especially butadiene. For low O_2/butane ratios, a high selectivity to alkenes was achieved for periods as long as 100 hours. This process is mildly catalyzed by ketonic C=O groups and occurs via a combination of parallel and sequential oxidation steps. A small amount of phosphorus greatly improved the selectivity by suppressing the combustion of hydrocarbons.

Transition metal oxides have been widely used as catalysts for the conversion of butane to C_4 alkenes, important industrial precursors for producing synthetic rubbers, plastics, and a number of industrially important chemicals. Despite a great deal of research, alkene selectivity in the current butane-to-butadiene process is severely limited (*1*). One important reason is that the unsaturated products are much more readily oxidized to CO_2 than is the starting alkane. The chemical complexity of polyvalent metal oxides, although found to be necessary for catalytic activity, impedes satisfactory selectivity through isolation of active sites (*2*–*6*). For this reason, the origin of the catalytic activity is debated, and there is as yet no generally accepted picture of the reaction mechanism (*7*, *8*).

Carbon materials have been reported to catalyze the oxidative dehydrogenation (ODH) of an aromatic molecule, ethylbenzene. However, conventional carbons, in particular activated carbon, underwent unavoidable deactivations

Downloaded from www.sciencemag.org on October 2, 2008

due to coking or combustion (*9*–*12*). Recently, it was shown that only well-nanostructured carbons are stable and coke-free catalysts for styrene synthesis (*12*, *13*). Activation of C–H bonds in the ethyl group is considered to be coordinated by the ketonic carbonyl (C=O) group. Ethylbenzene has an aromatic moiety that enables relatively facile activation. Here, we report on surface-modified carbon nanotubes (CNTs) as a high-performance catalyst for the ODH of the much less active butane. Relative to metal-based catalysts, CNTs displayed an enhanced selectivity to C_4 alkenes, especially butadiene.

We conducted the reaction at 400° or 450°C with an O_2/butane ratio of 2.0. The product mixture contained only 1-butene, 2-butene, butadiene, CO_2, CO, and residual reactants; the resulting carbon balance was 100 ± 3% (fig. S1A) (*14*). In a blank experiment without catalyst, the alkene yield was as low as 0.9%. Over pristine CNTs, 88.9% of the converted butane was burnt, yielding 1.6% alkenes (Fig. 1A). Considering the intensive stability of CNTs in O_2 (fig. S1B) (*14*), we conclude that the CO_2 during the reaction mainly originated from the oxidation of the hydrocarbon feedstock and not from burning of the carbon catalysts. Neither washing CNTs in HCl solution nor loading with acidic nitro group could enhance the selectivity to alkene (fig. S2) (*14*).

We then functionalized surfaces of pristine CNTs with oxygen-containing groups by refluxing and oxidizing them in concentrated HNO_3 (*15*). With the resulting oCNTs as catalyst, we observed an improved yield of 6.7% alkenes. The alkene yield was further enhanced to 13.8% after the oCNTs catalyst was additionally modified by passivating defects with phosphorus [P-oCNTs, 0.5 ± 0.1 weight percent (wt %) P]. The increase in alkene selectivity is partially explained in Fig. 1B, which compares the catalytic performance of oCNTs and P-oCNTs for three individual reactions: (i) ODH of butane, (ii) ODH of 1-butene, and (iii) combustion of butadiene. The passivation apparently suppresses the activation and deep oxidation of the alkene substrates.

A survey of recent literature showed that the P-oCNTs catalyst is as selective as the best V/MgO catalyst developed during the past 20 years (fig. S3A) (*14*). To compare the present reaction conditions to those previously used, we synthesized and evaluated two V/MgO samples. At the same conversion of butane, the $Mg_3V_2O_8$ and $Mg_3V_2O_7$ samples were less selective than P-oCNTs (fig. S3B) (*14*); in particular, relative to $Mg_3V_2O_7$, P-oCNTs gave twice the selectivity to butadiene (16.2%).

Safety can be a challenge when mixing hydrocarbons with oxidants. One solution is to operate the reaction under anaerobic conditions. After we reduced the O_2/butane ratio from 2.0 to 0.5, the P-oCNTs sample still exhibited outstanding stability. During a reaction lasting 100 hours, the butane and oxygen conversion remained almost unchanged, and the alkene selectivity stayed above 53% (Fig. 1C). To the best of our knowledge, the oxidative stability of P-oCNTs far exceeds those of metal oxide catalysts, which only work well with excess oxygen (O_2/butane ≥ 2), a condition necessary to prevent severe deactivation due to coke deposition.

In Fig. 1D, we show the ODH activity of oCNTs and P-oCNTs as a function of residence time. These results demonstrate that the overall reaction comprises a combination of parallel and sequential oxidation steps. The alkene selectivity at zero residence time was not unity (*16*), indicating that direct butane combustion occurred in parallel with the ODH reactions (i.e., butane to butenes, butane to butadiene). Two reaction pathways to butadiene were identified. Selectivity toward butadiene remained finite at the zero residence time, evidencing a primary ODH of butane to butadiene; it increased with the residence time as the selectivity of butenes deceased, revealing a secondary ODH of butenes to butadiene.

The effect of phosphorus as a promoter was studied by kinetic measurements. The initial rate

Fritz Haber Institute of the Max Planck Society, Faradayweg 4-6, D-14195 Berlin, Germany.

*To whom correspondence should be addressed. E-mail: dangsheng@fhi-berlin.mpg.de

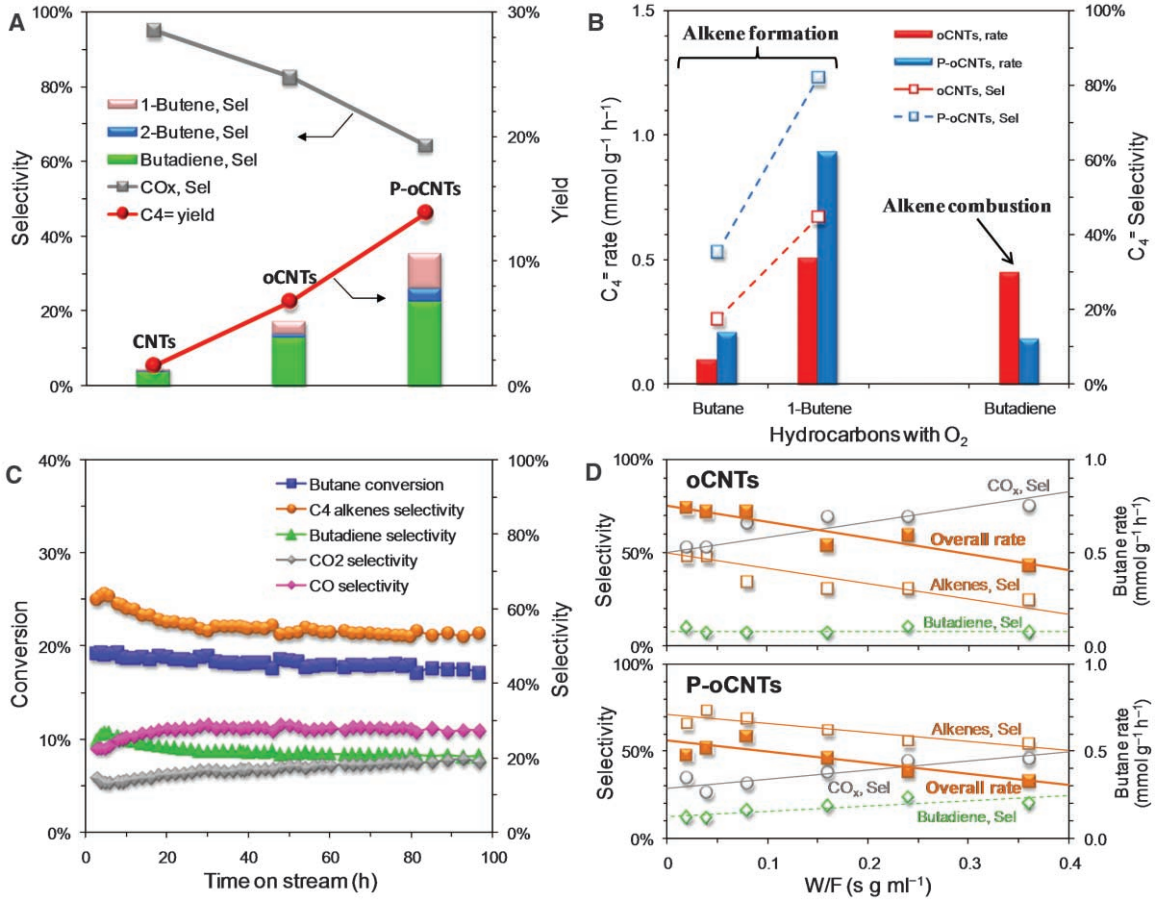

Fig. 1. ODH activities of various carbon nanotubes. (**A**) Performance of various CNTs for ODH of butane under oxygen-rich conditions: 0.18 g, 0.67% butane, O_2/butane = 2, 15 ml min^{-1}, 400°C. (**B**) Performance of modified CNTs in ODH reactions of butane and 1-butene and in combustion of butadiene: 0.18 g, 0.67% C_4 hydrocarbon, O_2/butane = 2, 15 ml min^{-1}, 400°C. (**C**) Stability of P-oCNTs catalyst for ODH of butane over 100 hours: 0.18 g, 2.7% butane, O_2/butane = 0.5, 10 ml min^{-1}, 450°C. (**D**) Dependence of product selectivity and reaction rate on residence time (*W/F*) in ODH reaction of butane: 0.005 to 0.09 g, 2.7% butane, O_2/butane = 0.5, 10 ml min^{-1}, 450°C. Helium was used as balance gas in all experiments.

Downloaded from www.sciencemag.org on October 2, 2008

constants for primary reactions were quantified as the residence time approached zero (*16*). After the modification with P, three important changes happened at the initial state: (i) The overall rate of converted butane decreased from 0.75 to 0.56 mmol g^{-1} $hour^{-1}$; (ii) the combustion of butane was reduced by as much as a factor of 2.3; and (iii) the formation rate of alkenes kept nearly unchanged at 0.38 to 0.40 mmol g^{-1} $hour^{-1}$. Therefore, P increased the selectivity by suppressing the combustion rate, rather than enhancing the formation rate of alkenes.

One of the key concerns in identifying and describing metal-free catalysis is the suspected influence of metal impurities in the catalyst. Commercial CNTs were prepared on supported metal catalysts, which inevitably remain as metal contaminants. Post-treatment by refluxing in strong acid effectively removed the residual metals to a great extent. X-ray fluorescence spectrometry revealed that the residual metals in the tested CNTs were very low (table S1) (*14*). The highest value of residual Fe was still as low as 0.09 wt %, as confirmed by energy-dispersive x-ray analysis (around 0.1 wt %). Furthermore, there was no signal of Fe or other metals in the surface layer at the limit of detection by synchrotron-excited x-ray photoelectron spectroscopy (XPS) (Fig. 2A). This difference suggests that if there is residual metal, it must be embedded in the carbon and not exposed to the reactants. This explanation is supported by the high-resolution transmission electron microscopy (HRTEM) image in Fig. 2B, which shows a catalyst particle encapsulated inside the CNTs. To fully exclude the role of Fe in the reaction, we deliberately added Fe to oCNTs in fractions ranging from 0.05 to 0.5 wt %. As shown in Fig. 2C, both the butane conversion and selectivity to C_4 alkenes gradually decreased with the increasing Fe content. Furthermore, there was no correlation of alkene selectivity with the residual metal content (fig. S4A) (*14*). We prepared a sample with 5% Fe phosphate in oCNTs; this sample also exhibited performance inferior to that of P-oCNTs without Fe (fig. S4B) (*14*). We can thus conclude that the reactivity originated exclusively from metal-free active sites on CNTs and that the residual metals played no positive role.

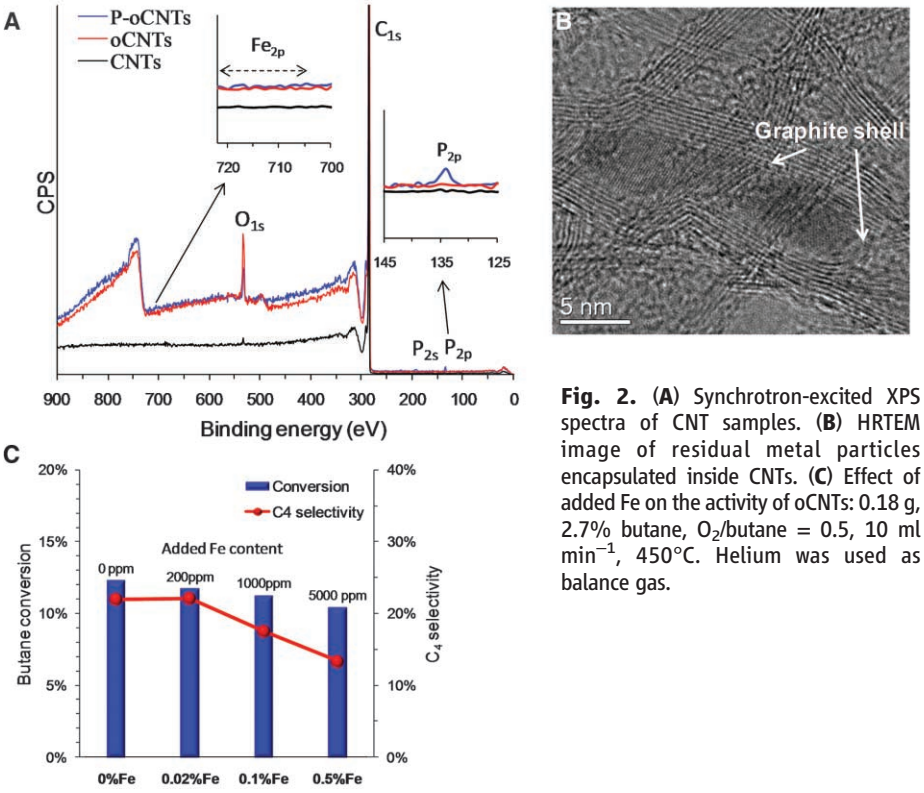

Fig. 2. (**A**) Synchrotron-excited XPS spectra of CNT samples. (**B**) HRTEM image of residual metal particles encapsulated inside CNTs. (**C**) Effect of added Fe on the activity of oCNTs: 0.18 g, 2.7% butane, O_2/butane = 0.5, 10 ml min^{-1}, 450°C. Helium was used as balance gas.

To elucidate the structure-activity relation, we studied the morphological features by TEM with elemental mapping. Figure 3A gives an overview elemental map from a typical area. Both P and O are dispersed throughout the sample without aggregation. After an ODH reaction that ran for more than 800 min, the morphology of the CNTs remained intact and no evidence for their combustion was identified (Fig. 3B), as expected from the thermal stability data (fig. S1B) (*14*). Some areas of the outer and inner walls of the CNTs were covered by thin layers of phosphorus, which obviously differs from fullerenoid carbon species on pristine CNTs originating from condensation of hydrocarbon fragments (fig. S5) (*14*). Most of the surface of the CNTs did not give rise to carbon deposition, which is one advantage of this metal-free catalyst.

We also monitored the working surface of CNTs with near-ambient XPS (*17*). The best P-oCNTs catalyst was heated in vacuum to 350°C; at this temperature, the less stable groups (anhydride, carboxyl, ester, and nitro) would already have desorbed from the surface (fig. S6) (*14*). We identified two contributions from ketonic C=O groups (531.2 ± 0.2 eV) and from C–O groups (533.1 ± 0.2 eV) (i.e., ether and hydroxyl) (*15*, *18*). Relative amounts of C–O and C=O are represented in Fig. 3C by the ratio

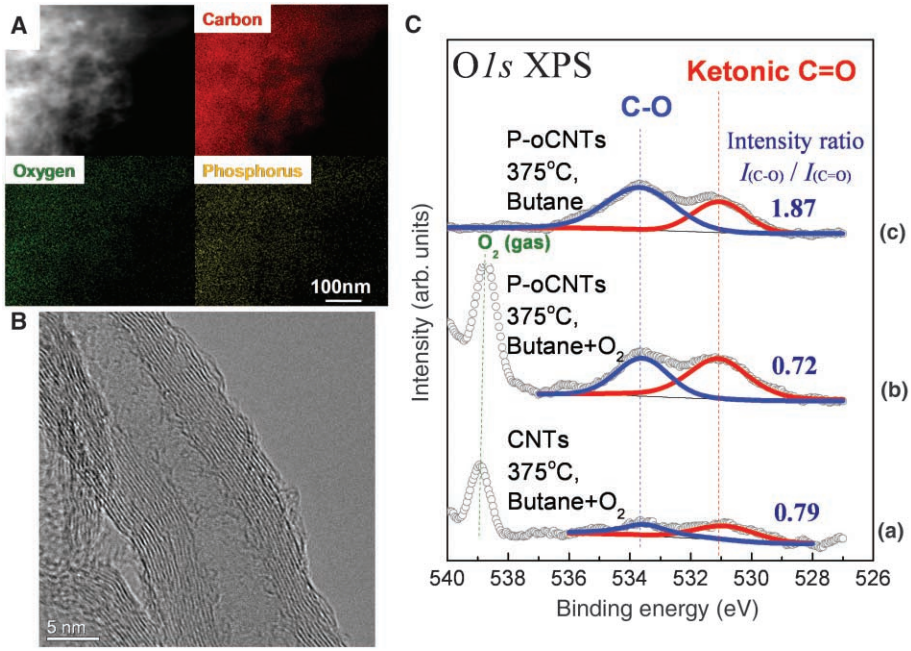

Fig. 3. (**A**) Elemental maps and (**B**) HRTEM image of the used P-oCNTs in Fig. 1A. (**C**) In situ O1*s* XPS spectra of working catalysts taken at 350° to 375°C: (a) CNTs: butane + O_2 (1:1), 0.25 mbar; (b) P-oCNTs: butane + O_2 (1:1), 0.25 mbar; (c) P-oCNTs: butane, 0.125 mbar.

Downloaded from www.sciencemag.org on October 2, 2008

of their intensities, $I_{(C-O)}/I_{(C=O)}$. Under ODH conditions (butane + O_2, 1:1, 0.25 atm, 350° to 375°C), $I_{(C-O)}/I_{(C=O)}$ values ranged from 0.72 to 0.80. However, after switching off O_2, the $I_{(C-O)}/I_{(C=O)}$ value sharply increased to 1.87 (Fig. 3C) and the activity went to almost zero. This finding indicates that ketonic C=O groups are a critical ingredient of the active sites, whereas C–O groups constitute inactive intermediates or adsorbates.

Figure 4A summarizes our proposed mechanism for the CNTs-catalyzed butane oxidation. For this purpose, surface oxygen species are classified into electrophilic (superoxide O_2^-, peroxide O_2^{2-}) and nucleophilic (O^{2-}) types (*19*). Electrophilic oxygen species are electron-deficient and attack the electron-rich C=C bonds in alkenes, leading to the rupture of the carbon skeleton and subsequent combustion. Pristine CNTs were produced from chemical vapor deposition of unsaturated hydrocarbons, resulting in a number of structural defects and terminal carbon fragments. Below 600°C, these defect sites or edges of graphene have been reported to convert O_2 molecules to electrophilic oxygen species (*20*) and thus cause low selectivity to alkenes.

More controlled oxidation of carbon surfaces can be carried out in liquid-phase oxidants (*21*). After refluxing in HNO_3, defect sites were functionalized by O^{2-} anions into various functional groups. For example, ketonic C=O, a nucleophilic species with high electron density, preferentially reacts with electron-poor saturated bonds. However, at the reaction temperature, desorption of less stable groups results in new graphitic defects that subsequently generate new electrophilic oxygen sites, thus partially limiting the selectivity to alkenes on oCNTs. The addition of phosphate reacting with these defects suppresses the formation of electrophilic oxygen species (*22*). Thus, P-oCNTs displayed a lower overall activity but a much better selectivity.

We used density functional theory (DFT) calculations with the CASTEP code and the Perdew-Burke-Ernzerhof generalized gradient approximation (*23*, *24*) to study the ODH reaction over ketonic C=O groups. These calculations are independent of the precise mechanism and the transition state of each elementary step. We used the graphitic zigzag edge as a model to anchor the ketonic C=O groups (Fig. 4B). Conversion of butane is energetically controlled by the abstraction of the first H atom, which was predicted to be mildly endothermic at 0.92 eV. To convert butane into 1- or 2-butene, two C=O sites would ultimately be needed, and each one returns a single electron to the surrounding graphene as the reservoir. The remaining H atoms combine with surrounding oxygen to water, thereby closing the primary ODH cycle. The enthalpy of formation of water compensates for the endothermic dehydrogenation of butane. As a consequence, the calculated free energies for formation of 1- and 2-butenes were −0.88 eV and −1.03 eV, respectively. Another pathway to regenerate active sites is that H atoms recombine into H_2 molecules. However, as expected, such a direct dehydrogenation reaction is energetically unfavorable, because energy barriers are as high as 1.45 to 1.60 eV.

The DFT calculation also provides insights into the reaction pathways to butadiene. Butadiene may directly form from butane as primary product with an overall energy of −1.97 eV. However, the need for neighboring C=O sites to accommodate four H atoms in one elementary step does not seem to be pronounced, accounting for a much lower rate than the secondary ODH from butenes (Fig. 1D). It is more likely that C=O primarily activates butenes (rather than butane) to butadiene. The energy for the abstraction of the first H from butenes ($\Delta E_{butenes,1H}$), 0.25 to 0.40 eV, is much lower than that from butane ($\Delta E_{butane,1H}$), 0.92 eV. In this way, we can understand the influence of residence time. Because the residence time is long enough for the butenes produced to diffuse and react with the surrounding C=O sites, butadiene will be primarily generated from the secondary ODH, as demonstrated by the prevailing fraction of butadiene in C_4 alkenes in an integral reaction, 63 to 74% (Fig. 1A).

Our work contains some implications for catalysis in general. It is possible to imitate heterogeneously the concepts of homogeneous metal-free catalysis. The function of oxygen heteroatoms in molecular catalysts is reproduced by defects of bent graphitic sheets. The catalytic principle of site isolation can be realized by electronic localization of charges at the defect sites corresponding to molecular analogs of double bonds. The operation mode of ODH reactions can be studied on metal-free catalysts with greater precision than in metal oxide systems. There is neither lattice nor structural oxygen, but only oxygen at active sites. The present catalysts are free of polyvalent metal sites with complex electronic and spin structures, allowing for a facile theoretical treatment. Finally, the application of a heterogeneous CNTs catalyst is attractive because of favorable management of energy over a good thermal and electronic conductor.

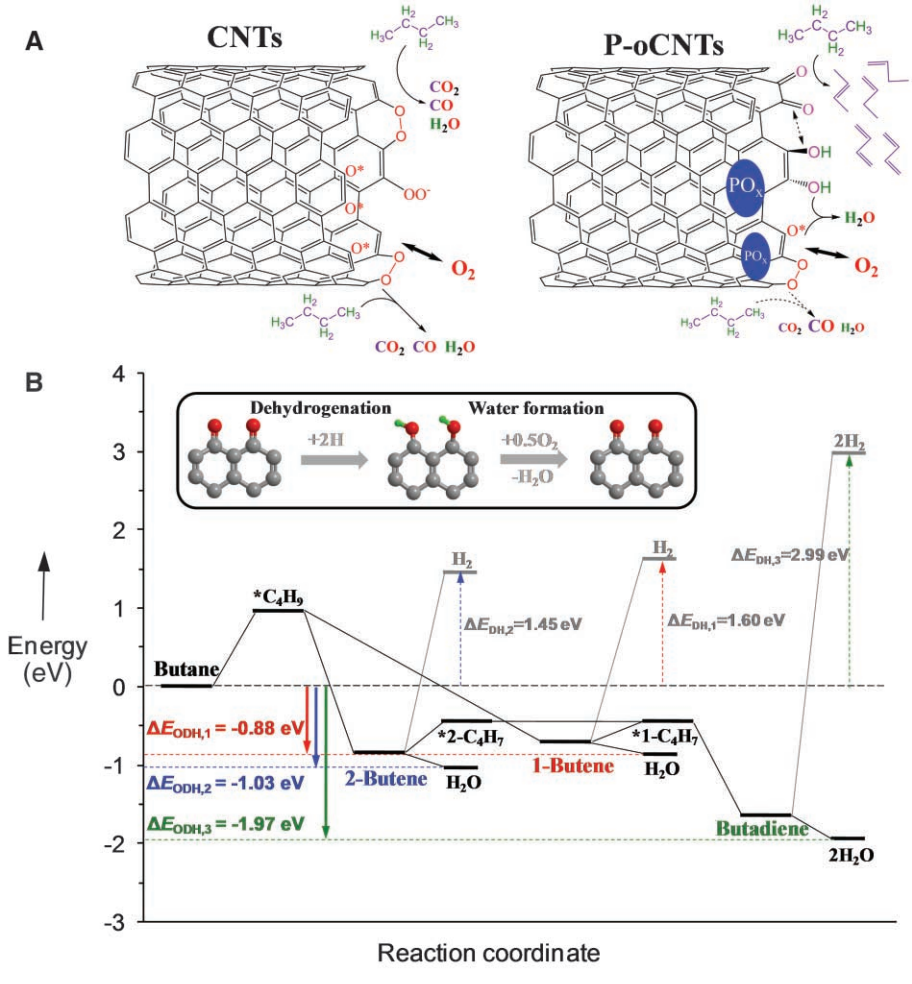

Fig. 4. (**A**) Schematic reaction and (**B**) energy steps of butane oxidation on pristine and P-modified CNTs.

References and Notes

1. F. Cavani, F. Trifirò, *Appl. Catal. A* **133**, 219 (1995).
2. R. Grabowski, *Catal. Rev.* **48**, 199 (2006).
3. K. D. Chen, A. T. Bell, E. Iglesia, *J. Catal.* **209**, 35 (2002).
4. G. I. Panov, K. A. Dubkov, E. V. Starokon, *Catal. Today* **117**, 148 (2006).
5. A. Miyakoshi, A. Ueno, M. Ichikawa, *Appl. Catal. A* **219**, 249 (2001).
6. L. B.-Tapia, I. H. Pérez, P. Schacht, I. R. Córdova, G. G. Aguilar-Ríos, *J. Catal.* **107–108**, 371 (2005).
7. E. V. Kondratenko, M. Cherian, M. Baerns, *Catal. Today* **99**, 59 (2005).

Downloaded from www.sciencemag.org on October 2, 2008

8. C. Resini, T. Montanari, G. Busca, J.-M. Jehng, I. E. Wachs, *Catal. Today* **99**, 105 (2005).
9. T. G. Alkhazov, E. A. Ismailov, A. Yu, A. I. Kozharov, *Kinet. Katal.* **19**, 611 (1978).
10. M. S. Kane, L. C. Kao, R. K. Mariwala, D. F. Hilscher, H. C. Foley, *Ind. Eng. Chem. Res.* **35**, 3319 (1996).
11. M. F. R. Pereira, J. J. M. Órfão, J. L. Figueiredo, *Appl. Catal. A* **218**, 307 (2001).
12. J. Zhang *et al.*, *Angew. Chem. Int. Ed.* **46**, 7319 (2007).
13. G. Mestl, N. I. Maksimova, N. Keller, V. V. Roddatis, R. Schlögl, *Angew. Chem. Int. Ed.* **40**, 2066 (2001).
14. See supporting material on *Science* Online.
15. J.-H. Zhou *et al.*, *Carbon* **9**, 1379 (2007).
16. K. D. Chen, E. Iglesia, A. T. Bell, *J. Phys. Chem. B* **105**, 646 (2001).
17. M. Salmeron, R. Schlögl, *Surf. Sci. Rep.* **63**, 169 (2008).
18. T. I. T. Okpalugo, P. Papakonstantinou, H. Murphy, J. McLaughlin, N. M. D. Brown, *Carbon* **43**, 153 (2005).
19. L. M. Madeira, M. F. Portela, *Catal. Rev.* **44**, 247 (2002).
20. F. Atamny *et al.*, *Mol. Phys.* **76**, 851 (1992).
21. M. L. Toebes, J. M. P. van Heeswijk, J. H. Bitter, A. J. van Dillen, K. P. de Jong, *Carbon* **42**, 307 (2004).
22. A. M. Puziy, O. I. Poddubnaya, A. M. Ziatdinov, *Appl. Surf. Sci.* **252**, 8036 (2006).
23. S. J. Clark *et al.*, *Z. Kristallogr.* **220**, 567 (2005).
24. J. P. Perdew, K. Burke, M. Ernzerhof, *Phys. Rev. Lett.* **77**, 3865 (1996).

25. We thank the Max Planck Society; U. Wild, A. Klein-Hoffmann, and J. Thielemann for technical assistance; Berliner Elektronenspeicherring-Gesellschaft für Synchrotronstrahlung for support of in situ XPS measurements; and M. A Smith for helpful discussions. Supported by the CANAPE project of the 6th Framework Programme of European Commission and the ENERCHEM project of the Max Planck Society.

Supporting Online Material

www.sciencemag.org/cgi/content/full/322/5898/73/DC1
Materials and Methods
Figs. S1 to S6
Table S1
References

17 June 2008; accepted 21 August 2008
10.1126/science.1161916

Merging Photoredox Catalysis with Organocatalysis: The Direct Asymmetric Alkylation of Aldehydes

David A. Nicewicz and David W. C. MacMillan*

Photoredox catalysis and organocatalysis represent two powerful fields of molecule activation that have found widespread application in the areas of inorganic and organic chemistry, respectively. We merged these two catalysis fields to solve problems in asymmetric chemical synthesis. Specifically, the enantioselective intermolecular α-alkylation of aldehydes has been accomplished using an interwoven activation pathway that combines both the photoredox catalyst $Ru(bpy)_3Cl_2$ (where bpy is 2,2′-bipyridine) and an imidazolidinone organocatalyst. This broadly applicable, yet previously elusive, alkylation reaction is now highly enantioselective and operationally trivial.

Nature's ability to convert solar energy to chemical energy in photosynthesis has inspired the development of a host of photoredox systems in efforts to mimic this process. Arguably the most studied one-electron photoredox catalyst has been $Ru(bpy)_3^{2+}$ (where bpy is 2,2′-bipyridine): an inorganic complex that has facilitated important advances in the areas of energy storage, hydrogen and oxygen evolution from water, and methane production from carbon dioxide (*1*, *2*). Given its proven ability to mediate electron transfer, it is surprising that $Ru(bpy)_3^{2+}$ has not found a substantial application in organic synthesis, wherein a large number of fundamental reactions rely on the generation and exploitation of radicals or single-electron intermediates (*3*).

Over the past decade, the field of organocatalysis has grown at a dramatic pace, providing more than 130 chemical reactions that rapidly facilitate enantioselective C–C, C–O, C–N, and C–halogen bond formation (*4*, *5*). Whereas a broad range of reaction types have recently succumbed to this mode of catalysis (including aldol, Friedel-Crafts, and cycloadditions), it is important to consider that nearly all organocatalytic bond constructions are restricted to two-electron pathways, wherein the highest occupied molecular orbital of an electron-rich substrate reacts with the lowest unoccupied molecular orbital of an electron-deficient partner. Recently, however, our laboratory introduced the concept of organo–singly occupied molecular orbital (SOMO) catalysis, a one-electron mode of activation that has enabled the development of several useful transformations (*6*–*10*).

Given the widespread success of both electron transfer catalysis and organocatalysis, we recently questioned whether it might be possible to merge these two powerful areas, with the goal of solving long-standing, yet elusive problems in chemical synthesis. More specifically, as a blueprint for reaction invention, we hoped to exploit the lessons of photoredox enzymatic catalysis (*11*), wherein a series of consecutive low-barrier, open-shell steps are energetically preferred to high-barrier, two-electron pathways. On this basis, we hypothesized that the enantioselective catalytic α-alkylation of aldehydes (*12*–*15*), a widely sought yet elusive transformation, might be brought to fruition via the marriage of inorganic electron transfer and organic catalysis (Fig. 1).

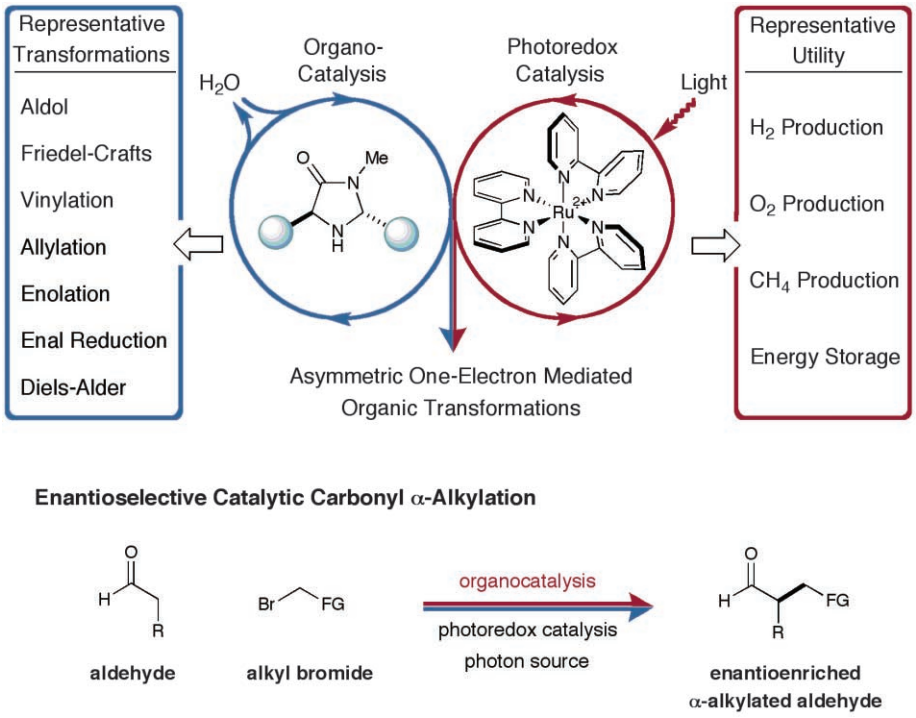

Fig. 1. Merging amine catalysis and organometallic photoredox catalysis to enable asymmetric organic transformations. Me, methyl; R, generic organic substituent; FG, electron-withdrawing functional group.

Contribution from Merck Center for Catalysis, Department of Chemistry, Princeton University, Princeton, NJ 08544, USA.

*To whom correspondence should be addressed. E-mail: dmacmill@princeton.edu

Downloaded from www.sciencemag.org on October 2, 2008

EXTENDED PDF FORMAT
SPONSORED BY
usb
Products from Affymetrix
www.usbweb.com

Merging Photoredox Catalysis with Organocatalysis: The Direct Asymmetric Alkylation of Aldehydes

David A. Nicewicz, *et al.*

Science **322**, 77 (2008);
DOI: 10.1126/science.1161976

The following resources related to this article are available online at www.sciencemag.org (this information is current as of October 2, 2008):

Updated information and services, including high-resolution figures, can be found in the online version of this article at:
http://www.sciencemag.org/cgi/content/full/322/5898/77

Supporting Online Material can be found at:
http://www.sciencemag.org/cgi/content/full/1161976/DC1

This article **cites 16 articles**, 1 of which can be accessed for free:
http://www.sciencemag.org/cgi/content/full/322/5898/77#otherarticles

This article appears in the following **subject collections**:
Chemistry
http://www.sciencemag.org/cgi/collection/chemistry

Information about obtaining **reprints** of this article or about obtaining **permission to reproduce this article** in whole or in part can be found at:
http://www.sciencemag.org/about/permissions.dtl

Downloaded from www.sciencemag.org on October 2, 2008

Science (print ISSN 0036-8075; online ISSN 1095-9203) is published weekly, except the last week in December, by the American Association for the Advancement of Science, 1200 New York Avenue NW, Washington, DC 20005. Copyright 2008 by the American Association for the Advancement of Science; all rights reserved. The title *Science* is a registered trademark of AAAS.

8. C. Resini, T. Montanari, G. Busca, J.-M. Jehng, I. E. Wachs, *Catal. Today* **99**, 105 (2005).
9. T. G. Alkhazov, E. A. Ismailov, A. Yu, A. I. Kozharov, *Kinet. Katal.* **19**, 611 (1978).
10. M. S. Kane, L. C. Kao, R. K. Mariwala, D. F. Hilscher, H. C. Foley, *Ind. Eng. Chem. Res.* **35**, 3319 (1996).
11. M. F. R. Pereira, J. J. M. Órfão, J. L. Figueiredo, *Appl. Catal. A* **218**, 307 (2001).
12. J. Zhang *et al.*, *Angew. Chem. Int. Ed.* **46**, 7319 (2007).
13. G. Mestl, N. I. Maksimova, N. Keller, V. V. Roddatis, R. Schlögl, *Angew. Chem. Int. Ed.* **40**, 2066 (2001).
14. See supporting material on *Science* Online.
15. J.-H. Zhou *et al.*, *Carbon* **9**, 1379 (2007).
16. K. D. Chen, E. Iglesia, A. T. Bell, *J. Phys. Chem. B* **105**, 646 (2001).
17. M. Salmeron, R. Schlögl, *Surf. Sci. Rep.* **63**, 169 (2008).
18. T. I. T. Okpalugo, P. Papakonstantinou, H. Murphy, J. McLaughlin, N. M. D. Brown, *Carbon* **43**, 153 (2005).
19. L. M. Madeira, M. F. Portela, *Catal. Rev.* **44**, 247 (2002).
20. F. Atamny *et al.*, *Mol. Phys.* **76**, 851 (1992).
21. M. L. Toebes, J. M. P. van Heeswijk, J. H. Bitter, A. J. van Dillen, K. P. de Jong, *Carbon* **42**, 307 (2004).
22. A. M. Puziy, O. I. Poddubnaya, A. M. Ziatdinov, *Appl. Surf. Sci.* **252**, 8036 (2006).
23. S. J. Clark *et al.*, *Z. Kristallogr.* **220**, 567 (2005).
24. J. P. Perdew, K. Burke, M. Ernzerhof, *Phys. Rev. Lett.* **77**, 3865 (1996).

25. We thank the Max Planck Society; U. Wild, A. Klein-Hoffmann, and J. Thielemann for technical assistance; Berliner Elektronenspeicherring-Gesellschaft für Synchrotronstrahlung for support of in situ XPS measurements; and M. A Smith for helpful discussions. Supported by the CANAPE project of the 6th Framework Programme of European Commission and the ENERCHEM project of the Max Planck Society.

Supporting Online Material

www.sciencemag.org/cgi/content/full/322/5898/73/DC1
Materials and Methods
Figs. S1 to S6
Table S1
References

17 June 2008; accepted 21 August 2008
10.1126/science.1161916

Merging Photoredox Catalysis with Organocatalysis: The Direct Asymmetric Alkylation of Aldehydes

David A. Nicewicz and David W. C. MacMillan*

Photoredox catalysis and organocatalysis represent two powerful fields of molecule activation that have found widespread application in the areas of inorganic and organic chemistry, respectively. We merged these two catalysis fields to solve problems in asymmetric chemical synthesis. Specifically, the enantioselective intermolecular α-alkylation of aldehydes has been accomplished using an interwoven activation pathway that combines both the photoredox catalyst $Ru(bpy)_3Cl_2$ (where bpy is 2,2′-bipyridine) and an imidazolidinone organocatalyst. This broadly applicable, yet previously elusive, alkylation reaction is now highly enantioselective and operationally trivial.

Nature's ability to convert solar energy to chemical energy in photosynthesis has inspired the development of a host of photoredox systems in efforts to mimic this process. Arguably the most studied one-electron photoredox catalyst has been $Ru(bpy)_3^{2+}$ (where bpy is 2,2′-bipyridine): an inorganic complex that has facilitated important advances in the areas of energy storage, hydrogen and oxygen evolution from water, and methane production from carbon dioxide (*1*, *2*). Given its proven ability to mediate electron transfer, it is surprising that $Ru(bpy)_3^{2+}$ has not found a substantial application in organic synthesis, wherein a large number of fundamental reactions rely on the generation and exploitation of radicals or single-electron intermediates (*3*).

Over the past decade, the field of organocatalysis has grown at a dramatic pace, providing more than 130 chemical reactions that rapidly facilitate enantioselective C–C, C–O, C–N, and C–halogen bond formation (*4*, *5*). Whereas a broad range of reaction types have recently succumbed to this mode of catalysis (including aldol, Friedel-Crafts, and cycloadditions), it is important to consider that nearly all organocatalytic bond constructions are restricted to two-electron pathways, wherein the highest occupied molecular orbital of an electron-rich substrate reacts with the lowest unoccupied molecular orbital of an electron-deficient partner. Recently, however, our laboratory introduced the concept of organo–singly occupied molecular orbital (SOMO) catalysis, a one-electron mode of activation that has enabled the development of several useful transformations (*6*–*10*).

Given the widespread success of both electron transfer catalysis and organocatalysis, we recently questioned whether it might be possible to merge these two powerful areas, with the goal of solving long-standing, yet elusive problems in chemical synthesis. More specifically, as a blueprint for reaction invention, we hoped to exploit the lessons of photoredox enzymatic catalysis (*11*), wherein a series of consecutive low-barrier, open-shell steps are energetically preferred to high-barrier, two-electron pathways. On this basis, we hypothesized that the enantioselective catalytic α-alkylation of aldehydes (*12*–*15*), a widely sought yet elusive transformation, might be brought to fruition via the marriage of inorganic electron transfer and organic catalysis (Fig. 1).

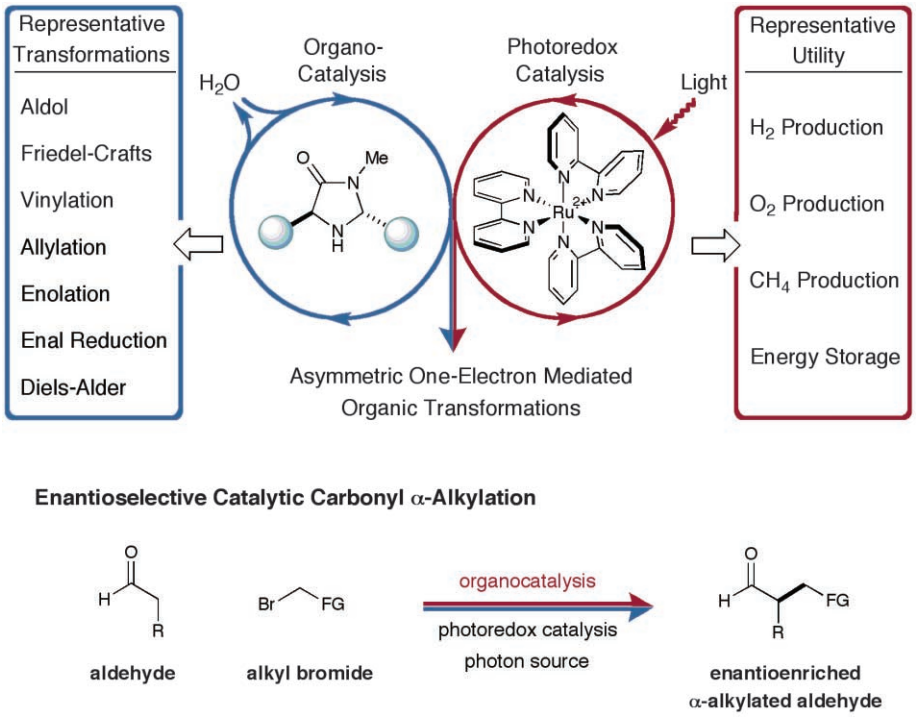

Fig. 1. Merging amine catalysis and organometallic photoredox catalysis to enable asymmetric organic transformations. Me, methyl; R, generic organic substituent; FG, electron-withdrawing functional group.

Contribution from Merck Center for Catalysis, Department of Chemistry, Princeton University, Princeton, NJ 08544, USA.

*To whom correspondence should be addressed. E-mail: dmacmill@princeton.edu

Downloaded from www.sciencemag.org on October 2, 2008

We proposed that two interwoven catalytic cycles might be engineered to simultaneously generate an electron-rich enamine from the condensation of an aldehyde and an amine catalyst and an electron-deficient alkyl radical via reduction of an alkyl bromide with a Ru photoredox catalyst (Fig. 2). Given that electron-deficient radicals are known to rapidly combine with π-rich olefins to forge even the most elusive C–C bonds (*16*, *17*), we hoped that this dual-catalysis mechanism would successfully converge to enable the direct coupling of aldehydes with α-bromo ketones or esters. As a critical design element, we presumed that the use of a suitable chiral amine catalyst would induce high enantioselectivity. Moreover, we recognized that the interaction of a SOMOphilic enamine with an electron-deficient radical is the converse mechanism to our previously described SOMO activation studies. As such, a complementary array of catalytic bond constructions should be possible.

A detailed description of our dual-catalysis aldehyde alkylation is presented in Fig. 2. It has long been established that $Ru(bpy)_3^{2+}$ (**1**) will readily accept a photon from a variety of light sources to populate the $^*Ru(bpy)_3^{2+}$ (**2**) metal-to-ligand charge transfer (MLCT) excited state (*1*, *2*). Although $^*Ru(bpy)_3^{2+}$ (**2**) can function as a reductant or an oxidant, we postulated that this high-energy intermediate would efficiently remove a single electron from a sacrificial quantity of enamine, to initiate our first catalytic cycle and provide the electron-rich $Ru(bpy)_3^{+}$ (**3**). Given that $Ru(bpy)_3^{+}$ (**3**) has been shown to be a potent reductant [–1.33 V versus saturated calomel electrode (SCE) in CH_3CN] (*18*), we anticipated that single-electron transfer (SET) to the α-bromocarbonyl substrate **4** would rapidly furnish the electron-deficient alkyl radical **5** while returning $Ru(bpy)_3^{2+}$ (**1**) to the catalytic cycle ($E_{1/2}$ for phenacyl bromide = –0.49 V versus SCE in CH_3CN, where $E_{1/2}$ is the half reduction potential) (*19*–*22*). As a central design consideration, we recognized that the redox potentials of $Ru(bpy)_3^{2+}$ can be readily fine-tuned by ligand modification (*1*).

Concurrent with this photoredox pathway, the organocatalytic cycle would begin with condensation of the imidazolidinone catalyst **6** and the aldehyde substrate **7** to form enamine **8**. At this stage, we expected the two catalytic cycles to intersect via the addition of the SOMOphilic enamine **8** to the electron-deficient alkyl radical **5**, thereby achieving the key alkylation step. This coupling event would concomitantly produce an electron-rich α-amino radical **9**, a single-electron species that has a low barrier to oxidation (–0.92 to –1.12 V versus SCE in CH_3CN) (*23*). Once again, convergence of our catalytic cycles should ensure SET from α-amino radical **9** to the $^*Ru(bpy)_3^{2+}$ (**2**) excited state to produce the iminium ion **10** and regenerate the active reductant, $Ru(bpy)_3^{+}$ (**3**)—a step that would close the photoredox cycle (*24*). Hydrolysis of the resulting iminium **10** would reconstitute the amine catalyst **6** while delivering the requisite enantioenriched α-alkyl aldehyde product.

From the outset, we understood that the utility of this alkylation reaction would rely on the identification of an amine catalyst that could generically enforce high levels of enantiocontrol in the coupling of the pivotal π-rich enamine with a diverse array of electron-deficient radicals. On the basis of density functional theory (DFT) calculations (*25*, *26*), we proposed that the imidazolidinone catalyst **6** should selectively form an enamine **8** (DFT-**8**), that projects the 2π electron system away from the bulky *tert*-butyl group, whereas the electron-rich olefin will selectively populate an (*E*)-configuration to minimize nonbonding interactions with the imidazolidinone ring (Fig. 2). In terms of enantiofacial discrimination, the calculated DFT-**8** structure also reveals that the methyl group on the catalyst system will effectively shield the *Re* face of the enamine, leaving the *Si* face exposed for enantioselective radical addition. We have found that the trans methyl, *tert*-butyl 2,5-disubstituted imidazolidinone **6** is an excellent enamine catalyst for transformations performed at room temperature. Specifically, catalyst **6** provides excellent levels of kinetic enantiocontrol yet does not readily participate in enamine formation with the 2,2′-disubstituted aldehyde-alkylation adduct, a step that would erode product enantiopurity via epimerization.

This new asymmetric alkylation protocol was first examined using octanal and bromo diethylmalonate as the coupling partners, along with a catalyst combination of $Ru(bpy)_3Cl_2$ (**1**) and imidazolidinone **6**, and a 15-W fluorescent light source (Table 1) (*27*). To our great delight, preliminary studies revealed the successful execution of our dual-cycle design ideals to provide (*R*)-2-malonyloctanal with excellent levels of enantiocontrol and reaction efficiency [entry 1, 93% yield, 90% enantiomeric excess (ee)]. Experiments that probe the scope of the aldehyde component in this new alkylation reaction are summarized in Table 1 (entries 1 to 6). Chemical functionalities that are often prone to either oxidation or reduction (e.g., olefins, esters, carbamates, and arenes) were found to be inert to these mild redox conditions (entries 2 to 5, 66 to 92% yield, 90 to 95% ee). Moreover, the steric demand of the α-formyl substituent has little impact on the efficiency and enantioinduction of the alkylation process (entries 1 and 4, substituent is *n*-hexyl versus cyclohexyl, 83 to 93% yield, 90 to 95% ee), a point that is underscored by the successful use of adamantyl acetaldehyde (entry 6, 63% yield, 93% ee).

A broad array of electron-deficient α-bromo carbonyls can effectively serve as alkylating agents

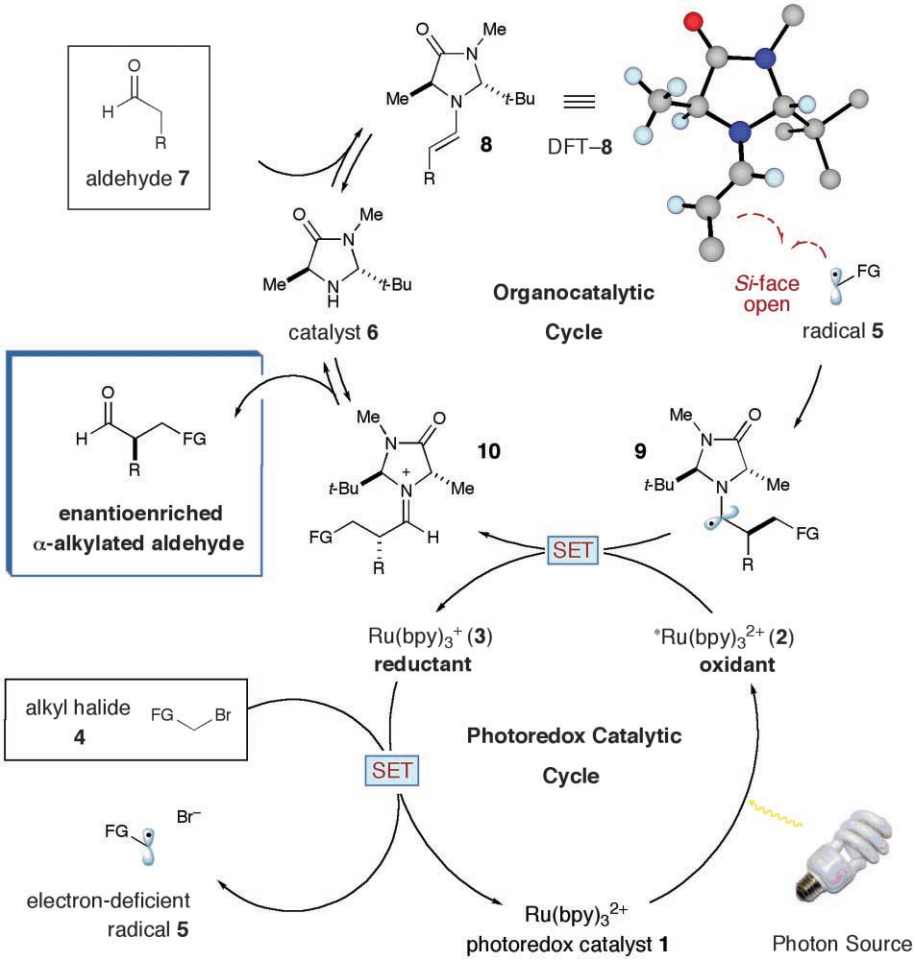

Fig. 2. Merging photoredox catalysis with organocatalysis. Proposed mechanism. *t*-Bu, *tert*-butyl.

Downloaded from www.sciencemag.org on October 2, 2008

Table 1. Survey of the bromide and aldehyde scope in the direct α-alkylation of aldehydes. Y, any organic substituent (alkyl, aryl, alkenyl, alkynyl, etc.); DMF, *N*,*N*′-dimethylformamide; Tf, triflate; Me, methyl; Et, ethyl; Hex, hexyl; Ph, phenyl; *t*-Bu, *tert*-butyl; Boc, *tert*-butyl carbamoyl.

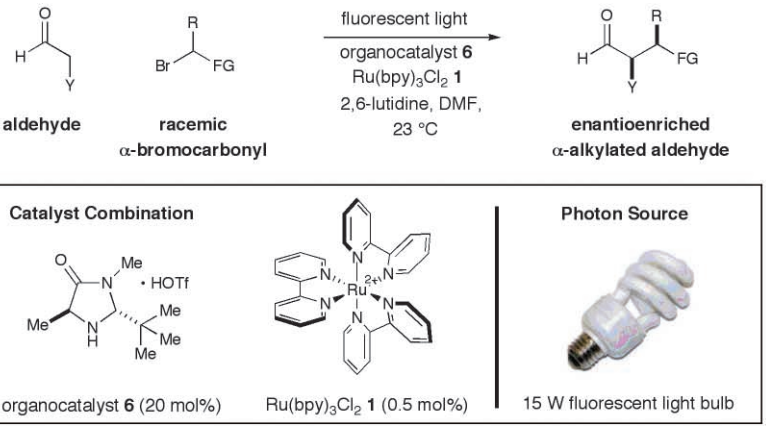

entry	aldehyde	product*
1	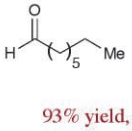	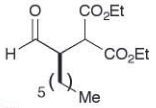 93% yield, 90% ee
2	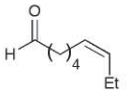	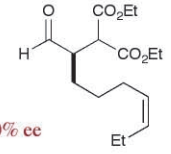 86% yield, 90% ee
3	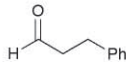	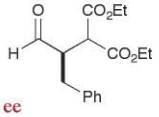 92% yield, 90% ee
4	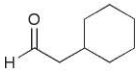	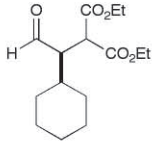 83% yield, 95% ee
5	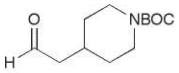	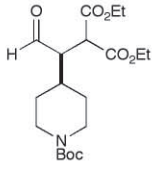 66% yield, 91% ee
6		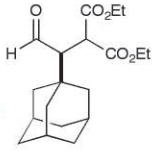 63% yield†, 93% ee

entry	α-bromocarbonyl	product‡
7	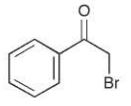	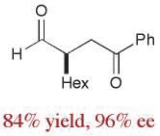 84% yield, 96% ee
8	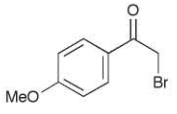	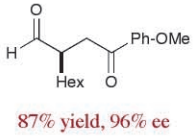 87% yield, 96% ee
9	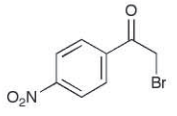	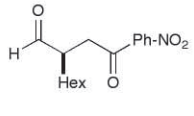 84% yield, 95% ee
10	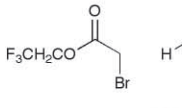	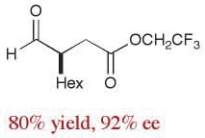 80% yield, 92% ee
11	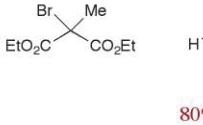	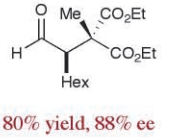 80% yield, 88% ee
12	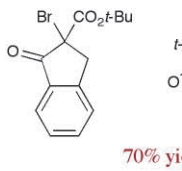	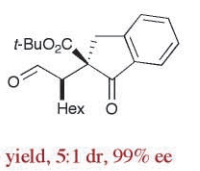 70% yield, 5:1 dr, 99% ee

*Reactions performed with diethyl bromomalonate. †40 mole percent of organocatalyst **6** was employed. ‡Reactions performed with octanal.

in this tandem catalysis manifold (Table 1, entries 7 to 12). For example, bromoacetophenone systems of diverse electronic orientation (*p*-OMe, *p*-NO_2, *p*-H) provide almost identical selectivity and efficiency profiles (entries 7 to 9; 84 to 87% yield, 95 to 96% ee). Whereas α-bromo esters are readily tolerated ($BrCH_2CO_2Et$, 53% yield, 94% ee), we have found that superior yields are obtained with markedly electron-deficient carbonyls such as the trifluoroethyl ester (80% yield, 92% ee). As a testament to the versatility and power of one-electron mediated pathways, we have found that tertiary bromo-substituted alkylating agents can be readily employed to forge all-carbon quaternary centers, (entries 11 and 12, ≥70% yield, 88 to 99% ee). Moreover, racemic α-bromo radical precursors can be employed to generate quaternary stereocenters with appreciable levels of diastereocontrol (entry 12, 5:1 diastereomeric ratio), illustrating the capacity of the pivotal enamine intermediate to differentiate the enantiotopic faces of a trisubstituted carbon-centered radical. The sense of asymmetric induction observed in all cases (Table 1) is consistent with selective addition of the electron-deficient radical to the *Si* face of the enamine **8**, in complete accord with the calculated structure DFT-**8**.

With respect to operational convenience, it is important to consider that this alkylation protocol does not require any heating or cooling, all of the components employed in this study (substrates, catalysts, and solvents) are commercially available and inexpensive, and a simple household 15-W fluorescent light bulb can be employed as a suitable light source. A 2-g alkylation was readily accomplished using the outlined procedure (entry 7).

We have conducted a series of control experiments and luminescence quenching studies to test the validity of our proposed dual-cycle pathway and gain further insight into the photonic requirements for metal-mediated redox catalysis. The control experiments were performed using octanal with α-bromoacetophenone or diethyl bromomalonate in the presence of various catalyst combinations and a 15-W fluorescent light source (unless otherwise stated). Several observations are of note: Rigorous exclusion of light failed to produce even trace quantities of the coupling adduct. Moreover, removal of $Ru(bpy)_3^{2+}$ from our standard protocol resulted in <10% alkylation product over an extended timeframe (24 hours). High levels of reaction efficiency (>80%) can be obtained in the absence of $Ru(bpy)_3^{2+}$ if a high-energy UV irradiation source (300 to 350 nm) is employed in a photobox environment. In this specific case, we assume that a monocyclic catalysis mechanism is operable wherein the α-bromocarbonyl is converted to the requisite electron-deficient radical via photolytic bond homolysis (as opposed to catalytic SET reduction). Execution of our standard reaction with a light source specifically tuned to the $Ru(bpy)_3^{2+}$ MLCT absorption band (465 ± 20 nm full width

Downloaded from www.sciencemag.org on October 2, 2008

at half maximum, 500 mW) resulted in a dramatic acceleration in overall rate (90 min) as compared with the use of a typical household 15-W fluorescent bulb (6 hours), which operates with a wide spectral window (~400 to 700 nm). The use of the same 465-nm photon source in the absence of $Ru(bpy)_3^{2+}$ resulted in only trace product formation (<5%) (*28*). These experiments provide strong evidence of the participation of the $*Ru(bpy)_3^{2+}$ (**2**) excited state in the catalytic cycle.

With respect to our luminescence quenching studies, it has long been established that certain electron-deficient C–Br bonds can quench the emission intensity of $*Ru(bpy)_3^{2+}$ by SET (*29*). However, we did not observe a decrease in $*Ru(bpy)_3^{2+}$ luminescence in the presence of α-bromoacetophenone or diethyl bromomalonate, a result that negates the possibility that $*Ru(bpy)_3^{2+}$ (**2**) is participating as a reductant in our tandem catalysis sequence. In contrast, enamine **8** (pregenerated in stoichiometric quantities) does decrease the $*Ru(bpy)_3^{2+}$ emission intensity with a small but significant Stern-Volmer constant of 10 M^{-1} (see fig. S1) (*30*). These observations collectively support our mechanistic proposal that the $*Ru(bpy)_3^{2+}$ (**2**) excited state behaves as an oxidant in our photoredox cycle.

We have also gained circumstantial evidence that enamine **8** is the organocatalytic intermediate that participates in the key bond-forming step. More specifically, exposure of 2-phenylcyclopropyl acetaldehyde to our standard reaction protocol resulted in clean conversion (83% yield) to the corresponding alkylation product (see supporting online material). Failure of this radical clock substrate to undergo cyclopropyl ring opening clearly indicates that a 3π electron SOMO activated intermediate is not operative in the organocatalytic cycle.

References and Notes

1. K. Kalyanasundaram, *Coord. Chem. Rev.* **46**, 159 (1982).
2. A. Juris *et al.*, *Coord. Chem. Rev.* **84**, 85 (1988).
3. P. Renaud, M. P. Sibi, Eds., *Radicals in Organic Synthesis* (Wiley-VCH, Weinheim, Germany, 2001).
4. A. Berkessel, H. Gröger, Eds., *Asymmetric Organocatalysis: From Biomimetic Concepts to Applications in Asymmetric Synthesis* (Wiley-VCH, Weinheim, Germany, 2005).
5. P. I. Dalko, Ed., *Enantioselective Organocatalysis: Reactions and Experimental Procedures* (Wiley-VCH, Weinheim, Germany, 2007).
6. T. D. Beeson, A. Mastracchio, J. B. Hong, K. Ashton, D. W. C. MacMillan, *Science* **316**, 582 (2007); published online 28 March 2007 (10.1126/science. 1142696).
7. H. Jang, J. B. Hong, D. W. C. MacMillan, *J. Am. Chem. Soc.* **129**, 7004 (2007).
8. H. Kim, D. W. C. MacMillan, *J. Am. Chem. Soc.* **130**, 398 (2008).
9. A SOMO activation mechanism has also been reported for the α-oxidation of aldehydes (*10*).
10. M. Sibi, M. Hasegawa, *J. Am. Chem. Soc.* **129**, 4124 (2007).
11. H. B. Gray, J. R. Winkler, *Annu. Rev. Biochem.* **65**, 537 (1996).
12. An intramolecular α-formyl alkylation has been reported (*13*).
13. N. Vignola, B. List, *J. Am. Chem. Soc.* **126**, 450 (2004).
14. For a catalytic enantioselective alkylation of racemic α-bromoesters, see (*15*).
15. X. Dai, N. A. Strotman, G. C. Fu, *J. Am. Chem. Soc.* **130**, 3302 (2008).
16. P. Renaud, S. Schubert, **1990**, *Synlett* 624 (1990).
17. G. A. Russell, K. Wang, *J. Org. Chem.* **56**, 3475 (1991).
18. C. R. Bock *et al.*, *J. Am. Chem. Soc.* **101**, 4815 (1979).
19. Value was corrected from the $Ag/Ag^+ClO_4^-$ electrode (*20*).
20. D. D. Tanner, H. K. Singh, *J. Org. Chem.* **51**, 5182 (1986).
21. $Ru(bpy)_3^+$ has previously been shown to reduce phenacyl bromide (*22*).
22. S. Fukuzumi, S. Mochizuki, T. Tanaka, *J. Phys. Chem.* **94**, 722 (1990).
23. D. D. M. Wayner, J. J. Dannenberg, D. Griller, *Chem. Phys. Lett.* **131**, 189 (1986).
24. The possibility of direct one-electron reduction of the α-bromocarbonyl by the α-amino radical as a propagation step cannot be excluded.
25. DFT calculations were performed with the use of B3LYP/6-311+G(2d,2p)//B3LYP/6-31G(d).
26. A conformer that positions the enamine olefin toward the *tert*-butyl group was also found to be energetically relevant in these calculations. Because of the pseudo C_2-symmetric nature of catalyst **6**, this enamine conformer also exists with the *Si* face open and the *Re* face blocked in a manner similar to DFT–**8**.
27. Materials and methods are available as supporting material on *Science* Online.
28. No rate enhancement was observed in the absence of $Ru(bpy)_3^{2+}$ with additive bpy or Bu_4NCl.
29. S. Oishi, N. Furuta, *Chem. Lett.* **7**, 45 (1978).
30. None of the remaining reaction components (aldehyde, amine catalyst, 2,6-lutidine, or 2,6-lutidinium bromide) quenched $*Ru(bpy)_3^{2+}$.

31. We thank S. Bernhard for his assistance in performing quenching experiments, as well as many insightful discussions. Additionally, we thank T. J. Rainey for performing DFT calculations. Financial support was provided by the NIH General Medical Sciences (grant R01 GM078201-01-01) and gifts from Merck, Amgen, and Bristol-Myers Squibb. D.A.N. is grateful for a NIH National Service Research Award fellowship (F32GM076816).

Supporting Online Material

www.sciencemag.org/cgi/content/full/1161976/DC1
Materials and Methods
Figs. S1 to S3
References

18 June 2008; accepted 8 August 2008
Published online 4 September 2008;
10.1126/science.1161976
Include this information when citing this paper.

Temperature-Induced Hydrophobic-Hydrophilic Transition Observed by Water Adsorption

Hai-Jing Wang, Xue-Kui Xi, Alfred Kleinhammes, Yue Wu*

The properties of nanoconfined and interfacial water in the proximity of hydrophobic surfaces play a pivotal role in a variety of important phenomena such as protein folding. Water inside single-walled carbon nanotubes (SWNTs) can provide an ideal system for investigating such nanoconfined interfacial water on hydrophobic surfaces, provided that the nanotubes can be opened without introducing excess defects. Here, we report a hydrophobic-hydrophilic transition upon cooling from 22°C to 8°C via the observation of water adsorption isotherms in SWNTs measured by nuclear magnetic resonance. A considerable slowdown in molecular reorientation of such adsorbed water was also detected. The observed transition demonstrates that the structure of interfacial water could depend sensitively on temperature, which could lead to intriguing temperature dependences involving interfacial water on hydrophobic surfaces.

Water in the immediate vicinity of hydrophobic surfaces plays a crucial role in various important phenomena such as the folding and activity of proteins (*1*, *2*), but experimental signatures of these water layers have proven difficult to obtain. One possibility is that the structures and dynamics of nanoconfined interfacial water could possess distinctive temperature dependences (analogous perhaps to the anomalous density maximum manifested by bulk water at 4°C). A temperature dependence in the properties of interfacial water could be important for various processes, such as the cold denaturation of proteins (*2*).

Single-walled carbon nanotubes (SWNTs) provide a model system for investigating the properties of nanoconfined interfacial water (*3*–*9*). Because each nanotube with diameter of 1.4 nm can only accommodate one layer of water molecules on their inside surface (*5*), the behavior of adsorbed water inside such SWNTs could provide important insight into the properties of nanoconfined interfacial water. A previous theoretical study showed that water could fill the interior of carbon nanotubes through favorable structural effects on the local excess chemical potential (*3*). This result implies that water could be adsorbed inside SWNTs below saturated vapor pressure, as demonstrated by previous studies (*10*, *11*). However, in those studies, the defect density and principal adsorption sites (PAS), known to alter water adsorption isotherms in activated carbon (*12*), were likely too high to reveal the intrinsic adsorption properties of SWNTs. Water

Department of Physics and Astronomy, University of North Carolina, Chapel Hill, NC 27599–3255, USA.

*To whom correspondence should be addressed. E-mail: yuewu@physics.unc.edu

Downloaded from www.sciencemag.org on October 2, 2008

EXTENDED PDF FORMAT
SPONSORED BY
usb
Products from Affymetrix
www.usbweb.com

Temperature-Induced Hydrophobic-Hydrophilic Transition Observed by Water Adsorption

Hai-Jing Wang, *et al.*

Science **322**, 80 (2008);
DOI: 10.1126/science.1162412

The following resources related to this article are available online at www.sciencemag.org (this information is current as of October 2, 2008):

Updated information and services, including high-resolution figures, can be found in the online version of this article at:
http://www.sciencemag.org/cgi/content/full/322/5898/80

Supporting Online Material can be found at:
http://www.sciencemag.org/cgi/content/full/322/5898/80/DC1

This article **cites 28 articles**, 4 of which can be accessed for free:
http://www.sciencemag.org/cgi/content/full/322/5898/80#otherarticles

This article appears in the following **subject collections**:
Chemistry
http://www.sciencemag.org/cgi/collection/chemistry

Information about obtaining **reprints** of this article or about obtaining **permission to reproduce this article** in whole or in part can be found at:
http://www.sciencemag.org/about/permissions.dtl

Downloaded from www.sciencemag.org on October 2, 2008

Science (print ISSN 0036-8075; online ISSN 1095-9203) is published weekly, except the last week in December, by the American Association for the Advancement of Science, 1200 New York Avenue NW, Washington, DC 20005. Copyright 2008 by the American Association for the Advancement of Science; all rights reserved. The title *Science* is a registered trademark of AAAS.

at half maximum, 500 mW) resulted in a dramatic acceleration in overall rate (90 min) as compared with the use of a typical household 15-W fluorescent bulb (6 hours), which operates with a wide spectral window (~400 to 700 nm). The use of the same 465-nm photon source in the absence of $Ru(bpy)_3^{2+}$ resulted in only trace product formation (<5%) (*28*). These experiments provide strong evidence of the participation of the $*Ru(bpy)_3^{2+}$ (**2**) excited state in the catalytic cycle.

With respect to our luminescence quenching studies, it has long been established that certain electron-deficient C–Br bonds can quench the emission intensity of $*Ru(bpy)_3^{2+}$ by SET (*29*). However, we did not observe a decrease in $*Ru(bpy)_3^{2+}$ luminescence in the presence of α-bromoacetophenone or diethyl bromomalonate, a result that negates the possibility that $*Ru(bpy)_3^{2+}$ (**2**) is participating as a reductant in our tandem catalysis sequence. In contrast, enamine **8** (pregenerated in stoichiometric quantities) does decrease the $*Ru(bpy)_3^{2+}$ emission intensity with a small but significant Stern-Volmer constant of 10 M^{-1} (see fig. S1) (*30*). These observations collectively support our mechanistic proposal that the $*Ru(bpy)_3^{2+}$ (**2**) excited state behaves as an oxidant in our photoredox cycle.

We have also gained circumstantial evidence that enamine **8** is the organocatalytic intermediate that participates in the key bond-forming step. More specifically, exposure of 2-phenylcyclopropyl acetaldehyde to our standard reaction protocol resulted in clean conversion (83% yield) to the corresponding alkylation product (see supporting online material). Failure of this radical clock substrate to undergo cyclopropyl ring opening clearly indicates that a 3π electron SOMO activated intermediate is not operative in the organocatalytic cycle.

References and Notes

1. K. Kalyanasundaram, *Coord. Chem. Rev.* **46**, 159 (1982).
2. A. Juris *et al.*, *Coord. Chem. Rev.* **84**, 85 (1988).
3. P. Renaud, M. P. Sibi, Eds., *Radicals in Organic Synthesis* (Wiley-VCH, Weinheim, Germany, 2001).
4. A. Berkessel, H. Gröger, Eds., *Asymmetric Organocatalysis: From Biomimetic Concepts to Applications in Asymmetric Synthesis* (Wiley-VCH, Weinheim, Germany, 2005).
5. P. I. Dalko, Ed., *Enantioselective Organocatalysis: Reactions and Experimental Procedures* (Wiley-VCH, Weinheim, Germany, 2007).
6. T. D. Beeson, A. Mastracchio, J. B. Hong, K. Ashton, D. W. C. MacMillan, *Science* **316**, 582 (2007); published online 28 March 2007 (10.1126/science. 1142696).
7. H. Jang, J. B. Hong, D. W. C. MacMillan, *J. Am. Chem. Soc.* **129**, 7004 (2007).
8. H. Kim, D. W. C. MacMillan, *J. Am. Chem. Soc.* **130**, 398 (2008).
9. A SOMO activation mechanism has also been reported for the α-oxidation of aldehydes (*10*).
10. M. Sibi, M. Hasegawa, *J. Am. Chem. Soc.* **129**, 4124 (2007).
11. H. B. Gray, J. R. Winkler, *Annu. Rev. Biochem.* **65**, 537 (1996).
12. An intramolecular α-formyl alkylation has been reported (*13*).
13. N. Vignola, B. List, *J. Am. Chem. Soc.* **126**, 450 (2004).
14. For a catalytic enantioselective alkylation of racemic α-bromoesters, see (*15*).
15. X. Dai, N. A. Strotman, G. C. Fu, *J. Am. Chem. Soc.* **130**, 3302 (2008).
16. P. Renaud, S. Schubert, **1990**, *Synlett* 624 (1990).
17. G. A. Russell, K. Wang, *J. Org. Chem.* **56**, 3475 (1991).
18. C. R. Bock *et al.*, *J. Am. Chem. Soc.* **101**, 4815 (1979).
19. Value was corrected from the $Ag/Ag^+ClO_4^-$ electrode (*20*).
20. D. D. Tanner, H. K. Singh, *J. Org. Chem.* **51**, 5182 (1986).
21. $Ru(bpy)_3^+$ has previously been shown to reduce phenacyl bromide (*22*).
22. S. Fukuzumi, S. Mochizuki, T. Tanaka, *J. Phys. Chem.* **94**, 722 (1990).
23. D. D. M. Wayner, J. J. Dannenberg, D. Griller, *Chem. Phys. Lett.* **131**, 189 (1986).
24. The possibility of direct one-electron reduction of the α-bromocarbonyl by the α-amino radical as a propagation step cannot be excluded.
25. DFT calculations were performed with the use of B3LYP/6-311+G(2d,2p)//B3LYP/6-31G(d).
26. A conformer that positions the enamine olefin toward the *tert*-butyl group was also found to be energetically relevant in these calculations. Because of the pseudo C_2-symmetric nature of catalyst **6**, this enamine conformer also exists with the *Si* face open and the *Re* face blocked in a manner similar to DFT–**8**.
27. Materials and methods are available as supporting material on *Science* Online.
28. No rate enhancement was observed in the absence of $Ru(bpy)_3^{2+}$ with additive bpy or Bu_4NCl.
29. S. Oishi, N. Furuta, *Chem. Lett.* **7**, 45 (1978).
30. None of the remaining reaction components (aldehyde, amine catalyst, 2,6-lutidine, or 2,6-lutidinium bromide) quenched $*Ru(bpy)_3^{2+}$.

31. We thank S. Bernhard for his assistance in performing quenching experiments, as well as many insightful discussions. Additionally, we thank T. J. Rainey for performing DFT calculations. Financial support was provided by the NIH General Medical Sciences (grant R01 GM078201-01-01) and gifts from Merck, Amgen, and Bristol-Myers Squibb. D.A.N. is grateful for a NIH National Service Research Award fellowship (F32GM076816).

Supporting Online Material

www.sciencemag.org/cgi/content/full/1161976/DC1
Materials and Methods
Figs. S1 to S3
References

18 June 2008; accepted 8 August 2008
Published online 4 September 2008;
10.1126/science.1161976
Include this information when citing this paper.

Temperature-Induced Hydrophobic-Hydrophilic Transition Observed by Water Adsorption

Hai-Jing Wang, Xue-Kui Xi, Alfred Kleinhammes, Yue Wu*

The properties of nanoconfined and interfacial water in the proximity of hydrophobic surfaces play a pivotal role in a variety of important phenomena such as protein folding. Water inside single-walled carbon nanotubes (SWNTs) can provide an ideal system for investigating such nanoconfined interfacial water on hydrophobic surfaces, provided that the nanotubes can be opened without introducing excess defects. Here, we report a hydrophobic-hydrophilic transition upon cooling from 22°C to 8°C via the observation of water adsorption isotherms in SWNTs measured by nuclear magnetic resonance. A considerable slowdown in molecular reorientation of such adsorbed water was also detected. The observed transition demonstrates that the structure of interfacial water could depend sensitively on temperature, which could lead to intriguing temperature dependences involving interfacial water on hydrophobic surfaces.

Water in the immediate vicinity of hydrophobic surfaces plays a crucial role in various important phenomena such as the folding and activity of proteins (*1*, *2*), but experimental signatures of these water layers have proven difficult to obtain. One possibility is that the structures and dynamics of nanoconfined interfacial water could possess distinctive temperature dependences (analogous perhaps to the anomalous density maximum manifested by bulk water at 4°C). A temperature dependence in the properties of interfacial water could be important for various processes, such as the cold denaturation of proteins (*2*).

Single-walled carbon nanotubes (SWNTs) provide a model system for investigating the properties of nanoconfined interfacial water (*3*–*9*). Because each nanotube with diameter of 1.4 nm can only accommodate one layer of water molecules on their inside surface (*5*), the behavior of adsorbed water inside such SWNTs could provide important insight into the properties of nanoconfined interfacial water. A previous theoretical study showed that water could fill the interior of carbon nanotubes through favorable structural effects on the local excess chemical potential (*3*). This result implies that water could be adsorbed inside SWNTs below saturated vapor pressure, as demonstrated by previous studies (*10*, *11*). However, in those studies, the defect density and principal adsorption sites (PAS), known to alter water adsorption isotherms in activated carbon (*12*), were likely too high to reveal the intrinsic adsorption properties of SWNTs. Water

Department of Physics and Astronomy, University of North Carolina, Chapel Hill, NC 27599–3255, USA.

*To whom correspondence should be addressed. E-mail: yuewu@physics.unc.edu

Downloaded from www.sciencemag.org on October 2, 2008

adsorption isotherms in SWNTs depend on both the interaction with the surface and the structure of adsorbed water, which could depend on temperature. Here, we report a hydrophobic-hydrophilic transition upon cooling from 22.1°C to 8.0°C, revealed by water adsorption isotherms on the inside surface of low-defect SWNTs. Strong evidence is provided for the formation of monolayer water inside SWNTs at 8.0°C. Nuclear magnetic resonance (NMR) studies of the dynamics of reorientation of nanoconfined water molecules are shown to be much slower than in bulk water. In addition to various important biological processes, this new phenomenon could also shed light on the intrinsic adsorption mechanism of water in nanoporous carbon (*12*, *13*).

We synthesized SWNTs by laser ablation using 0.6 weight percent (each) Ni/Co as catalysts. The raw material was purified by refluxing in 20% H_2O_2 solution at 100°C for 12 hours and rinsing in CS_2 and then in methanol. The purified SWNTs were then annealed at 800°C. The tube diameter of 1.4 nm was determined from the Raman spectrum. Details of the sample preparation were described previously (*14*). The transmission electron microscope (TEM) image of the SWNTs is shown in fig. S1 (*15*). SWNTs after annealing usually have end caps that prevent the guest molecules from being adsorbed inside. Several techniques can be used to open the ends of SWNTs. In our previous study, etching by strong acids was used to cut tubes into short segments (*10*, *16*, *17*). Although this method is effective for opening tubes, it introduces a considerable amount of defect sites and functional groups acting as PAS that could have a strong influence on the water adsorption behavior. The high defect density in cut SWNTs could obscure the intrinsic adsorption behavior of SWNTs (*10*).

To reduce the influence of PAS and to reveal the intrinsic adsorption behavior, a much gentler method was adopted here to remove end caps (*18*). The SWNTs were heated at around 350°C in a thermogravimetric analyzer under air flow for more than 20 min until a weight loss of about 3% was reached. The ^{1}H NMR spectrum of ethane (fig. S2) (*15*) adsorbed in such treated SWNTs shows clear signatures of opened SWNTs (*16*, *17*). Water adsorption isotherms were measured by ^{1}H NMR at 0.8 T (34 MHz ^{1}H NMR frequency) equipped with an in situ water loading system with controlled vapor pressure and temperature. The ^{1}H NMR signal of vapor is negligible because of its low pressure (~2 kPa); no bulk water is condensed outside SWNTs below the saturated vapor pressure (P_0). Furthermore, water molecules are too large to access the interstitial sites of 1.4-nm diameter SWNTs bundles (*16*). Thus, the ^{1}H NMR signal is associated predominantly with the water adsorbed inside the SWNTs (*11*). The water content is calibrated by ethane ^{1}H NMR spectra as described in details elsewhere (*10*, *16*).

The amount of adsorbed water measured by ^{1}H NMR versus the relative pressure P/P_0 at 8.0°C, 18.4°C, and 22.1°C is shown in Fig. 1A. All three isotherms differ substantially from the S-shaped type V isotherm as observed in activated carbon and defective cut SWNTs, where adsorption increases slowly at low relative pressure but increases sharply above $P/P_0 = 0.5$, quickly reaching the level of saturation (*10*). Such an S-shaped adsorption isotherm in activated carbon is often attributed to PAS (*12*). Figure 1A shows that this ubiquitous sharp increase in the isotherms of activated carbon near $P/P_0 = 0.5$ is absent in low-defect SWNTs. The isotherm at 22.1°C exhibits a concave pattern as a type III isotherm, typical for clean hydrophobic surfaces with surface-water interactions weaker than water-water interactions (*19*). Interestingly, the isotherm at 8.0°C exhibits a convex pattern, a type II isotherm observed on hydrophilic surfaces (*20*). The isotherm at 18.4°C shows a linear pattern, which is a transitional pattern between the hydrophilic isotherm at 8.0°C and the hydrophobic isotherm at 22.1°C.

The water content was about 15 mmol/g when the relative pressure first reached the saturated pressure of $P/P_0 = 1$. This value is in good agreement with the calculated adsorption capacity of 13 mmol/g when SWNTs are supposed to be completely filled with water. This estimate is made by assuming that the van der Waals diameter of (10, 10) SWNTs is 0.99 nm (*5*) and the density of water is comparable to those at the hydrophobic interface, about 0.9 g/cm^3 (*21*). Further exposure at $P/P_0 = 1$ will lead to further increase of adsorption caused by condensation outside SWNTs.

More insight can be gained by analyzing the isotherm at 8.0°C with the Dubinin-Radushkevitch-Kaganer equation (*19*). It describes monolayer adsorption, given by

$$\log_{10} x = \log_{10} x_m - D[\log_{10} P_0/P)]^2 \quad (1)$$

where x is the adsorbed water content, x_m is the monolayer capacity, and D is a constant related to the temperature. A logarithmic plot of the adsorbed water versus $[\log_{10}(P_0/P)]^2$ is shown in Fig. 1C. Using the linear fit of data below the pressure of condensation and extrapolating to $[\log_{10}(P_0/P)]^2 = 0$, the monolayer capacity x_m is evaluated to be 8.7 ± 0.4 mmol/g. This value agrees well with the calculated value of 9.5 mmol/g for monolayer coverage of the inner surface of SWNTs. The monolayer water forms a tubular structure under the confinement of nanotubes, as illustrated in Fig. 1B (*22*). The convex shape of the water adsorption isotherm at 8.0°C and its upward turn at $P/P_0 \approx 0.8$ are also evidences of molecular layering on the adsorbed surface (*23*). This layering effect is commonly seen in liquid films (above the triple point temperature of the bulk liquid) of simple hydrocarbons and inert gases on graphite.

Water adsorption is a process of balancing the chemical potential of the confined water and the vapor. When water is confined in SWNTs, the energy loss from the breaking of hydrogen bonding (~20 kJ/mol) will not be completely compensated by the van der Waals interaction (<15 kJ/mol) (*24*). However, the local excess chemical potential is dominated not by the aver-

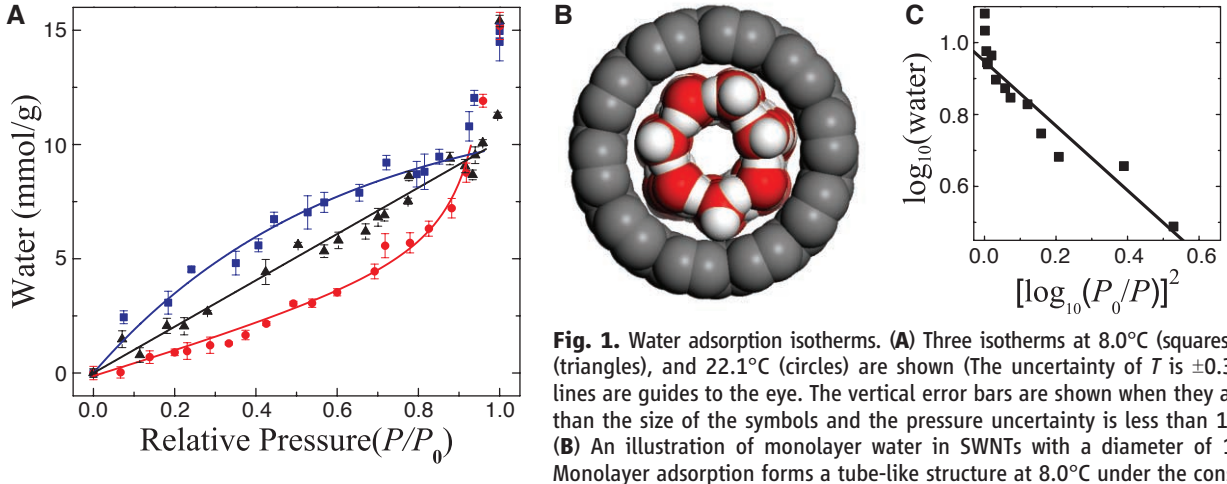

Fig. 1. Water adsorption isotherms. (**A**) Three isotherms at 8.0°C (squares), 18.4°C (triangles), and 22.1°C (circles) are shown (The uncertainty of T is ±0.3°C). The lines are guides to the eye. The vertical error bars are shown when they are larger than the size of the symbols and the pressure uncertainty is less than 1% of P_0. (**B**) An illustration of monolayer water in SWNTs with a diameter of 1.36 nm. Monolayer adsorption forms a tube-like structure at 8.0°C under the constraint of SWNTs. (**C**) A logarithmic plot of water content versus $[\log_{10}(P_0/P)]^2$ for the isotherm at 8.0°C, following the Dubbin-Radushkevitch-Kaganer equation.

Downloaded from www.sciencemag.org on October 2, 2008

age binding energy but by the low binding energy part, as determined by

$$\exp(\beta\mu^{ex}) = \langle\exp(\beta u)\rangle = \int p_{bind}(u)\exp(\beta u)du \quad (2)$$

where $\beta = 1/k_BT$, $p_{bind}(u)$ is the probability distribution of binding energy u ($u < 0$), and μ^{ex} is the local excess chemical potential defined as the difference between the chemical potential of water and that of an ideal gas under the same condition (*3*).

At 8.0°C, water adsorption proceeds so as to form a monolayer. The binding energy for adsorbed water with an ordered water nanotube structure, as predicted theoretically (*25*, *26*), is expected to be distributed more sharply than in bulk water. States of low binding energy are less frequently occupied. The chemical potential could be lower than that of saturated vapor. Thus, substantial adsorption could happen even at low relative pressure at 8.0°C, as shown in Fig. 1A. At 22.1°C, the adsorbed water in SWNTs could possess a variety of local structures and a broader distribution in binding energy. More states could be located in the low binding energy region, leading to higher chemical potential and an unfavorable condition for adsorption. Thus, much less water was adsorbed in SWNTs at 22.1°C than at 8.0°C.

To investigate the dynamics of adsorbed water molecules, the correlation time of molecular motion was estimated with ^{1}H spin-lattice relaxation time (T_1) and transverse relaxation time (T_2). The ^{1}H T_1 in water is determined by interaction fluctuations induced by molecular motions characterized by a correlation time τ. Assuming that the intramolecular proton-proton dipolar interaction of water molecules dominates the relaxation process, T_1 is given by (*27*)

$$\left(\frac{1}{T_1}\right) = \frac{3\gamma^4\hbar^2}{10r^6}\left(\frac{\tau}{1+\omega_0^2\tau^2} + \frac{4\tau}{1+4\omega_0^2\tau^2}\right) \quad (3)$$

where γ is the gyromagnetic ratio of proton, $2\pi\hbar$ is the Planck constant, r is the distance between the two hydrogen atoms in a water molecule, and $\omega_0/2\pi$ is the Larmor frequency (34 MHz at 0.8 T). A quantitative relation between T_2 and τ can also be established (*28*).

$$\left(\frac{1}{T_2}\right) = \frac{3\gamma^4\hbar^2}{20r^6} \times \left(3\tau + \frac{5\tau}{1+\omega_0^2\tau^2} + \frac{2\tau}{1+4\omega_0^2\tau^2}\right) \quad (4)$$

Figure 2C plots the theoretical values of T_1 and T_2 versus τ. The measured T_1 values versus pressure at 8.0°C and 18.4°C are shown in Fig. 2A. The T_1 at 8.0°C is shorter than that of 18.4°C at the same relative pressure until the saturated pressure is reached, where T_1 values at both temperatures converge to the same value. At 8.0°C, T_1 decreases slowly with increasing pressure up to $P/P_0 = 1.0$. At 18.4°C, however, T_1 decreases slowly with increasing pressure below $P/P_0 = 0.8$ but decreases rapidly with pressure above $P/P_0 = 0.8$.

Similarly, at 8.0°C, T_2 (Fig. 2B) increases slowly with pressure up to $P/P_0 = 1.0$, whereas at 18.4°C, T_2 increases very slowly below $P/P_0 = 0.8$ but increases sharply above $P/P_0 = 0.8$. T_2 is longer at 8.0°C than at 18.4°C at low relative pressure and becomes comparable at saturated pressure. This measurement reveals that T_2 is much shorter than T_1. Also, T_2 increases while T_1 decreases with either increasing relative pressure or decreasing temperature. Thus, the measured T_1 values are situated to the right of the T_1 minimum (slow-motion limit), as illustrated in Fig. 2C by the data at $P/P_0 = 0.75$. The measured T_2 values at $P/P_0 = 0.75$ are shorter than theoretical predictions, as plotted in Fig. 2C. The theoretical prediction of T_2 considers only intramolecular dipolar interaction and underestimates the relaxation rate $1/T_2$, which also depends on the intermolecular dipolar interactions. The molecular motions under confinement are anisotropic, and the intermolecular dipolar interaction cannot be easily averaged to zero (*29*, *30*).

The correlation time changes from 132 ns when T_1 is 7 ms (18.4°C, $P/P_0 = 0.75$) to 46 ns when T_1 is 3 ms (8.0°C, $P/P_0 = 0.75$). They are several orders of magnitude longer than 3.5 ps of bulk water at 20°C (on the left edge of Fig. 2C). The correlation time at 8.0°C is shorter than that at 18.4°C at low relative pressure, and the amount of adsorbed water at a given relative pressure below $P/P_0 = 0.9$ is different at these two temperatures. The structure and density of adsorbed water are also expected to be different and could lead to the observed difference in the correlation time. The correlation time at these two temperatures did become the same at $P/P_0 = 1.0$ (26 ns), where the amount of water became comparable. This suggests that the structure is similar at these two temperatures when the SWNTs are filled with water.

Because the intramolecular dipolar interaction dominates the spin-lattice relaxation, the long correlation time τ suggests that there is a substantial slowdown in molecular reorientation. The slowdown of certain dynamics of water in proximity to small hydrophobic groups has been shown previously (*31*). Here, we show a similar slowdown of water reorientation in proximity to an extended nonpolar surface.

Although the hydrophobic effect is widely known to be temperature dependent, our observation demonstrates that such temperature dependence could cause a qualitative change, as manifested by the hydrophobic-hydrophilic transition. At lower temperatures, well-defined layered structures of nanoconfined water on hydrophobic surfaces lead to a narrower probability distribution of the binding energy, making adsorption favorable in terms of the free energy. When such ordered structure is weakened at higher temperature, the distribution of the binding energy broadens, making adsorption unfavorable.

The hydrophobicity should not be considered as an absolute property of a surface under nanoconfinement without considering the structure of interfacial water. The correlation time of water reorientation in SWNTs is determined to be on the order of 10 to 100 ns. This result shows that the dynamics of water reorientation is hin-

Downloaded from www.sciencemag.org on October 2, 2008

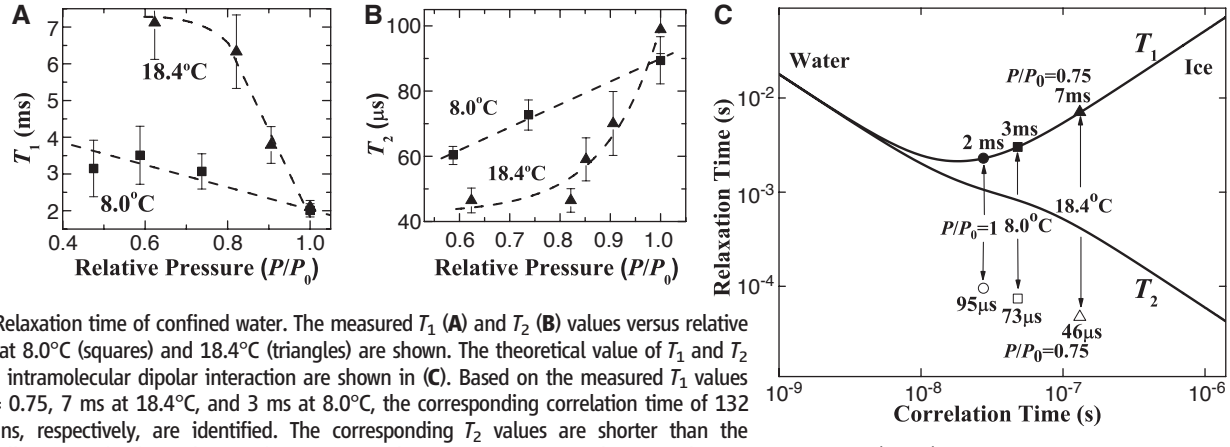

Fig. 2. Relaxation time of confined water. The measured T_1 (**A**) and T_2 (**B**) values versus relative pressure at 8.0°C (squares) and 18.4°C (triangles) are shown. The theoretical value of T_1 and T_2 based on intramolecular dipolar interaction are shown in (**C**). Based on the measured T_1 values at $P/P_0 = 0.75$, 7 ms at 18.4°C, and 3 ms at 8.0°C, the corresponding correlation time of 132 and 46 ns, respectively, are identified. The corresponding T_2 values are shorter than the theoretically expected values. The correlation time at these two temperatures becomes the same at $P/P_0 = 1$ (26 ns).

dered compared with bulk water, consistent with the dynamics of water molecules in proximity to small hydrophobic groups (*31*). The confined and interfacial water are prevalent in biological systems, such as the water in ion channels and in proximity to proteins. The affinity change due to temperature-induced structural change of water could be relevant to various phenomena, including in biological systems, such as the cold denaturation of proteins (*2*).

References and Notes

1. D. Chandler, *Nature* **437**, 640 (2005).
2. C. J. Tsai, J. V. Maizel, R. Nussinov, *Crit. Rev. Biochem. Mol. Biol.* **37**, 55 (2002).
3. G. Hummer, J. C. Rasaiah, J. P. Noworyta, *Nature* **414**, 188 (2001).
4. K. Koga, G. T. Gao, H. Tanaka, X. C. Zeng, *Physica A* **314**, 462 (2002).
5. R. J. Mashl, S. Joseph, N. R. Aluru, E. Jakobsson, *Nano Lett.* **3**, 589 (2003).
6. A. I. Kolesnikov *et al.*, *Phys. Rev. Lett.* **93**, 035503 (2004).
7. Y. Maniwa *et al.*, *Chem. Phys. Lett.* **401**, 534 (2005).
8. A. Striolo *et al.*, *Adsorption* **11**, 397 (2005).
9. J. K. Holt *et al.*, *Science* **312**, 1034 (2006).
10. S. H. Mao, A. Kleinhammes, Y. Wu, *Chem. Phys. Lett.* **421**, 513 (2006).
11. Q. Chen *et al.*, *Nano Lett.* **8**, 1902 (2008).
12. R. S. Vartapetyan, A. M. Voloshchuk, *Usp. Khim.* **64**, 1055 (1995).
13. T. Ohba, H. Kanoh, K. Kaneko, *J. Am. Chem. Soc.* **126**, 1560 (2004).
14. X. P. Tang *et al.*, *Science* **288**, 492 (2000).
15. Materials and methods are available as supporting material on *Science* Online.
16. A. Kleinhammes *et al.*, *Phys. Rev. B* **68**, 075418 (2003).
17. H. Z. Geng *et al.*, *Chem. Phys. Lett.* **399**, 109 (2004).
18. Y. Maniwa *et al.*, *Nat. Mater.* **6**, 135 (2007).
19. S. J. Gregg, K. S. W. Sing, *Adsorption, Surface Area, and Porosity* (Academic Press, London, New York, ed. 2, 1982).
20. J. Pires, M. L. Pinto, A. Carvalho, M. B. de Carvalho, *Adsorption* **9**, 303 (2003).
21. T. R. Jensen *et al.*, *Phys. Rev. Lett.* **90**, 086101 (2003).
22. O. Byl *et al.*, *J. Am. Chem. Soc.* **128**, 12090 (2006).
23. D. Beaglehole, H. K. Christenson, *J. Phys. Chem.* **96**, 3395 (1992).
24. G. R. Birkett, D. D. Do, *J. Phys. Chem. C* **111**, 5735 (2007).
25. T. Kurita, S. Okada, A. Oshiyama, *Phys. Rev. B* **75**, 205424 (2007).
26. D. Takaiwa, I. Hatano, K. Koga, H. Tanaka, *Proc. Natl. Acad. Sci. U.S.A.* **105**, 39 (2008).
27. A. Abragam, *The Principles of Nuclear Magnetism* (Clarendon Press, Oxford, 1961).
28. R. Kubo, K. Tomita, *J. Phys. Soc. Jpn.* **9**, 888 (1954).
29. J. P. Korb, S. Xu, J. Jonas, *J. Chem. Phys.* **98**, 2411 (1993).
30. J. Baugh *et al.*, *Science* **294**, 1505 (2001).
31. Y. L. A. Rezus, H. J. Bakker, *Phys. Rev. Lett.* **99**, 148301 (2007).

32. This work was supported by NSF under contract DMR 0513915. We thank O. Zhou for help in SWNTs synthesis.

Supporting Online Material

www.sciencemag.org/cgi/content/full/322/5898/80/DC1
Figs. S1 and S2

26 June 2008; accepted 19 August 2008
10.1126/science.1162412

Atmospheric CO_2 and Climate on Millennial Time Scales During the Last Glacial Period

Jinho Ahn* and Edward J. Brook

Reconstructions of ancient atmospheric carbon dioxide (CO_2) variations help us better understand how the global carbon cycle and climate are linked. We compared CO_2 variations on millennial time scales between 20,000 and 90,000 years ago with an Antarctic temperature proxy and records of abrupt climate change in the Northern Hemisphere. CO_2 concentration and Antarctic temperature were positively correlated over millennial-scale climate cycles, implying a strong connection to Southern Ocean processes. Evidence from marine sediment proxies indicates that CO_2 concentration rose most rapidly when North Atlantic Deep Water shoaled and stratification in the Southern Ocean was reduced. These increases in CO_2 concentration occurred during stadial (cold) periods in the Northern Hemisphere, several thousand years before abrupt warming events in Greenland.

The last glacial period was characterized by abrupt climate and environmental changes on millennial time scales. Prominent examples include abrupt warming and cooling in Greenland ice core records (Dansgaard-Oeschger, or DO, events) (*1*, *2*) and abrupt iceberg discharges in the North Atlantic (Heinrich, or H, events) (*3*), the latter appearing to predate the longest and largest DO events (Fig. 1A). Age synchronization between Greenland and Antarctic ice cores through atmospheric CH_4 variations reveals that Antarctic and Greenlandic temperature are linked, but not in phase (*4*, *5*) (Fig. 1, A, B, and D). Antarctic warming started before warming in Greenland for most of the large millennial events in the records, and Antarctic temperatures began to decline when Greenland rapidly warmed. Model and ice core studies suggest that this link is maintained by changes in meridional overturning circulation (*6*, *7*).

In contrast to the interhemispheric climate link, the relation between atmospheric CO_2 and climate, in the glacial period [~20 to 120 thousand years ago (ka)], has not been as well documented because of scatter in data sets (*8*) and/or chronological uncertainties (*9*). Understanding CO_2 variability is important, however, because of the direct role of CO_2 as a greenhouse gas and the probable influence of changes in ocean circulation on past atmospheric CO_2 concentrations. Here, we provide high-resolution atmospheric CO_2 data from the Byrd ice core (*10*), with a chronology well synchronized with the Greenland ice cores via CH_4 correlation (*4*). The data cover the period of 20 to 90 ka (Fig. 1C), including previously published results for 47 to 65 ka (*11*). We also measured CH_4 in 36 samples from Byrd to better constrain the chronology of the 67- to 87-ka time period [the time of DO-19, 20, and 21 and Antarctic events A5 to A7 (*4*)] (Fig. 1D). Rapid increases in CH_4 concentration are essentially synchronous with abrupt warming in Greenland within decades (*12*–*14*). With CH_4 and CO_2 data from the same core, and in many cases from the same samples, we could directly study the phasing between CO_2 and Greenland temperature variations, circumventing uncertainties due to age differences between ice and gas in ice core records (*12*–*14*).

We call attention to two distinct features of atmospheric CO_2 variations associated with climate changes in the Northern and Southern Hemispheres. First, CO_2 variation is strongly correlated with $\delta^{18}O_{ice}$ in the Byrd core, a proxy for site temperature, but whereas CO_2 remained relatively stable for about 1 to 2 ka after reaching maximum levels associated with peaks in Antarctic warming, Antarctic temperature dropped rapidly (Fig. 1, B and C, and fig. S1). In contrast to the slow decline of CO_2 relative to Antarctic cooling, the onsets of CO_2 increases are generally synchronous with Antarctic warming within data and age uncertainties (fig. S1).

Second, an increase in CO_2 predates, by 2 to 5 ka, the abrupt warming in Greenland associated with DO events, 8, 12, 14, 17, 20 and 21, the largest and longest abrupt events in the Greenland record over this time period (Figs. 1, A and C, and 2) (DO-19 may be an exception, but the timing of the onset of CO_2 rise is difficult to determine). The CO_2 increase slowed just after the abrupt warming of those events. We do not resolve any similar CO_2 variability associated with the shorter DO climate oscillations in the 37- to 65-ka period (DO-9, 11, 13, 15) with the current data set, but small variations associated with the shorter DO cycles cannot be excluded. Between 19 and 37 ka, there are some variations that may be associated with DO events 2 to 7, particularly a CO_2 peak at ~28 ka, which may be related to DO-4 and the stadial period preceding it. Higher-resolution data will be needed to further understand this variability.

Models of millennial-scale CO_2 variations suggest that changes in North Atlantic Deep

Department of Geosciences, Oregon State University, Corvallis, OR 97331–5506, USA.

*To whom correspondence should be addressed. E-mail: jinhoahn@gmail.com

Downloaded from www.sciencemag.org on October 2, 2008

EXTENDED PDF FORMAT
SPONSORED BY
usb
Products from Affymetrix
www.usbweb.com

Atmospheric CO2 and Climate on Millennial Time Scales During the Last Glacial Period

Jinho Ahn, *et al.*

Science **322**, 83 (2008);
DOI: 10.1126/science.1160832

The following resources related to this article are available online at www.sciencemag.org (this information is current as of October 2, 2008):

Updated information and services, including high-resolution figures, can be found in the online version of this article at:
http://www.sciencemag.org/cgi/content/full/322/5898/83

Supporting Online Material can be found at:
http://www.sciencemag.org/cgi/content/full/1160832/DC1

This article **cites 29 articles**, 3 of which can be accessed for free:
http://www.sciencemag.org/cgi/content/full/322/5898/83#otherarticles

This article appears in the following **subject collections**:
Atmospheric Science
http://www.sciencemag.org/cgi/collection/atmos

Information about obtaining **reprints** of this article or about obtaining **permission to reproduce this article** in whole or in part can be found at:
http://www.sciencemag.org/about/permissions.dtl

Downloaded from www.sciencemag.org on October 2, 2008

Science (print ISSN 0036-8075; online ISSN 1095-9203) is published weekly, except the last week in December, by the American Association for the Advancement of Science, 1200 New York Avenue NW, Washington, DC 20005. Copyright 2008 by the American Association for the Advancement of Science; all rights reserved. The title *Science* is a registered trademark of AAAS.

dered compared with bulk water, consistent with the dynamics of water molecules in proximity to small hydrophobic groups (*31*). The confined and interfacial water are prevalent in biological systems, such as the water in ion channels and in proximity to proteins. The affinity change due to temperature-induced structural change of water could be relevant to various phenomena, including in biological systems, such as the cold denaturation of proteins (*2*).

References and Notes

1. D. Chandler, *Nature* **437**, 640 (2005).
2. C. J. Tsai, J. V. Maizel, R. Nussinov, *Crit. Rev. Biochem. Mol. Biol.* **37**, 55 (2002).
3. G. Hummer, J. C. Rasaiah, J. P. Noworyta, *Nature* **414**, 188 (2001).
4. K. Koga, G. T. Gao, H. Tanaka, X. C. Zeng, *Physica A* **314**, 462 (2002).
5. R. J. Mashl, S. Joseph, N. R. Aluru, E. Jakobsson, *Nano Lett.* **3**, 589 (2003).
6. A. I. Kolesnikov *et al.*, *Phys. Rev. Lett.* **93**, 035503 (2004).
7. Y. Maniwa *et al.*, *Chem. Phys. Lett.* **401**, 534 (2005).
8. A. Striolo *et al.*, *Adsorption* **11**, 397 (2005).
9. J. K. Holt *et al.*, *Science* **312**, 1034 (2006).
10. S. H. Mao, A. Kleinhammes, Y. Wu, *Chem. Phys. Lett.* **421**, 513 (2006).
11. Q. Chen *et al.*, *Nano Lett.* **8**, 1902 (2008).
12. R. S. Vartapetyan, A. M. Voloshchuk, *Usp. Khim.* **64**, 1055 (1995).
13. T. Ohba, H. Kanoh, K. Kaneko, *J. Am. Chem. Soc.* **126**, 1560 (2004).
14. X. P. Tang *et al.*, *Science* **288**, 492 (2000).
15. Materials and methods are available as supporting material on *Science* Online.
16. A. Kleinhammes *et al.*, *Phys. Rev. B* **68**, 075418 (2003).
17. H. Z. Geng *et al.*, *Chem. Phys. Lett.* **399**, 109 (2004).
18. Y. Maniwa *et al.*, *Nat. Mater.* **6**, 135 (2007).
19. S. J. Gregg, K. S. W. Sing, *Adsorption, Surface Area, and Porosity* (Academic Press, London, New York, ed. 2, 1982).
20. J. Pires, M. L. Pinto, A. Carvalho, M. B. de Carvalho, *Adsorption* **9**, 303 (2003).
21. T. R. Jensen *et al.*, *Phys. Rev. Lett.* **90**, 086101 (2003).
22. O. Byl *et al.*, *J. Am. Chem. Soc.* **128**, 12090 (2006).
23. D. Beaglehole, H. K. Christenson, *J. Phys. Chem.* **96**, 3395 (1992).
24. G. R. Birkett, D. D. Do, *J. Phys. Chem. C* **111**, 5735 (2007).
25. T. Kurita, S. Okada, A. Oshiyama, *Phys. Rev. B* **75**, 205424 (2007).
26. D. Takaiwa, I. Hatano, K. Koga, H. Tanaka, *Proc. Natl. Acad. Sci. U.S.A.* **105**, 39 (2008).
27. A. Abragam, *The Principles of Nuclear Magnetism* (Clarendon Press, Oxford, 1961).
28. R. Kubo, K. Tomita, *J. Phys. Soc. Jpn.* **9**, 888 (1954).
29. J. P. Korb, S. Xu, J. Jonas, *J. Chem. Phys.* **98**, 2411 (1993).
30. J. Baugh *et al.*, *Science* **294**, 1505 (2001).
31. Y. L. A. Rezus, H. J. Bakker, *Phys. Rev. Lett.* **99**, 148301 (2007).

32. This work was supported by NSF under contract DMR 0513915. We thank O. Zhou for help in SWNTs synthesis.

Supporting Online Material

www.sciencemag.org/cgi/content/full/322/5898/80/DC1
Figs. S1 and S2

26 June 2008; accepted 19 August 2008
10.1126/science.1162412

Atmospheric CO_2 and Climate on Millennial Time Scales During the Last Glacial Period

Jinho Ahn* and Edward J. Brook

Reconstructions of ancient atmospheric carbon dioxide (CO_2) variations help us better understand how the global carbon cycle and climate are linked. We compared CO_2 variations on millennial time scales between 20,000 and 90,000 years ago with an Antarctic temperature proxy and records of abrupt climate change in the Northern Hemisphere. CO_2 concentration and Antarctic temperature were positively correlated over millennial-scale climate cycles, implying a strong connection to Southern Ocean processes. Evidence from marine sediment proxies indicates that CO_2 concentration rose most rapidly when North Atlantic Deep Water shoaled and stratification in the Southern Ocean was reduced. These increases in CO_2 concentration occurred during stadial (cold) periods in the Northern Hemisphere, several thousand years before abrupt warming events in Greenland.

The last glacial period was characterized by abrupt climate and environmental changes on millennial time scales. Prominent examples include abrupt warming and cooling in Greenland ice core records (Dansgaard-Oeschger, or DO, events) (*1*, *2*) and abrupt iceberg discharges in the North Atlantic (Heinrich, or H, events) (*3*), the latter appearing to predate the longest and largest DO events (Fig. 1A). Age synchronization between Greenland and Antarctic ice cores through atmospheric CH_4 variations reveals that Antarctic and Greenlandic temperature are linked, but not in phase (*4*, *5*) (Fig. 1, A, B, and D). Antarctic warming started before warming in Greenland for most of the large millennial events in the records, and Antarctic temperatures began to decline when Greenland rapidly warmed. Model and ice core studies suggest that this link is maintained by changes in meridional overturning circulation (*6*, *7*).

In contrast to the interhemispheric climate link, the relation between atmospheric CO_2 and climate, in the glacial period [~20 to 120 thousand years ago (ka)], has not been as well documented because of scatter in data sets (*8*) and/or chronological uncertainties (*9*). Understanding CO_2 variability is important, however, because of the direct role of CO_2 as a greenhouse gas and the probable influence of changes in ocean circulation on past atmospheric CO_2 concentrations. Here, we provide high-resolution atmospheric CO_2 data from the Byrd ice core (*10*), with a chronology well synchronized with the Greenland ice cores via CH_4 correlation (*4*). The data cover the period of 20 to 90 ka (Fig. 1C), including previously published results for 47 to 65 ka (*11*). We also measured CH_4 in 36 samples from Byrd to better constrain the chronology of the 67- to 87-ka time period [the time of DO-19, 20, and 21 and Antarctic events A5 to A7 (*4*)] (Fig. 1D). Rapid increases in CH_4 concentration are essentially synchronous with abrupt warming in Greenland within decades (*12*–*14*). With CH_4 and CO_2 data from the same core, and in many cases from the same samples, we could directly study the phasing between CO_2 and Greenland temperature variations, circumventing uncertainties due to age differences between ice and gas in ice core records (*12*–*14*).

We call attention to two distinct features of atmospheric CO_2 variations associated with climate changes in the Northern and Southern Hemispheres. First, CO_2 variation is strongly correlated with $\delta^{18}O_{ice}$ in the Byrd core, a proxy for site temperature, but whereas CO_2 remained relatively stable for about 1 to 2 ka after reaching maximum levels associated with peaks in Antarctic warming, Antarctic temperature dropped rapidly (Fig. 1, B and C, and fig. S1). In contrast to the slow decline of CO_2 relative to Antarctic cooling, the onsets of CO_2 increases are generally synchronous with Antarctic warming within data and age uncertainties (fig. S1).

Second, an increase in CO_2 predates, by 2 to 5 ka, the abrupt warming in Greenland associated with DO events, 8, 12, 14, 17, 20 and 21, the largest and longest abrupt events in the Greenland record over this time period (Figs. 1, A and C, and 2) (DO-19 may be an exception, but the timing of the onset of CO_2 rise is difficult to determine). The CO_2 increase slowed just after the abrupt warming of those events. We do not resolve any similar CO_2 variability associated with the shorter DO climate oscillations in the 37- to 65-ka period (DO-9, 11, 13, 15) with the current data set, but small variations associated with the shorter DO cycles cannot be excluded. Between 19 and 37 ka, there are some variations that may be associated with DO events 2 to 7, particularly a CO_2 peak at ~28 ka, which may be related to DO-4 and the stadial period preceding it. Higher-resolution data will be needed to further understand this variability.

Models of millennial-scale CO_2 variations suggest that changes in North Atlantic Deep

Department of Geosciences, Oregon State University, Corvallis, OR 97331–5506, USA.

*To whom correspondence should be addressed. E-mail: jinhoahn@gmail.com

Downloaded from www.sciencemag.org on October 2, 2008

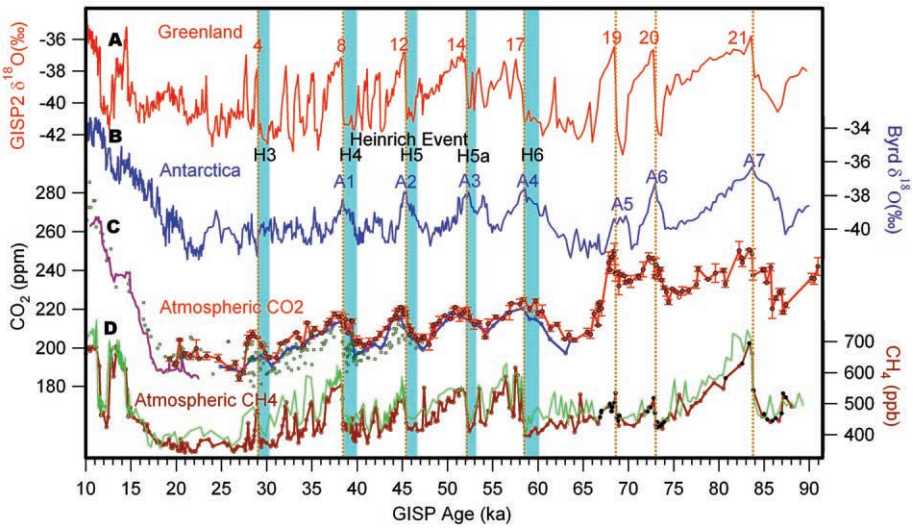

Fig. 1. Atmospheric CO_2 composition and climate during the last glacial period. (**A**) Greenlandic temperature proxy, $\delta^{18}O_{ice}$ (*2*). Red numbers denote DO events. (**B**) Byrd Station, Antarctica temperature proxy, $\delta^{18}O_{ice}$ (*4*). A1 to A7, Antarctic warming events (*4*). (**C**) Atmospheric CO_2 concentrations. Red dots [this study and early results for 47 to 65 ka (*11*) at Oregon State University] and green circles (*8*) (results from University of Bern) are from Byrd ice cores. Red dots are averages of replicates, and red open circles at ~73 and 76 ka are single data [this study and (*11*)]. The chronology used for Byrd CO_2 is described in (*10*). Blue line is from Taylor Dome ice core (*9*) on the GISP2 time scale (*11*). Purple line is from EPICA Dome C (*27*). (**D**) CH_4 concentrations from Greenland (green) (*4*) and Byrd ice cores (brown) [(*4*) and this study]. Black dots, new measurements for this study. Vertical blue bars, timing of Heinrich events (H3 to H6) (*25*, *26*). Brown dotted lines, abrupt warming in Greenland.

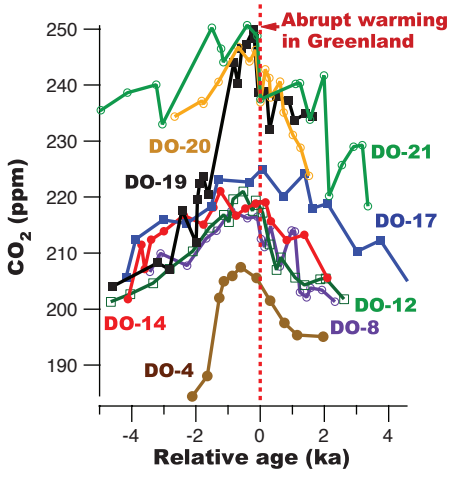

Fig. 2. Atmospheric CO_2 variations relative to abrupt warming in Greenland. The sequence of Byrd CO_2 variations [this study and (*11*)] associated with each DO event is numbered. Red dotted line indicates the timing of the abrupt warming in Greenland defined by the rapid rise in CH_4 concentration in the Byrd ice core.

Water (NADW) formation can affect atmospheric CO_2 concentration through both physical and biological processes in the ocean and terrestrial biosphere. Comparing model results is difficult because of differences in boundary conditions, amount and duration of freshwater forcing, and treatment of the terrestrial biosphere and other relevant processes. Model results suggest that several different mechanisms may relate changes in NADW to changes in atmospheric CO_2 concentration, including increases in Southern Ocean sea surface temperatures and decreased salinity in the North Atlantic (*15*), and reduced Southern Ocean stratification and release of CO_2 (*16*). Climate-induced changes in the terrestrial biosphere caused by changes in ocean circulation may also affect the atmospheric CO_2 (*17*, *18*), but the magnitude of this effect is not yet clear.

To explore the possible link between ocean circulation and CO_2, we compared our data with the benthic foraminiferal $\delta^{13}C$ from Iberian margin sediments at depth of 3146 m, using $\delta^{13}C$ as a proxy for the balance between northern source and southern source deep waters at this site (*19*) (Fig. 3C). We also used bulk sediment $\delta^{15}N$ from the Chile margin in intermediate depths as a proxy for input of the Subantarctic Mode Water to this region (*20*). Following (*20*), we interpreted this proxy as an indicator of the reduction of stratification in the Southern Ocean (Fig. 3D), which may result from changes in NADW. The two data sets are inversely correlated (note the reverse scale of the $\delta^{13}C$) in most time intervals, implying that shoaling NADW is linked to reduction of stratification in the Southern Ocean. The rate of change of CO_2 concentration peaks when these proxies indicate a maximum in NADW shoaling and reduction of stratification in the Southern Ocean (Fig. 3, B to D), implying CO_2 release to the atmosphere during maxima in Southern Ocean destratification, as suggested in model experiments (*16*). At around 19 to 37 ka, the correlations among the two marine proxies and the rate of change of CO_2 are not as clear as they are in the 37- to 91-ka time period. Other, perhaps longer-term processes may have controlled atmospheric CO_2 during this time period. Alternatively, the geochemical proxies plotted in Fig. 3 may not directly reflect millennial change in ocean circulation as climate approached the last glacial maximum. Models of long-term glacial-interglacial CO_2 variations indicate that destratification in the Southern Ocean should cause CO_2 to increase (*21*, *22*), although it is not clear if these model results are directly applicable to millennial-scale variations. Other mechanisms that may contribute to glacial-interglacial cycles and may be important on millennial time scales include changes in CO_2 outgassing due to variations in sea ice extent (*23*) and changes in iron fertilization (*24*) in the Southern Ocean.

Heinrich events are associated with the cold periods before major DO events, and one scenario that could explain CO_2 variations is that large freshwater fluxes associated with Heinrich events cause changes in ocean circulation and release of CO_2 to the atmosphere through mechanisms discussed above (*15*, *16*). However, based on existing age constraints (*3*, *25*, *26*), H events 3, 4, 5, 5a, and 6 appear to have occurred 0 to 3 ka after CO_2 started to rise (Fig. 1 and fig. S2). Unfortunately, precise comparison of CO_2 and all of the H events is prevented by chronological uncertainties. In some cases the relative timing of H events and events in the ice core record can be constrained via correlations between temperature proxies in marine records and ice core data, and identification of ash layers (*3*, *25*, *26*). For example, the abrupt warming at DO-15 (defined by the rapid rise in CH_4 concentration, fig. S2) has a correlative feature in North Atlantic sediment records (*26*) and occurred before H5a, whereas the CO_2 rise associated with A3 started during or before DO-15, and therefore also before H-5a. However, for other H events, the timing of the associated CO_2 rise cannot be precisely determined in this way given the current time resolution of the ice core records.

The data also indicate abrupt increases in CO_2 concentration of ~10 parts per million (ppm) at the times of abrupt warming associated with DO-19, 20, and 21 (Figs. 1 and 2). The magnitude of these jumps is similar to those during the last Termination (*27*), when the CO_2 level and temperature are similar to those of DO-19, 20, and 21 (65 to 90 ka). During the intervening period (20 to 65 ka), this type of variability is not as apparent in our record. The origin of these brief periods of elevated CO_2 is not clear, but may be related to increases in sea surface temperature in the Northern Hemisphere or release of CO_2 from the terrestrial biosphere by respiration, associated with abrupt warming in Greenland.

Another notable feature is the rapid decrease in CO_2 concentration of ~43 ppm at ~68 ka [Greenland Ice Sheet Project 2 (GISP2) time scale] after DO-19 (Figs. 1C and 4). The magnitude of the CO_2 drop is about half the total CO_2

Downloaded from www.sciencemag.org on October 2, 2008

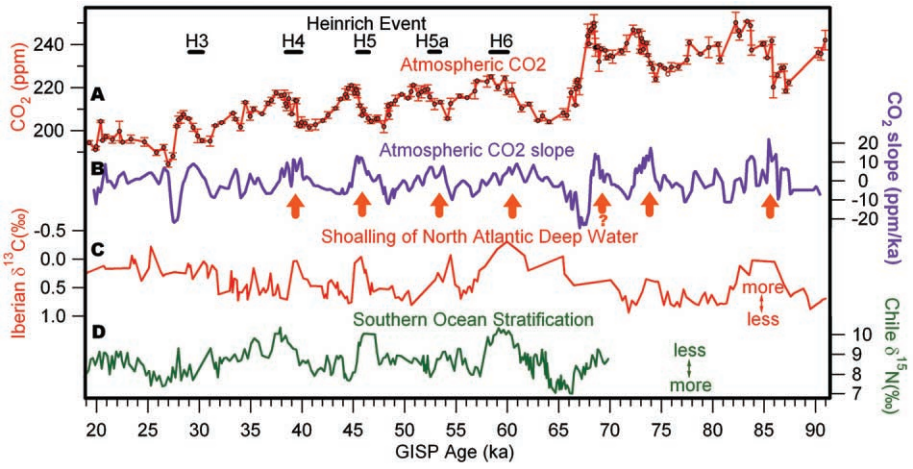

Fig. 3. Atmospheric CO_2 and change in ocean circulation. (**A**) Atmospheric CO_2 concentrations from the Antarctic Byrd ice core [this study and (*11*)], measured at Oregon State University (table S1). (**B**) Derivative of the Byrd CO_2 concentrations shown in (A). Nine-point running mean of the first derivative is calculated from data interpolated to 100-year spacing. (**C**) Benthic foraminifera (*Cibicidoides* wuellerstorfi) $\delta^{13}C$ from the Iberian margin sediment core (*19*). Ages are synchronized by correlation between planktonic foraminifera from the same sediment core and Greenland $\delta^{18}O_{ice}$ (*19*). (**D**) Bulk sediment $\delta^{15}N$ from the Chile Margin as a proxy for the reduction of the Southern Ocean stratification (*20*). Ages are synchronized by benthic foraminifera $\delta^{18}O$ correlation with that from Iberian margin (*20*). Orange arrows show the positive correlation between CO_2 derivative and reduced stratification in the Southern Ocean or shoaling NADW. The arrow with a question mark indicates an unclear correlation due to lack of resolution in the $\delta^{13}C$ record. Horizontal black bars, timing of Heinrich events (H3 to H6) (*25*, *26*).

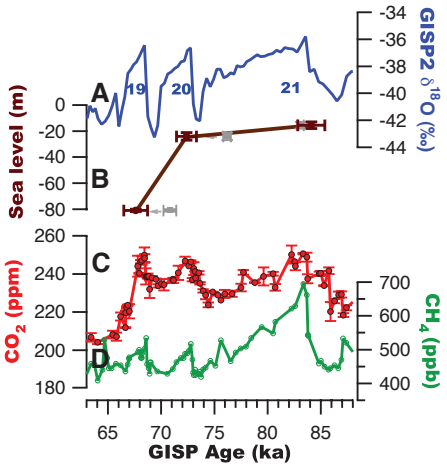

Fig. 4. Comparison of the rapid drop in CO_2 concentration with coral sea-level proxy. (**A**) Greenland temperature proxy (*2*). Blue numbers denote DO events. (**B**) Coral sea-level records (*33*). Original U-Th absolute ages (*33*) (gray dots) are adjusted to the GISP2 time scale (brown dots) by means of the correlations between Sanbao speleothem $\delta^{18}O$ (*34*) and GISP2 $\delta^{18}O_{ice}$ (*2*). The sea-level age uncertainties on the GISP2 time scale were calculated with age uncertainties from coral U-Th (±0.3 to 0.6 ka) and speleothem U-Th (±0.5 to 0.65 ka), and correlations between GISP2 and speleothem $\delta^{18}O$ (±0.5 to 1.0 ka) and between GISP2 $\delta^{18}O_{ice}$ and Byrd CO_2 records (±0.3 to 0.5 ka). (**C**) Atmospheric CO_2 concentration from Byrd ice core [this study and (*11*)]. (**D**) Atmospheric CH_4 concentration from Byrd ice core [(*4*) and this study].

variations during long-term glacial-interglacial cycles. The fastest rate of decrease during the event is ~11 ppm/ka, but the true value could have been even larger. A similar decrease of ~40 ppm at this time is also observed in low-resolution Vostok (*28*) and Dome Fuji records (*29*). A large sea-level drop appears to predate the CO_2 decline (Fig. 4). It is notable that a rapid increase of dust flux occurred in the equatorial Pacific and Antarctica at around the same time (*30*, *31*).

Our results support the idea that atmospheric CO_2 concentration is controlled by oceanic processes, especially those associated with proxies for the reduction of stratification in the Southern Ocean, but also affected by the Northern Hemisphere climate. Reductions in overturning circulation in the Northern Hemisphere appear to be associated with increases in atmospheric CO_2. On the basis of these data, if global warming causes a decrease in the overturning circulation (*32*), we might expect a positive feedback from additional CO_2 emissions to the atmosphere. However, the application of those observations to the future carbon cycle should be done cautiously because of differences between glacial and interglacial climate boundary conditions (*17*). It is likely that higher-resolution records of CO_2 will reveal more details about precise timing between Antarctic and Greenlandic temperature and atmospheric CO_2.

References and Notes

1. W. Dansgaard *et al.*, *Nature* **364**, 218 (1993).
2. P. M. Grootes, M. Stuiver, J. W. C. White, S. J. Johnsen, J. Jouzel, *Nature* **366**, 552 (1993).
3. G. Bond *et al.*, *Nature* **365**, 143 (1993).
4. T. Blunier, E. J. Brook, *Science* **291**, 109 (2001).
5. EPICA Community Members, *Nature* **444**, 195 (2006).
6. A. Ganopolski, S. Rahmstorf, *Nature* **409**, 153 (2001).
7. T. F. Stocker, S. J. Johnsen, *Paleoceanography* **18**, 10.1029/2003PA000920 (2003).
8. B. Stauffer *et al.*, *Nature* **392**, 59 (1998).
9. A. Indermühle, E. Monnin, B. Stauffer, T. F. Stocker, M. Wahlen, *Geophys. Res. Lett.* **27**, 735 (2000).
10. Materials and methods are available as supporting material on *Science* Online.
11. J. Ahn, E. J. Brook, *Geophys. Res. Lett.* **34**, L10703 10.1029/2007GL029551 (2007).
12. J. Severinghaus, A. Grachev, M. Spencer, R. Alley, E. J. Brook, *Geophys. Res. Abstr.* **5** (suppl.), 04455 (2003); available at www.cosis.net/abstracts/EAE03/04455/EAE03-J-04455.pdf.
13. C. Huber *et al.*, *Earth Planet. Sci. Lett.* **243**, 504 (2006).
14. A. Grachev, E. J. Brook, *Geophys. Res. Lett.* **34**, L20703, 10.1029/2007GL029799 (2007).
15. O. Marchal, T. F. Stocker, F. Joos, *Paleoceanography* **13**, 225 (1998).
16. A. Schmittner, E. J. Brook, J. Ahn, in *Ocean Circulation: Mechanisms and Impacts*, A. Schmittner, J. Chiang, S. Hemming, Eds. (AGU Geophysical Monograph Series, American Geophysical Union, Washington, DC, 2007), vol. 173, pp. 315–334.
17. P. Köhler, F. Joos, S. Gerber, R. Knutti, *Clim. Dyn.* **25**, 689 (2005).
18. L. Menviel, A. Timmermann, A. Mouchet, O. Timm, *Paleoceanography* **23**, 10.1029/2007PA001445 (2008).
19. N. J. Shackleton, M. A. Hall, E. Vincent, *Paleoceanography* **15**, 565 (2000).
20. R. Robinson, A. Mix, P. Martinez, *Quat. Sci. Rev.* **26**, 201 (2007).
21. A. J. Watson, A. C. N. Garabato, *Tellus* **58B**, 73 (2006).
22. J. R. Toggweiler, J. L. Russell, S. R. Carson, *Paleoceanography* **21**, 10.1029/2005PA001154 (2006).
23. B. B. Stephens, R. F. Keeling, *Nature* **404**, 171 (2000).
24. R. Röthlisberger *et al.*, *Geophys. Res. Lett.* **31**, 10.1029/2004GL020338 (2004).
25. M. Sarnthein *et al.*, in *The Northern North Atlantic: A Changing Environment*, P. Schäfer, M. Schlüter, W. Ritzrau, J. Thiede, Eds. (Springer, New York, 2001), pp. 365–410.
26. H. Rashid, R. Hesse, D. J. W. Piper, *Paleoceanography* **18**, 10.1029/2003PA000913 (2003).
27. E. Monnin *et al.*, *Science* **291**, 112 (2001).
28. J. R. Petit *et al.*, *Nature* **399**, 429 (1999).
29. K. Kawamura *et al.*, *Nature* **448**, 912 (2007).
30. G. Winckler, R. F. Anderson, M. Q. Fleisher, D. McGee, N. Mahowald, *Science* **320**, 93 (2008).
31. F. Lambert *et al.*, *Nature* **452**, 616 (2008).
32. IPCC, *Climate Change: The Physical Science Basis. Contribution of Working Group I to the Fourth Assessment Report of the Intergovernmental Panel on Climate Change*, S. Solomon *et al.*, Eds. (Cambridge Univ. Press, New York, 2007).
33. K. B. Cutler *et al.*, *Earth Planet. Sci. Lett.* **206**, 253 (2003).
34. Y. Wang *et al.*, *Nature* **451**, 1090 (2008).

35. We thank K. Howell, Q. Ouada, J. Lee, and L. Mitchell for assistance in gas chromatographic analysis; the staff of the National Ice Core Lab for ice sampling and curation; and S. Terhune for invaluable technical assistance. We also thank P. Clark, A. Schmittner, A. Mix, N. Pisias, and J. Stoner (Oregon State University) for helpful discussions. Financial support was provided by the Gary Comer Science and Education Foundation, and NSF grants OPP 0337891 and ATM 0602395.

Supporting Online Material

www.sciencemag.org/cgi/content/full/1160832/DC1
Materials and Methods
Figs. S1 and S2
Table S1
References

22 May 2008; accepted 2 September 2008
Published online 11 September 2008;
10.1126/science.1160832
Include this information when citing this paper.

Downloaded from www.sciencemag.org on October 2, 2008

EXTENDED PDF FORMAT
SPONSORED BY
usb
Products from Affymetrix
www.usbweb.com

Rates of Molecular Evolution Are Linked to Life History in Flowering Plants

Stephen A. Smith, *et al.*

Science **322**, 86 (2008);
DOI: 10.1126/science.1163197

The following resources related to this article are available online at www.sciencemag.org (this information is current as of October 2, 2008):

Updated information and services, including high-resolution figures, can be found in the online version of this article at:
http://www.sciencemag.org/cgi/content/full/322/5898/86

Supporting Online Material can be found at:
http://www.sciencemag.org/cgi/content/full/322/5898/86/DC1

This article **cites 34 articles**, 12 of which can be accessed for free:
http://www.sciencemag.org/cgi/content/full/322/5898/86#otherarticles

This article appears in the following **subject collections**:
Evolution
http://www.sciencemag.org/cgi/collection/evolution

Information about obtaining **reprints** of this article or about obtaining **permission to reproduce this article** in whole or in part can be found at:
http://www.sciencemag.org/about/permissions.dtl

Downloaded from www.sciencemag.org on October 2, 2008

Science (print ISSN 0036-8075; online ISSN 1095-9203) is published weekly, except the last week in December, by the American Association for the Advancement of Science, 1200 New York Avenue NW, Washington, DC 20005. Copyright 2008 by the American Association for the Advancement of Science; all rights reserved. The title *Science* is a registered trademark of AAAS.

Rates of Molecular Evolution Are Linked to Life History in Flowering Plants

Stephen A. Smith* and Michael J. Donoghue

Variable rates of molecular evolution have been documented across the tree of life, but the cause of this observed variation within and among clades remains uncertain. In plants, it has been suggested that life history traits are correlated with the rate of molecular evolution, but previous studies have yielded conflicting results. Exceptionally large phylogenies of five major angiosperm clades demonstrate that rates of molecular evolution are consistently low in trees and shrubs, with relatively long generation times, as compared with related herbaceous plants, which generally have shorter generation times. Herbs show much higher rates of molecular change but also much higher variance in rates. Correlates of life history attributes have long been of interest to biologists, and our results demonstrate how changes in the rate of molecular evolution that are linked to life history traits can affect measurements of the tempo of evolution as well as our ability to identify and conserve biodiversity.

Variation in the rate of molecular evolution has been attributed to a number of factors, including differences in body size, metabolic rate, DNA repair, and generation time (e.g., *1*–*4*). In plants, differences in rates of molecular evolution have been noted between annuals and perennials (*5*) and between woody and herbaceous species (*6*, *7*). These differences have been presumed to reflect differences in generation time (the time from seed germination to the production of fruits/seeds). However, in plants the relationship between life history and the average length of time before a nucleotide is copied either through replication or repair [nucleotide generation time (*1*)] is complicated by the fact that somatic mutations can accumulate during growth and can be transmitted through gametes (*8*, *9*). Variation in breeding system and/or seed-banking by annual plants (*9*) may also affect the ability to detect a correlation between molecular rate and generation time.

Previous studies have been inconclusive with respect to the extent and the correlates of rate heterogeneity in plants (*5*, *7*, *9*, *10*). Studies focused on individual smaller clades, or on single gene regions, have yielded results of uncertain generality (*7*), whereas broader phylogenetic studies have suffered from limited taxon sampling and, hence, comparisons among very distant relatives (*11*). Some tests have failed to account for phylogenetic relatedness (*9*).

We assembled molecular sequence data for five major branches within the flowering plants: three clades of asterids (Apiales, Dipsacales, and Primulales), one clade of rosids (Moraceae/Urticaceae), and one of monocotyledons (Commelinidae). We used group-to-group profile alignments (*12*) that take advantage of previously recognized clades within the groups analyzed (*13*) and yield denser data matrices (containing less missing data) than those produced using other strategies (*14*). Specifically, we identified alignable clusters of homologous gene regions, which were then concatenated with profile alignment (*13*). To minimize missing data, only phylogenetically informative clusters (with at least four taxa) were used. The gene regions varied among the five matrices but in each case included markers from the chloroplast, nuclear, and mitochondrial genomes (figs. S1 and S2 and table S2). The average gene region in our analyses contained 305 species; the smallest contained 10 species. This process resulted in an Apiales matrix of 1593 species by 9522 sites (>15 megabases); for Dipsacales, it was 366 by 11374 (>4 megabases); for Primulales, 529 by 11505 (>6 megabases); for Moraceae/Urticaceae, 457 by 7820 (>3.5 megabases); and for Commelinidae, 4657 by 22391 sites (>104 megabases).

Phylogenetic trees (Fig. 1) were inferred under maximum-likelihood (ML) with RAxML (vers.7.0.0) (*15*), with gene regions treated as separate partitions (*13*). We conducted 100 rapid bootstrap analyses, using every 10th bootstrap tree as a starting tree for a full ML search, and chose the tree with the highest likelihood score; owing to the size of the Commelinidae matrix, only a single ML search was conducted. For all clades but Commelinidae, we used nonparametric rate smoothing (*16*) to set branch lengths proportional to time; we used the PATHd8 method (*17*) for the exceptionally large commelinid analysis. Published studies were used to calibrate each phylogeny, using multiple calibration points to limit the impact of clade-specific rate heterogeneity (*13*, *18*–*21*). For Apiales and Primulales, we separately calibrated the major subclades identified in previous analyses, which also accommodated the fact that our analyses included some taxa not represented in previous studies.

Ancestral states of the life history trait "trees/shrubs" versus "herbs" (a proxy for generation time) (*6*, *7*, *22*) were inferred with ML methods (Fig. 1) (*13*); palms (Arecaceae, Commelinidae), which do not produce true wood (secondary xylem), were scored as trees/shrubs. For each branch on each phylogeny, we calculated the number of substitutions per nucleotide site per million years using branch lengths estimated from the dated molecular trees. Branch calculations were binned on the basis of inferred life history to produce box plots for each clade (Fig. 1). Outliers (values >1.5 times beyond the first and third quartiles) were excluded as artifacts of divergence-time estimation (e.g., those with zero or near-zero branch lengths). Within each major clade, we noted that trees/shrubs were consistently evolving more slowly than related herbaceous plants. Median rates of nucleotide divergence were 2.7 to 10 times as high in herbs as in trees/shrubs; herbs also showed higher ranges and variances (Fig. 1). None of the tree/shrub lineages examined here showed high rates of molecular evolution, but some herbaceous lineages were inferred to have low evolutionary rates, in the range characteristic of trees/shrubs. This asymmetry in variance may reflect the fact that, although most trees/shrubs are not able to reproduce within the first few years (*23*, *24*), as most herbs can, some herbs take as long as trees to flower. Consistent with the view that generation time influences the rate of molecular evolution within the Commelinidae (Fig. 1), the longer-lived bromeliads [which take up to 18 years to reproduce (*25*)] have remarkably short branches, with even fewer substitutions per site per million years than palms (0.00059 and 0.0014, respectively). Other factors, such as population size, breeding system, and seed-banking, may also relate to the observed asymmetry; for example, the rate of fixation of mutations by selection increases in large populations. Although we do not dismiss these variables in explaining the observed variance, they are less clearly correlated with the life history distinction than is generation time [e.g., (*26*)].

To explore whether the difference in rates of molecular evolution has remained constant over time, we compared substitutions per site per million years through 10-million-year segments for each dated phylogeny (Fig. 2) (*13*). We found that the trend in rate heterogeneity holds through time, with some noteworthy exceptions in the earliest time periods. For example, woody Dipsacales are estimated to have a high rate of evolution before the herbaceous habit is inferred to have evolved in this lineage (Fig. 2B). Fossil data might help to distinguish whether these results are best explained by incorrect reconstructions (i.e., perhaps the first Dipsacales were herbaceous), by faster evolution of woody lineages during earlier times (e.g., due to warmer climate in the early Tertiary), or by the extinction of early woody lineages.

Because these comparisons do not directly take into account phylogenetic relationships or examine the effects of evolutionary change from one life history state to the other, we calculated branch length contrasts (*27*) around each inferred evolutionary shift in life history (Fig. 3) (*13*). Specifically, we calculated the average accumulation of molecular changes from each branch tip to the shared ancestor of a tree/shrub clade and

Department of Ecology and Evolutionary Biology, 21 Sachem Street, Post Office Box 208105, Yale University, New Haven, CT 06520–8105, USA.

*To whom correspondence should be addressed. E-mail: stephen.smith@yale.edu

Downloaded from www.sciencemag.org on October 2, 2008

compared this to the average accumulation in its herbaceous sister clade. We started from the most nested clades and worked toward the root, excising any nested contrasts from the more inclusive calculations to avoid measuring any node more than once. We omitted contrasts containing only one tree/shrub or one herb branch to lessen the impact of incorrectly estimating singleton branches (branch lengths were averaged in clades with two or more species).

Of the 13 contrasts identified using these criteria (Table 1 and Fig. 3), 12 showed a slower rate of molecular evolution in trees/shrubs than in herbs (sign test, $P = 0.00342$). On average, herbs evolve 2.5 times as fast as trees/shrubs. A maximum rate difference of 4.75 times was found between *Dorstenia* (Moraceae) and its tree/shrub sister clade. The single exception occurred within *Sambucus* (Dipsacales), where the tree/shrub species showed a slightly higher rate than the herbs (0.0075 and 0.0061, respectively). This case involved the smallest

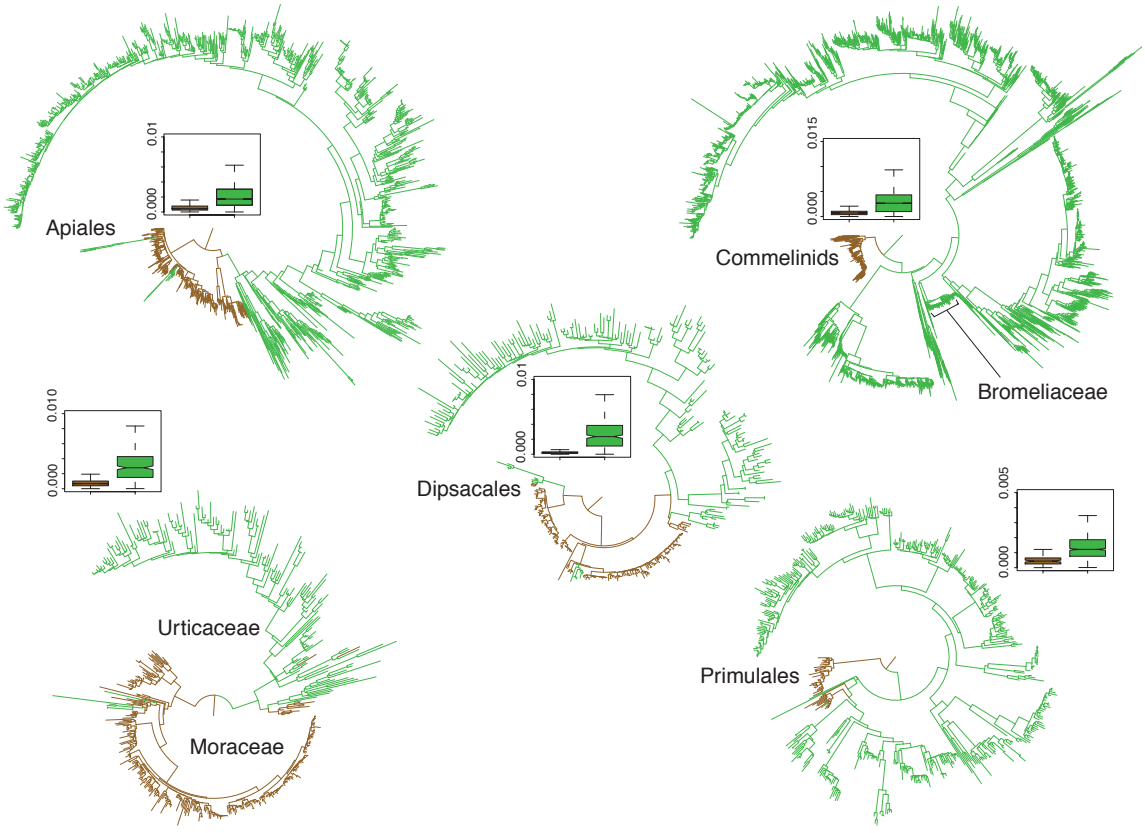

Fig. 1. Phylogenies of five angiosperm clades with branch lengths proportional to substitutions per site. Branch colors represent inferred life history states (brown for trees/shrubs; green for herbs). Box plots show substitutions per site per million years for the inferred life history categories; centerline represents the median, hinges mark the first and third quartiles, whiskers extend to the lowest and highest nonoutlier. Outliers (not shown) have values >1.5 times beyond the first or third quartiles.

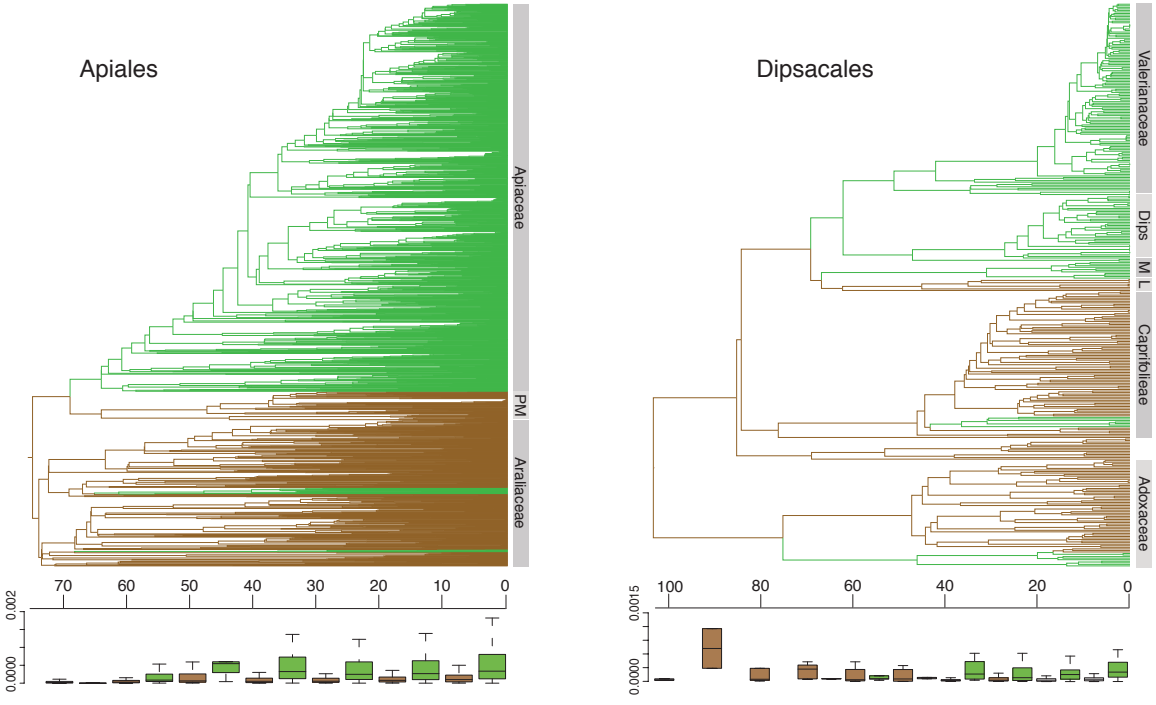

Fig. 2. Dated phylogenies for Apiales and Dipsacales with substitutions per site per million years plotted for 10-million-year intervals through the life of the clade. Branch colors represent inferred life history states (brown for trees/shrubs; green for herbs). Box plots as in Fig. 1. PM, Pittosporaceae and Myodocarpaceae; Dips, Dipsacaceae; M, Morinaceae; L, Linnaceae.

Downloaded from www.sciencemag.org on October 2, 2008

numbers of species (three shrubby species versus three herbs) and also presented the greatest difficulty in assigning life history states (the herbaceous species are subshrubby and the woody species mature rapidly). As such uncertainties are inherent in large comparative analyses, we explored whether alternative phylogenetic hypotheses (*13*) affected the results for the smallest clade examined here, the Dipsacales, as well as the effect of scoring all *Sambucus* species as trees/shrubs. These alternatives (Table 1 and Fig. 3) yielded a similarly strong historical correlation ($P = 0.00049$), as did the exclusion of these contrasts altogether ($P = 0.00195$).

On the basis of our trees and broader phylogenetic studies of angiosperms [reviewed in (*28*); see also (*29*)], the likely direction of evolution of plant habit was from trees/shrubs to the herbaceous condition in Apiales, Dipsacales, and Primulales, and with less certainly in Moraceae/Urticaceae. The palms (Arecaceae) within the Commelinidae present the one clear instance in our sample of the evolution of trees/shrubs from herbaceous ancestors (*30*). From our comparisons and a broader analysis of monocotyledons (*11*), the shift to the tree/shrub habit in palms was associated with a marked decrease in the rate of molecular evolution (palms evolve 2.7 times as slow as their sister commelinids), as predicted by the hypothesis that generation time drives the rate of molecular evolution.

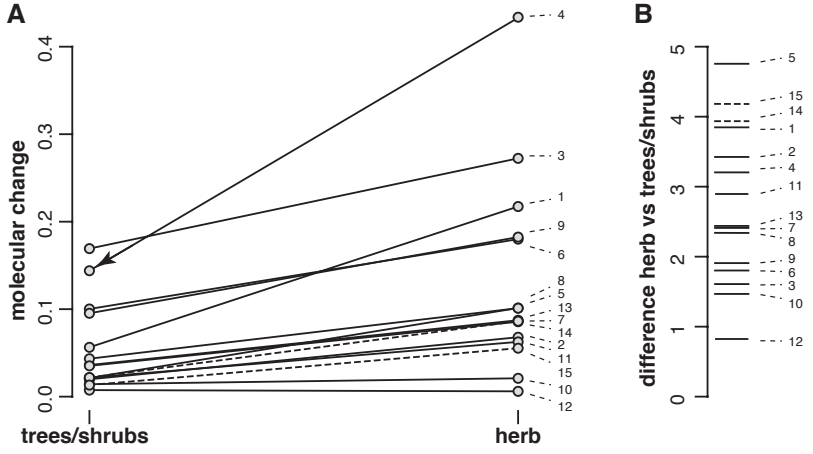

Fig. 3. Branch-length contrasts for trees/shrubs versus herbs. (**A**) Lines are drawn between the accumulated average molecular branch lengths for each tree/shrub clade and its sister herbaceous clade (numbers correspond to those in Table 1). All evolutionary shifts were inferred to be from trees/shrubs to herbs except for the evolution of palms within monocotyledons (arrowhead in contrast 4). Contrasts 1 to 13 were used in an initial sign test ($P = 0.00342$). Alternative contrasts within the Dipsacales (14 and 15) are marked by dotted lines and were substituted for 11 to 13 in one test ($P = 0.00049$); contrasts 11 to 15 were omitted in a third test ($P = 0.00195$). (**B**) Magnitude of change between each tree/shrub clade and its herbaceous sister clades; values above 1 show higher rates of molecular evolution in herbs than in trees/shrubs.

Table 1. Branch length contrasts 1 to 13 derive from the trees in Fig. 1 [see (*13*) for more exact locations of the nodes in question]. Plants in the first taxon in each pair of representative taxa are trees/shrubs; plants in the second are herbs. Within Dipsacales, we explored alternative contrasts, substituting contrasts 14 and 15 for 11 to 13 in one test and omitting contrasts 11 to 15 in another.

Major clade		Representative taxa	Trees/shrubs	Herbs	Difference
Apiales	1	*Astrotricha–Hydrocotyle*	0.0564	0.2173	3.8538
	2	*Aralia–Panax*	0.0198	0.0679	3.4224
	3	Pittosporaceae–Apiaceae	0.1692	0.2724	1.6097
Commelinidae	4	Arecales–remaining Commelinidae	0.1363	0.4350	3.1915
Moraceae–Urticaceae	5	*Brosimum–Dorstenia*	0.0213	0.1013	4.7527
	6	Moraceae–Urticaceae	0.1002	0.1800	1.7967
	7	*Cecropia/Coussapoa–Boehmeria*	0.0361	0.0873	2.4169
Primulales	8	*Ardisia*–sister Myrsinaceae	0.0433	0.1011	2.3330
	9	Theophrastaceae–Myrsinaceae/Primulaceae	0.0953	0.1824	1.9138
Dipsacales	10	*Symphoricarpos–Triosteum*	0.0142	0.0210	1.4747
	11	Linnaeeae–Morinaceae	0.0217	0.0626	2.8912
	12	Woody *Sambucus*–herbaceous *Sambucus*	0.0075	0.0061	0.8130
	13	*Viburnum–Adoxa*	0.0352	0.0856	2.4304
	14	Linnaeeae–Morinaceae/Dipsacaceae/Valerianaceae	0.0219	0.0863	3.9432
	15	"Woody" *Sambucus–Adoxa*	0.0133	0.0554	4.1783

Differences in rates of evolution associated with generation time may be reflected most clearly in synonymous substitutions within coding sequences (*31*). We analyzed 1208 commelinid *rbcL* sequences, pruning species lacking an *rbcL* sequence in GenBank from our Commelinidae phylogeny and using RAxML to estimate branch lengths for several partitions of the data (Table 2) (*13*). As expected, estimated amino acid branch lengths showed the least difference in rate between life history classes (2.1 times as fast as in herbs), with first and second nucleotide positions being next smallest (3.2 times as fast). The rate difference in the full Commelinidae data set (all species, all genes) fell between these two values (2.7 times as fast in herbs). The third positions showed the greatest difference in rate (4.98 times as fast in herbs). These findings are similar to those based on a much smaller sample of *rbcL* sequences from grasses and palms (*11*).

Our findings highlight the need for the methods used to date phylogenies to address the form of clade-dependent heterogeneity documented here. A rate of nucleotide substitution obtained from an herbaceous group cannot be used to calibrate a clade of trees/shrubs, or vice versa, without confounding age estimates. Likewise, relaxed clock methods [e.g., (*32*)] are likely to estimate that slowly evolving groups are younger, and that rapidly evolving groups are older, than their true ages. It may be possible to avoid mixing clades with very different life histories in designing dating studies. Otherwise, as we have attempted here, the use of multiple calibration points spanning clades that differ in life history may help alleviate this problem. Also, as shown here for Commelinidae, the use of amino acid sequences (or the removal of third sites) may be useful. Bayesian models that do not assume an autocorrelated rate of molecular evolution [e.g., (*33*)] are promising, but current methods are incapable of analyzing large data sets.

We hope that our results will also focus new attention on the extent to which molecular and morphological evolution are coupled [see (*34*, *35*)]. Are rates of morphological evolution also slower in trees/shrubs than in herbs [e.g., (*36*)]? Until this question is addressed, we urge caution in assuming that morphological change scales with molecular change and in using molecular branch lengths alone to assess "feature diversity" and design conservation strategies [e.g., (*37*)]. A related issue is the likely success of "barcoding" methods

Downloaded from www.sciencemag.org on October 2, 2008

Table 2. Branch length contrast estimates for different partitions of *rbcL* sequences from Commelinidae.

Estimate data	Palms	Rest of Commelinidae	Difference
Third sites	0.0369	0.1842	4.9872
First, second, and third sites	0.0331	0.1284	3.8808
First and second sites	0.0313	0.1007	3.2180
Amino acids	0.0464	0.0993	2.1379
All genes/species	0.1363	0.4350	3.1915

for identifying plant species from short DNA sequences [reviewed in (*33*)]. We predict that the chloroplast genes proposed as universal barcode loci will be most successful in resolving herbaceous species and may be incapable of confidently distinguishing closely related woody species.

Finally, our studies underscore the need for better and more accessible information on the underlying drivers of rates of molecular evolution. In addition to data on generation times, we need better knowledge of effective population sizes. Past analyses (e.g., in mammals) have assumed that larger, longer-lived organisms have smaller population sizes, but this may be reversed in plants, where tropical trees often appear to have large population sizes (*31*). Our analyses imply that somatic mutation has not counteracted the influence of generation time on rates of evolution, but more data are needed on the rate and fate of such mutations (*8*). In any event, our analyses demonstrate a general pattern that must now be taken into account in evolutionary studies and whose existence demands the elaboration of a cohesive causal explanation.

References and Notes

1. A. P. Martin, S. R. Palumbi, *Proc. Natl. Acad. Sci. U.S.A.* **90**, 4087 (1993).
2. A. O. Mooers, P. H. Harvey, *Mol. Phylogenet. Evol.* **3**, 344 (1994).
3. L. Bromham, A. Rambaut, P. H. Harvey, *J. Mol. Evol.* **43**, 610 (1996).
4. J. F. Gillooly, A. P. Allen, G. B. West, J. H. Brown, *Proc. Natl. Acad. Sci. U.S.A.* **102**, 140 (2005).
5. K. Andreasen, B. G. Baldwin, *Mol. Biol. Evol.* **18**, 936 (2001).
6. J. Laroche, P. Li, L. Maggia, J. Bousquet, *Proc. Natl. Acad. Sci. U.S.A.* **94**, 5722 (1997).
7. K. M. Kay, J. B. Whittall, S. A. Hodges, *BMC Evol. Biol.* **6**, 36 (2006).
8. E. J. Klekowski, P. J. Godfrey, *Nature* **340**, 389 (1989).
9. C. A. Whittle, M. O. Johnston, *J. Mol. Evol.* **56**, 223 (2003).
10. K. Andreasen, *Conserv. Genet.* **6**, 399 (2005).
11. B. S. Gaut, B. R. Morton, B. C. McCaig, M. T. Clegg, *Proc. Natl. Acad. Sci. U.S.A.* **93**, 10274 (1996).
12. R. C. Edgar, *Nucleic Acids Res.* **32**, 1792 (2004).
13. Materials and methods are available as supporting material on *Science* Online.
14. M. M. McMahon, M. J. Sanderson, *Syst. Biol.* **55**, 818 (2006).
15. A. Stamatakis, *Bioinformatics* **22**, 2688 (2006).
16. M. J. Sanderson, *Mol. Biol. Evol.* **14**, 1218 (1997).
17. T. Britton, C. L. Anderson, D. Jacquet, S. Lundqvist, K. Bremer, *Syst. Biol.* **56**, 741 (2007).
18. K. Bremer, E. M. Friis, B. Bremer, *Syst. Biol.* **53**, 496 (2004).
19. C. D. Bell, M. J. Donoghue, *Am. J. Bot.* **92**, 284 (2005).
20. N. J. C. Zerega, W. L. Clement, S. L. Datwyler, G. D. Weiblen, *Mol. Phylogenet. Evol.* **37**, 402 (2005).
21. T. Janssen, K. Bremer, *Bot. J. Linn. Soc.* **146**, 385 (2004).
22. J. Bousquet, S. H. Strauss, A. H. Doerksen, R. A. Price, *Proc. Natl. Acad. Sci. U.S.A.* **89**, 7844 (1992).
23. R. J. Petit, A. Hampe, *Annu. Rev. Ecol. Evol. Syst.* **37**, 187 (2006).
24. M. Verdú, *Evol. Int. J. Org. Evol.* **56**, 1352 (2002).
25. P. Hietz, J. Ausserer, G. Schindler, *J. Trop. Ecol.* **18**, 177 (2002).
26. S. S. Renner, R. E. Ricklefs, *Evol. Int. J. Org. Evol.* **82**, 596 (1995).
27. T. J. Davies, V. Savolainen, *Evol. Int. J. Org. Evol.* **60**, 476 (2006).
28. D. E. Soltis, P. S. Soltis, P. K. Endress, M. W. Chase, *Phylogeny and Evolution of Angiosperms* (Sinaur Associates, Sunderland, MA, 2005).
29. P. F. Stevens, Angiosperm Phylogeny Website, www.mobot.org/MOBOT/research/APweb (2008).
30. M. W. Chase *et al.*, *Aliso* **22**, 63 (2006).
31. T. Ohta, *Proc. Natl. Acad. Sci. U.S.A.* **90**, 10676 (1993).
32. M. J. Sanderson, *Mol. Biol. Evol.* **19**, 101 (2002).
33. A. J. Drummond, S. Y. W. Ho, M. J. Phillips, A. Rambaut, *PLoS Biol.* **4**, e88 (2006).
34. R. Lahaye, *Proc. Natl. Acad. Sci. U.S.A.* **105**, 2923 (2008).
35. T. G. Barraclough, V. Savolainen, *Evol. Int. J. Org. Evol.* **55**, 677 (2001).
36. E. W. Sinnott, *Am. Nat.* **50**, 466 (1916).
37. F. Forest *et al.*, *Nature* **445**, 757 (2007).

38. We thank D. Tank, J. Beaulieu, S. Stearns, D. Weinreich, C. Dunn, and E. Edwards for helpful discussions. Funded by the NSF through the Cyberinfrastructure for Phylogenetic Research (EF-0331654) and the angiosperm Assembling the Tree of Life (EF-0431258) projects.

Supporting Online Material

www.sciencemag.org/cgi/content/full/322/5898/86/DC1
Materials and Methods
Fig. S1 to S8
Tables S1 and S2
References

14 July 2008; accepted 5 September 2008
10.1126/science.1163197

Chemokine Signaling Controls Endodermal Migration During Zebrafish Gastrulation

Sreelaja Nair and Thomas F. Schilling*

Directed cell movements during gastrulation establish the germ layers of the vertebrate embryo and coordinate their contributions to different tissues and organs. Anterior migration of the mesoderm and endoderm has largely been interpreted to result from epiboly and convergent-extension movements that drive body elongation. We show that the chemokine Cxcl12b and its receptor Cxcr4a restrict anterior migration of the endoderm during zebrafish gastrulation, thereby coordinating its movements with those of the mesoderm. Depletion of either gene product causes disruption of integrin-dependent cell adhesion, resulting in separation of the endoderm from the mesoderm; the endoderm then migrates farther anteriorly than it normally would, resulting in bilateral duplication of endodermal organs. This process may have relevance to human gastrointestinal bifurcations and other organ defects.

A crucial feature of vertebrate embryogenesis is the coordinated morphogenesis of germ layers (endoderm, mesoderm, and ectoderm) during gastrulation (*1*). Interactions between the endoderm and mesoderm specify organ locations and symmetries (*2*). Defects in the endoderm alter the morphogenesis of mesodermal organs (e.g., heart, kidneys, and blood), whereas mesodermal defects disrupt the locations of the liver and pancreas (*2*–*5*). Morphogenesis is regulated by Wnt (*6*) and Nodal signaling (*7*) when cells are intermingled in a bipotential "mesendoderm" (*8*). However, relatively little is known about germ layer–specific pathways that establish organ rudiments. In zebrafish, mesendodermal organ progenitors involute at the gastrula margin (blastopore) and move anteriorly toward the animal pole (future head) while converging toward the midline (convergent extension).

The chemokine receptor CXCR4 controls directional migration in many contexts and is expressed in the endoderm. It is up-regulated by the endodermal determinants Mixer and Sox17β (*9*–*13*) and is required for gastrointestinal vascularization (*14*). Of the two closely related zebrafish Cxcr4s, Cxcr4b regulates the migration of many cell types (*12*, *15*–*18*), but no roles have been reported for Cxcr4a during embryogenesis.

Zebrafish embryos deficient in Cxcr4a or Cxcl12b, generated by injection with antisense morpholino oligonucleotides (MO), appeared morphologically normal (Fig. 1, A to C, and fig. S1). However, analysis of *Tg(gutGFP)*^{s854} transgenic embryos in which the entire gut fluoresces [(*19*); GFP, green fluorescent protein] revealed duplications of endodermal organs at 56 hours post-fertilization (hpf) (Fig. 1, D to F, and fig. S2), including the pancreas (normally on the right; fig. S3, A to F) and liver (normally

Department of Developmental and Cell Biology, University of California, Irvine, CA 92697, USA.

*To whom correspondence should be addressed. E-mail: tschilli@uci.edu

Downloaded from www.sciencemag.org on October 2, 2008

EXTENDED PDF FORMAT
SPONSORED BY
usb
Products from Affymetrix
www.usbweb.com

Chemokine Signaling Controls Endodermal Migration During Zebrafish Gastrulation

Sreelaja Nair, *et al.*

Science **322**, 89 (2008);
DOI: 10.1126/science.1160038

The following resources related to this article are available online at www.sciencemag.org (this information is current as of October 2, 2008):

Updated information and services, including high-resolution figures, can be found in the online version of this article at:
http://www.sciencemag.org/cgi/content/full/322/5898/89

Supporting Online Material can be found at:
http://www.sciencemag.org/cgi/content/full/1160038/DC1

This article **cites 36 articles**, 6 of which can be accessed for free:
http://www.sciencemag.org/cgi/content/full/322/5898/89#otherarticles

This article appears in the following **subject collections**:
Development
http://www.sciencemag.org/cgi/collection/development

Information about obtaining **reprints** of this article or about obtaining **permission to reproduce this article** in whole or in part can be found at:
http://www.sciencemag.org/about/permissions.dtl

Downloaded from www.sciencemag.org on October 2, 2008

Science (print ISSN 0036-8075; online ISSN 1095-9203) is published weekly, except the last week in December, by the American Association for the Advancement of Science, 1200 New York Avenue NW, Washington, DC 20005. Copyright 2008 by the American Association for the Advancement of Science; all rights reserved. The title *Science* is a registered trademark of AAAS.

Table 2. Branch length contrast estimates for different partitions of *rbcL* sequences from Commelinidae.

Estimate data	Palms	Rest of Commelinidae	Difference
Third sites	0.0369	0.1842	4.9872
First, second, and third sites	0.0331	0.1284	3.8808
First and second sites	0.0313	0.1007	3.2180
Amino acids	0.0464	0.0993	2.1379
All genes/species	0.1363	0.4350	3.1915

for identifying plant species from short DNA sequences [reviewed in (*33*)]. We predict that the chloroplast genes proposed as universal barcode loci will be most successful in resolving herbaceous species and may be incapable of confidently distinguishing closely related woody species.

Finally, our studies underscore the need for better and more accessible information on the underlying drivers of rates of molecular evolution. In addition to data on generation times, we need better knowledge of effective population sizes. Past analyses (e.g., in mammals) have assumed that larger, longer-lived organisms have smaller population sizes, but this may be reversed in plants, where tropical trees often appear to have large population sizes (*31*). Our analyses imply that somatic mutation has not counteracted the influence of generation time on rates of evolution, but more data are needed on the rate and fate of such mutations (*8*). In any event, our analyses demonstrate a general pattern that must now be taken into account in evolutionary studies and whose existence demands the elaboration of a cohesive causal explanation.

References and Notes

1. A. P. Martin, S. R. Palumbi, *Proc. Natl. Acad. Sci. U.S.A.* **90**, 4087 (1993).
2. A. O. Mooers, P. H. Harvey, *Mol. Phylogenet. Evol.* **3**, 344 (1994).
3. L. Bromham, A. Rambaut, P. H. Harvey, *J. Mol. Evol.* **43**, 610 (1996).
4. J. F. Gillooly, A. P. Allen, G. B. West, J. H. Brown, *Proc. Natl. Acad. Sci. U.S.A.* **102**, 140 (2005).
5. K. Andreasen, B. G. Baldwin, *Mol. Biol. Evol.* **18**, 936 (2001).
6. J. Laroche, P. Li, L. Maggia, J. Bousquet, *Proc. Natl. Acad. Sci. U.S.A.* **94**, 5722 (1997).
7. K. M. Kay, J. B. Whittall, S. A. Hodges, *BMC Evol. Biol.* **6**, 36 (2006).
8. E. J. Klekowski, P. J. Godfrey, *Nature* **340**, 389 (1989).
9. C. A. Whittle, M. O. Johnston, *J. Mol. Evol.* **56**, 223 (2003).
10. K. Andreasen, *Conserv. Genet.* **6**, 399 (2005).
11. B. S. Gaut, B. R. Morton, B. C. McCaig, M. T. Clegg, *Proc. Natl. Acad. Sci. U.S.A.* **93**, 10274 (1996).
12. R. C. Edgar, *Nucleic Acids Res.* **32**, 1792 (2004).
13. Materials and methods are available as supporting material on *Science* Online.
14. M. M. McMahon, M. J. Sanderson, *Syst. Biol.* **55**, 818 (2006).
15. A. Stamatakis, *Bioinformatics* **22**, 2688 (2006).
16. M. J. Sanderson, *Mol. Biol. Evol.* **14**, 1218 (1997).
17. T. Britton, C. L. Anderson, D. Jacquet, S. Lundqvist, K. Bremer, *Syst. Biol.* **56**, 741 (2007).
18. K. Bremer, E. M. Friis, B. Bremer, *Syst. Biol.* **53**, 496 (2004).
19. C. D. Bell, M. J. Donoghue, *Am. J. Bot.* **92**, 284 (2005).
20. N. J. C. Zerega, W. L. Clement, S. L. Datwyler, G. D. Weiblen, *Mol. Phylogenet. Evol.* **37**, 402 (2005).
21. T. Janssen, K. Bremer, *Bot. J. Linn. Soc.* **146**, 385 (2004).
22. J. Bousquet, S. H. Strauss, A. H. Doerksen, R. A. Price, *Proc. Natl. Acad. Sci. U.S.A.* **89**, 7844 (1992).
23. R. J. Petit, A. Hampe, *Annu. Rev. Ecol. Evol. Syst.* **37**, 187 (2006).
24. M. Verdú, *Evol. Int. J. Org. Evol.* **56**, 1352 (2002).
25. P. Hietz, J. Ausserer, G. Schindler, *J. Trop. Ecol.* **18**, 177 (2002).
26. S. S. Renner, R. E. Ricklefs, *Evol. Int. J. Org. Evol.* **82**, 596 (1995).
27. T. J. Davies, V. Savolainen, *Evol. Int. J. Org. Evol.* **60**, 476 (2006).
28. D. E. Soltis, P. S. Soltis, P. K. Endress, M. W. Chase, *Phylogeny and Evolution of Angiosperms* (Sinaur Associates, Sunderland, MA, 2005).
29. P. F. Stevens, Angiosperm Phylogeny Website, www.mobot.org/MOBOT/research/APweb (2008).
30. M. W. Chase *et al.*, *Aliso* **22**, 63 (2006).
31. T. Ohta, *Proc. Natl. Acad. Sci. U.S.A.* **90**, 10676 (1993).
32. M. J. Sanderson, *Mol. Biol. Evol.* **19**, 101 (2002).
33. A. J. Drummond, S. Y. W. Ho, M. J. Phillips, A. Rambaut, *PLoS Biol.* **4**, e88 (2006).
34. R. Lahaye, *Proc. Natl. Acad. Sci. U.S.A.* **105**, 2923 (2008).
35. T. G. Barraclough, V. Savolainen, *Evol. Int. J. Org. Evol.* **55**, 677 (2001).
36. E. W. Sinnott, *Am. Nat.* **50**, 466 (1916).
37. F. Forest *et al.*, *Nature* **445**, 757 (2007).

38. We thank D. Tank, J. Beaulieu, S. Stearns, D. Weinreich, C. Dunn, and E. Edwards for helpful discussions. Funded by the NSF through the Cyberinfrastructure for Phylogenetic Research (EF-0331654) and the angiosperm Assembling the Tree of Life (EF-0431258) projects.

Supporting Online Material

www.sciencemag.org/cgi/content/full/322/5898/86/DC1
Materials and Methods
Fig. S1 to S8
Tables S1 and S2
References

14 July 2008; accepted 5 September 2008
10.1126/science.1163197

Chemokine Signaling Controls Endodermal Migration During Zebrafish Gastrulation

Sreelaja Nair and Thomas F. Schilling*

Directed cell movements during gastrulation establish the germ layers of the vertebrate embryo and coordinate their contributions to different tissues and organs. Anterior migration of the mesoderm and endoderm has largely been interpreted to result from epiboly and convergent-extension movements that drive body elongation. We show that the chemokine Cxcl12b and its receptor Cxcr4a restrict anterior migration of the endoderm during zebrafish gastrulation, thereby coordinating its movements with those of the mesoderm. Depletion of either gene product causes disruption of integrin-dependent cell adhesion, resulting in separation of the endoderm from the mesoderm; the endoderm then migrates farther anteriorly than it normally would, resulting in bilateral duplication of endodermal organs. This process may have relevance to human gastrointestinal bifurcations and other organ defects.

A crucial feature of vertebrate embryogenesis is the coordinated morphogenesis of germ layers (endoderm, mesoderm, and ectoderm) during gastrulation (*1*). Interactions between the endoderm and mesoderm specify organ locations and symmetries (*2*). Defects in the endoderm alter the morphogenesis of mesodermal organs (e.g., heart, kidneys, and blood), whereas mesodermal defects disrupt the locations of the liver and pancreas (*2*–*5*). Morphogenesis is regulated by Wnt (*6*) and Nodal signaling (*7*) when cells are intermingled in a bipotential "mesendoderm" (*8*). However, relatively little is known about germ layer–specific pathways that establish organ rudiments. In zebrafish, mesendodermal organ progenitors involute at the gastrula margin (blastopore) and move anteriorly toward the animal pole (future head) while converging toward the midline (convergent extension).

The chemokine receptor CXCR4 controls directional migration in many contexts and is expressed in the endoderm. It is up-regulated by the endodermal determinants Mixer and Sox17β (*9*–*13*) and is required for gastrointestinal vascularization (*14*). Of the two closely related zebrafish Cxcr4s, Cxcr4b regulates the migration of many cell types (*12*, *15*–*18*), but no roles have been reported for Cxcr4a during embryogenesis.

Zebrafish embryos deficient in Cxcr4a or Cxcl12b, generated by injection with antisense morpholino oligonucleotides (MO), appeared morphologically normal (Fig. 1, A to C, and fig. S1). However, analysis of *Tg(gutGFP)*^{s854} transgenic embryos in which the entire gut fluoresces [(*19*); GFP, green fluorescent protein] revealed duplications of endodermal organs at 56 hours post-fertilization (hpf) (Fig. 1, D to F, and fig. S2), including the pancreas (normally on the right; fig. S3, A to F) and liver (normally

Department of Developmental and Cell Biology, University of California, Irvine, CA 92697, USA.

*To whom correspondence should be addressed. E-mail: tschilli@uci.edu

Downloaded from www.sciencemag.org on October 2, 2008

on the left; fig. S3, A to C and G to I), a phenotype we call "viscera bifida" (*cxcl12b*MO, 78%, *n* = 23; *cxcr4a*MO, 68%, *n* = 37). At 26 hpf, the intestine was also split bilaterally (Fig. 1, G to I; *12b*MO, 78%, *n* = 18; *4a*MO, 76%, *n* = 34), as revealed by *foxa2* expression, whereas the floor plate of the neural tube was unaffected (Fig. 1, H and I). No defects were detected in the mesoderm or ectoderm (fig. S3, J to O, and fig. S4).

During gastrulation, *cxcl12b* is expressed in mesoderm (Fig. 2, A, C, and E, and fig. S5, A and B), whereas *cxcr4a* is expressed in endoderm (Fig. 2, B, D, and F, and fig. S5, E and F), and both require Nodal signaling (fig. S5, C, D, G, and H), suggesting that chemokine signaling regulates endoderm-mesoderm interactions. At the onset of gastrulation (6 hpf), *sox32*$^{+}$ endodermal cells appeared normal in number but were displaced slightly anteriorly in *cxc12b* (83%, *n* = 82) and *cxcr4a* (74%, *n* = 62) morphants (Fig. 1, J to L). Displacement became more pronounced by 8 hpf, as revealed by *foxa2* expression (Fig. 1, M to O; *12b*MO, 88%, *n* = 34; *4a*MO, 85%, *n* = 55). In controls, the trailing edge of *foxa2*$^{+}$ cells was 50 to 100 μm from the margin, whereas in morphants this gap was larger by a factor of >3 (178 to 275 μm dorsally, 170 to 310 μm laterally, 186 to 340 μm ventrally) (Fig. 1P). The leading edge was also displaced up to 100 μm, particularly ventrally. Displacement was not due to precocious endodermal internalization (fig. S6), which suggests a later requirement for chemokine signaling in restricting endodermal movements anteriorly, toward the animal pole. We refer to this as endodermal tethering.

Despite displacement of the endoderm, the mesoderm was unaffected, as assayed by *no tail* (*ntl*) at 6 hpf (Fig. 1, J to L), *tbx16* in paraxial mesoderm at 8 hpf (fig. S4, A to C), and *hand2* in lateral plate mesoderm at 11 hpf (LPM; fig. S4, D to F). Our results reveal an early distinction between endodermal and mesodermal cell behaviors before they separate from the mesendoderm, thereby implicating the Cxcl12b-Cxcr4a system as among the earliest known signals in endodermal morphogenesis.

If Cxcl12b in mesoderm binds Cxcr4a in endodermal cells to restrict (tether) their movements, Cxcr4a should be required cell-autonomously in the endoderm. To test this, we transplanted endoderm-targeted *cxcr4a* morphant cells into wild-type hosts (Fig. 2, G to L). As an internal control, these cells were cotransplanted with wild-type endoderm into the same locations (Fig. 2, G, I, and K) in unlabeled hosts at 4 hpf, and cell distributions were compared 4 hours later (Fig. 2, H, J, and L). *cxcr4a* morphant endodermal cells moved, on average, 200 μm farther anteriorly than did controls (Fig. 2M), demonstrating a cell-autonomous requirement.

How does Cxcl2b-Cxcr4a signaling regulate endoderm migration? Because *cxcl12b* is maternally deposited and localized to the mesoderm, from which endodermal cells separate during gastrulation, it seems unlikely to act as a chemoattractant here. However, increasing evidence suggests that chemokine signaling modulates ex-

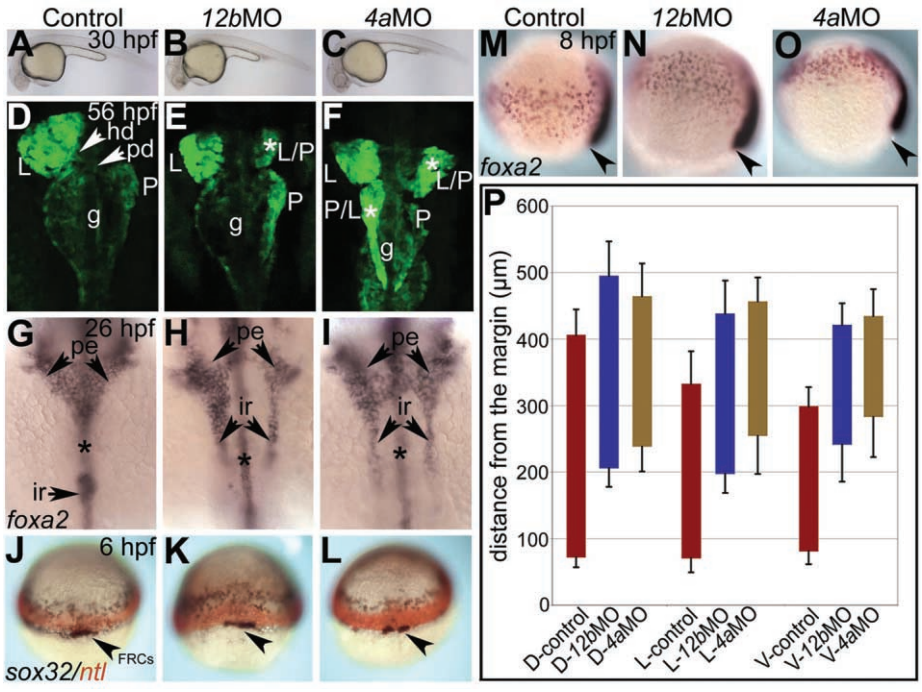

Fig. 1. *cxcl12b* and *cxcr4a* are required for endodermal morphogenesis. (**A** to **C**) Bright-field images, live embryos, 30 hpf; (A) control, (B) *cxcl12b* morphant, (C) *cxcr4a* morphant. (**D** to **L**) Dorsal views, anterior to the top. [(D) to (F)] *Tg(gutGFP)*^{s854}, 56 hpf, reveals duplicated liver (L) and pancreas (P) (asterisks) in confocal projections of *cxcl12b* (E) and *cxcr4a* (F) morphants. g, gut; hd, hepatic duct; pd, pancreatic duct. [(G) to (I)] *foxa2*, 26 hpf; the intestinal rod (ir) bifurcates, but not the floor plate (asterisks); pe, pharyngeal endoderm. [(J) to (L)] Double in situ hybridizations for *sox32* (endoderm, blue) and *ntl* (mesoderm, red), 6 hpf; *sox32*$^{+}$ cells, but not *ntl*$^{+}$ or *sox32*$^{+}$ forerunner cells (FRCs, arrowheads), move anteriorly (toward the animal pole and away from the margin). (**M** to **O**) *foxa2*, 8 hpf; lateral view. Morphant endoderm moves anteriorly (arrowheads indicate margin). (**P**) Quantitation of displacement of *foxa2*$^{+}$ cells at dorsal (D), lateral (L, 90° from D), and ventral (V, 180° from D) positions, 8 hpf. Controls, red bars; *cxcl12b* morphants, blue bars; *cxcr4a* morphants, gold bars.

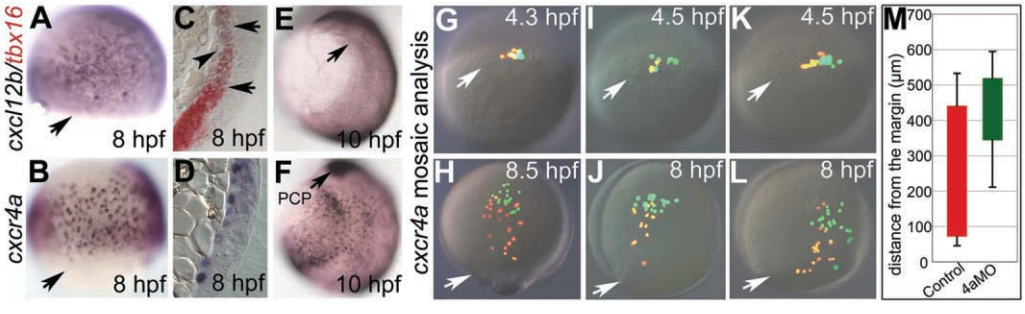

Fig. 2. Mesoderm expresses *cxcl12b* and endoderm requires *cxcr4a* cell-autonomously. (**A** to **F**) Whole-mount in situ hybridizations, dorsal right [except (C) and (D), transverse sections of gastrulae]. (A) *cxcl12b* in mesoderm, 8 hpf; arrow indicates margin. (B) *cxcr4a* in endoderm. (C) Double in situ hybridizations for *cxcl12b* (blue) and *tbx16* (red), 8 hpf, confirms coexpression in region indicated by arrows, but not in endoderm (arrowhead). (D) Endodermal *cxcr4a* expression. (E) *cxcl12b* in lateral mesoderm (arrow), 10 hpf. (F) *cxcr4a* in endoderm and prechordal plate (PCP, arrow), 10 hpf. (**G** to **L**) *cxcr4a* morphant (green; fluorescein) and control cells (red; rhodamine) grafted into unlabeled hosts, lateral views at 4.3 to 4.5 hpf [(G), (I), (K)] and 8 to 8.5 hpf [(H), (J), (L)]. (**M**) Average leading and trailing positions of control (red bar) and cxcr*4a* morphant (green bar) transplanted cells (*n* = 7).

Downloaded from www.sciencemag.org on October 2, 2008

tracellular matrix (ECM) proteins [e.g., fibronectin (FN), laminin] and their receptors (integrins), which are required for gastrulation (*20*–*24*). FN in ECM binds secreted CXCL12 and presents it to CXCR4, causing its redistribution to leading edges of migrating cells (*25*). Of several *fn*s in zebrafish, *fn1* is expressed by mesoderm during gastrulation (*26*). Thus, FN in the mesodermal ECM might bind and present Cxcl12b to Cxcr4a-expressing endoderm, sensitizing it to chemokines. CXCR4 activation by CXCL12 also enhances integrin-dependent adhesion of renal carcinoma and small-cell lung cancer cells to FN (*22*, *27*). Thus, we considered both FNs and integrins as potential downstream effectors during endoderm migration.

If this is correct, interfering with FN-integrin interactions should also disrupt endoderm migration. To test this, we treated gastrulating zebrafish embryos with RGD peptides (containing the tripeptide motif Arg-Gly-Asp), which bind integrins and block signaling (*28*). This caused anterior displacement of the endoderm at 8 hpf, similar to *cxcl12b* and *cxcr4a* morphants (Fig. 3, A and B; 40%, $n = 52$), and delayed convergence of endoderm toward the midline (fig. S7, A to F; 55%, $n = 20$). In contrast, convergence of LPM, which is required for gut morphogenesis (*5*), was unaffected (fig. S7, G and H), as in morphants (fig. S4, D to F). RGD peptide treatments of transgenic *Tg(gutGFP)*^{s854} embryos caused viscera bifida (Fig. 3, C and D; 42%, $n = 65$) or situs inversus (fig. S7, I and J; 14%, $n = 64$), even when applied at mid- to late gastrula stages (viscera bifida, 32%, $n = 22$; situs inversus, 18%, $n = 22$), indicating that integrin-dependent interactions are essential throughout gastrulation.

These results argue against the presentation of FN-bound Cxcl12b to Cxcr4a and instead suggest that chemokines control ECM-integrin–dependent adhesive interactions of the endoderm. To test this, we conducted in vitro cell adhesion assays to determine the ability of *cxcr4a* morphant endodermal cells to adhere to FN-coated surfaces. Relative to controls, the number of morphant cells that remained attached was reduced by one-third; adhesion was rescued by coinjection of *integrin beta 1b* (*itgb1b*) mRNA (Fig. 3E), which confirmed that chemokine signaling directly regulates adhesion of endoderm to FN.

Molecular interactions between CXCL12 and CXCR4 up-regulate levels of integrin α and β mRNAs in renal carcinoma cells to enhance their adhesion to FN (*22*). Thus, Cxcl12b-Cxcr4a signaling in the endoderm may similarly regulate integrin levels. Of the integrin βs expressed in zebrafish, *itgb1b* is expressed maternally and ubiquitously during gastrulation (*29*). Quantitative real-time polymerase chain reaction (qPCR) revealed a reduction in *itgb1b* mRNA levels in whole embryos and in *cxcr4a*MO endoderm (fig. S7K); this finding suggests that the link between chemokines and integrins is, at least in part, a transcriptional one.

If endodermal defects in *cxcl12b-cxcr4a* morphants reflect disruption of ECM-integrin signaling, injecting *itgb1b* mRNA into morphants should rescue these defects. *itgb1b* mRNA injected into *cxcl12b* and *cxcr4a* morphants rescued intestinal bifurcations in a dose-dependent manner (Fig. 3, F to K), either unilaterally (50 to 75 pg; Fig. 3, I and J) or completely (100 pg; Fig. 3K and table S1). Taken together, our results suggest that Cxcl12b-Cxcr4a interactions promote integrin-mediated adhesion to tether the endoderm to the mesoderm during gastrulation.

Cell adhesion is a key regulator of gastrulation movements. E-cadherin mediates epiboly and anterior migration of prechordal mesoderm (*30*), integrin-αB allows mesendodermal cells to

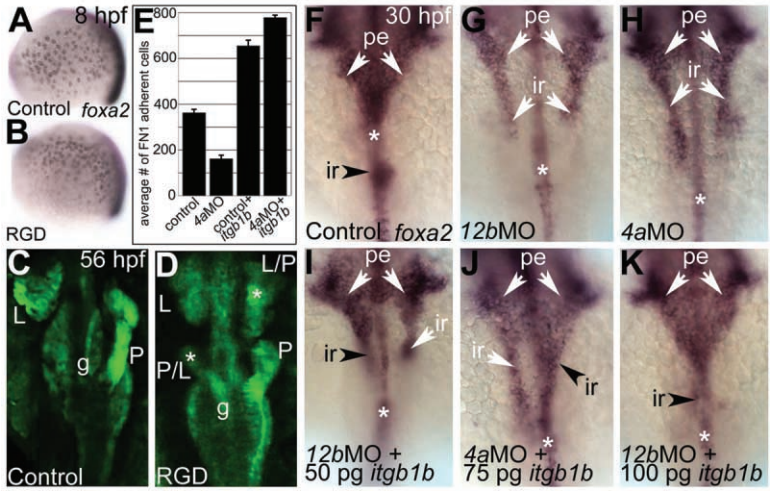

Fig. 3. FN-integrin–mediated cell adhesion restricts anterior migration of endoderm. (**A** and **B**) Whole-mount in situ hybridizations for *foxa2*, 8 hpf; lateral view, dorsal (right). *foxa2*$^{+}$ cells move anteriorly in RGD-treated embryos. (**C** and **D**) *Tg(gutGFP)*^{s854}, 56 hpf; liver (L) and pancreas (P) duplications (asterisks) in RGD-treated embryos. (**E**) Reduced adhesion of *cxcr4a* morphant endoderm to a FN1-coated surface, and rescue by *itgb1b* overexpression ($P = 0.003$ and 0.0003, respectively). (**F** to **K**) *foxa2*, 30 hpf; dorsal views, anterior to the top, showing expression in pharyngeal endoderm (pe), floor plate (asterisk), and intestinal rod (ir, arrowhead), which bifurcates in morphants (white arrows). Injection of 50 pg (I), 75 pg (J), and 100 pg (K) of *itgb1b* mRNA rescues the intestine partially [arrowheads, (I) and (J)] or completely [arrowhead, (K)].

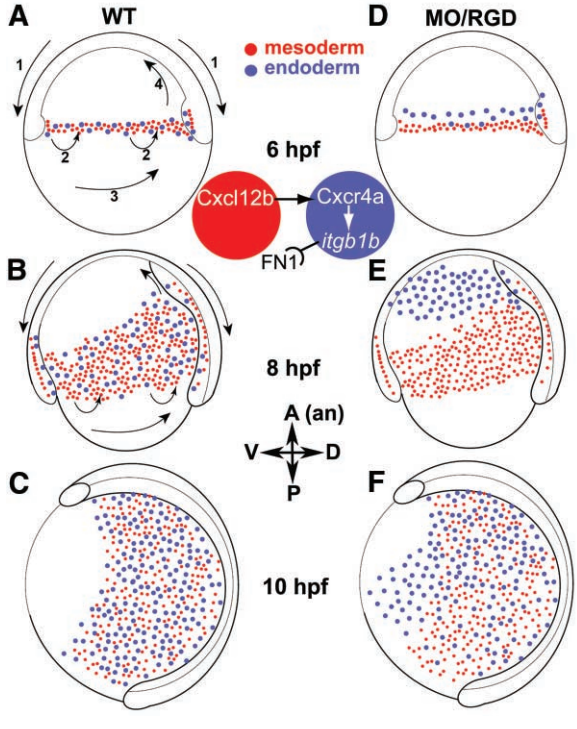

Fig. 4. A chemokine-mediated tether model for endodermal morphogenesis. Diagrams of a wild-type (WT) gastrula at 6, 8, and 10 hpf, and *cxcl12b*/*cxcr4a* morphants or RGD-treated (MO/RGD) embryos, lateral view, animal pole (top), dorsal (right). Endoderm, blue; mesoderm, red. Arrows: epiboly (1), involution (2), convergent extension (3), and anterior migration (4). (**A**) At onset of gastrulation, *cxcl12b*$^{+}$ mesoderm tethers *cxcr4a*$^{+}$ endoderm, which coordinates mesendoderm migration. (**B** and **C**) By the end of gastrulation, midline convergence clears ventral cells. (**D**) In morphants or RGD-treated embryos, endoderm released from this tether migrates anteriorly. (**E** and **F**) Displaced endoderm in anterior and ventral positions does not reach the midline [ectopic ventral blue dots in (F)], leading to organ duplication. Enlarged cells at center depict a molecular model in which Cxcl12b from mesoderm signals through Cxcr4a in endoderm to up-regulate *itgb1b* expression, which binds FN1 in the mesodermal extracellular matrix.

Downloaded from www.sciencemag.org on October 2, 2008

crawl on FN along the blastocoel roof (*31*), and *fn1* controls migration of myocardial progenitors toward the midline (*26*, *32*)—a process that also requires another chemokine, *apelin* (*33*, *34*). However, gut defects have generally been interpreted as secondary to defects in mesoderm migration. In contrast, our studies reveal an earlier requirement for ECM-integrin interactions directly in endoderm migration.

We have shown that endoderm migration toward the anterior is genetically separable from other gastrulation movements (*35*). We propose that chemokine-dependent expression of integrin tethers the endoderm to the mesoderm, and that loss of this tether releases the endoderm to move anteriorly (Fig. 4); a secondary result is viscera bifida, because endodermal cells on either side [presumably containing organ progenitors (*8*)] have farther to converge dorsally and do not reach the midline in time to fuse. Viscera bifida–like syndromes in humans, including intestinal cysts and ectopic pancreatic or liver tissue, are relatively common and are not associated with spina bifida (ectoderm) (*36*), and defects in the CXCL12-CXCR4 signaling pathway may be an underlying cause.

For zebrafish endodermal cells, regulation of migration by controlling adhesion reconciles the recent observation that involuted endodermal cells initially move via a "random walk" rather than the directed migration displayed by the mesoderm (*37*). Classically, chemokines are cytokines that induce chemotaxis in responding cells; CXCL12-CXCR4 interactions control homing of hematopoietic stem cells to the bone marrow, as well as migration of germ cells, neuronal progenitors, and several metastatic cancers (*15*–*18*, *27*). In some of these cases, however, there is evidence for a system more like the tether described here, where receptor-expressing cells are confined to a territory defined by ligand-expressing cells. Thus, chemokine-dependent changes in adhesion to the ECM may influence cell migration rates and directionality in many developmental and disease contexts.

References and Notes

1. L. Solnica-Krezel, *Curr. Biol.* **15**, R213 (2005).
2. D. J. Roberts, *Dev. Dyn.* **219**, 109 (2000).
3. J. Alexander *et al.*, *Dev. Biol.* **215**, 343 (1999).
4. F. Biemar *et al.*, *Dev. Biol.* **230**, 189 (2001).
5. E. A. Ober *et al.*, *Nature* **442**, 688 (2006).
6. R. Keller, *Science* **298**, 1950 (2002).
7. A. F. Schier, *Annu. Rev. Cell Dev. Biol.* **19**, 589 (2003).
8. R. M. Warga, C. Nusslein-Volhard, *Development* **126**, 827 (1999).
9. S. W. Chong *et al.*, *Mech. Dev.* **109**, 347 (2001).
10. K. Dickinson *et al.*, *Dev. Dyn.* **235**, 368 (2006).
11. A. Fukui *et al.*, *Biochem. Biophys. Res. Commun.* **354**, 472 (2007).
12. K. E. McGrath *et al.*, *Dev. Biol.* **213**, 442 (1999).
13. F. Yusuf *et al.*, *Anat. Embryol.* **210**, 35 (2005).
14. K. Tachibana *et al.*, *Nature* **393**, 591 (1998).
15. N. B. David *et al.*, *Proc. Natl. Acad. Sci. U.S.A.* **99**, 16297 (2002).
16. H. Knaut *et al.*, *Neuron* **47**, 653 (2005).
17. Q. Li *et al.*, *J. Neurosci.* **25**, 1711 (2005).
18. E. Raz, *Curr. Opin. Cell Biol.* **16**, 169 (2004).
19. H. A. Field *et al.*, *Dev. Biol.* **253**, 279 (2003).
20. T. N. Hartmann *et al.*, *Oncogene* **24**, 4462 (2005).
21. J. E. Howard *et al.*, *Mech. Dev.* **38**, 109 (1992).
22. J. Jones *et al.*, *Exp. Cell Res.* **313**, 4051 (2007).
23. F. M. Watt, K. J. Hodivala, *Curr. Biol.* **4**, 270 (1994).
24. R. Winklbauer, R. E. Keller, *Dev. Biol.* **177**, 413 (1996).
25. A. J. Pelletier *et al.*, *Blood* **96**, 2682 (2000).
26. L. A. Trinh, D. Y. Stainier, *Dev. Cell* **6**, 371 (2004).
27. J. Juarez, L. Bendall, *Histol. Histopathol.* **19**, 299 (2004).
28. E. Ruoslahti, *Annu. Rev. Cell Dev. Biol.* **12**, 697 (1996).
29. A. P. Mould *et al.*, *BMC Cell Biol.* **7**, 24 (2006).
30. J. A. Montero *et al.*, *Development* **132**, 1187 (2005).
31. R. Winklbauer *et al.*, *Int. J. Dev. Biol.* **40**, 305 (1996).
32. T. Sakaguchi *et al.*, *Development* **133**, 4063 (2006).
33. I. C. Scott *et al.*, *Dev. Cell* **12**, 403 (2007).
34. X. X. Zeng *et al.*, *Dev. Cell* **12**, 391 (2007).
35. R. Keller *et al.*, *Differentiation* **71**, 171 (2003).
36. R. E. Stevenson *et al.*, *Human Malformations and Related Anomalies* (Oxford Univ. Press, New York, 1993).
37. G. Pezeron *et al.*, *Curr. Biol.* **18**, 276 (2008).

38. We thank E. Raz for *cxcl12b* and *cxcr4a* constructs; our laboratory colleagues, especially S. Piloto for help with qPCR and T. Hoffman for help with itgb1b constructs; and I. Blitz for reviewing the manuscript. Supported by NIH grants R01NS41353 and R01DE13828.

Supporting Online Material

www.sciencemag.org/cgi/content/full/1160038/DC1
Materials and Methods
Figs. S1 to S7
Table S1
References

5 May 2008; accepted 13 August 2008
Published online 21 August 2008;
10.1126/science.1160038
Include this information when citing this paper.

Molecular Architecture of the "Stressosome," a Signal Integration and Transduction Hub

Jon Marles-Wright,[1]* Tim Grant,[2]* Olivier Delumeau,[1]† Gijs van Duinen,[2]‡ Susan J. Firbank,[1] Peter J. Lewis,[3] James W. Murray,[1]§ Joseph A. Newman,[1] Maureen B. Quin,[1] Paul R. Race,[1] Alexis Rohou,[2] Willem Tichelaar,[2]‖ Marin van Heel,[2]¶ Richard J. Lewis[1]¶

A commonly used strategy by microorganisms to survive multiple stresses involves a signal transduction cascade that increases the expression of stress-responsive genes. Stress signals can be integrated by a multiprotein signaling hub that responds to various signals to effect a single outcome. We obtained a medium-resolution cryo–electron microscopy reconstruction of the 1.8-megadalton "stressosome" from *Bacillus subtilis*. Fitting known crystal structures of components into this reconstruction gave a pseudoatomic structure, which had a virus capsid–like core with sensory extensions. We suggest that the different sensory extensions respond to different signals, whereas the conserved domains in the core integrate the varied signals. The architecture of the stressosome provides the potential for cooperativity, suggesting that the response could be tuned dependent on the magnitude of chemophysical insult.

Microorganisms experiencing a fluctuating environment commonly exhibit a short-lived, reversible response that allows survival and recovery of the cell (*1*). In Gram-positive bacteria such as *Bacillus subtilis*, one such signaling cascade ultimately leads to the activation of the general stress sigma factor, σ^B (fig. S1), and enhanced transcription of its large regulon to provide a global response to the imposed stress (*2*, *3*). The stressosome is the signaling hub that integrates multiple physical stress signals (*4*–*7*) and orchestrates a single signaling outcome: the activation of σ^B. The stressosome is found in many microbial phyla, including representatives of the Methanomicrobiales branch of the Euryarchaea and, within Bacteria, the Proteobacteria, the Firmicutes, the Actinobacteria, the Cyanobacteria, and the *Bacteroides* and *Deinococcus* groups (*8*). The downstream chromosomal organization in these organisms points to the involvement of stressosome orthologs in regulating aerotaxis, a variety of two-component signaling systems, and the biosynthesis of secondary messenger signaling molecules. Thus, the stressosome appears to have evolved to provide a common solution to the problem of signal integration.

In *Bacillus*, the stressosome is a ~1.8 MD supramolecular complex comprising multiple copies of the regulator of sigma B proteins: RsbS, RsbR, and four paralogs of RsbR (*7*, *9*–*13*). The C-terminal domain of RsbR and its paralogs is conserved and is similar in sequence to RsbS. By contrast, the N-terminal domains of the RsbR paralogs show high sequence variability, suggesting that they function as sensors, whereas the C-terminal domains integrate the various signals. A third protein, RsbT, interacts with RsbR:RsbS complexes (*9*) to transmit integrated environmental signals into the σ^B activation pathway. The ability of stressosomes to integrate multiple inputs to effect a single output represents a departure from the more common one- and two-component signaling systems in prokaryotes (*14*). These systems typically convert a single signal into a single outcome, usually the transcriptional modulation of small regulons in response to specific metabolic changes (*15*). The activity of the stressosome can be reconstituted both in vitro and in vivo by complexes consisting

Downloaded from www.sciencemag.org on October 2, 2008

EXTENDED PDF FORMAT
SPONSORED BY
usb
Products from Affymetrix
www.usbweb.com

Molecular Architecture of the "Stressosome," a Signal Integration and Transduction Hub

Jon Marles-Wright, *et al.*

Science **322**, 92 (2008);
DOI: 10.1126/science.1159572

The following resources related to this article are available online at www.sciencemag.org (this information is current as of October 2, 2008):

Updated information and services, including high-resolution figures, can be found in the online version of this article at:
http://www.sciencemag.org/cgi/content/full/322/5898/92

Supporting Online Material can be found at:
http://www.sciencemag.org/cgi/content/full/322/5898/92/DC1

This article **cites 31 articles**, 20 of which can be accessed for free:
http://www.sciencemag.org/cgi/content/full/322/5898/92#otherarticles

This article appears in the following **subject collections**:
Biochemistry
http://www.sciencemag.org/cgi/collection/biochem

Information about obtaining **reprints** of this article or about obtaining **permission to reproduce this article** in whole or in part can be found at:
http://www.sciencemag.org/about/permissions.dtl

Downloaded from www.sciencemag.org on October 2, 2008

Science (print ISSN 0036-8075; online ISSN 1095-9203) is published weekly, except the last week in December, by the American Association for the Advancement of Science, 1200 New York Avenue NW, Washington, DC 20005. Copyright 2008 by the American Association for the Advancement of Science; all rights reserved. The title *Science* is a registered trademark of AAAS.

crawl on FN along the blastocoel roof (*31*), and *fn1* controls migration of myocardial progenitors toward the midline (*26*, *32*)—a process that also requires another chemokine, *apelin* (*33*, *34*). However, gut defects have generally been interpreted as secondary to defects in mesoderm migration. In contrast, our studies reveal an earlier requirement for ECM-integrin interactions directly in endoderm migration.

We have shown that endoderm migration toward the anterior is genetically separable from other gastrulation movements (*35*). We propose that chemokine-dependent expression of integrin tethers the endoderm to the mesoderm, and that loss of this tether releases the endoderm to move anteriorly (Fig. 4); a secondary result is viscera bifida, because endodermal cells on either side [presumably containing organ progenitors (*8*)] have farther to converge dorsally and do not reach the midline in time to fuse. Viscera bifida–like syndromes in humans, including intestinal cysts and ectopic pancreatic or liver tissue, are relatively common and are not associated with spina bifida (ectoderm) (*36*), and defects in the CXCL12-CXCR4 signaling pathway may be an underlying cause.

For zebrafish endodermal cells, regulation of migration by controlling adhesion reconciles the recent observation that involuted endodermal cells initially move via a "random walk" rather than the directed migration displayed by the mesoderm (*37*). Classically, chemokines are cytokines that induce chemotaxis in responding cells; CXCL12-CXCR4 interactions control homing of hematopoietic stem cells to the bone marrow, as well as migration of germ cells, neuronal progenitors, and several metastatic cancers (*15*–*18*, *27*). In some of these cases, however, there is evidence for a system more like the tether described here, where receptor-expressing cells are confined to a territory defined by ligand-expressing cells. Thus, chemokine-dependent changes in adhesion to the ECM may influence cell migration rates and directionality in many developmental and disease contexts.

References and Notes

1. L. Solnica-Krezel, *Curr. Biol.* **15**, R213 (2005).
2. D. J. Roberts, *Dev. Dyn.* **219**, 109 (2000).
3. J. Alexander *et al.*, *Dev. Biol.* **215**, 343 (1999).
4. F. Biemar *et al.*, *Dev. Biol.* **230**, 189 (2001).
5. E. A. Ober *et al.*, *Nature* **442**, 688 (2006).
6. R. Keller, *Science* **298**, 1950 (2002).
7. A. F. Schier, *Annu. Rev. Cell Dev. Biol.* **19**, 589 (2003).
8. R. M. Warga, C. Nusslein-Volhard, *Development* **126**, 827 (1999).
9. S. W. Chong *et al.*, *Mech. Dev.* **109**, 347 (2001).
10. K. Dickinson *et al.*, *Dev. Dyn.* **235**, 368 (2006).
11. A. Fukui *et al.*, *Biochem. Biophys. Res. Commun.* **354**, 472 (2007).
12. K. E. McGrath *et al.*, *Dev. Biol.* **213**, 442 (1999).
13. F. Yusuf *et al.*, *Anat. Embryol.* **210**, 35 (2005).
14. K. Tachibana *et al.*, *Nature* **393**, 591 (1998).
15. N. B. David *et al.*, *Proc. Natl. Acad. Sci. U.S.A.* **99**, 16297 (2002).
16. H. Knaut *et al.*, *Neuron* **47**, 653 (2005).
17. Q. Li *et al.*, *J. Neurosci.* **25**, 1711 (2005).
18. E. Raz, *Curr. Opin. Cell Biol.* **16**, 169 (2004).
19. H. A. Field *et al.*, *Dev. Biol.* **253**, 279 (2003).
20. T. N. Hartmann *et al.*, *Oncogene* **24**, 4462 (2005).
21. J. E. Howard *et al.*, *Mech. Dev.* **38**, 109 (1992).
22. J. Jones *et al.*, *Exp. Cell Res.* **313**, 4051 (2007).
23. F. M. Watt, K. J. Hodivala, *Curr. Biol.* **4**, 270 (1994).
24. R. Winklbauer, R. E. Keller, *Dev. Biol.* **177**, 413 (1996).
25. A. J. Pelletier *et al.*, *Blood* **96**, 2682 (2000).
26. L. A. Trinh, D. Y. Stainier, *Dev. Cell* **6**, 371 (2004).
27. J. Juarez, L. Bendall, *Histol. Histopathol.* **19**, 299 (2004).
28. E. Ruoslahti, *Annu. Rev. Cell Dev. Biol.* **12**, 697 (1996).
29. A. P. Mould *et al.*, *BMC Cell Biol.* **7**, 24 (2006).
30. J. A. Montero *et al.*, *Development* **132**, 1187 (2005).
31. R. Winklbauer *et al.*, *Int. J. Dev. Biol.* **40**, 305 (1996).
32. T. Sakaguchi *et al.*, *Development* **133**, 4063 (2006).
33. I. C. Scott *et al.*, *Dev. Cell* **12**, 403 (2007).
34. X. X. Zeng *et al.*, *Dev. Cell* **12**, 391 (2007).
35. R. Keller *et al.*, *Differentiation* **71**, 171 (2003).
36. R. E. Stevenson *et al.*, *Human Malformations and Related Anomalies* (Oxford Univ. Press, New York, 1993).
37. G. Pezeron *et al.*, *Curr. Biol.* **18**, 276 (2008).

38. We thank E. Raz for *cxcl12b* and *cxcr4a* constructs; our laboratory colleagues, especially S. Piloto for help with qPCR and T. Hoffman for help with itgb1b constructs; and I. Blitz for reviewing the manuscript. Supported by NIH grants R01NS41353 and R01DE13828.

Supporting Online Material

www.sciencemag.org/cgi/content/full/1160038/DC1
Materials and Methods
Figs. S1 to S7
Table S1
References

5 May 2008; accepted 13 August 2008
Published online 21 August 2008;
10.1126/science.1160038
Include this information when citing this paper.

Molecular Architecture of the "Stressosome," a Signal Integration and Transduction Hub

Jon Marles-Wright,[1]* Tim Grant,[2]* Olivier Delumeau,[1]† Gijs van Duinen,[2]‡ Susan J. Firbank,[1] Peter J. Lewis,[3] James W. Murray,[1]§ Joseph A. Newman,[1] Maureen B. Quin,[1] Paul R. Race,[1] Alexis Rohou,[2] Willem Tichelaar,[2]‖ Marin van Heel,[2]¶ Richard J. Lewis[1]¶

A commonly used strategy by microorganisms to survive multiple stresses involves a signal transduction cascade that increases the expression of stress-responsive genes. Stress signals can be integrated by a multiprotein signaling hub that responds to various signals to effect a single outcome. We obtained a medium-resolution cryo–electron microscopy reconstruction of the 1.8-megadalton "stressosome" from *Bacillus subtilis*. Fitting known crystal structures of components into this reconstruction gave a pseudoatomic structure, which had a virus capsid–like core with sensory extensions. We suggest that the different sensory extensions respond to different signals, whereas the conserved domains in the core integrate the varied signals. The architecture of the stressosome provides the potential for cooperativity, suggesting that the response could be tuned dependent on the magnitude of chemophysical insult.

Microorganisms experiencing a fluctuating environment commonly exhibit a short-lived, reversible response that allows survival and recovery of the cell (*1*). In Gram-positive bacteria such as *Bacillus subtilis*, one such signaling cascade ultimately leads to the activation of the general stress sigma factor, σ^B (fig. S1), and enhanced transcription of its large regulon to provide a global response to the imposed stress (*2*, *3*). The stressosome is the signaling hub that integrates multiple physical stress signals (*4*–*7*) and orchestrates a single signaling outcome: the activation of σ^B. The stressosome is found in many microbial phyla, including representatives of the Methanomicrobiales branch of the Euryarchaea and, within Bacteria, the Proteobacteria, the Firmicutes, the Actinobacteria, the Cyanobacteria, and the *Bacteroides* and *Deinococcus* groups (*8*). The downstream chromosomal organization in these organisms points to the involvement of stressosome orthologs in regulating aerotaxis, a variety of two-component signaling systems, and the biosynthesis of secondary messenger signaling molecules. Thus, the stressosome appears to have evolved to provide a common solution to the problem of signal integration.

In *Bacillus*, the stressosome is a ~1.8 MD supramolecular complex comprising multiple copies of the regulator of sigma B proteins: RsbS, RsbR, and four paralogs of RsbR (*7*, *9*–*13*). The C-terminal domain of RsbR and its paralogs is conserved and is similar in sequence to RsbS. By contrast, the N-terminal domains of the RsbR paralogs show high sequence variability, suggesting that they function as sensors, whereas the C-terminal domains integrate the various signals. A third protein, RsbT, interacts with RsbR:RsbS complexes (*9*) to transmit integrated environmental signals into the σ^B activation pathway. The ability of stressosomes to integrate multiple inputs to effect a single output represents a departure from the more common one- and two-component signaling systems in prokaryotes (*14*). These systems typically convert a single signal into a single outcome, usually the transcriptional modulation of small regulons in response to specific metabolic changes (*15*). The activity of the stressosome can be reconstituted both in vitro and in vivo by complexes consisting

Downloaded from www.sciencemag.org on October 2, 2008

solely of RsbS and RsbR (*9*, *10*, *16*–*19*); thus, to gain insight into the organization of the stressosome, we have determined by single-particle cryo–electron microscopy (EM) reconstruction the three-dimensional structures of the complex of the C-terminal domain of RsbR with RsbS ($RsbR_{146-274}$:RsbS), the RsbR:RsbS binary complex, and the ternary RsbR:RsbS:RsbT complex to 6.5, 8.0, and 8.3 Å, respectively (*20*).

We first generated a stressosome core structure from $RsbR_{146-274}$:RsbS. The reconstruction reveals that the core of the complex, with a radius of 90 Å, displays an approximate icosahedral symmetry (Fig. 1A and fig. S2A), though it is an order of magnitude smaller than that of most icosahedral viruses. We then investigated stressosomes comprising full-length RsbR with RsbS (RsbR:RsbS). This structure displays an unusual mixed symmetry with the same pseudo-icosahedral symmetric core supporting 20 protruding "turrets." The arrangement of RsbR N-terminal domains is consistent only with D_2 point-group symmetry (Fig. 1B and fig. S2B). The mismatch of symmetry, though unusual, has been observed previously in the packaging of nucleic acid portal translocases at the vertices of icosahedral bacteriophages (*21*) and in multicomponent proteasome-type complexes (*22*). The radius of the RsbR:RsbS complex is 150 Å; the increase of 60 Å is due to the presence of the N-terminal domains of RsbR that form the turrets that protrude from the core. Finally, we solved the structure of the RsbR:RsbS:RsbT complex. In the absence of environmental stress, the RsbT kinase is believed to be sequestered by the stressosome (*9*) and in our reconstruction, electron density corresponding to RsbT is located above the core RsbS regions, thus occupying spaces between the sensory turrets (Fig. 1C and fig. S2C).

These medium-resolution stressosome reconstructions can be interpreted at higher resolution from the known structures of N-RsbR (*19*), the RsbT homolog SpoIIAB (*23*), and the RsbS ortholog from *Moorella thermoacetica* (*Mt*RsbS), which we have determined by x-ray crystallography and present here (*20*) (table S1). The $RsbR_{146-274}$:RsbS stressosome core can be constructed with icosahedral symmetry operators to build the entire 60-chain structure after fitting a single *Mt*RsbS molecule in the molecular envelope of the cryo-EM reconstruction (Figs. 1A and 2A). In the structure, the 20 projections were fitted with the dimeric N-RsbR domain (thus, there are 40 copies of RsbR) and corresponding regions of the core assigned as the C terminus of RsbR (Fig. 1B). The N-terminal domains of RsbR are found at two of the three positions at each three-fold and thus obey D_2 point-group symmetry. This fitting enabled us to discriminate between RsbR and RsbS STAS (sulfate transporter and anti-sigma factor) domains in the $RsbR_{146-274}$:RsbS stressosome core (Fig. 1A), assuming that the coexpressed $RsbR_{146-274}$:RsbS and RsbR:RsbS complexes assemble identically. To complete the interpretation of the RsbR:RsbS:RsbT reconstruction, we positioned a copy of the RsbT homolog and fitted it in density above each of the 20 copies of RsbS (Fig. 2B). The density corresponding to the N-RsbR domains in Fig. 1, B and C, appears different. However, these domains are relatively flexible in comparison to the rigid core, and their positions may be affected by the presence of RsbT in the ternary complex.

The RsbR and RsbS C-terminal helices project into an area of density at the two-fold axis of the

[1]Institute for Cell and Molecular Biosciences, Newcastle University, Newcastle-upon-Tyne NE2 4HH, UK. [2]Faculty of Natural Sciences, Division of Molecular Biosciences, Imperial College London, London SW7 2AZ, UK. [3]School of Environmental and Life Sciences, University of Newcastle, Callaghan, Newcastle, NSW 2308, Australia.

*These authors contributed equally to this work.
†Present address: Laboratoire de Génétique Microbienne, Domaine de Vilvert, Institut de la Recherche Agronomique INRA, 78350 Jouy-en-Josas, France.
‡Present address: FEI Europe, Achtseweg Noord 5, 5651 GG Eindhoven, Netherlands.
§Present address: Faculty of Natural Sciences, Division of Molecular Biosciences, Imperial College London, London SW7 2AZ, UK.
‖Present address: European Molecular Biology Laboratory, Meyerhofstrasse 1, 69117 Heidelberg, Germany.
¶To whom correspondence should be addressed. E-mail: r.lewis@ncl.ac.uk and m.vanheel@imperial.ac.uk

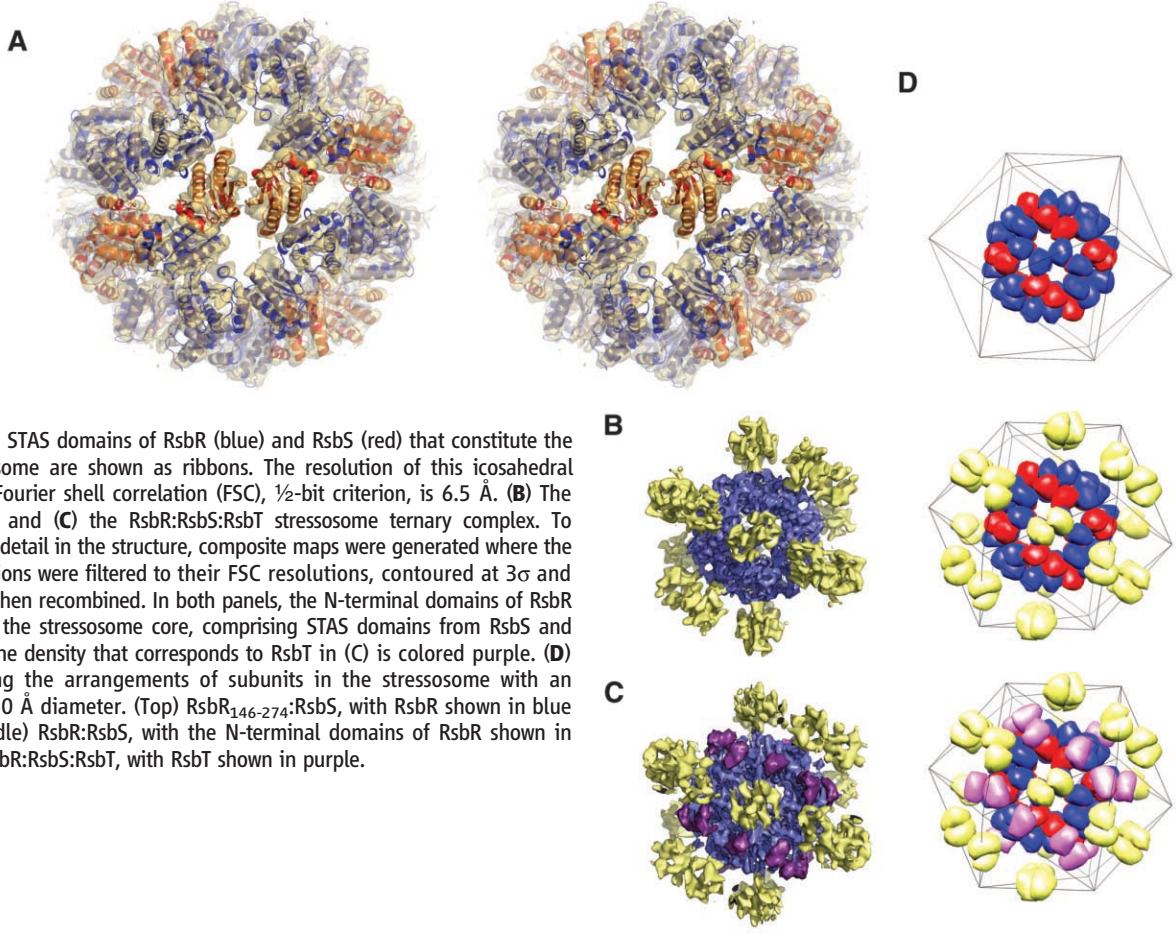

Fig. 1. Cryo-EM envelopes of stressosome structures. The cryo-EM envelopes of the three stressosome reconstructions shown in surface representation. (**A**) The final experimental EM-derived icosahedral molecular envelope of the $RsbR_{146-274}$:RsbS core is shown in stereo as a gold semi-transparent surface, with the map contoured at 3.0σ, and the STAS domains of RsbR (blue) and RsbS (red) that constitute the scaffold of the stressosome are shown as ribbons. The resolution of this icosahedral reconstruction, by the Fourier shell correlation (FSC), ½-bit criterion, is 6.5 Å. (**B**) The RsbR:RsbS stressosome and (**C**) the RsbR:RsbS:RsbT stressosome ternary complex. To demonstrate clearly the detail in the structure, composite maps were generated where the core and peripheral regions were filtered to their FSC resolutions, contoured at 3σ and 1.5σ, respectively, and then recombined. In both panels, the N-terminal domains of RsbR are colored yellow and the stressosome core, comprising STAS domains from RsbS and RsbR, is colored blue. The density that corresponds to RsbT in (C) is colored purple. (**D**) "Bean" models showing the arrangements of subunits in the stressosome with an icosahedral mesh of 150 Å diameter. (Top) $RsbR_{146-274}$:RsbS, with RsbR shown in blue and RsbS in red; (middle) RsbR:RsbS, with the N-terminal domains of RsbR shown in yellow; and (bottom) RsbR:RsbS:RsbT, with RsbT shown in purple.

Downloaded from www.sciencemag.org on October 2, 2008

core of the stressosome that may act as a pivot to propagate the structural changes that are brought about by the activation of the N-terminal signaling domains in the stressosome. The domains in the stressosome are arranged such that the serine and threonine residues in RsbR (Thr^{171} and Thr^{205}) and RsbS (Ser^{59}), which are phosphorylated by RsbT (*24*, *25*), are solvent accessible. Upon receipt of a stress signal, RsbT phosphorylates the stressosome and then disassociates to activate its alternative binding partner, the phosphatase RsbU (*9*, *26*, *27*); this stimulation is a prerequisite of σ^B activation (*17*) (fig. S1). Each of the 20 copies of RsbS, in the RsbR:RsbS:RsbT structure, is in close proximity to a copy of RsbT such that the adenosine 5′-triphosphate (ATP) lid of RsbT is positioned above Ser^{59} of RsbS, poised to catalyze phosphoryl transfer (Figs. 1C and 2B). In our structures, the phosphorylatable residues in RsbR are sterically hindered from forming a stable interaction with RsbT, indicating that some movements must occur in the stressosome to phosphorylate RsbR.

To link our structural studies of the stressosome with the cell biology of *Bacillus*, we have visualized stressosome formation using immunofluorescence and assessed σ^B activation in vivo with a reporter gene fusion. Using RsbR-specific antibodies, we determined the location and distribution of the complexes in live cells, before and after the imposition of stress. In cells that had not been subjected to environmental stress, ~20 bright foci per cell were observed in the cytoplasm directly adjacent to the nucleoids (Fig. 3, A and B). Each focus is predicted to correspond to a single stressosome. These foci maintained the same subcellular localization pattern over a 120-min period after induction of environmental stress. Thus, stressosomes are highly robust complexes that exist before stress induction and do not dissociate after their activation by RsbT-dependent phosphorylation. This is illustrated in Fig. 3C, which shows cells 20 min after stress induction when σ^B activity is maximal (*6*, *10*, *13*, *26*–*28*). No foci are seen in an *rsbR*-null mutant strain of *B. subtilis*, BSK5 (Fig. 3, D and E), the construction of which does not affect the expression of the downstream gene products in the *rsb* operon (*29*). Hence, the number of foci per cell is consistent with the cellular concentration of the Rsb proteins (*13*, *28*), given the multimeric organization of the stressosome. The distribution of the stressosomes throughout the cell is compatible with the requirement of the cell to sample its entire environment for physical insults.

The sequestration of multiple copies of RsbT by the stressosome suggests a mechanism of activation whereby the release of a single RsbT molecule reduces the affinity of neighboring ones so that multiple copies of RsbT are released in a cooperative manner. We used a σ^B-dependent *ctc-lacZ* reporter gene fusion to quantify σ^B activity as a function of the concentration of ethanol and NaCl. Both these stimuli induce the σ^B response and represent independent agonists of the σ^B pathway that are likely to enter the cell by different routes. The σ^B response in these two experiments was sigmoidal (Fig. 4, A and B), indicating that the response to environmental stress is complex and cooperative in at least one point in the σ^B pathway. The multisubunit stressosome is a logical point where the cooperative stage of the response, the release of RsbT by the stressosome, could commence. By contrast, when azide was used to induce the nutritional stress σ^B pathway, which is independent of the stressosome, the σ^B response was hyperbolic (Fig. 4C), confirming that the sigmoidal effect we observed is specific to the environmental stress signaling pathway. Presumably, the stressosome oligomer has evolved to provide cooperativity because small, diffusible complexes containing RsbT and its antagonist would provide a less finely controlled response to physical stress.

The structures presented are consistent with biochemical, biophysical, and cell biology data. The calculated mass of the RsbR:RsbS complex is 1.5 MD, consistent with measurements made by sedimentation velocity (*9*). When RsbT is bound, the mass of the stressosome increases to 1.8 MD. The distance between the end of the N-terminal domain of RsbR and the beginning of the C-terminal domain of RsbR is 30 Å, consistent with a 13-residue α-helical linker between the two domains that is absent in the crystallographic models; this structure is modeled in Fig. 2C. Small differences that are seen between the turrets in the RsbR:RsbS and RsbR:RsbS:RsbT maps are due to the inherent flexibility of the structures. That RsbT is bound above RsbS agrees with the knowledge that RsbT phosphorylates RsbS, in the RsbR:RsbS complex, more rapidly than it phosphorylates RsbR in vitro (*9*). The requirement for the correct interaction between RsbS and RsbT is crucial for signaling the stress response; *rsbS*-null mutant strains exhibit a small-cell phenotype indicative of severely compromised growth, and the mutation of Ser^{59} to Asp in RsbS—which mimics phosphorylation—is lethal, presumably as a result of constitutive σ^B activity (*16*). Point mutations in *rsbS* that also give rise to increased σ^B activity (*17*) map to regions involved in RsbT binding in our RsbR:RsbS:RsbT model (Fig. 2B).

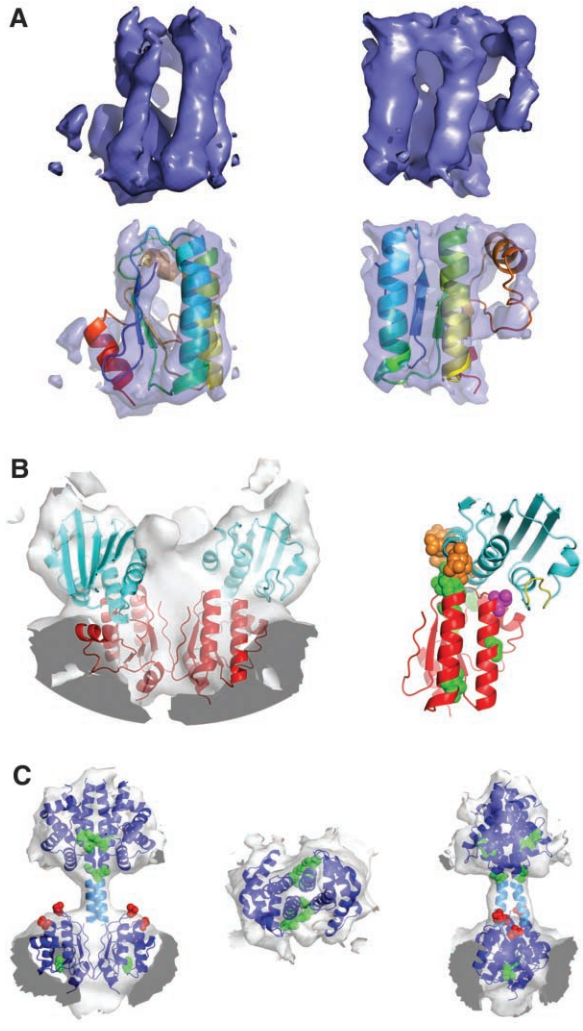

Fig. 2. The quasi-atomic structure of the stressosome. (**A**) Two orthogonal views of the secondary-structure fit of a single RsbS STAS domain in the icosahedral reconstruction of the $RsbR_{146-274}$:RsbS. (Top) The electron density map contoured at 3.0σ (to emphasize α helices); (bottom) the map shown as a semitransparent surface with RsbS fitted and shown as a cartoon continuously color-ramped from N terminus (blue) to C terminus (red). The experimental map is displayed as a semitransparent surface at 3.0σ (to emphasize the α helices). (**B**) Orthogonal views of the interactions between RsbS (red) and RsbT (cyan) in the stressosome. (Left) The final RsbR:RsbS:RsbT EM envelope is shown as a semitransparent surface contoured at 1.5σ. (Right) A view of a single molecule of RsbT poised above a single copy of RsbS to catalyze phosphorylation of Ser^{59} (magenta spheres) on receipt of stress. The residues known to be affected in the binding of RsbT to RsbS, or that are defective in signaling, are shown as spheres and colored green in RsbS and orange in RsbT (*29*). The peptide backbone of the ATP lid in RsbT is colored yellow. (**C**) Cartoon views of the sensory extensions of RsbR (blue) in the RsbR:RsbS complex that protrude from the core of the stressosome. The models for the N-terminal globin domain and C-terminal STAS domains are shown with an idealized helix illustrating the neck region (shown in cyan). Mutations that affect the activity of RsbR are shown as spheres and colored green, and phosphorylatable threonine residues are shown as red spheres (*17*, *19*). The experimental map is shown as a semitransparent surface at 1.5σ.

Downloaded from www.sciencemag.org on October 2, 2008

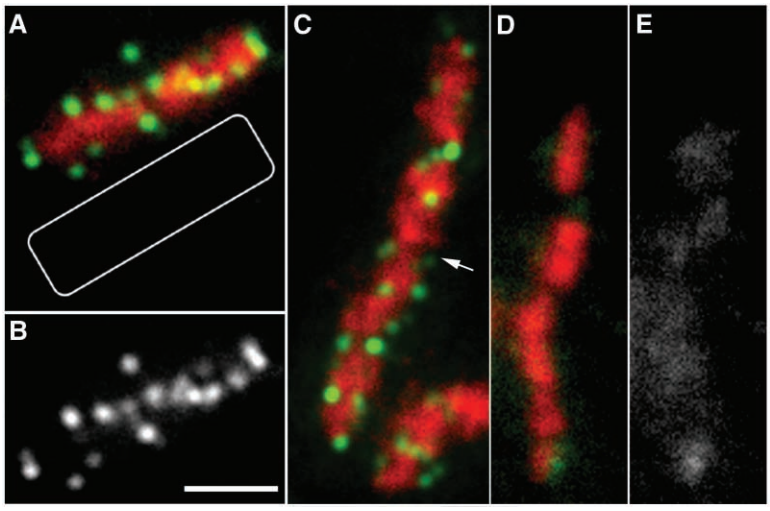

Fig. 3. Immunolocalization of stressosomes. (**A**) Pseudocolored image of stressosomes (green) and DNA (red) before induction of stress. A cartoon representation of the *Bacillus* (below) reveals the boundary of the cell. This cell contains two nucleoids. (**B**) The stressosomes immunolocalized with RsbR-specific antibodies from (A) are shown in monochrome. (**C**) A pseudocoloured image of a pair of cells 20 min after the induction of stress when σ^B activity is maximal, with stressosomes shown in green and DNA in red. The arrow indicates the position of the division septum between the two cells. (**D**) As in (C) but in the *rsbR*-null mutant strain, BSK5, with the green channel levels raised to show a faint background staining but no localization of stressosomes. (**E**) Monochrome version of (D). Scale bar, 2 μm.

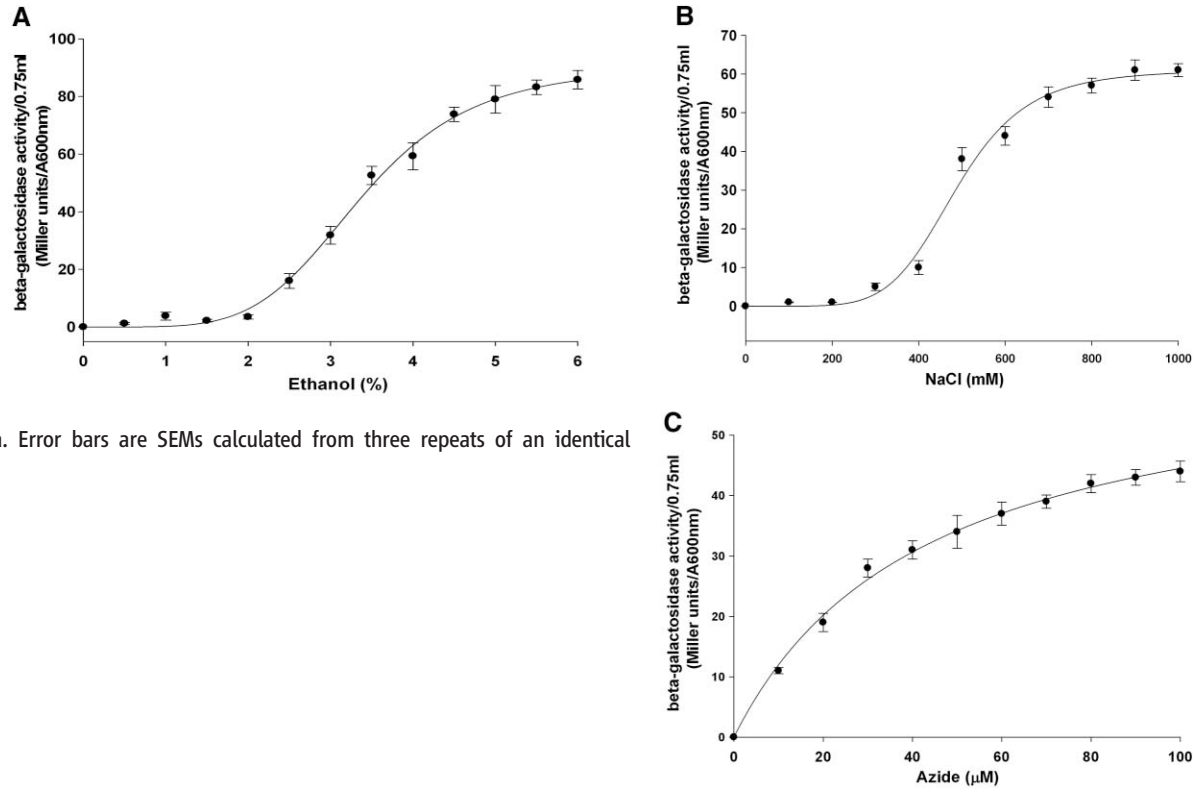

Fig. 4. Response of *B. subtilis* to stress. Plots of differential β-galactosidase activity versus inducer concentration for ethanol (**A**), sodium chloride (**B**), and sodium azide (**C**). All data were collected and analyzed as described in the supporting online material. Data were fitted to either a three-parameter Hill equation or a single rectangular hyperbola. Error bars are SEMs calculated from three repeats of an identical experiment.

In addition, mutations in RsbT that abrogate binding to RsbR:RsbS complexes are concentrated at the RsbT interface to RsbS (*30*, *31*). Thus, the structural model of the RsbR:RsbS:RsbT complex provides a molecular explanation of all the phenotypes of stress-associated mutants described previously (*16*, *17*, *30*, *31*).

Our results suggest a model for stressosome activation. Although no activating signal is known for RsbR, structures of the N-terminal domain of the light-responsive RsbR paralog YtvA have been reported recently (*32*). These show that upon activation by light, there are movements of helices at the C-terminal end of this domain, analogous to that of N-RsbR. This movement, in the context of the stressosome ternary complex that we describe, could allow transmission of the stress signals to RsbT, resulting in conformational changes to allow the phosphorylation of RsbS and RsbR by RsbT. Potentially, activation of the sensory domains is communicated to the stressosome core domains and is propagated via the C-terminal helices of the N-terminal domains to neighboring chains to allow optimal positioning of RsbT at the RsbS phosphorylation site. Phosphorylation ensues, RsbT is released to activate RsbU, and hence the large σ^B regulon is transcribed to protect the cell from the imposed stress. That the N-terminal domains of RsbR are not in direct contact with RsbT indicates that the stressosome is a dynamic complex. Other structures are required to fully elucidate all steps in the pathway leading to activation of the stressosome and to determine the precise role of the phosphorylation of RsbR (*9*, *10*, *33*). The structure of the stressosome reveals that the sensory domains are, however, ideally located to interact with trigger cues that range in size from photons of ultraviolet light to macromolecules. The sequestration of multiple copies of RsbT in a single structure, until the arrival of a single stress signal, may allow allosteric control over the activation of σ^B.

References and Notes

1. G. Storz, R. Hengge-Aronis, *Bacterial Stress Responses* (American Society for Microbiology, Washington, DC, 2000).
2. C. W. Price *et al.*, *Mol. Microbiol.* **41**, 757 (2001).

Downloaded from www.sciencemag.org on October 2, 2008

3. A. Petersohn *et al.*, *J. Bacteriol.* **183**, 5617 (2001).
4. M. Avila-Perez, K. J. Hellingwerf, R. Kort, *J. Bacteriol.* **188**, 6411 (2006).
5. A. K. Benson, W. G. Haldenwang, *J. Bacteriol.* **175**, 1929 (1993).
6. S. A. Boylan, A. R. Redfield, M. S. Brody, C. W. Price, *J. Bacteriol.* **175**, 7931 (1993).
7. T. A. Gaidenko, T. J. Kim, A. L. Weigel, M. S. Brody, C. W. Price, *J. Bacteriol.* **188**, 6387 (2006).
8. J. Pané-Farré, R. J. Lewis, J. Stülke, *J. Mol. Microbiol. Biotechnol.* **9**, 65 (2005).
9. C. C. Chen, R. J. Lewis, R. Harris, M. D. Yudkin, O. Delumeau, *Mol. Microbiol.* **49**, 1657 (2003).
10. T. J. Kim, T. A. Gaidenko, C. W. Price, *J. Mol. Biol.* **341**, 135 (2004).
11. S. Akbar *et al.*, *J. Bacteriol.* **183**, 1329 (2001).
12. O. Delumeau, C. C. Chen, J. W. Murray, M. D. Yudkin, R. J. Lewis, *J. Bacteriol.* **188**, 7885 (2006).
13. A. Dufour, U. Voelker, A. Voelker, W. G. Haldenwang, *J. Bacteriol.* **178**, 3701 (1996).
14. L. E. Ulrich, E. V. Koonin, I. B. Zhulin, *Trends Microbiol.* **13**, 52 (2005).
15. T. Mascher, J. D. Helmann, G. Unden, *Microbiol. Mol. Biol. Rev.* **70**, 910 (2006).
16. C. M. Kang, M. S. Brody, S. Akbar, X. Yang, C. W. Price, *J. Bacteriol.* **178**, 3846 (1996).
17. A. Reeves, W. G. Haldenwang, *J. Bacteriol.* **189**, 1531 (2007).
18. T. J. Kim, T. A. Gaidenko, C. W. Price, *J. Bacteriol.* **186**, 6124 (2004).
19. J. W. Murray, O. Delumeau, R. J. Lewis, *Proc. Natl. Acad. Sci. U.S.A.* **102**, 17320 (2005).
20. Materials and Methods are available as supporting material on *Science* Online.
21. P. Dube, P. Tavares, R. Lurz, M. van Heel, *EMBO J.* **12**, 1303 (1993).
22. F. Beuron *et al.*, *J. Struct. Biol.* **123**, 248 (1998).
23. S. Masuda *et al.*, *J. Mol. Biol.* **340**, 941 (2004).
24. T. A. Gaidenko, X. Yang, Y. M. Lee, C. W. Price, *J. Mol. Biol.* **288**, 29 (1999).
25. S. Zhang, W. G. Haldenwang, *J. Bacteriol.* **185**, 5714 (2003).
26. C. M. Kang, K. Vijay, C. W. Price, *Mol. Microbiol.* **30**, 189 (1998).
27. O. Delumeau *et al.*, *J. Biol. Chem.* **279**, 40927 (2004).
28. O. Delumeau, R. J. Lewis, M. D. Yudkin, *J. Bacteriol.* **184**, 5583 (2002).
29. S. Kuo, S. Zhang, R. L. Woodbury, W. G. Haldenwang, *Microbiology* **150**, 4125 (2004).
30. S. W. Hardwick *et al.*, *J. Biol. Chem.* **282**, 11562 (2007).
31. R. L. Woodbury, T. Luo, L. Grant, W. G. Haldenwang, *J. Bacteriol.* **186**, 2789 (2004).
32. A. Möglich, K. Moffat, *J. Mol. Biol.* **373**, 112 (2007).
33. C. C. Chen, M. D. Yudkin, O. Delumeau, *J. Bacteriol.* **186**, 6830 (2004).

34. This work was supported by the Biotechnology and Biological Sciences Research Council (BBSRC), Newcastle University (UK), Australian Research Council, University of Newcastle (Australia) by grants from the European Union (NOE, Contract LSHG-CT-2004-502828), and the Dutch Ministry of Economic Affairs ("Cyttron", BSIK 03036). The electron microscopes used for this work were purchased with financial support from the BBSRC, Glaxo Wellcome, and SmithKline Beecham. We are grateful to M. Schatz (Image Science, Berlin, Germany) for IMAGIC software support and to W. Haldenwang for strain BSK5. We thank R. Harris, H. Gilbert, M. Embley, and N. Robinson for advice and useful comments on the manuscript and E. Lowe for help with curve fitting. We are grateful for access to the Diamond synchrotron light source and its beamline scientists for help during data collection. Coordinates and structure factors for *Mt*RsbS are deposited in the Protein Databank with the accession number 2VY9. Electron microscopy–derived molecular envelopes are deposited in the Electron Microscopy Database at the Macromolecular Structure Database Group with the following accession numbers: $RsbR_{(146-274)}$:RsbS, 1558; RsbR:RsbS, 1555; and RsbR:RsbS:RsbT 1556.

Supporting Online Material

www.sciencemag.org/cgi/content/full/322/5898/92/DC1
Materials and Methods
SOM Text
Figs. S1 to S8
Table S1
References
Movie S1

24 April 2008; accepted 10 September 2008
10.1126/science.1159572

Internally Generated Reactivation of Single Neurons in Human Hippocampus During Free Recall

Hagar Gelbard-Sagiv,[1] Roy Mukamel,[2] Michal Harel,[1] Rafael Malach,[1] Itzhak Fried[2,3]*

The emergence of memory, a trace of things past, into human consciousness is one of the greatest mysteries of the human mind. Whereas the neuronal basis of recognition memory can be probed experimentally in human and nonhuman primates, the study of free recall requires that the mind declare the occurrence of a recalled memory (an event intrinsic to the organism and invisible to an observer). Here, we report the activity of single neurons in the human hippocampus and surrounding areas when subjects first view cinematic episodes consisting of audiovisual sequences and again later when they freely recall these episodes. A subset of these neurons exhibited selective firing, which often persisted throughout and following specific episodes for as long as 12 seconds. Verbal reports of memories of these specific episodes at the time of free recall were preceded by selective reactivation of the same hippocampal and entorhinal cortex neurons. We suggest that this reactivation is an internally generated neuronal correlate for the subjective experience of spontaneous emergence of human recollection.

The human hippocampus and its associated structures in the medial temporal lobe (MTL) transform present experience into future conscious recollections (*1*–*4*). Human MTL neurons respond in a highly specific manner to complex stimulus features (*5*), to complex stimulus categories (*5*, *6*), to individual persons or landmarks (*7*–*9*), and to previously seen and novel stimuli (*5*, *10*, *11*). These responses have been demonstrated for stationary stimuli and are usually brief, often lasting between 300 and 600 ms following stimulus onset, and rarely persist beyond 1 to 2 s (*8*). However, the human experience is seldom that of stationary stimuli; rather, we live and operate in a constantly changing environment. In this environment, we encounter complex stimuli constituting episodes, series of variant multimodal representations linked in temporal succession. It is such temporally sequenced information that is processed by the human MTL (*12*, *13*) and later becomes available for conscious recollection. For this reason, we set out to examine how neurons in the MTL respond to cinematic sequences depicting specific episodes, and, later, when these episodes spontaneously come to mind in the absence of external stimuli, in a free-recall situation that can be reported by individual subjects.

Subjects were patients with pharmacologically intractable epilepsy implanted with depth electrodes to localize the focus of seizure onset. For each patient, the placement of the depth

[1]Department of Neurobiology, Weizmann Institute of Science, Rehovot, 76100, Israel. [2]Department of Neurosurgery, David Geffen School of Medicine, and Semel Institute for Neuroscience and Human Behavior, University of California Los Angeles, Los Angeles, CA 90095, USA. [3]Functional Neurosurgery Unit, Tel Aviv Medical Center and Sackler School of Medicine, Tel Aviv University, Tel Aviv, 64239, Israel.

*To whom correspondence should be addressed. E-mail: ifried@mednet.ucla.edu

Fig. 1. A single-unit in the right entorhinal cortex was activated during viewing and recall of an episode from the TV series *The Simpsons*. (**A**) Cell responses to a selection of 48 different episodes (movie clips) presented to the patient in three different viewing sessions (parts 1 to 3). For each clip, the corresponding raster plots (six trials, order of trials is from top to bottom) and post–stimulus time histogram (500-ms bins) are given. Vertical dashed lines indicate clip onset and offset (5 s apart); 5-s blank periods were presented occasionally within groups of successive clips and were used to calculate the baseline firing rate, denoted by a gray horizontal line. Red boxes indicate sustained responses. (**B**) Trial-by-trial response of the neuron. Order of clips is for the purpose of illustration; more intervening clips separated successive *Simpsons* clips in the actual experiment. Spike raster plot and instantaneous firing rate (spike train convolved with a Gaussian of the full width at half maximum of 1200 ms) are displayed together. (**C**) Free-recall session that followed the third viewing session (part 3). (Bottom) Sound amplitude of patient voice; (top) a spike raster plot and instantaneous firing rate; gray dashed line denotes the average firing rate during the recall session + 3 SD; numbered dots denote onset time of verbal report of recall events, corresponding to clip numbers in (A). Note the distinct elevation of firing rate just before the patient reported the recall of the *Simpsons* clip (red arrow). (**D**) A 50-s window around the *Simpsons* recall event [blue area in (C)]. Patient's words are below the bottom panel. Note that the cell's firing rate rose significantly above baseline 1500 ms before onset of verbal report of the *Simpsons* clip and returned to baseline after more than 10 s.

Downloaded from www.sciencemag.org on October 2, 2008

EXTENDED PDF FORMAT
SPONSORED BY
usb
Products from Affymetrix
www.usbweb.com

Internally Generated Reactivation of Single Neurons in Human Hippocampus During Free Recall

Hagar Gelbard-Sagiv, *et al.*

Science **322**, 96 (2008);
DOI: 10.1126/science.1164685

The following resources related to this article are available online at www.sciencemag.org (this information is current as of October 2, 2008):

Updated information and services, including high-resolution figures, can be found in the online version of this article at:
http://www.sciencemag.org/cgi/content/full/322/5898/96

Supporting Online Material can be found at:
http://www.sciencemag.org/cgi/content/full/1164685/DC1

This article **cites 34 articles**, 11 of which can be accessed for free:
http://www.sciencemag.org/cgi/content/full/322/5898/96#otherarticles

This article appears in the following **subject collections**:
Neuroscience
http://www.sciencemag.org/cgi/collection/neuroscience

Information about obtaining **reprints** of this article or about obtaining **permission to reproduce this article** in whole or in part can be found at:
http://www.sciencemag.org/about/permissions.dtl

Downloaded from www.sciencemag.org on October 2, 2008

Science (print ISSN 0036-8075; online ISSN 1095-9203) is published weekly, except the last week in December, by the American Association for the Advancement of Science, 1200 New York Avenue NW, Washington, DC 20005. Copyright 2008 by the American Association for the Advancement of Science; all rights reserved. The title *Science* is a registered trademark of AAAS.

3. A. Petersohn *et al.*, *J. Bacteriol.* **183**, 5617 (2001).
4. M. Avila-Perez, K. J. Hellingwerf, R. Kort, *J. Bacteriol.* **188**, 6411 (2006).
5. A. K. Benson, W. G. Haldenwang, *J. Bacteriol.* **175**, 1929 (1993).
6. S. A. Boylan, A. R. Redfield, M. S. Brody, C. W. Price, *J. Bacteriol.* **175**, 7931 (1993).
7. T. A. Gaidenko, T. J. Kim, A. L. Weigel, M. S. Brody, C. W. Price, *J. Bacteriol.* **188**, 6387 (2006).
8. J. Pané-Farré, R. J. Lewis, J. Stülke, *J. Mol. Microbiol. Biotechnol.* **9**, 65 (2005).
9. C. C. Chen, R. J. Lewis, R. Harris, M. D. Yudkin, O. Delumeau, *Mol. Microbiol.* **49**, 1657 (2003).
10. T. J. Kim, T. A. Gaidenko, C. W. Price, *J. Mol. Biol.* **341**, 135 (2004).
11. S. Akbar *et al.*, *J. Bacteriol.* **183**, 1329 (2001).
12. O. Delumeau, C. C. Chen, J. W. Murray, M. D. Yudkin, R. J. Lewis, *J. Bacteriol.* **188**, 7885 (2006).
13. A. Dufour, U. Voelker, A. Voelker, W. G. Haldenwang, *J. Bacteriol.* **178**, 3701 (1996).
14. L. E. Ulrich, E. V. Koonin, I. B. Zhulin, *Trends Microbiol.* **13**, 52 (2005).
15. T. Mascher, J. D. Helmann, G. Unden, *Microbiol. Mol. Biol. Rev.* **70**, 910 (2006).
16. C. M. Kang, M. S. Brody, S. Akbar, X. Yang, C. W. Price, *J. Bacteriol.* **178**, 3846 (1996).
17. A. Reeves, W. G. Haldenwang, *J. Bacteriol.* **189**, 1531 (2007).
18. T. J. Kim, T. A. Gaidenko, C. W. Price, *J. Bacteriol.* **186**, 6124 (2004).
19. J. W. Murray, O. Delumeau, R. J. Lewis, *Proc. Natl. Acad. Sci. U.S.A.* **102**, 17320 (2005).
20. Materials and Methods are available as supporting material on *Science* Online.
21. P. Dube, P. Tavares, R. Lurz, M. van Heel, *EMBO J.* **12**, 1303 (1993).
22. F. Beuron *et al.*, *J. Struct. Biol.* **123**, 248 (1998).
23. S. Masuda *et al.*, *J. Mol. Biol.* **340**, 941 (2004).
24. T. A. Gaidenko, X. Yang, Y. M. Lee, C. W. Price, *J. Mol. Biol.* **288**, 29 (1999).
25. S. Zhang, W. G. Haldenwang, *J. Bacteriol.* **185**, 5714 (2003).
26. C. M. Kang, K. Vijay, C. W. Price, *Mol. Microbiol.* **30**, 189 (1998).
27. O. Delumeau *et al.*, *J. Biol. Chem.* **279**, 40927 (2004).
28. O. Delumeau, R. J. Lewis, M. D. Yudkin, *J. Bacteriol.* **184**, 5583 (2002).
29. S. Kuo, S. Zhang, R. L. Woodbury, W. G. Haldenwang, *Microbiology* **150**, 4125 (2004).
30. S. W. Hardwick *et al.*, *J. Biol. Chem.* **282**, 11562 (2007).
31. R. L. Woodbury, T. Luo, L. Grant, W. G. Haldenwang, *J. Bacteriol.* **186**, 2789 (2004).
32. A. Möglich, K. Moffat, *J. Mol. Biol.* **373**, 112 (2007).
33. C. C. Chen, M. D. Yudkin, O. Delumeau, *J. Bacteriol.* **186**, 6830 (2004).

34. This work was supported by the Biotechnology and Biological Sciences Research Council (BBSRC), Newcastle University (UK), Australian Research Council, University of Newcastle (Australia) by grants from the European Union (NOE, Contract LSHG-CT-2004-502828), and the Dutch Ministry of Economic Affairs ("Cyttron", BSIK 03036). The electron microscopes used for this work were purchased with financial support from the BBSRC, Glaxo Wellcome, and SmithKline Beecham. We are grateful to M. Schatz (Image Science, Berlin, Germany) for IMAGIC software support and to W. Haldenwang for strain BSK5. We thank R. Harris, H. Gilbert, M. Embley, and N. Robinson for advice and useful comments on the manuscript and E. Lowe for help with curve fitting. We are grateful for access to the Diamond synchrotron light source and its beamline scientists for help during data collection. Coordinates and structure factors for *Mt*RsbS are deposited in the Protein Databank with the accession number 2VY9. Electron microscopy–derived molecular envelopes are deposited in the Electron Microscopy Database at the Macromolecular Structure Database Group with the following accession numbers: $RsbR_{(146-274)}$:RsbS, 1558; RsbR:RsbS, 1555; and RsbR:RsbS:RsbT 1556.

Supporting Online Material

www.sciencemag.org/cgi/content/full/322/5898/92/DC1
Materials and Methods
SOM Text
Figs. S1 to S8
Table S1
References
Movie S1

24 April 2008; accepted 10 September 2008
10.1126/science.1159572

Internally Generated Reactivation of Single Neurons in Human Hippocampus During Free Recall

Hagar Gelbard-Sagiv,[1] Roy Mukamel,[2] Michal Harel,[1] Rafael Malach,[1] Itzhak Fried[2,3]*

The emergence of memory, a trace of things past, into human consciousness is one of the greatest mysteries of the human mind. Whereas the neuronal basis of recognition memory can be probed experimentally in human and nonhuman primates, the study of free recall requires that the mind declare the occurrence of a recalled memory (an event intrinsic to the organism and invisible to an observer). Here, we report the activity of single neurons in the human hippocampus and surrounding areas when subjects first view cinematic episodes consisting of audiovisual sequences and again later when they freely recall these episodes. A subset of these neurons exhibited selective firing, which often persisted throughout and following specific episodes for as long as 12 seconds. Verbal reports of memories of these specific episodes at the time of free recall were preceded by selective reactivation of the same hippocampal and entorhinal cortex neurons. We suggest that this reactivation is an internally generated neuronal correlate for the subjective experience of spontaneous emergence of human recollection.

The human hippocampus and its associated structures in the medial temporal lobe (MTL) transform present experience into future conscious recollections (*1*–*4*). Human MTL neurons respond in a highly specific manner to complex stimulus features (*5*), to complex stimulus categories (*5*, *6*), to individual persons or landmarks (*7*–*9*), and to previously seen and novel stimuli (*5*, *10*, *11*). These responses have been demonstrated for stationary stimuli and are usually brief, often lasting between 300 and 600 ms following stimulus onset, and rarely persist beyond 1 to 2 s (*8*). However, the human experience is seldom that of stationary stimuli; rather, we live and operate in a constantly changing environment. In this environment, we encounter complex stimuli constituting episodes, series of variant multimodal representations linked in temporal succession. It is such temporally sequenced information that is processed by the human MTL (*12*, *13*) and later becomes available for conscious recollection. For this reason, we set out to examine how neurons in the MTL respond to cinematic sequences depicting specific episodes, and, later, when these episodes spontaneously come to mind in the absence of external stimuli, in a free-recall situation that can be reported by individual subjects.

Subjects were patients with pharmacologically intractable epilepsy implanted with depth electrodes to localize the focus of seizure onset. For each patient, the placement of the depth

[1]Department of Neurobiology, Weizmann Institute of Science, Rehovot, 76100, Israel. [2]Department of Neurosurgery, David Geffen School of Medicine, and Semel Institute for Neuroscience and Human Behavior, University of California Los Angeles, Los Angeles, CA 90095, USA. [3]Functional Neurosurgery Unit, Tel Aviv Medical Center and Sackler School of Medicine, Tel Aviv University, Tel Aviv, 64239, Israel.

*To whom correspondence should be addressed. E-mail: ifried@mednet.ucla.edu

Fig. 1. A single-unit in the right entorhinal cortex was activated during viewing and recall of an episode from the TV series *The Simpsons*. (**A**) Cell responses to a selection of 48 different episodes (movie clips) presented to the patient in three different viewing sessions (parts 1 to 3). For each clip, the corresponding raster plots (six trials, order of trials is from top to bottom) and post–stimulus time histogram (500-ms bins) are given. Vertical dashed lines indicate clip onset and offset (5 s apart); 5-s blank periods were presented occasionally within groups of successive clips and were used to calculate the baseline firing rate, denoted by a gray horizontal line. Red boxes indicate sustained responses. (**B**) Trial-by-trial response of the neuron. Order of clips is for the purpose of illustration; more intervening clips separated successive *Simpsons* clips in the actual experiment. Spike raster plot and instantaneous firing rate (spike train convolved with a Gaussian of the full width at half maximum of 1200 ms) are displayed together. (**C**) Free-recall session that followed the third viewing session (part 3). (Bottom) Sound amplitude of patient voice; (top) a spike raster plot and instantaneous firing rate; gray dashed line denotes the average firing rate during the recall session + 3 SD; numbered dots denote onset time of verbal report of recall events, corresponding to clip numbers in (A). Note the distinct elevation of firing rate just before the patient reported the recall of the *Simpsons* clip (red arrow). (**D**) A 50-s window around the *Simpsons* recall event [blue area in (C)]. Patient's words are below the bottom panel. Note that the cell's firing rate rose significantly above baseline 1500 ms before onset of verbal report of the *Simpsons* clip and returned to baseline after more than 10 s.

Downloaded from www.sciencemag.org on October 2, 2008

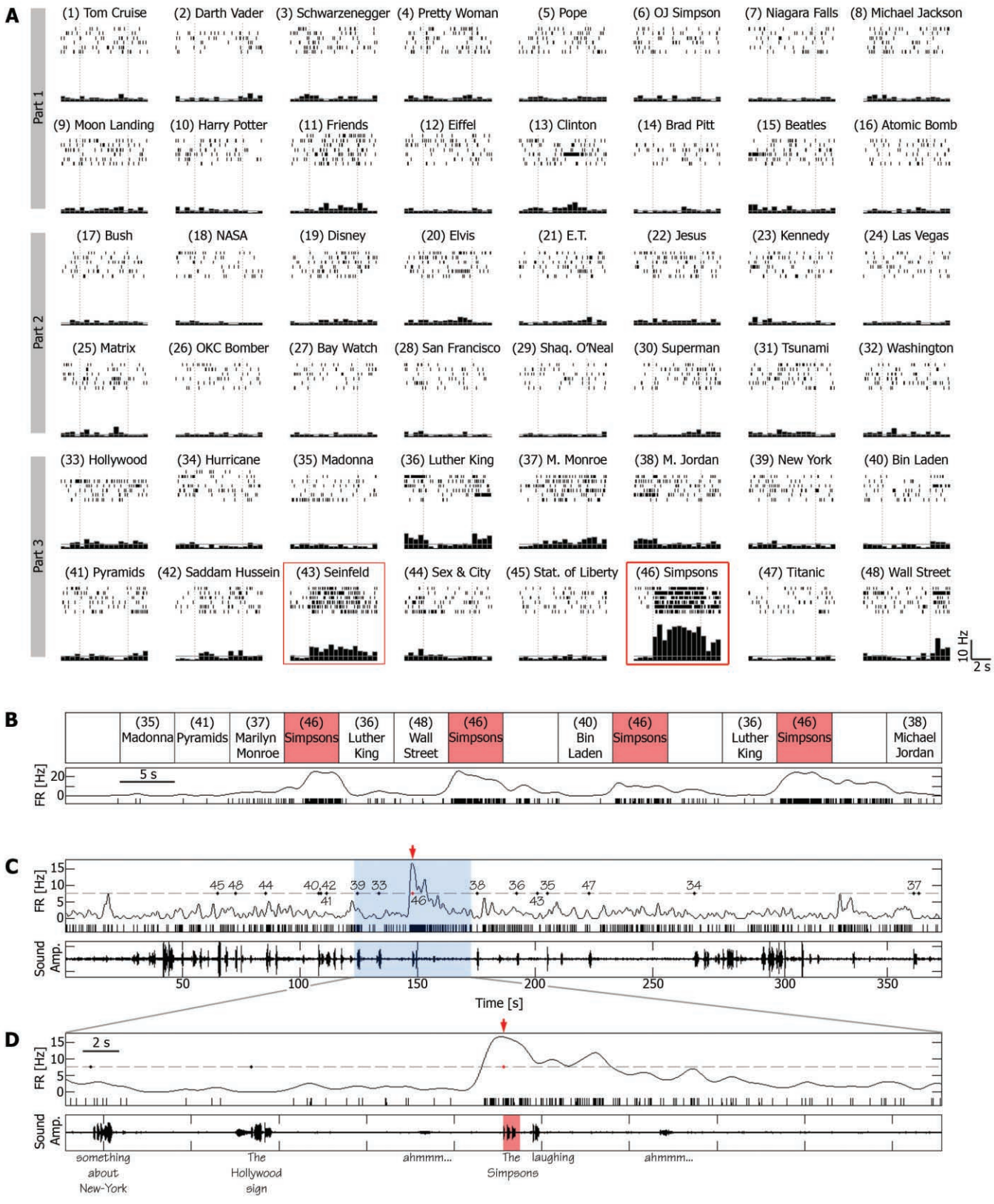

Downloaded from www.sciencemag.org on October 2, 2008

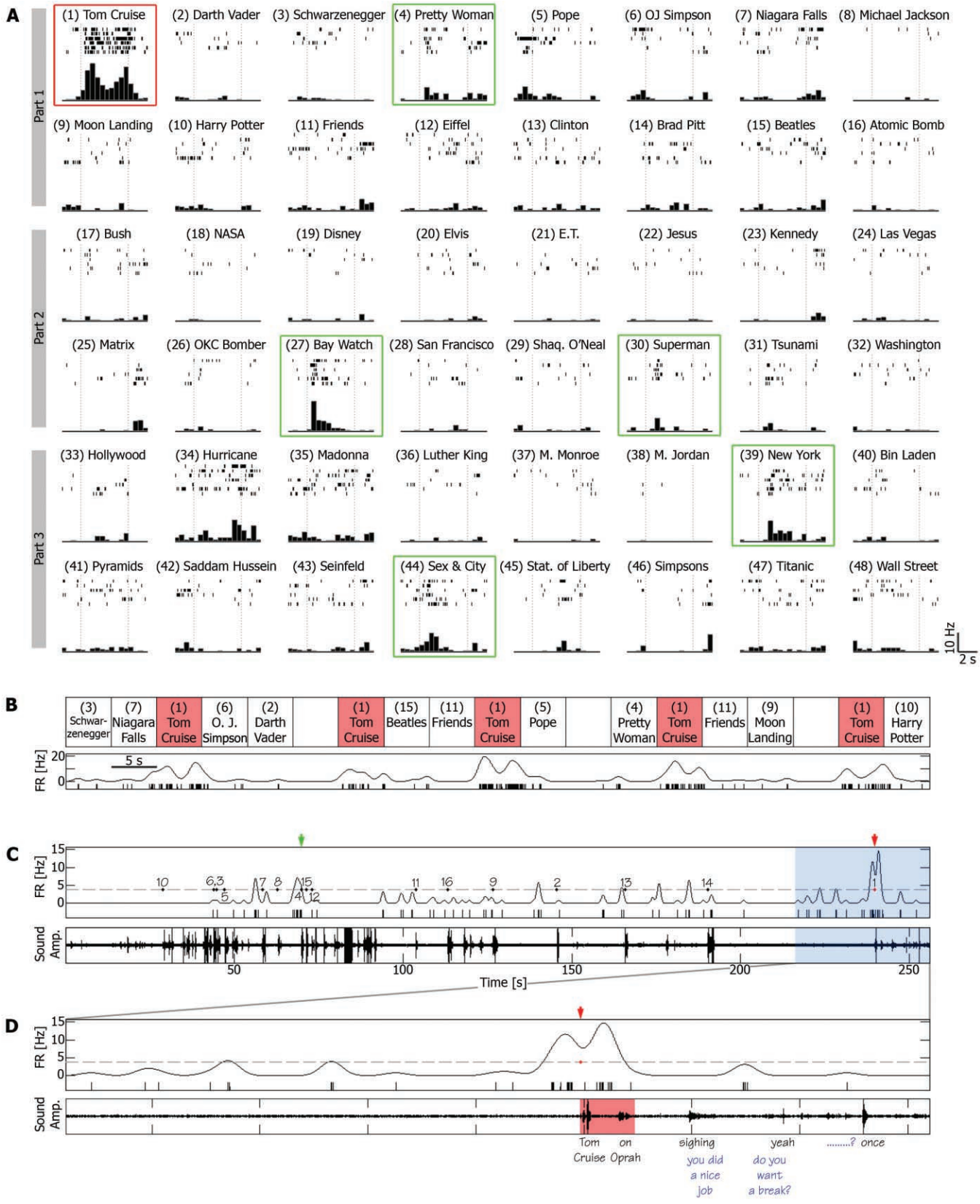

Fig. 2. A single-unit in the left anterior hippocampus is activated during viewing and recall of an episode (conventions as in Fig. 1). (**A** and **B**) Note the sustained elevation of firing rate during the episode depicting actor Tom Cruise during an interview on the *Oprah Winfrey Show* (red box). Note also the transient responses to various clips (green boxes). (**C** and **D**) Free-recall session that followed the first viewing session (part 1). Note that the burst of spikes that accompanied the recall of the Tom Cruise clip began 1500 ms before onset of verbal report ("Tom Cruise … on Oprah"). Blue words indicate experimenter's speech.

Downloaded from www.sciencemag.org on October 2, 2008

electrodes was determined exclusively by clinical criteria (*14*, *15*). Patients first participated in a viewing session in which they viewed a series of audiovisual clips lasting 5 to 10 s each. Each clip depicted an "episode" featuring famous people, characters, or animals engaged in activity, or landmarks described from various views, and was presented 5 to 10 times in a pseudorandomized order (*15*). After the viewing session, patients performed an intervening task (1 to 5 min) (*15*), after which they were asked to freely recall the clips they had seen and to verbally report immediately when a specific clip "came to mind" (free-recall session). Patients spontaneously recalled a mean of 83.2% (±5% SEM) of the clips presented.

Thirteen patients participated in a total of 43 viewing and recall sessions. We recorded from a total of 857 units (441 single units and 416 multi units) (*15*) in the MTL and the medial frontal cortex (table S1). A unit was considered responsive to a specific clip if it showed a consistent elevated pattern of firing in all trials of that clip. Overall, the majority of recorded neurons, 475 units (54.9%), showed a significant response to one or more of the clips, i.e., consistently increased firing rate in at least one 500-ms segment of clip presentation (*15*). There were no differences in proportion of responsive units among the various regions sampled in this study [$P > 0.05$, $\chi^2(5) = 7.6$] (table S1). Of the responsive units, 46 (9.7%) showed a sustained response to at least one clip, i.e., a significant elevation of firing rate through most of the clip duration (although not necessarily at a fixed level) (*15*). Of these 46 cells, 44 were in MTL and only 2 in medial frontal lobe [$P < 0.03$, $\chi^2(1) = 5.2$] (table S1, fig. S1). Twenty of these cells maintained their elevated firing rate at least 1 s beyond clip offset, and in some cases, up to 5 s beyond clip offset. Responses observed were as long as 12 s and were usually attenuated only by the onset of the next clip.

For example, a single unit in the right entorhinal cortex of a patient, presented with a selection of 48 different clips, responded in a sustained manner to an episode from the animated television (TV) series *The Simpsons* (Fig. 1A). Each time this clip was shown, the firing rate was elevated to an average of 15.57 Hz, compared with 2.11 and 2.23 Hz during other clips and blank periods, respectively ($P < 10^{-9}$, two-sample t test). The response persisted for the entire 5-s duration of the clip, continued in some of the trials up to 5 s after clip offset, and appeared to be silenced only by the onset of a different clip (Fig. 1B and movie S1a).

The neuron did not respond exclusively to this *Simpsons* episode. Even within the limited selection of 48 clips, there was a considerably weaker, yet significant, response to another clip, an episode from the TV situational comedy (sitcom) *Seinfeld*. Of the 46 units with sustained responses, a unit responded in a sustained manner to an average of 1.4 ± 0.1 SEM clips (or an average of 5.7% ± 0.5 SEM of clips presented). For another example, see fig. S2.

In a second example, a neuron in left anterior hippocampus responded with elevated firing rate throughout a single clip from a choice of 48 clips—that of the actor Tom Cruise during an interview (Fig. 2, A and B, and movie S2a). Note that this cell also exhibited shorter, transient (*15*) neuronal responses to other clips, i.e., consistent elevation of firing rate above baseline only during particular segments of the clip (green boxes in Fig. 2A), possibly reflecting the preference of the cell to a specific feature of the clip or to an episode within the clip. Additional examples are shown in figs. S3 and S4. Overall, responsive units significantly responded in a sustained or transient manner to an average of

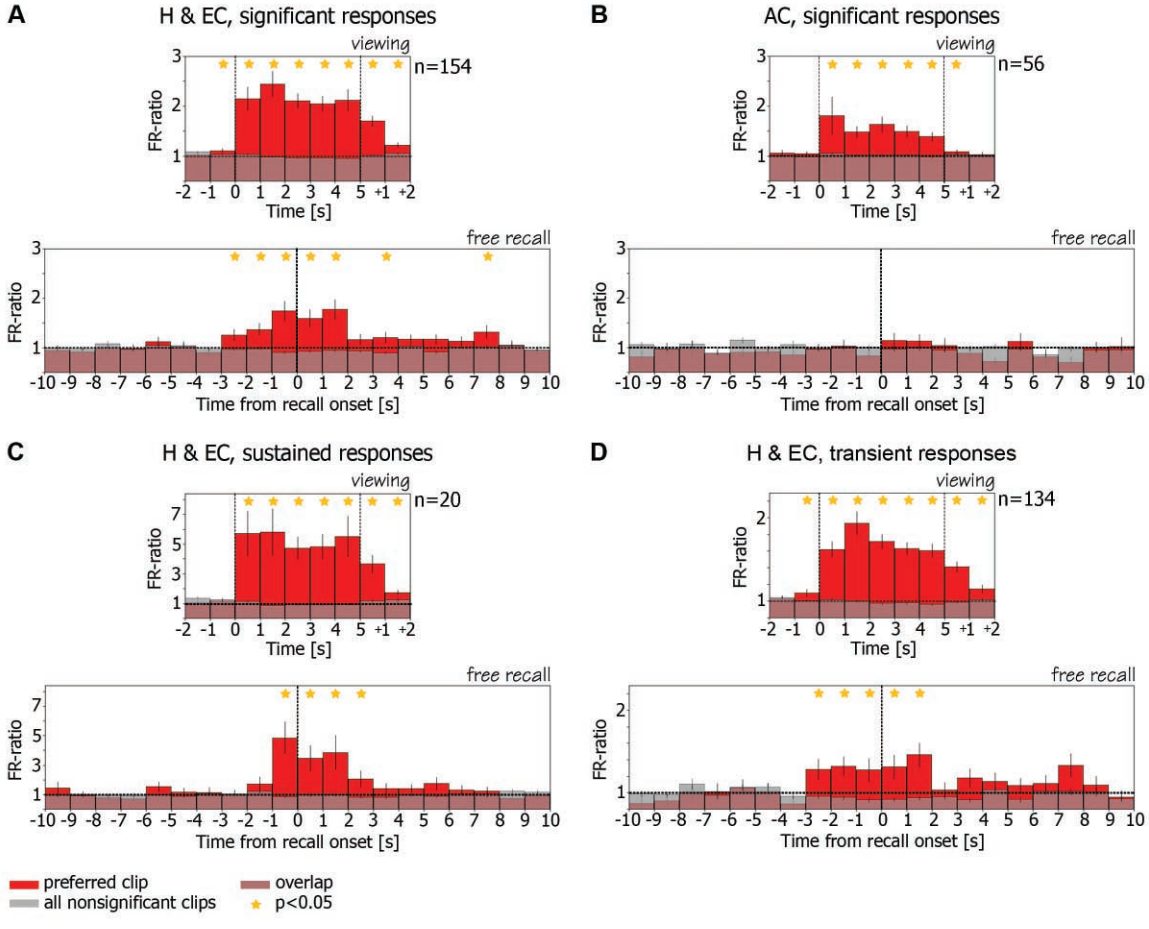

Fig. 3. Average FR ratio histograms during viewing and during free recall. (**A**) (Top) Ratio of firing rate during viewing of clips to baseline firing rate is averaged across all responsive hippocampal and entorhinal cortex cells ($n = 154$). Vertical dashed lines denote clip onset and offset. Cells increased their firing rate significantly above baseline during and following viewing of their preferred clip (*15*) (red bars). Note small elevation before clip onset, probably attributable to anticipatory effect. These cells remained at baseline firing rate (FR ratio = 1) during viewing of other clips (*15*) (gray bars). (Bottom) FR ratio during recall events is averaged across the same cells from the top panel. Traces were aligned on the onset time of the verbal report of recall (zero time, vertical dashed line). Note that the same cells increased their firing rate significantly above baseline in the 3 s before onset of verbal report of their preferred clips (red bars) and maintained this elevated firing rate in the ensuing 2 s. However, these cells remained at baseline during recall of clips that did not elicit significant responses during viewing (gray bars). Stars denote statistical significance of $P < 0.05$ (t test) (*15*). (**B**) Same as (A) but for cells from anterior cingulate ($n = 56$). Note that, in contrast to hippocampal and entorhinal cortex cells, although these cells exhibited selectivity during viewing (top), this selectivity was not maintained during free recall (bottom). (**C** and **D**) are the same as (A) but for sustained and transient responses separately.

Downloaded from www.sciencemag.org on October 2, 2008

17.7% ± 0.7 SEM of the clips presented (or 4.0 ± 0.2 SEM clips) (fig. S5).

We next examined the neuronal firing at the time of free recall when no external representation of the stimulus was present, no external cue was provided, and no external constraint was placed on the recall process. We found that the neurons that responded during viewing of a particular clip also responded during recall of that clip, with a robust elevation of firing rate for several seconds that could be detected during a single recall trial. This is illustrated for the entorhinal cortex neuron that responded selectively during viewing of a 5-s video clip from the cartoon *The Simpsons* (Fig. 1, A and B); when all 16 clips were freely recalled, the maximal firing rate was obtained in conjunction with recall of *The Simpsons* episode (Fig. 1C). The unit's firing rate rose to more than 3 SD above baseline (*15*) about 1500 ms before onset of the verbal report of recall, peaked about 100 ms before verbal report onset, but returned to baseline only after 10 s or more (see also movie S1b). Similar examples are illustrated in Fig. 2 and movie S2b, and in figures S6 to S10.

This recurrence of selective activity during recall was not an isolated observation found in a few neurons, but was also evident when the population of responsive units was examined as a whole. We calculated the average ratio of firing rate during viewing of clips to baseline firing rate (FR ratio) (*15*), for all responsive entorhinal cortex and hippocampal units (Fig. 3A, top). The FR ratio during viewing of the "preferred clip" (*15*) (red bars) is compared with the average FR ratio across all other clips with nonsignificant responses in the same viewing session (gray bars). The composite graph shows a marked elevation of the ratio following onset of the preferred clip, during viewing and, notably, also 3 s after clip offset. The FR ratio histogram for the recall is then shown in the bottom of Fig. 3A, averaged across the same units with respect to the onset time of verbal report of recall (*15*). During recall of the preferred clip (red), the averaged firing rate of the neurons increased significantly above baseline in the 3 s before onset of verbal report of recall and remained significantly above baseline in the ensuing 2 s ($P < 0.05$, Student's t test) (*15*). These neurons remained at baseline firing during recall of clips that did not elicit significant responses during viewing (gray). This recurrence during free recall of the same selective neuronal responses present during viewing was found in the population of hippocampal and entorhinal units but not in medial frontal units (compare bottom panels of Fig. 3, A and B). These frontal units exhibited a significant selective increase in firing rate during viewing, but not during recall (Fig. 3B, top and bottom, respectively). This episode-specific reactivation phenomenon was weak in amygdala and absent from parahippocampal gyrus (fig. S11), but was particularly striking for hippocampal and entorhinal neurons with sustained responses (Fig. 3C). We also noted reactivation of inhibitory responses, but because of the low baseline firing rate, these inhibitory responses were evident only at the population level (fig. S12). This phenomenon was most prominent in entorhinal cortex cells. For further details, see supporting online text.

In conclusion, we report here that a subset of neurons in the human hippocampus and entorhinal cortex exhibited highly reliable and specific responses during viewing of video episodes. These responses persisted throughout an episode or appeared during specific segments. The same neurons showed an increased firing rate again with free conscious recall, before the verbal report, when the sequence of physical sensory stimuli was absent and no external cues were provided. This recurrence during recall of specific past neuronal activity was not observed in medial frontal cortex sites. However, it is possible that top-down early recall signals do originate in other frontal or temporal lobe regions not sampled in this study (*16*–*20*).

Could the findings reported here be attributed to the neurological pathology of the patients? Although these results should be viewed with caution, such interpretation is unlikely for various reasons. Epileptic activity is characterized by highly correlated activity in large groups of neighboring neurons. The neuronal responses reported here were extremely sparse and seen selectively in individual neurons out of dozens of nonresponsive neurons that were recorded in their immediate vicinity. Furthermore, only 27% of the units were recorded from within the epileptogenic seizure foci. No significant difference was detected when these units were excluded from the analysis (see supporting online text for more details).

The responses to episodes observed here were often remarkably selective and relatively sparse; yet it is clear, even by a simple statistical reasoning, that these neurons must display selective responses to multiple other clips that have not been presented, as only a minute fraction of the vast set of possible episodes was tested in our study (*9*). Whether multiple clips to which a neuron responds may be related by some abstract association rule is not clear at present. However, some intriguing examples in our data suggest that such rules may exist (see supporting online text and figs. S2, S9, and S13 to S15). It is also important to exercise caution in claims as to what exact aspect of the clips the cell responded to. The critical point, however, is that the same selective responses recur during free recall.

Several neuroimaging studies show that brain activity present during the learning of information, as indirectly measured by the BOLD signal, is reinstated during cued or free recall (*21*–*24*), although spatiotemporal limits of fMRI restrict the possible conclusions. Selective increases in single-unit activation during mental imagery of stationary stimuli have been reported (*25*). However, unlike the situation in our study, subjects were cued by an external, content-specific, sensory stimulus.

The sparse neuronal responses arising from a very low baseline to robust firing during a specific episode are reminiscent of the responses of hippocampal place cells in rodents (*26*), in which a cell responds whenever the animal is in a particular place in the environment. Internally generated replay of previous firing sequences by hippocampal neurons has been reported in rodents, mostly during sleep and rest states after locomotion (*27*–*29*), but also during the awake state (*30*, *31*) and at decision points of a spatial memory task (*32*), where it might be predictive of the animal's future choice (*33*). However, the relation of such replay in rodents to recall of past navigation events has been merely conjectural. Our results from conscious human patients, who can spontaneously declare their memories, now directly link free recall and neuronal replay in hippocampus and entorhinal cortex. The hippocampal and entorhinal machinery used in spatial navigation in rodents may have been preserved in humans but put to a more elaborate and abstract use (*5*, *34*–*36*).

References and Notes

1. W. B. Scoville, B. Milner, *J. Neurol. Neurosurg. Psychiatry* **20**, 11 (1957).
2. L. R. Squire, C. E. Stark, R. E. Clark, *Annu. Rev. Neurosci.* **27**, 279 (2004).
3. H. Eichenbaum, *Neuron* **44**, 109 (2004).
4. M. Moscovitch, L. Nadel, G. Winocur, A. Gilboa, R. S. Rosenbaum, *Curr. Opin. Neurobiol.* **16**, 179 (2006).
5. I. Fried, K. A. MacDonald, C. L. Wilson, *Neuron* **18**, 753 (1997).
6. G. Kreiman, C. Koch, I. Fried, *Nat. Neurosci.* **3**, 946 (2000).
7. G. Heit, M. E. Smith, E. Halgren, *Nature* **333**, 773 (1988).
8. R. Q. Quiroga, L. Reddy, G. Kreiman, C. Koch, I. Fried, *Nature* **435**, 1102 (2005).
9. R. Q. Quiroga, G. Kreiman, C. Koch, I. Fried, *Trends Cogn. Sci.* **12**, 87 (2008).
10. U. Rutishauser, A. N. Mamelak, E. M. Schuman, *Neuron* **49**, 805 (2006).
11. I. V. Viskontas, B. J. Knowlton, P. N. Steinmetz, I. Fried, *J. Cogn. Neurosci.* **18**, 1654 (2006).
12. N. J. Fortin, K. L. Agster, H. B. Eichenbaum, *Nat. Neurosci.* **5**, 458 (2002).
13. J. E. Lisman, *Neuron* **22**, 233 (1999).
14. I. Fried *et al.*, *J. Neurosurg.* **91**, 697 (1999).
15. Materials and methods are available as supporting material on *Science* Online.
16. Y. Miyashita, *Science* **306**, 435 (2004).
17. R. N. Henson, M. D. Rugg, T. Shallice, R. J. Dolan, *J. Cogn. Neurosci.* **12**, 913 (2000).
18. G. A. Ojemann, J. Schoenfield-McNeill, D. P. Corina, *Nat. Neurosci.* **5**, 64 (2002).
19. S. M. Polyn, M. J. Kahana, *Trends Cogn. Sci.* **12**, 24 (2008).
20. D. L. Schacter, *Philos. Trans. R. Soc. Lond. B Biol. Sci.* **352**, 1689 (1997).
21. S. M. Polyn, V. S. Natu, J. D. Cohen, K. A. Norman, *Science* **310**, 1963 (2005).
22. L. Nyberg, R. Habib, A. R. McIntosh, E. Tulving, *Proc. Natl. Acad. Sci. U.S.A.* **97**, 11120 (2000).
23. M. E. Wheeler, S. E. Petersen, R. L. Buckner, *Proc. Natl. Acad. Sci. U.S.A.* **97**, 11125 (2000).
24. I. Kahn, L. Davachi, A. D. Wagner, *J. Neurosci.* **24**, 4172 (2004).
25. G. Kreiman, C. Koch, I. Fried, *Nature* **408**, 357 (2000).
26. J. O'Keefe, J. Dostrovsky, *Brain Res.* **34**, 171 (1971).
27. M. A. Wilson, B. L. McNaughton, *Science* **265**, 676 (1994).
28. W. E. Skaggs, B. L. McNaughton, *Science* **271**, 1870 (1996).
29. A. K. Lee, M. A. Wilson, *Neuron* **36**, 1183 (2002).
30. K. Diba, G. Buzsáki, *Nat. Neurosci.* **10**, 1241 (2007).
31. D. J. Foster, M. A. Wilson, *Nature* **440**, 680 (2006).
32. A. Johnson, A. D. Redish, *J. Neurosci.* **27**, 12176 (2007).
33. E. Pastalkova, V. Itskov, A. Amarasingham, G. Buzsáki, *Science* **321**, 1322 (2008).
34. J. O'Keefe, L. Nadel, *The Hippocampus as a Cognitive Map* (Oxford Univ. Press, Oxford, 1978), pp. 380–410.

Downloaded from www.sciencemag.org on October 2, 2008

35. E. R. Wood, P. A. Dudchenko, H. Eichenbaum, *Nature* **397**, 613 (1999).
36. C. M. Bird, N. Burgess, *Nat. Rev. Neurosci.* **9**, 182 (2008).
37. We thank the patients for their cooperation and participation in this study. We also thank E. Ho, B. Scott, E. Behnke, R. Kadivar, T. Fields, A. Postolova, K. Laird, C. Wilson, R. Quian-Quiroga, A. Kraskov, F. Mormann, and M. Cerf for assistance with data acquisition; B. Salaz and I. Wainwright for administrative help; and I. Kahn, Y. Nir, G. Buzsáki, E. Pastalkova, and S. Gilaie-Dotan for discussions and comments on this manuscript. This work was supported by NINDS (to I. Fried), Israel Science Foundation (to R. Malach), Binational United States–Israel grant (to I. Fried and R. Malach), and Human Frontier Science Program Organization (HFSPO) fellowship (to R. Mukamel).

Supporting Online Material
www.sciencemag.org/cgi/content/full/1164685/DC1
Materials and Methods
Figs. S1 to S15
Table S1
References
Movies S1 and S2

14 August 2008; accepted 28 August 2008
Published online 4 September 2008;
10.1126/science.1164685
Include this information when citing this paper.

A Physical Map of the 1-Gigabase Bread Wheat Chromosome 3B

Etienne Paux,[1] Pierre Sourdille,[1] Jérôme Salse,[1] Cyrille Saintenac,[1] Frédéric Choulet,[1] Philippe Leroy,[1] Abraham Korol,[2] Monika Michalak,[3] Shahryar Kianian,[3] Wolfgang Spielmeyer,[4] Evans Lagudah,[4] Daryl Somers,[5] Andrzej Kilian,[6] Michael Alaux,[7] Sonia Vautrin,[8] Hélène Bergès,[8] Kellye Eversole,[9] Rudi Appels,[10] Jan Safar,[11] Hana Simkova,[11] Jaroslav Dolezel,[11] Michel Bernard,[1] Catherine Feuillet[1]

As the staple food for 35% of the world's population, wheat is one of the most important crop species. To date, sequence-based tools to accelerate wheat improvement are lacking.
As part of the international effort to sequence the 17–billion–base-pair hexaploid bread wheat genome ($2n = 6x = 42$ chromosomes), we constructed a bacterial artificial chromosome (BAC)–based integrated physical map of the largest chromosome, 3B, that alone is 995 megabases. A chromosome-specific BAC library was used to assemble 82% of the chromosome into 1036 contigs that were anchored with 1443 molecular markers, providing a major resource for genetic and genomic studies. This physical map establishes a template for the remaining wheat chromosomes and demonstrates the feasibility of constructing physical maps in large, complex, polyploid genomes with a chromosome-based approach.

Among plants providing food for humans and animals, one of the oldest and most widespread is wheat (*Triticum aestivum* L.). Despite its socioeconomic importance and the challenges that agriculture is facing today (*1*), wheat genomics and its application to crop improvement are lagging behind those of most other important crops. The wheat genome has always been viewed as impossible to sequence because of its large amount of repetitive sequences (>80%) and its size of 17 Gb, which is five times larger than the human genome. The largest wheat chromosome (3B) alone is more than twice the size of the entire 370-Mb rice genome (*2*), whereas the entire maize genome (2.6 Gb) is about the size of three wheat chromosomes (table S1). Further complicating the challenge, bread wheat is a relatively recent hexaploid ($2n = 6x = 42$) containing three homoeologous A, B, and D genomes of related progenitor species, meiotic recombination is not distributed homogeneously along the chromosomes, and intervarietal polymorphism is very low.

Genome sequencing is the foundation for understanding the molecular basis of phenotypic variation, accelerating breeding, and improving the exploitation of genetic diversity to develop new crop varieties with increased yield and improved resistance to biotic and abiotic stresses. These new varieties will be critical for meeting the challenges of the 21st century, such as climatic changes, modifications of diets, human population growth, and the increased demand for biofuels. Physical maps are essential for high-quality sequence assembly regardless of the sequencing strategy used [such as bacterial artificial chromosome (BAC)–by–BAC or whole-genome shotgun strategies], and they will remain pivotal for de novo sequencing even with the advent of short-read technologies (*3*). As the foundation for genome sequencing, physical maps have been established for a dozen plants species so far, including cereals such as maize, rice, and sorghum (*4*–*6*). Recently, the development of new genomic resources for analyzing wheat paved the way for physically mapping and ultimately sequencing a species for which this was unthinkable a few years ago.

A physical map with 10-fold coverage of the 17-Gb bread wheat genome would require more than 1.4 million BAC clones to be fingerprinted, assembled into contigs, and anchored to genetic maps. Although whole-genome BAC libraries are available and fingerprinting millions of BAC clones is technically feasible with high-information-content fingerprinting (HICF) (*7*), assembly to accurately depict individual chromosomes and the anchoring of homoeologous BAC contigs onto genetic maps remains daunting. To address these issues, we used a chromosome-based approach (*8*) to construct a physical map of the largest hexaploid wheat chromosome (3B) and, to compensate for the inherent limits of the wheat genome (the lack of recombination and polymorphism), we deployed a combination of genetic mapping strategies for anchoring the physical map.

Fingerprinting and contig assembly were performed with BAC clones originating from sorted 3B wheat chromosomes of Chinese Spring (*9*), the reference cultivar chosen for genome sequencing by the International Wheat Genome Sequencing Consortium because of its previous use for cytogenetic studies and the availability of a set of aneuploid lines (*10*). 67,968 3B BAC clones were fingerprinted with a modified (*11*) HICF SNaPshot protocol (*7*), and a total of 56,952 high-quality fingerprints (84%) was obtained. A first automated assembly (*11*) resulted in a final build of 1991 contigs with an average size of 482 kb for a total length of 960 Mb (table S2). One hundred ninety-seven contigs were larger than 1 Mb; the largest was 3852 kb in size. A minimal tiling path (MTP) consisting of 7440 overlapping BAC clones was defined for further analyses. After the preliminary automated assembly, contigs were merged manually (*11*), resulting in a final assembly of 1036 contigs with an average size of 783 kb (table S2) covering 811 Mb (~82%) of the estimated 995 Mb (*12*) constituting chromosome 3B.

Contig assembly was validated through BAC library screening with markers derived from BAC-end sequences (BESs) (*13*) and by genetic mapping (*11*). Out of 421 markers derived from BESs, 369 (88%) correctly identified the BAC clones belonging to computationally identified contigs. Conversely, 35 markers originating from the same contigs mapped to the same genetic

[1]Institut National de la Recherche Agronomique, Université Blaise Pascal (INRA-UBP), UMR 1095, Genetics Diversity and Ecophysiology of Cereals, Clermont-Ferrand, France. [2]Institute of Evolution, University of Haifa, Haifa, Israel. [3]Department of Plant Sciences, North Dakota State University, Fargo, ND, USA. [4]Commonwealth Scientific and Industrial Research Organization Plant Industry, Canberra, Australia. [5]Agriculture and Agri-Food Canada, Cereal Research Centre, Winnipeg, Canada. [6]Diversity Arrays Technology, Yarralumla, Canberra, Australia. [7]INRA–Unité de Recherches en Génomique-Info, Versailles, France. [8]INRA–Centre National de Ressources Génomiques Végétales, Toulouse, France. [9]International Wheat Genome Sequencing Consortium, Eversole Associates, Bethesda, MD, USA. [10]Centre for Comparative Genomics, Murdoch University, Perth, Australia. [11]Laboratory of Molecular Cytogenetics and Cytometry, Institute of Experimental Botany, Olomouc, Czech Republic.

Downloaded from www.sciencemag.org on October 2, 2008

EXTENDED PDF FORMAT
SPONSORED BY
usb
Products from Affymetrix
www.usbweb.com

A Physical Map of the 1-Gigabase Bread Wheat Chromosome 3B

Etienne Paux, *et al.*

Science **322**, 101 (2008);
DOI: 10.1126/science.1161847

The following resources related to this article are available online at www.sciencemag.org (this information is current as of October 2, 2008):

Updated information and services, including high-resolution figures, can be found in the online version of this article at:
http://www.sciencemag.org/cgi/content/full/322/5898/101

Supporting Online Material can be found at:
http://www.sciencemag.org/cgi/content/full/322/5898/101/DC1

A list of selected additional articles on the Science Web sites **related to this article** can be found at:

This article **cites 23 articles**, 7 of which can be accessed for free:
http://www.sciencemag.org/cgi/content/full/322/5898/101#otherarticles

This article appears in the following **subject collections**:
Botany
http://www.sciencemag.org/cgi/collection/botany

Information about obtaining **reprints** of this article or about obtaining **permission to reproduce this article** in whole or in part can be found at:
http://www.sciencemag.org/about/permissions.dtl

Downloaded from www.sciencemag.org on October 2, 2008

Science (print ISSN 0036-8075; online ISSN 1095-9203) is published weekly, except the last week in December, by the American Association for the Advancement of Science, 1200 New York Avenue NW, Washington, DC 20005. Copyright 2008 by the American Association for the Advancement of Science; all rights reserved. The title *Science* is a registered trademark of AAAS.

35. E. R. Wood, P. A. Dudchenko, H. Eichenbaum, *Nature* **397**, 613 (1999).
36. C. M. Bird, N. Burgess, *Nat. Rev. Neurosci.* **9**, 182 (2008).
37. We thank the patients for their cooperation and participation in this study. We also thank E. Ho, B. Scott, E. Behnke, R. Kadivar, T. Fields, A. Postolova, K. Laird, C. Wilson, R. Quian-Quiroga, A. Kraskov, F. Mormann, and M. Cerf for assistance with data acquisition; B. Salaz and I. Wainwright for administrative help; and I. Kahn, Y. Nir, G. Buzsáki, E. Pastalkova, and S. Gilaie-Dotan for discussions and comments on this manuscript. This work was supported by NINDS (to I. Fried), Israel Science Foundation (to R. Malach), Binational United States–Israel grant (to I. Fried and R. Malach), and Human Frontier Science Program Organization (HFSPO) fellowship (to R. Mukamel).

Supporting Online Material
www.sciencemag.org/cgi/content/full/1164685/DC1
Materials and Methods
Figs. S1 to S15
Table S1
References
Movies S1 and S2

14 August 2008; accepted 28 August 2008
Published online 4 September 2008;
10.1126/science.1164685
Include this information when citing this paper.

A Physical Map of the 1-Gigabase Bread Wheat Chromosome 3B

Etienne Paux,[1] Pierre Sourdille,[1] Jérôme Salse,[1] Cyrille Saintenac,[1] Frédéric Choulet,[1] Philippe Leroy,[1] Abraham Korol,[2] Monika Michalak,[3] Shahryar Kianian,[3] Wolfgang Spielmeyer,[4] Evans Lagudah,[4] Daryl Somers,[5] Andrzej Kilian,[6] Michael Alaux,[7] Sonia Vautrin,[8] Hélène Bergès,[8] Kellye Eversole,[9] Rudi Appels,[10] Jan Safar,[11] Hana Simkova,[11] Jaroslav Dolezel,[11] Michel Bernard,[1] Catherine Feuillet[1]

As the staple food for 35% of the world's population, wheat is one of the most important crop species. To date, sequence-based tools to accelerate wheat improvement are lacking.
As part of the international effort to sequence the 17–billion–base-pair hexaploid bread wheat genome ($2n = 6x = 42$ chromosomes), we constructed a bacterial artificial chromosome (BAC)–based integrated physical map of the largest chromosome, 3B, that alone is 995 megabases. A chromosome-specific BAC library was used to assemble 82% of the chromosome into 1036 contigs that were anchored with 1443 molecular markers, providing a major resource for genetic and genomic studies. This physical map establishes a template for the remaining wheat chromosomes and demonstrates the feasibility of constructing physical maps in large, complex, polyploid genomes with a chromosome-based approach.

Among plants providing food for humans and animals, one of the oldest and most widespread is wheat (*Triticum aestivum* L.). Despite its socioeconomic importance and the challenges that agriculture is facing today (*1*), wheat genomics and its application to crop improvement are lagging behind those of most other important crops. The wheat genome has always been viewed as impossible to sequence because of its large amount of repetitive sequences (>80%) and its size of 17 Gb, which is five times larger than the human genome. The largest wheat chromosome (3B) alone is more than twice the size of the entire 370-Mb rice genome (*2*), whereas the entire maize genome (2.6 Gb) is about the size of three wheat chromosomes (table S1). Further complicating the challenge, bread wheat is a relatively recent hexaploid ($2n = 6x = 42$) containing three homoeologous A, B, and D genomes of related progenitor species, meiotic recombination is not distributed homogeneously along the chromosomes, and intervarietal polymorphism is very low.

Genome sequencing is the foundation for understanding the molecular basis of phenotypic variation, accelerating breeding, and improving the exploitation of genetic diversity to develop new crop varieties with increased yield and improved resistance to biotic and abiotic stresses. These new varieties will be critical for meeting the challenges of the 21st century, such as climatic changes, modifications of diets, human population growth, and the increased demand for biofuels. Physical maps are essential for high-quality sequence assembly regardless of the sequencing strategy used [such as bacterial artificial chromosome (BAC)–by–BAC or whole-genome shotgun strategies], and they will remain pivotal for de novo sequencing even with the advent of short-read technologies (*3*). As the foundation for genome sequencing, physical maps have been established for a dozen plants species so far, including cereals such as maize, rice, and sorghum (*4*–*6*). Recently, the development of new genomic resources for analyzing wheat paved the way for physically mapping and ultimately sequencing a species for which this was unthinkable a few years ago.

A physical map with 10-fold coverage of the 17-Gb bread wheat genome would require more than 1.4 million BAC clones to be fingerprinted, assembled into contigs, and anchored to genetic maps. Although whole-genome BAC libraries are available and fingerprinting millions of BAC clones is technically feasible with high-information-content fingerprinting (HICF) (*7*), assembly to accurately depict individual chromosomes and the anchoring of homoeologous BAC contigs onto genetic maps remains daunting. To address these issues, we used a chromosome-based approach (*8*) to construct a physical map of the largest hexaploid wheat chromosome (3B) and, to compensate for the inherent limits of the wheat genome (the lack of recombination and polymorphism), we deployed a combination of genetic mapping strategies for anchoring the physical map.

Fingerprinting and contig assembly were performed with BAC clones originating from sorted 3B wheat chromosomes of Chinese Spring (*9*), the reference cultivar chosen for genome sequencing by the International Wheat Genome Sequencing Consortium because of its previous use for cytogenetic studies and the availability of a set of aneuploid lines (*10*). 67,968 3B BAC clones were fingerprinted with a modified (*11*) HICF SNaPshot protocol (*7*), and a total of 56,952 high-quality fingerprints (84%) was obtained. A first automated assembly (*11*) resulted in a final build of 1991 contigs with an average size of 482 kb for a total length of 960 Mb (table S2). One hundred ninety-seven contigs were larger than 1 Mb; the largest was 3852 kb in size. A minimal tiling path (MTP) consisting of 7440 overlapping BAC clones was defined for further analyses. After the preliminary automated assembly, contigs were merged manually (*11*), resulting in a final assembly of 1036 contigs with an average size of 783 kb (table S2) covering 811 Mb (~82%) of the estimated 995 Mb (*12*) constituting chromosome 3B.

Contig assembly was validated through BAC library screening with markers derived from BAC-end sequences (BESs) (*13*) and by genetic mapping (*11*). Out of 421 markers derived from BESs, 369 (88%) correctly identified the BAC clones belonging to computationally identified contigs. Conversely, 35 markers originating from the same contigs mapped to the same genetic

[1]Institut National de la Recherche Agronomique, Université Blaise Pascal (INRA-UBP), UMR 1095, Genetics Diversity and Ecophysiology of Cereals, Clermont-Ferrand, France. [2]Institute of Evolution, University of Haifa, Haifa, Israel. [3]Department of Plant Sciences, North Dakota State University, Fargo, ND, USA. [4]Commonwealth Scientific and Industrial Research Organization Plant Industry, Canberra, Australia. [5]Agriculture and Agri-Food Canada, Cereal Research Centre, Winnipeg, Canada. [6]Diversity Arrays Technology, Yarralumla, Canberra, Australia. [7]INRA–Unité de Recherches en Génomique-Info, Versailles, France. [8]INRA–Centre National de Ressources Génomiques Végétales, Toulouse, France. [9]International Wheat Genome Sequencing Consortium, Eversole Associates, Bethesda, MD, USA. [10]Centre for Comparative Genomics, Murdoch University, Perth, Australia. [11]Laboratory of Molecular Cytogenetics and Cytometry, Institute of Experimental Botany, Olomouc, Czech Republic.

Downloaded from www.sciencemag.org on October 2, 2008

locus. The wheat genome has a high content of long terminal repeat retrotransposons (> 67%) (*13*) and a large number of tandemly repeated sequences, which may result in the misassembly of BAC clones. A statistical analysis (*11*) indicated that less than 10% of the fragments were randomly shared between any two nonoverlapping BAC clones. We calculated that approximately 58% overlap between fingerprints was required for automated assembly (fig. S1), and therefore with the high stringency (Sulston score = le = 75) used for the assembly (*11*), the repeated sequences did not affect the quality of the contig build.

The physical map was anchored with 685 microsatellites [simple sequence repeats (SSRs)], some of which were designed from the BESs, as well as expressed sequence tag (EST) markers (table S3) previously mapped to chromosome 3B (*14*) and identified on the basis of their synteny with rice chromosome 1. In total, 291 SSR markers were anchored to 203 contigs representing 219 Mb, and 394 ESTs were anchored to 250 individual contigs representing 283 Mb (Fig. 1 and table S3). Four hundred seventy-two additional contigs representing 452 Mb were then anchored with 711 insertion site–based polymorphism (ISBP) markers derived from 19,400 BESs (*13*) (Fig. 1 and table S3). We also tested the multiplexed and genomewide Diversity Arrays Technology (DArT) (*15*) by hybridizing a wheat array composed of 5000 DArT markers with three-dimensional pools of the MTP (*11*). Thirty-five DArTs were unambiguously assigned and anchored to 25 individual contigs (19 Mb) (table S3).

In total, 1443 molecular markers were linked to 680 BAC contigs representing 611 Mb and 75% of the 3B physical map. The longer contigs were anchored more easily (fig. S2), and more than 80% of contigs longer than 900 kb were anchored. Very few contigs (50, <80 Mb) were anchored with all marker types, and most (463 out of 680) were anchored by a single marker type (Fig. 1). This indicates that the different classes of markers cover different regions of the genome and should be used in combination to ensure optimal representation of the chromosome.

The anchored physical map can expedite map-based cloning, but its full value is achieved by determining the relative contig order along the chromosome and producing an integrated physical map. To integrate the 3B physical map, we used deletion mapping [in which the absence of two genetic sites in the same deletion line (that is, one of many lines containing small deletions in specific sites along the chromosome) is a measure of the maximal distance between them] and meiotic mapping (in which the relative order of markers is determined on the basis of recombination). This combined approach was necessary because in wheat, the resolution of meiotic mapping is limited by both the nonhomogeneous distribution of recombination events along the chromosome arms (for example, on chromosome 3B, 42% of the physical map length is represented by only 2.2% of the genetic map length in the centromeric regions) and the low level of polymorphism in the cultivated pool.

Deletion mapping resulted in the integration of 599 contigs (556 Mb, ~56% of the chromosome) in 16 physical intervals along chromosome 3B (table S3). To assess whether our physical map accurately depicts 3B, we systematically compared the total size of the contigs present in the 16 intervals defined by genetic deletions (so-called deletion bins) with the size of the genetic deletion as estimated cytologically from the chromosomes in the corresponding deletion line stocks (*16*) (table S3). Coverage within the bins ranged from 33 to 99%, with an average of 56% (fig. S3). The most terminal bin on the short arm (bin 3BS3-0.87-1.00) was only 10% covered and had a smaller average contig size (630 kb) than other bins (957 kb), suggesting that the telomeric and heterochromatic region of the short arm may be underrepresented in our BAC library.

We tested high-resolution radiation hybrid (RH) mapping, which relies on lines carrying specific radiation-induced chromosomal fragments in nonhomoeologous backgrounds (*17*) and measures the distance between genetic sites as the frequency with which they remain together after fragmentation. A panel of 184 RH lines developed for chromosome 3B (*11*) was tested with 65 ISBP markers (table S5) and indicated a resolution of about 263 kb per break. In addition, with a limited set of critical RH lines, we were able to order 35 loci (32 contigs) previously assigned to 3BL7-0.63-1.00 (table S5). We are in the process of increasing the number of RH lines for mapping all the contigs along chromosome 3B.

Further integration of the 3B physical map was achieved through meiotic mapping with a reference genetic map developed from an F_2 population (CsRe) derived from a cross between Chinese Spring (Cs) and the French cultivar Renan (Re). Because the physical contigs originate from Chinese Spring, anchoring them to the CsRe genetic map guarantees high accuracy in ordering. Because BAC libraries are available for both cultivars, this physical map also provides an efficient platform for single-nucleotide polymorphism discovery. To date, 102 SSR and ISBP markers have been mapped with 376 F_2 individuals of the CsRe population (*11*). Eighty-nine of them were anchored to contigs, permitting the integration of 75 individual contigs (77 Mb) to the genetic map, of which 80% (60/75) were ordered. Using the same criteria as the IBM Neighbors map of maize (*18*), we also established a 3B neighbor map (*11*) containing 636 SSR, restriction fragment length polymorphism, sequence tagged site (STS), DArT, and ISBP markers (table S6). In total, 213 contigs were anchored on this map, providing 225 Mb of sequence information for map-based cloning. A Gbrowse interface displaying the integrated chromosome 3B physical map is available at http://urgi.versailles.inra.fr/projects/Triticum/eng/index.php.

We also aligned the wheat 3B physical map against the rice genome using the genic sequences (ESTs/STSs) present on the 75 contigs integrated to the CsRe genetic map (*11*). Twenty-seven contigs carried 49 ESTs/STSs with homology to 56 orthologous rice genes, including 14 contigs located in the terminal part of the short arm of chromosome 3B, which is collinear with rice chromosome 1S (table S7). In this region, we identified four inversions as well as noncol-

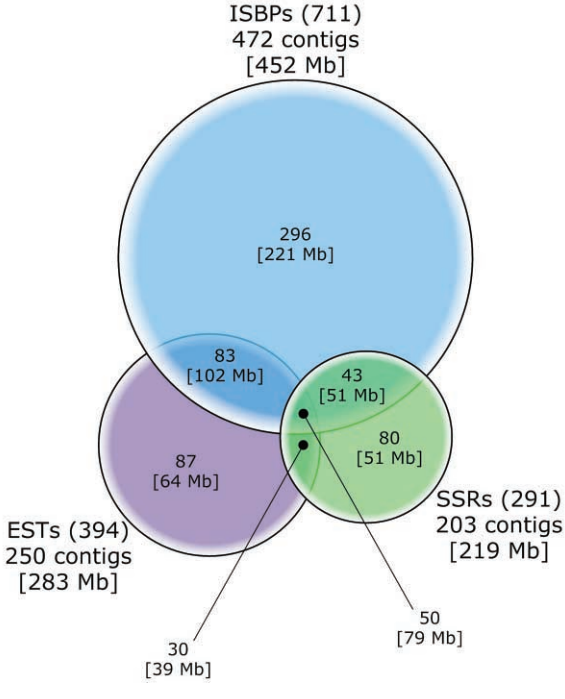

Fig. 1. Relative contribution of ISBP, EST, and SSR markers for anchoring the 3B physical map. Markers found in BAC contigs are indicated in parentheses after the marker type. The numbers of contigs anchored, as well as their physical size (in brackets), are provided for each marker type. The Venn diagram illustrates the relative contribution of each marker type, with the number and total size of contigs anchored by one or more types of markers.

Downloaded from www.sciencemag.org on October 2, 2008

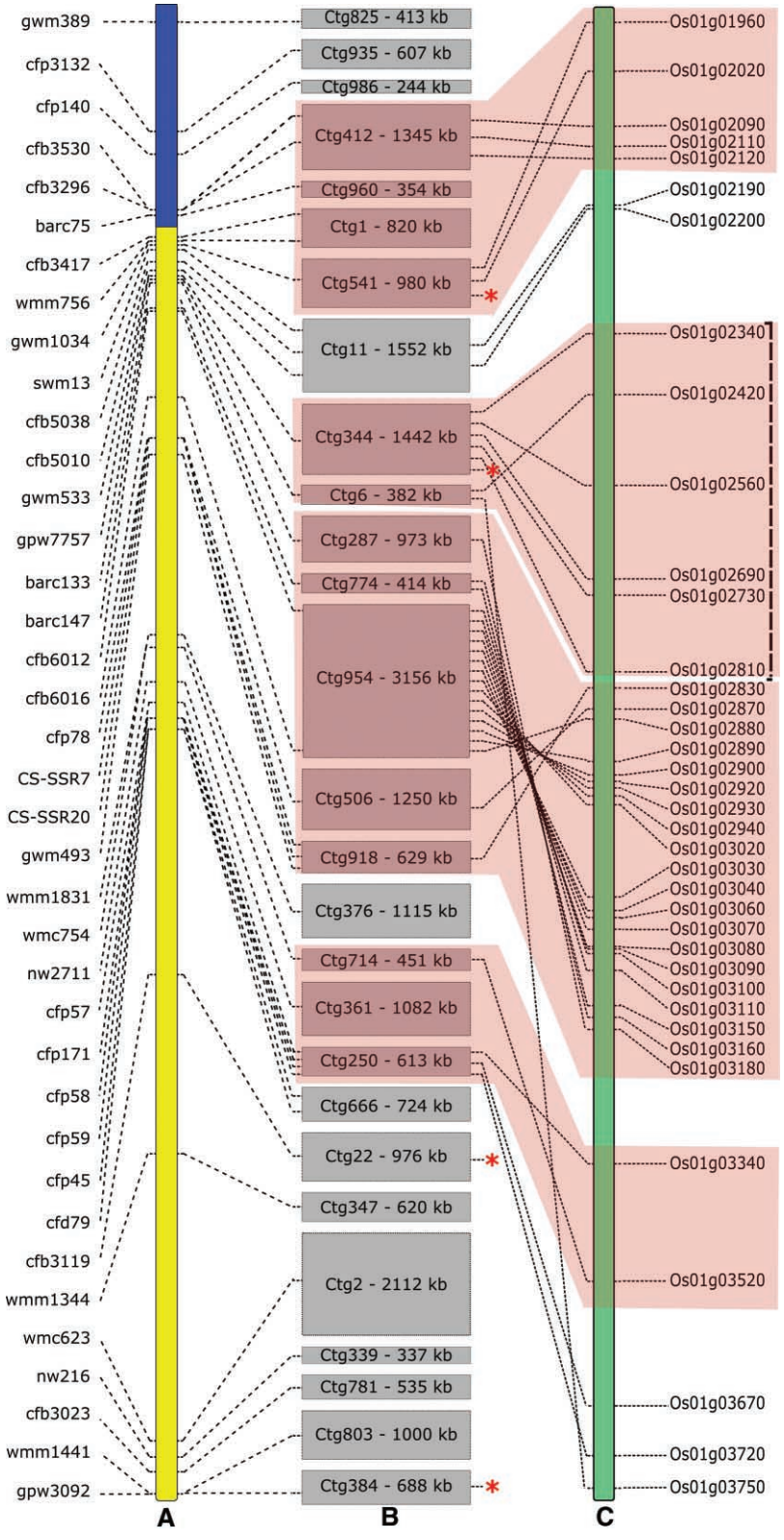

Fig. 2. Integrated physical map at the telomeric end of chromosome 3BS and colinearity with rice. (**A**) Genetic map of wheat chromosome 3B. The blue and yellow sectors represent the two distal deletion bins 3BS3-0.87-1.00 and 3BS8-0.78-0.87, respectively. (**B**) BAC contigs integrated to the genetic map. The names and sizes of the 27 contigs are displayed in gray boxes, the sizes of which reflect the relative contig sizes. (**C**) Rice chromosome 1. Each line represents the relationship between an EST located in a wheat BAC contig and the orthologous rice gene. The red sectors indicate rearrangements between the two chromosomes. The four red asterisks designate wheat ESTs for which rice orthologs were found on noncollinear regions or chromosomes other than chromosome 1. The vertical dashed bracket represents a region containing more than 30 kinase-related genes in rice.

linear genes (Fig. 2). This confirms, with a higher degree of resolution, rearrangements observed by deletion mapping between the two most conserved wheat and rice chromosomes (*19*) and suggests that many local rearrangements have occurred in globally collinear regions since the divergence of wheat and rice more than 50 million years ago. This result also indicates that predicting gene order from sequenced genomes that are not closely related so as to order the physical maps of other genomes requires great caution.

To date, less than a dozen wheat genes have been isolated through map-based cloning. About 40 genes and quantitative trait loci (QTLs) have been identified on chromosome 3B (http://wheat.pw.usda.gov/GG2/maps.shtml) and none have been cloned. Seventeen contigs representing 16.8 Mb are anchored with markers flanking or cosegregating with 16 of these genes and QTLs on our physical map (table S8). With an average contig size of 783 kb, the chromosome 3B physical map allows one to land on any target locus, in a single step, provided that recombination is compatible with fine mapping of the target gene. This has been carried out for the stem rust resistance gene *Sr2* (*20*) and the QTL *Fhb1* conferring resistance to Fusarium head blight (*21*) (table S8). The 3B physical map also provides the foundation for sequencing and in-depth studies of the wheat genome composition and organization. Sequencing and annotation are under way for 13 BAC contigs of 800 kb to 3.2 Mb, originating from different regions of chromosome 3B. These large sequenced regions will also aid in SSR and ISBP marker development. Finally, a 15-fold coverage physical map is under way for future chromosome 3B sequencing, which is envisaged for the near future.

By establishing a physical map of the largest wheat chromosome, we demonstrate that the chromosome-based approach is feasible and suitable for the construction of the hexaploid wheat genome physical map. With this physical map, the structure of agronomically important target loci can be defined in a single step and marker development can be accelerated (*22*), opening up new possibilities for accessing regions important for yield, disease resistance, and trait improvement in wheat. An international collaborative effort is under way now to exploit this new resource and, using the same strategy, projects have begun for the 20 remaining chromosomes (table S1; www.ueb.cas.cz/Olomouc1/LMCC/Resources/resources.html#chrs and www.wheatgenome.org/projects.php), opening the way to future sequencing of the wheat genome.

Finally, although chromosome sorting has so far been applied only to a few other cereals [barley, durum wheat, and rye (*8*)], important legumes (pea and bean), and trees (Norway spruce) (*23*), this work exemplifies its broader potential for other complex nonmodel genomes heretofore considered impossible to sequence

Downloaded from www.sciencemag.org on October 2, 2008

despite their socioeconomic importance. Until now, the selection of genomes for sequencing has been determined on the basis of genome simplicity and not agronomic relevance, with serious consequences for crop improvement and food security [for example, by neglecting wheat or choosing the diploid of cotton, *Gossypium raimondii*, to sequence first rather than focusing on the economically important tetraploid *G. hirsutum* (*24*)]. Our work may pave the way for a major change in how the next genomes for de novo sequencing are selected, thereby accelerating improvements in economically important crop species.

References and Notes

1. B. Wollenweber *et al.*, *Curr. Opin. Plant Biol.* **8**, 337 (2005).
2. T. Itoh *et al.*, *Genome Res.* **17**, 175 (2007).
3. R. L. Warren *et al.*, *Genome Res.* **16**, 768 (2006).
4. M. Chen *et al.*, *Plant Cell* **14**, 537 (2002).
5. P. E. Klein *et al.*, *Genome Res.* **10**, 789 (2000).
6. F. Wei *et al.*, *PLoS Genet.* **3**, e123 (2007).
7. M. C. Luo *et al.*, *Genomics* **82**, 378 (2003).
8. J. Dolezel *et al.*, *Chromosome Res.* **15**, 51 (2007).
9. J. Safar *et al.*, *Plant J.* **39**, 960 (2004).
10. T. R. Endo, B. S. Gill, *J. Hered.* **87**, 295 (1996).
11. Materials and methods are available as supporting material on *Science* Online.
12. B. S. Gill *et al.*, *Genome* **34**, 830 (1991).
13. E. Paux *et al.*, *Plant J.* **48**, 463 (2006).
14. J. D. Munkvold *et al.*, *Genetics* **168**, 639 (2004).
15. M. Akbari *et al.*, *Theor. Appl. Genet.* **113**, 1409 (2006).
16. M. Dilbirligi *et al.*, *Genetics* **166**, 461 (2004).
17. K. G. Hossain *et al.*, *Genetics* **168**, 415 (2004).
18. K. C. Cone *et al.*, *Plant Physiol.* **130**, 1598 (2002).
19. M. La Rota, M. E. Sorrells, *Funct. Integr. Genomics* **4**, 34 (2004).
20. R. Kota *et al.*, *Theor. Appl. Genet.* **112**, 492 (2006).
21. S. Liu *et al.*, *Funct. Integr. Genomics* **6**, 83 (2006).
22. M. D. McNeil *et al.*, *Mol. Breed.* **22**, 15 (2008).
23. J. Dolezel *et al.*, *Chromosome Res.* **12**, 77 (2004).
24. Z. J. Chen *et al.*, *Plant Physiol.* **145**, 1303 (2007).

25. We thank D. Boyer, K. Paux, and members of the GENTYANE platform for technical assistance; M. Ganal (Trait Genetics), P. Jack (RAGT), and F. Azanza (Syngenta) for providing SSR markers and genotyping data; the support of F. Legeai and D. Steinbach from Unité de Recherche en Génomique-Info in establishing the Gbrowse display of the integrated physical map; A. Kumar (Choudhury Charan Singh University Meerut), O. Riera-Lizarazu (Oregon State University), and Y. Gu (U.S. Department of Agriculture–Agricultural Research Service) for significant contributions to the RH mapping work; and F. Quetier (Agence Nationale de la Recherche) for support and discussions. Supported by the Agence Nationale de la Recherche (grant ANR-05-BLANC-0258-01) and the INRA.

Supporting Online Material

www.sciencemag.org/cgi/content/full/322/5898/101/DC1
Materials and Methods
Figs. S1 to S3
Tables S1 to S8
References

16 June 2008; accepted 10 September 2008
10.1126/science.1161847

High-Quality Binary Protein Interaction Map of the Yeast Interactome Network

Haiyuan Yu,[1,2]* Pascal Braun,[1,2]* Muhammed A. Yıldırım,[1,2,3]* Irma Lemmens,[4] Kavitha Venkatesan,[1,2] Julie Sahalie,[1,2] Tomoko Hirozane-Kishikawa,[1,2] Fana Gebreab,[1,2] Na Li,[1,2] Nicolas Simonis,[1,2] Tong Hao,[1,2] Jean-François Rual,[1,2] Amélie Dricot,[1,2] Alexei Vazquez,[5] Ryan R. Murray,[1,2] Christophe Simon,[1,2] Leah Tardivo,[1,2] Stanley Tam,[1,2] Nenad Svrzikapa,[1,2] Changyu Fan,[1,2] Anne-Sophie de Smet,[4] Adriana Motyl,[6] Michael E. Hudson,[6] Juyong Park,[1,7] Xiaofeng Xin,[8] Michael E. Cusick,[1,2] Troy Moore,[9] Charlie Boone,[8] Michael Snyder,[6] Frederick P. Roth,[1,10] Albert-László Barabási,[1,7] Jan Tavernier,[4] David E. Hill,[1,2] Marc Vidal[1,2]†

Current yeast interactome network maps contain several hundred molecular complexes with limited and somewhat controversial representation of direct binary interactions. We carried out a comparative quality assessment of current yeast interactome data sets, demonstrating that high-throughput yeast two-hybrid (Y2H) screening provides high-quality binary interaction information. Because a large fraction of the yeast binary interactome remains to be mapped, we developed an empirically controlled mapping framework to produce a "second-generation" high-quality, high-throughput Y2H data set covering ~20% of all yeast binary interactions. Both Y2H and affinity purification followed by mass spectrometry (AP/MS) data are of equally high quality but of a fundamentally different and complementary nature, resulting in networks with different topological and biological properties. Compared to co-complex interactome models, this binary map is enriched for transient signaling interactions and intercomplex connections with a highly significant clustering between essential proteins. Rather than correlating with essentiality, protein connectivity correlates with genetic pleiotropy.

A crucial step toward understanding cellular systems properties is mapping networks of physical DNA-, RNA-, and protein-protein interactions, the "interactome network," of an organism of interest as completely and accurately as possible. One approach consists in systematically testing all pairwise combinations of predicted proteins to derive the "binary" interactome. Early attempts at binary interactome mapping used high-throughput yeast two-hybrid (Y2H) screening, in which a protein interaction reconstitutes a transcription factor that activates expression of reporter genes. High-throughput Y2H maps have been generated for *Saccharomyces cerevisiae* (*1*–*3*), *Caenorhabditis elegans* (*4*–*6*), *Drosophila melanogaster* (*7*), and humans (*8*–*10*). An alternative approach consists in generating "co-complex" interactome maps, achievable by high-throughput coaffinity purification followed by mass spectrometry (AP/MS) to identify proteins bound to tagged baits, as done for *Escherichia coli* (*11*, *12*), *S. cerevisiae* (*13*–*16*), and humans (*17*).

To investigate fundamental questions of interactome network structure and function, it is necessary to understand how the size and quality of currently available maps, including thorough evaluation of differences between binary and co-complex maps, might have affected conclusions about global and local properties of interactome networks (*18*, *19*). Here, we address these issues using the yeast *S. cerevisiae* as a model system.

First, we compared the quality of existing high-throughput binary and co-complex data sets to information obtained from curating low-throughput experiments described in the literature (Fig. 1A). For binary interactions, we examined (i) the subset found by Uetz *et al.* in a proteome-scale all-by-all screen ("Uetz-screen"), excluding the pairs found in a focused, potentially biased experiment involving only 193 baits ("Uetz-array") (*2*); and (ii) the Ito *et al.* interactions found three times or more ("Ito-core"), independently from those found one or two times ("Ito-noncore"), a distinction recommended by the authors but seldom applied in the literature (*3*). For co-complex associations, we investigated two high-throughput AP/MS data sets referred to as "Gavin" (*15*) and "Krogan" (*16*). For literature-curated interactions, we considered only those curated from two or more publications ("LC-multiple") (*20*), which we judged of higher quality than those curated from a single publication.

To experimentally compare the quality of these data sets, we selected a representative sample of ~200 protein interaction pairs from each one and tested them by means of two independent interaction assays, Y2H and a yellow fluorescent protein complementation assay (PCA) (*21*) [Supporting Online Material (SOM) I]. In PCA, bait and prey proteins are fused to nonfluorescent fragments of yellow fluorescent protein that, when brought in close proximity by interacting proteins, reconstitute a fluorescent protein in mammalian cells. In con-

Downloaded from www.sciencemag.org on October 2, 2008

EXTENDED PDF FORMAT
SPONSORED BY
usb
Products from Affymetrix
www.usbweb.com

High-Quality Binary Protein Interaction Map of the Yeast Interactome Network

Haiyuan Yu, *et al.*

Science **322**, 104 (2008);
DOI: 10.1126/science.1158684

The following resources related to this article are available online at www.sciencemag.org (this information is current as of October 2, 2008):

Updated information and services, including high-resolution figures, can be found in the online version of this article at:
http://www.sciencemag.org/cgi/content/full/322/5898/104

Supporting Online Material can be found at:
http://www.sciencemag.org/cgi/content/full/1158684/DC1

This article **cites 45 articles**, 20 of which can be accessed for free:
http://www.sciencemag.org/cgi/content/full/322/5898/104#otherarticles

This article appears in the following **subject collections**:
Genetics
http://www.sciencemag.org/cgi/collection/genetics

Information about obtaining **reprints** of this article or about obtaining **permission to reproduce this article** in whole or in part can be found at:
http://www.sciencemag.org/about/permissions.dtl

Downloaded from www.sciencemag.org on October 2, 2008

Science (print ISSN 0036-8075; online ISSN 1095-9203) is published weekly, except the last week in December, by the American Association for the Advancement of Science, 1200 New York Avenue NW, Washington, DC 20005. Copyright 2008 by the American Association for the Advancement of Science; all rights reserved. The title *Science* is a registered trademark of AAAS.

despite their socioeconomic importance. Until now, the selection of genomes for sequencing has been determined on the basis of genome simplicity and not agronomic relevance, with serious consequences for crop improvement and food security [for example, by neglecting wheat or choosing the diploid of cotton, *Gossypium raimondii*, to sequence first rather than focusing on the economically important tetraploid *G. hirsutum* (*24*)]. Our work may pave the way for a major change in how the next genomes for de novo sequencing are selected, thereby accelerating improvements in economically important crop species.

References and Notes

1. B. Wollenweber *et al.*, *Curr. Opin. Plant Biol.* **8**, 337 (2005).
2. T. Itoh *et al.*, *Genome Res.* **17**, 175 (2007).
3. R. L. Warren *et al.*, *Genome Res.* **16**, 768 (2006).
4. M. Chen *et al.*, *Plant Cell* **14**, 537 (2002).
5. P. E. Klein *et al.*, *Genome Res.* **10**, 789 (2000).
6. F. Wei *et al.*, *PLoS Genet.* **3**, e123 (2007).
7. M. C. Luo *et al.*, *Genomics* **82**, 378 (2003).
8. J. Dolezel *et al.*, *Chromosome Res.* **15**, 51 (2007).
9. J. Safar *et al.*, *Plant J.* **39**, 960 (2004).
10. T. R. Endo, B. S. Gill, *J. Hered.* **87**, 295 (1996).
11. Materials and methods are available as supporting material on *Science* Online.
12. B. S. Gill *et al.*, *Genome* **34**, 830 (1991).
13. E. Paux *et al.*, *Plant J.* **48**, 463 (2006).
14. J. D. Munkvold *et al.*, *Genetics* **168**, 639 (2004).
15. M. Akbari *et al.*, *Theor. Appl. Genet.* **113**, 1409 (2006).
16. M. Dilbirligi *et al.*, *Genetics* **166**, 461 (2004).
17. K. G. Hossain *et al.*, *Genetics* **168**, 415 (2004).
18. K. C. Cone *et al.*, *Plant Physiol.* **130**, 1598 (2002).
19. M. La Rota, M. E. Sorrells, *Funct. Integr. Genomics* **4**, 34 (2004).
20. R. Kota *et al.*, *Theor. Appl. Genet.* **112**, 492 (2006).
21. S. Liu *et al.*, *Funct. Integr. Genomics* **6**, 83 (2006).
22. M. D. McNeil *et al.*, *Mol. Breed.* **22**, 15 (2008).
23. J. Dolezel *et al.*, *Chromosome Res.* **12**, 77 (2004).
24. Z. J. Chen *et al.*, *Plant Physiol.* **145**, 1303 (2007).

25. We thank D. Boyer, K. Paux, and members of the GENTYANE platform for technical assistance; M. Ganal (Trait Genetics), P. Jack (RAGT), and F. Azanza (Syngenta) for providing SSR markers and genotyping data; the support of F. Legeai and D. Steinbach from Unité de Recherche en Génomique-Info in establishing the Gbrowse display of the integrated physical map; A. Kumar (Choudhury Charan Singh University Meerut), O. Riera-Lizarazu (Oregon State University), and Y. Gu (U.S. Department of Agriculture–Agricultural Research Service) for significant contributions to the RH mapping work; and F. Quetier (Agence Nationale de la Recherche) for support and discussions. Supported by the Agence Nationale de la Recherche (grant ANR-05-BLANC-0258-01) and the INRA.

Supporting Online Material

www.sciencemag.org/cgi/content/full/322/5898/101/DC1
Materials and Methods
Figs. S1 to S3
Tables S1 to S8
References

16 June 2008; accepted 10 September 2008
10.1126/science.1161847

High-Quality Binary Protein Interaction Map of the Yeast Interactome Network

Haiyuan Yu,[1,2]* Pascal Braun,[1,2]* Muhammed A. Yıldırım,[1,2,3]* Irma Lemmens,[4] Kavitha Venkatesan,[1,2] Julie Sahalie,[1,2] Tomoko Hirozane-Kishikawa,[1,2] Fana Gebreab,[1,2] Na Li,[1,2] Nicolas Simonis,[1,2] Tong Hao,[1,2] Jean-François Rual,[1,2] Amélie Dricot,[1,2] Alexei Vazquez,[5] Ryan R. Murray,[1,2] Christophe Simon,[1,2] Leah Tardivo,[1,2] Stanley Tam,[1,2] Nenad Svrzikapa,[1,2] Changyu Fan,[1,2] Anne-Sophie de Smet,[4] Adriana Motyl,[6] Michael E. Hudson,[6] Juyong Park,[1,7] Xiaofeng Xin,[8] Michael E. Cusick,[1,2] Troy Moore,[9] Charlie Boone,[8] Michael Snyder,[6] Frederick P. Roth,[1,10] Albert-László Barabási,[1,7] Jan Tavernier,[4] David E. Hill,[1,2] Marc Vidal[1,2]†

Current yeast interactome network maps contain several hundred molecular complexes with limited and somewhat controversial representation of direct binary interactions. We carried out a comparative quality assessment of current yeast interactome data sets, demonstrating that high-throughput yeast two-hybrid (Y2H) screening provides high-quality binary interaction information. Because a large fraction of the yeast binary interactome remains to be mapped, we developed an empirically controlled mapping framework to produce a "second-generation" high-quality, high-throughput Y2H data set covering ~20% of all yeast binary interactions. Both Y2H and affinity purification followed by mass spectrometry (AP/MS) data are of equally high quality but of a fundamentally different and complementary nature, resulting in networks with different topological and biological properties. Compared to co-complex interactome models, this binary map is enriched for transient signaling interactions and intercomplex connections with a highly significant clustering between essential proteins. Rather than correlating with essentiality, protein connectivity correlates with genetic pleiotropy.

A crucial step toward understanding cellular systems properties is mapping networks of physical DNA-, RNA-, and protein-protein interactions, the "interactome network," of an organism of interest as completely and accurately as possible. One approach consists in systematically testing all pairwise combinations of predicted proteins to derive the "binary" interactome. Early attempts at binary interactome mapping used high-throughput yeast two-hybrid (Y2H) screening, in which a protein interaction reconstitutes a transcription factor that activates expression of reporter genes. High-throughput Y2H maps have been generated for *Saccharomyces cerevisiae* (*1*–*3*), *Caenorhabditis elegans* (*4*–*6*), *Drosophila melanogaster* (*7*), and humans (*8*–*10*). An alternative approach consists in generating "co-complex" interactome maps, achievable by high-throughput coaffinity purification followed by mass spectrometry (AP/MS) to identify proteins bound to tagged baits, as done for *Escherichia coli* (*11*, *12*), *S. cerevisiae* (*13*–*16*), and humans (*17*).

To investigate fundamental questions of interactome network structure and function, it is necessary to understand how the size and quality of currently available maps, including thorough evaluation of differences between binary and co-complex maps, might have affected conclusions about global and local properties of interactome networks (*18*, *19*). Here, we address these issues using the yeast *S. cerevisiae* as a model system.

First, we compared the quality of existing high-throughput binary and co-complex data sets to information obtained from curating low-throughput experiments described in the literature (Fig. 1A). For binary interactions, we examined (i) the subset found by Uetz *et al.* in a proteome-scale all-by-all screen ("Uetz-screen"), excluding the pairs found in a focused, potentially biased experiment involving only 193 baits ("Uetz-array") (*2*); and (ii) the Ito *et al.* interactions found three times or more ("Ito-core"), independently from those found one or two times ("Ito-noncore"), a distinction recommended by the authors but seldom applied in the literature (*3*). For co-complex associations, we investigated two high-throughput AP/MS data sets referred to as "Gavin" (*15*) and "Krogan" (*16*). For literature-curated interactions, we considered only those curated from two or more publications ("LC-multiple") (*20*), which we judged of higher quality than those curated from a single publication.

To experimentally compare the quality of these data sets, we selected a representative sample of ~200 protein interaction pairs from each one and tested them by means of two independent interaction assays, Y2H and a yellow fluorescent protein complementation assay (PCA) (*21*) [Supporting Online Material (SOM) I]. In PCA, bait and prey proteins are fused to nonfluorescent fragments of yellow fluorescent protein that, when brought in close proximity by interacting proteins, reconstitute a fluorescent protein in mammalian cells. In con-

Downloaded from www.sciencemag.org on October 2, 2008

trast, reconstitution of a transcription factor in Y2H experiments takes place in the nucleus of yeast cells. In terms of assay designs, Y2H and PCA can be considered as orthogonal assays and can be used to validate each other's results.

No single assay is expected to detect 100% of genuine interactions, and the actual fraction of positives detected is inherently linked to the stringency at which the assay is implemented. To identify the optimal scoring condition of each assay, we selected a set of ~100 well-documented yeast protein-protein interaction pairs ["positive reference set" (PRS)] and a set of ~100 random pairs ["random reference set" (RRS)] (Fig. 1B; SOM II). Because RRS pairs were picked uniformly from the 14×10^6 possible pairings of proteins within our yeast ORFeome collection (*22*) (excluding those reported as interacting), these pairs are extremely unlikely to be interacting.

Sampled pairs from binary Uetz-screen and Ito-core data sets tested positive at levels as high as those of the positive-control PRS, demonstrating their high quality (Fig. 1C). A sample of literature-curated LC-multiple interactions tested slightly lower with Y2H, while being indistinguishable by PCA (Fig. 1C), demonstrating that high-throughput Y2H data sets can be comparable in quality to literature-curated information. In marked contrast, sampled pairs from Ito-noncore tested positive at levels similar to those of the negative-control RRS, confirming the low quality of this particular data set (Fig. 1C).

Sampled pairs from Gavin and Krogan high-throughput AP/MS data sets tested poorly in our two binary interaction assays (Fig. 1C), albeit at levels similar to those of Munich Information Center for Protein Sequences (MIPS) complexes, a widely used "gold standard" (*23*). This observation demonstrates that, at least for detecting binary interactions, Y2H performs better than AP/MS.

Our experimental data quality assessment shows that binary Uetz-screen, Ito-core, and LC-multiple data sets are of high quality, whereas Ito-noncore should not be used. AP/MS data sets, although of intrinsically good quality (*15*, *16*), should be used cautiously when binary interaction information is needed.

Our experimental results contrast markedly with computational analyses that suggested that high-throughput Y2H data sets contain more false-positives than literature-curated or high-throughput AP/MS data sets (*24*, *25*). In computational analyses, the quality of a data set is often determined by the fraction of interactions also present in a predefined gold standard set (*24*). Generally, MIPS complexes have been considered as gold standard, with all proteins constituting a given complex modeled as interacting with each other. Such modeling results in limited and biased sampling issues against binary interactions because not all

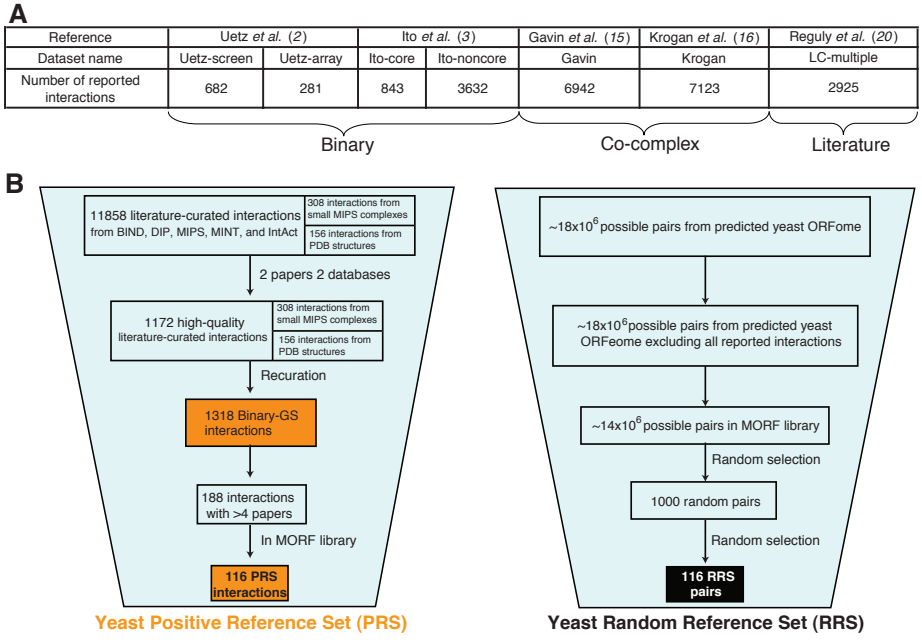

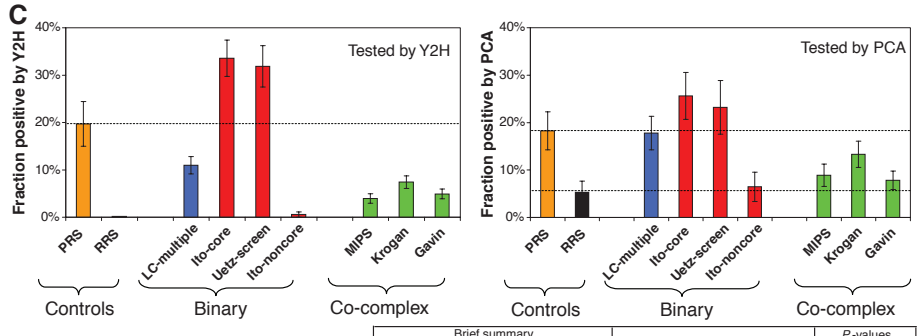

Brief summary (For detecting binary interactions)	Representative datasets	*P*-values Y2H	*P*-values PCA
1. Y2H is comparable to LC-multiple	Uetz-screen ≥ LC-multiple	$P<10^{-16}$	$P=0.1$
2. Ito-noncore is of extremely low quality	Ito-noncore ≈ RRS	$P=0.9$	$P=0.2$
3. Y2H performs better than AP/MS	Uetz-screen > Krogan	$P<10^{-30}$	$P<10^{-3}$
4. Y2H performs better than MIPS	Uetz-screen > MIPS	$P<10^{-41}$	$P<10^{-5}$

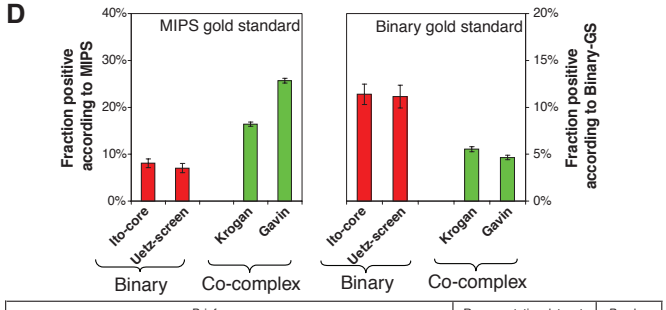

Brief summary	Representative datasets	*P*-values
1. AP/MS performs well at detecting co-complex associations according to MIPS	Uetz-screen < Krogan	$P<10^{-12}$
2. Y2H performs well at detecting binary interactions according to Binary-GS	Uetz-screen > Krogan	$P<10^{-5}$

Fig. 1. Evaluation of *S. cerevisiae* protein-protein interaction data sets. (**A**) Number of interactions reported in various large-scale *S. cerevisiae* protein-protein interaction data sets. (**B**) Schema of pipeline used to assemble binary positive and random reference sets. (**C**) Fraction of a random sample of interactions from each data set confirmed by Y2H and PCA. (**D**) Fraction of positive interactions in each data set calculated with MIPS and Binary-GS. Error bars indicate SE.

[1]Center for Cancer Systems Biology (CCSB), Dana-Farber Cancer Institute, Boston, MA 02115, USA. [2]Department of Cancer Biology, Dana-Farber Cancer Institute, and Department of Genetics, Harvard Medical School, Boston, MA 02115, USA. [3]School of Engineering and Applied Sciences, Harvard University, Cambridge, MA 02138, USA. [4]Department of Medical Protein Research, VIB, and Department of Biochemistry, Faculty of Medicine and Health Sciences, Ghent University, 9000 Ghent, Belgium. [5]The Simons Center for Systems Biology, Institute for Advanced Studies, Princeton, NJ 08540, USA. [6]Department of Molecular, Cellular, and Developmental Biology, Yale University, New Haven, CT 06620, USA. [7]Center for Complex Network Research and Departments of Physics, Biology, and Computer Science, Northeastern University, Boston, MA 02115, USA. [8]Banting and Best Department of Medical Research and Department of Medical Genetics and Microbiology, Terrence Donnelly Centre for Cellular and Biomolecular Research, University of Toronto, Toronto, ON M5S 3E1, Canada. [9]Open Biosystems, Huntsville, AL 35806, USA. [10]Department of Biological Chemistry and Molecular Pharmacology, Harvard Medical School, Boston, MA 02115, USA.

*These authors contributed equally to this work.
†To whom correspondence should be addressed. E-mail: marc_vidal@dfci.harvard.edu

Downloaded from www.sciencemag.org on October 2, 2008

proteins in a complex contact each other directly (fig. S1), and not all direct physical interactions occur within complexes (fig. S2 and SOM III). Hence, although MIPS complexes are appropriate for benchmarking co-complex membership data sets, they are not appropriate for binary interaction data sets. This distinction is corroborated by the poor experimental confirmation rate of pairs from MIPS complexes with binary assays (Fig. 1C).

To computationally reexamine the quality of existing yeast interactome data sets, we assembled a binary gold standard set ("Binary-GS") of 1318 high-confidence physical binary interactions (Fig. 1B and SOM III). Binary-GS includes direct physical interactions within well-established complexes, as well as conditional interactions (e.g., dependent on posttranslational modifications), and thus represents well-documented direct physical interactions in the yeast interactome (*26*). When measured against Binary-GS, the quality of high-throughput Y2H data sets (with the exception of Ito-noncore) was substantially better (SOM IV and V) than that of high-throughput AP/MS data sets (Fig. 1D). Our results demonstrate the distinct nature of binary and co-complex data. Generally, Y2H data sets contain high-quality direct binary interactions, whereas AP/MS co-complex data sets are composed of direct interactions mixed with preponderant indirect associations (SOM VI).

The proteome-wide binary data sets, Uetz-screen and Ito-core, contain 682 and 843 interactions, respectively (*2*, *3*). The overlap between these two data sets appears low (*3*, *24*): 19% of Uetz-screen and 15% of Ito-core interactions were detected in the other data set. Given our demonstration of high quality for these data sets (Fig. 1, C and D), we conclude that the small overlap stems primarily from low sensitivity (i.e., many false-negatives) rather than from low specificity (i.e., many false-positives, as previously suggested).

Several factors might affect sensitivity. First, the space of pairwise protein combinations actually tested in each data set might have been considerably different. We refer to the fraction of all possible pairs tested in a given screen as the "completeness." For example, missing 10% of open reading frames (ORFs) in each mapping project could reduce the common tested space down to 66% [(0.9 × 0.9) × (0.9 × 0.9)] of all possible pairwise combinations. Second, different protein interaction assays or even different versions of the same assay detect different subsets of pairs out of all possible interactions, which explains partly the limited overlap between data sets obtained with different Y2H versions. For any assay, the "assay sensitivity" is estimated as the fraction of PRS interactions detected, which for our Y2H assay was determined empirically to be ~20% (Fig. 1C). Finally, when screening tens if not hundreds of millions of protein pairs in any tested space, that search space might need to be sampled multiple times to report all or nearly all interactions detectable by the assay used. The fraction of all theoretically detectable interactions by a particular assay found in a given experiment is its "sampling sensitivity." These three parameters fully account for the seemingly small overlap between Ito-core and Uetz-screen (SOM VII), demonstrating that a large fraction of the *S. cerevisiae* binary interactome remains to be mapped. Therefore, we carried out a new proteome-scale yeast high-throughput Y2H screen (fig. S3).

We used 5796 Gateway-cloned ORFs available in the yeast movable ORF (MORF) collection (*22*). After subcloning these ORFs into Y2H vectors and removing autoactivators (*27*, *28*), our search space became 3917 DB-Xs against 5246 AD-Ys, representing a completeness of 77% (Fig. 2A and SOM VI), comparable to that of recent AP/MS data sets (*15*) (~78%; SOM VI).

To address sampling sensitivity, we determined what fraction of all detectable interactions is found in each pass after eight trials in a search space of 658 DB-X and 1249 AD-Y ORFs. A single trial identified about 60% of all possible interactions that can be detected with our high-throughput Y2H, whereas three to five repeats were required to obtain 80 to 90% (Fig. 2B and SOM VI). Consequently, we screened the whole search space three times independently to yield an estimated sampling sensitivity of 85% (Fig. 2B). In total, ~88,000 colonies were selected, of which 21,432 scored positive upon more detailed phenotyping (SOM I). After identifying all putative interaction pairs by sequencing, phenotypically retesting them with fresh cultures from archival stocks, and eliminating de novo autoactivators (*28*), we obtained a final data set, "CCSB-YI1," of 1809 interactions among 1278 proteins, which can be downloaded from our Web site (http://interactome.dfci.harvard.edu/S_cerevisiae).

To validate the overall quality of CCSB-YI1, we tested 94 randomly chosen interactions by PCA and mammalian protein-protein interaction trap (MAPPIT; SOM I) (*21*, *29*). MAPPIT takes place at the mammalian cell membrane and measures interactions via activation of signal transducer and activator of transcription 3 (STAT3)–dependent reporter expression. Using both PCA and MAPPIT, we found that the confirmation rate of CCSB-YI1 was similar to those of Ito-core and Uetz-screen (Fig. 1C). The precision [i.e., fraction of true positives in the data set (*30*)] of CCSB-YI1 is estimated at 94 to 100% (Fig. 2C, fig. S4, and SOM VI). Additionally, the performance of our high-throughput Y2H approach was confirmed via a larger RRS of 1000 random pairs (*30*) (Fig. 1B), none of which tested positive (SOM II).

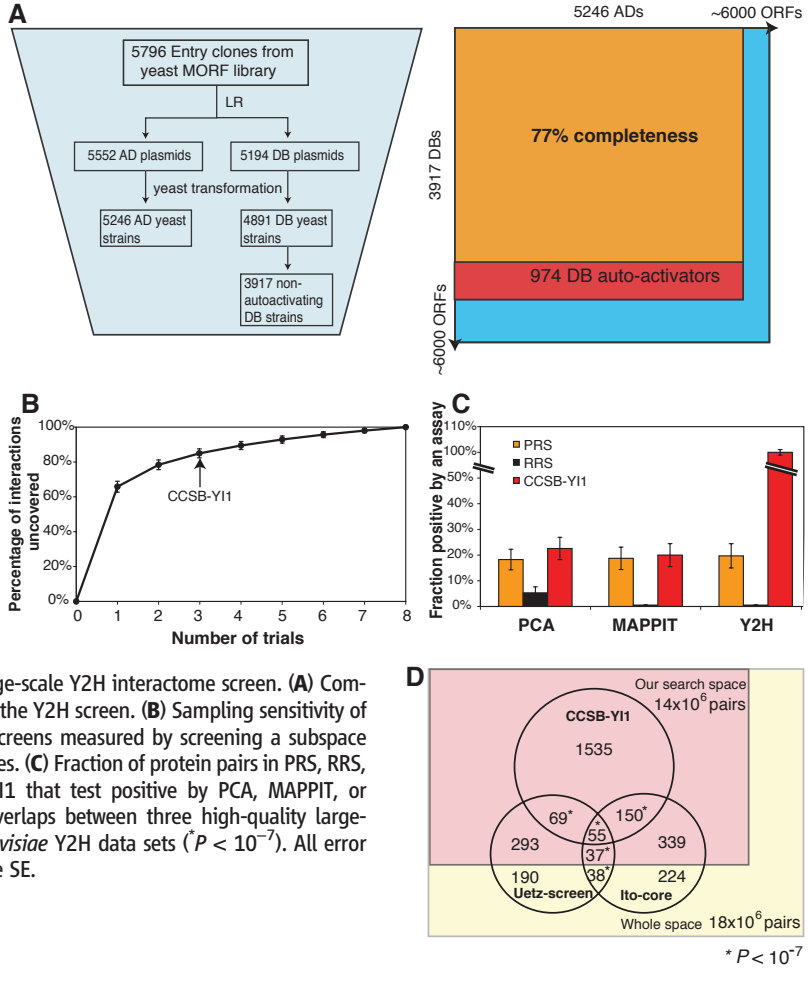

Fig. 2. Large-scale Y2H interactome screen. (**A**) Completeness of the Y2H screen. (**B**) Sampling sensitivity of CCSB Y2H screens measured by screening a subspace multiple times. (**C**) Fraction of protein pairs in PRS, RRS, and CCSB-YI1 that test positive by PCA, MAPPIT, or Y2H. (**D**) Overlaps between three high-quality large-scale *S. cerevisiae* Y2H data sets ($^*P < 10^{-7}$). All error bars indicate SE.

Downloaded from www.sciencemag.org on October 2, 2008

The overlaps of Uetz-screen (27%) and Ito-core (35%) with CCSB-YI1 (Fig. 2D) can be explained by the completeness, assay sensitivity, and sampling sensitivity of the three experiments (SOM VII) and agree well with the results of the pairwise confirmation of those two data sets (Fig. 1C). Similar principles apply to other large-scale experiments such as AP/MS, likely accounting for the low overlap between Krogan and Gavin (~25%; fig. S5B).

Factoring in completeness, precision, and assay and sampling sensitivity, we estimated that the yeast binary interactome consists of ~18,000 ± 4500 interactions (SOM VI), experimentally validating previous computational estimates of 17,000

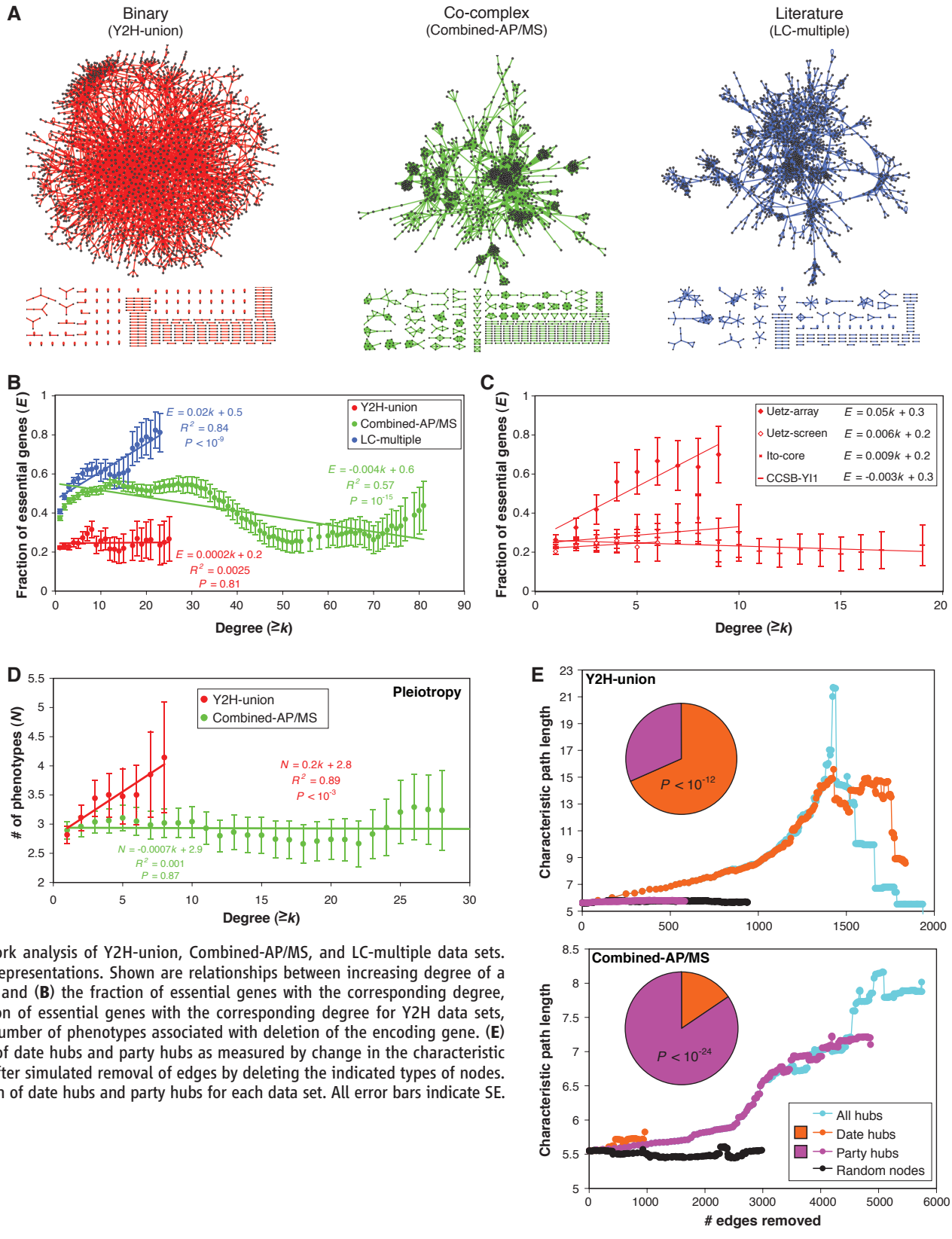

Fig. 3. Network analysis of Y2H-union, Combined-AP/MS, and LC-multiple data sets. (**A**) Network representations. Shown are relationships between increasing degree of a gene product and (**B**) the fraction of essential genes with the corresponding degree, (**C**) the fraction of essential genes with the corresponding degree for Y2H data sets, and (**D**) the number of phenotypes associated with deletion of the encoding gene. (**E**) Contribution of date hubs and party hubs as measured by change in the characteristic path length after simulated removal of edges by deleting the indicated types of nodes. (Inset) Fraction of date hubs and party hubs for each data set. All error bars indicate SE.

Downloaded from www.sciencemag.org on October 2, 2008

to 25,000 interactions (*31*, *32*). To obtain a more comprehensive map of the binary yeast interactome, we combined the three available high-quality proteome-scale Y2H data sets (SOM VII). The union of Uetz-screen, Ito-core, and CCSB-YI1, "Y2H-union," contains 2930 binary interactions among 2018 proteins, which, according to our empirical estimate of the interactome size, represents ~20% of the whole yeast binary interactome (Fig. 3A).

We reexamined global topological features of this new yeast interactome network, facing lower risk of overinterpreting properties due to limited sampling and various biases in the data (*18*). To contrast topological properties of the binary Y2H-union network with that of the co-complex network, we used an integrated AP/MS data set (*33*), which was generated by combining raw high-throughput AP/MS data (*15*, *16*). This "Combined-AP/MS" data set, composed of 9070 co-complex membership associations between 1622 proteins, attempts to model binary interactions from co-complex data (Fig. 3A).

As found previously for other macromolecular networks, the connectivity or "degree" distribution of all three data sets is best approximated by a power-law (*34*) (fig. S6 and SOM VIII). Highly connected proteins, or "hubs," are reportedly more likely encoded by essential genes than less-connected proteins (*35*). Surprisingly, Y2H-union lacked any correlation between degree and essentiality (Fig. 3B). This discrepancy might stem from biases in the data sets available at the time of the original observation: interactions reported in Uetz *et al*. (Uetz-array and Uetz-screen) and literature-curated interactions. Although Uetz-array is of high quality (fig. S7), its experimental design could negatively influence network analyses. Most hub proteins in Uetz-array were found as baits (fig. S8), and the percentage of essential proteins in the 193 bait proteins is twice as high (34.7%) as that of all protein-encoding ORFs in the yeast genome (18.4%), explaining the high correlation between degree and essentiality (Fig. 3C). Likewise, literature-curated interactions seem prone to sociological and other inspection biases (SOM VII). Thus, we refrain hereinafter from using LC-multiple in our further topological and biological analyses. No significant correlation between degree of connectedness and essentiality was observed in any of the three proteome-wide high-throughput binary data sets currently available (i.e., Ito-core, Uetz-screen, and CCSB-YI1; Fig. 3C), as well as in new versions of our *C. elegans* and human interactome maps (fig. S9 and SOM IX).

Hub proteins instead relate to pleiotropy, the number of phenotypes observed as a consequence of gene knockout (SOM I). There was a significant correlation in Y2H-union between connectivity and the number of phenotypes observed in global phenotypic profiling analyses of yeast genes (*36*) (Fig. 3D). Thus, the number of binary physical interactions mediated by a protein seems to better correlate with the number of cellular processes in which it participates than with its essentiality. The correlation between degree and number of phenotypes is not observed in Combined-AP/MS, likely because co-complex associations reflect the size of protein complexes more than the number of processes they might be involved in.

Fig. 4. Clustering of essential proteins. (**A**) Average fraction of essential proteins among proteins whose distance is equal to *d* from a protein selected from essential, nonessential, and all proteins. (**B**) Giant component size of network formed by essential proteins (arrow) compared to 100,000 random networks of same topological properties. (**C**) The number of interacting essential proteins that are also found in the same complex compared to 10,000 random selections of proteins of the same number as essential proteins (SOM IX).

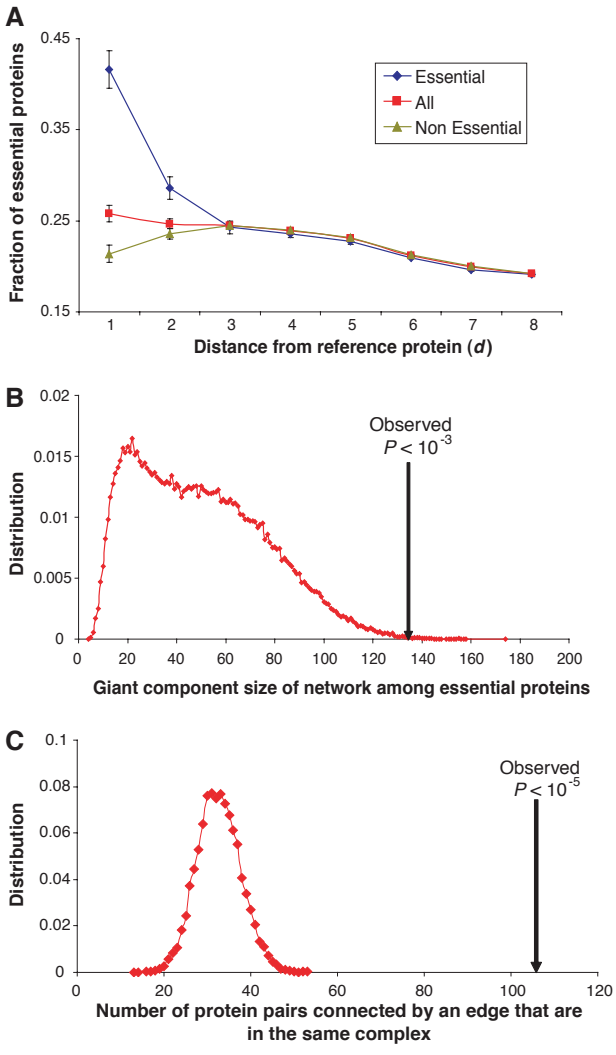

We confirmed the concept of modularity in the yeast interactome network, whereby date hubs that dynamically interact with their partners appear particularly central to global connectivity, whereas static party hubs appear to function locally in specific biological modules (*37*). The proportion of date and party hubs is substantially different between Y2H-union and Combined-AP/MS (Fig. 3E). There are significantly more date hubs in the binary network, whereas party hubs are prevalent in the co-complex network. In the binary network, date hubs are crucial to the topological integrity of the network, whereas party hubs have minimal effects. However, in the co-complex network, date and party hubs affect the topological integrity of the network equally, likely because most hubs in Combined-AP/MS reside in large stable complexes, whereas hubs in Y2H-union preferentially connect diverse cellular processes.

Surprisingly, essential proteins strongly tended to interact with each other (Fig. 4A and SOM IX). By concentrating on the subnetwork formed by interactions mediated by and among essential proteins (fig. S10), we found a giant component whose size is much larger than expected by chance (Fig. 4B). To better understand the clustering of essential proteins, we examined the interacting essential protein pairs that are also reported to be in the same complex; we found 106 interacting essential protein pairs, a number greater than expected by chance (Fig. 4C and SOM IX).

We investigated the overall relationships between Y2H-union and Gene Ontology (GO) attributes (*38*), phenotypic and expression profiling similarities (*39*), and transcriptional regulatory networks (*40*). Both Y2H-union and Combined-AP/MS show significant enrichment (all $P < 10^{-10}$) for functionally similar pairs in all three GO branches (Fig. 5A) (*41*). There is also significant enrichment of positive correlations of phenotypic profiles (*36*) between interacting pairs in both data sets (Fig. 5B and fig. S11). Such interactions, when supported by strong phenotypic information, constitute likely possibilities of functional relationships. Lastly, both data sets are significant-

Downloaded from www.sciencemag.org on October 2, 2008

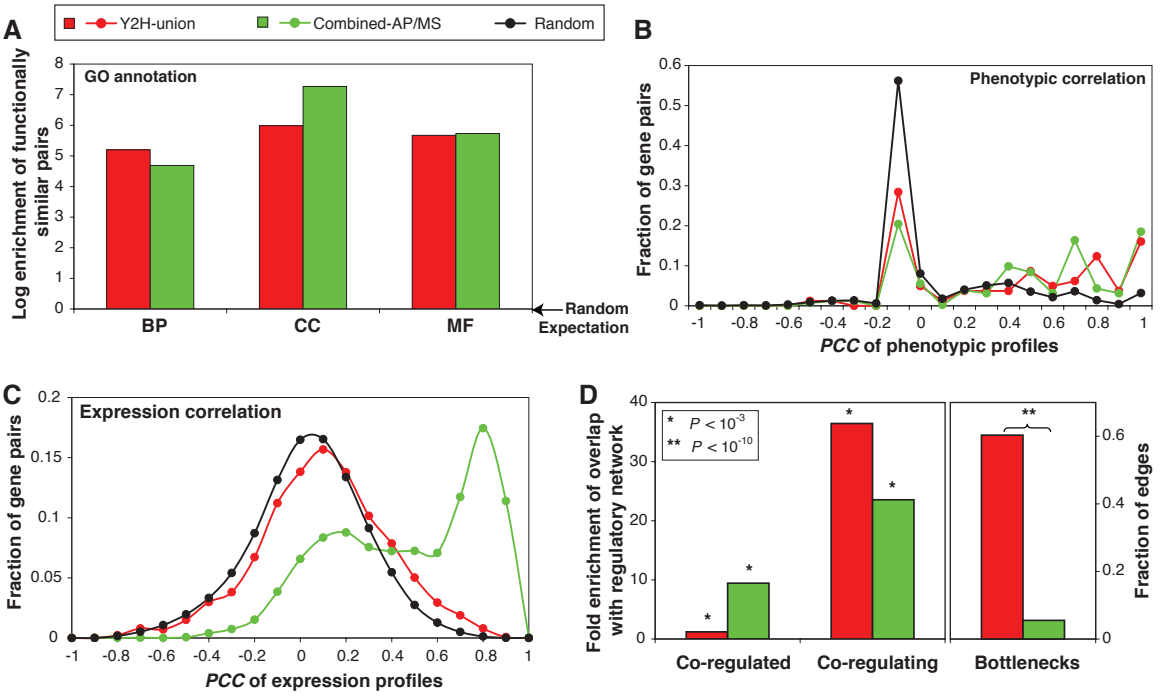

Fig. 5. Biological features of yeast interactome data sets. (**A**) Enrichment of interacting protein pairs (relative to random) that share GO annotations in the biological process, cellular component, and molecular function branches of GO ontology. (**B**) Pearson correlation coefficient (PCC) of phenotypic profiles between interacting pairs in different data sets. (**C**) Coexpression correlation between interacting pairs. (**D**) (Left) Enrichment of interacting proteins as targets of a common TF (co-regulated), and enrichment of interacting TFs in a common MIM (co-regulating) (*$P < 10^{-3}$). (Right) Fraction of bottlenecks from each data set in the combined network (SOM XI). Top 10% of edges with the highest betweenness are defined as "bottlenecks" (*45*).

ly enriched with pairs coexpressed across many conditions (fig. S12), although Combined-AP/MS shows higher enrichment (Fig. 5C), agreeing well with the different nature of the two assays: AP/MS aims at detecting stable complexes, whereas Y2H tends to detect more transient and condition-specific protein interactions. This observation is further supported by enrichment of kinase-substrate pairs in Y2H-union (SOM X and fig. S13).

To explore the mechanisms underlying coexpression of interacting protein pairs, we combined transcriptional regulatory networks with interactome network information (*40*). Interacting proteins in both networks tended to be co-regulated by common transcription factors (TFs; Fig. 5D). Similar to what we observed in the coexpression correlation analysis (Fig. 5C), the enrichment of interacting pairs in Combined-AP/MS was significantly higher than that of Y2H-union. Notably, we observed a significant enrichment of protein-protein interactions between TFs involved in a common "multi-input motif" (*42*, *43*) (MIM, where multiple TFs co-regulate a given set of genes; Fig. 5D and SOM X). The fraction of co-regulating TF pairs is much higher in the binary interactome than in the co-complex network, suggesting that various TFs function together to form transient complexes to differentially regulate transcriptional targets (*44*).

These observations suggest that our binary interactome data set is enriched in transient or condition-specific interactions linking different subcellular processes and molecular machines. To further explore this possibility, we calculated "edge-betweenness" for each interaction in a merged network of all available interactions (SOM XI), measuring the number of shortest paths between all protein pairs that traverse a given edge. The higher edge-betweenness of interactions from Y2H-union shows the tendency of Y2H to detect key interactions outside of complexes significantly more often than AP/MS (Fig. 5D). Several examples of such complex-to-complex connectivity are evident in a complete map of MIPS complexes connected by Y2H interactions (fig. S14).

Overall, we infer that Y2H interrogates a different subspace within the whole interactome than does AP/MS, and Y2H interactions represent key connections between different complexes and pathways. Y2H and AP/MS provide orthogonal information about the interactome and are both vital to obtaining a complete picture of cellular protein-protein interaction networks.

References and Notes

1. M. Fromont-Racine, J. C. Rain, P. Legrain, *Nat. Genet.* **16**, 277 (1997).
2. P. Uetz *et al.*, *Nature* **403**, 623 (2000).
3. T. Ito *et al.*, *Proc. Natl. Acad. Sci. U.S.A.* **98**, 4569 (2001).
4. A. J. Walhout *et al.*, *Science* **287**, 116 (2000).
5. J. Reboul *et al.*, *Nat. Genet.* **34**, 35 (2003).
6. S. Li *et al.*, *Science* **303**, 540 (2004).
7. L. Giot *et al.*, *Science* **302**, 1727 (2003).
8. F. Colland *et al.*, *Genome Res.* **14**, 1324 (2004).
9. J. F. Rual *et al.*, *Nature* **437**, 1173 (2005).
10. U. Stelzl *et al.*, *Cell* **122**, 957 (2005).
11. G. Butland *et al.*, *Nature* **433**, 531 (2005).
12. M. Arifuzzaman *et al.*, *Genome Res.* **16**, 686 (2006).
13. A. C. Gavin *et al.*, *Nature* **415**, 141 (2002).
14. Y. Ho *et al.*, *Nature* **415**, 180 (2002).
15. A. C. Gavin *et al.*, *Nature* **440**, 631 (2006).
16. N. J. Krogan *et al.*, *Nature* **440**, 637 (2006).
17. R. M. Ewing *et al.*, *Mol. Syst. Biol.* **3**, 89 (2007).
18. J. D. Han, D. Dupuy, N. Bertin, M. E. Cusick, M. Vidal, *Nat. Biotechnol.* **23**, 839 (2005).
19. D. Scholtens, M. Vidal, R. Gentleman, *Bioinformatics* **21**, 3548 (2005).
20. T. Reguly *et al.*, *J. Biol.* **5**, 11 (2006).
21. I. Remy, S. W. Michnick, *Methods Mol. Biol.* **261**, 411 (2004).
22. D. M. Gelperin *et al.*, *Genes Dev.* **19**, 2816 (2005).
23. H. W. Mewes *et al.*, *Nucleic Acids Res.* **34**, D169 (2006).
24. C. von Mering *et al.*, *Nature* **417**, 399 (2002).
25. J. S. Bader, A. Chaudhuri, J. M. Rothberg, J. Chant, *Nat. Biotechnol.* **22**, 78 (2004).
26. H. Yu *et al.*, *Genome Res.* **14**, 1107 (2004).
27. P. O. Vidalain, M. Boxem, H. Ge, S. Li, M. Vidal, *Methods* **32**, 363 (2004).
28. A. J. Walhout, M. Vidal, *Genome Res.* **9**, 1128 (1999).
29. S. Eyckerman *et al.*, *Nat. Cell Biol.* **3**, 1114 (2001).
30. R. Jansen, M. Gerstein, *Curr. Opin. Microbiol.* **7**, 535 (2004).
31. A. Grigoriev, *Nucleic Acids Res.* **31**, 4157 (2003).
32. R. Jansen *et al.*, *Science* **302**, 449 (2003).
33. S. R. Collins *et al.*, *Mol. Cell. Proteomics* **6**, 439 (2007).
34. A. L. Barabási, R. Albert, *Science* **286**, 509 (1999).
35. H. Jeong, S. P. Mason, A. L. Barabasi, Z. N. Oltvai, *Nature* **411**, 41 (2001).
36. A. M. Dudley, D. M. Janse, A. Tanay, R. Shamir, G. M. Church, *Mol. Syst. Biol.* **1**, 0001 (2005).
37. J. D. Han *et al.*, *Nature* **430**, 88 (2004).
38. Gene Ontology Consortium, *Nucleic Acids Res.* **36**, D440 (2008).
39. M. Vidal, *Cell* **104**, 333 (2001).
40. H. Yu, M. Gerstein, *Proc. Natl. Acad. Sci. U.S.A.* **103**, 14724 (2006).
41. H. Yu, R. Jansen, G. Stolovitzky, M. Gerstein, *Bioinformatics* **23**, 2163 (2007).
42. T. I. Lee *et al.*, *Science* **298**, 799 (2002).
43. R. Milo *et al.*, *Science* **298**, 824 (2002).
44. N. M. Luscombe *et al.*, *Nature* **431**, 308 (2004).
45. H. Yu, P. M. Kim, E. Sprecher, V. Trifonov, M. Gerstein, *PLOS Comput. Biol.* **3**, e59 (2007).

46. Supported by funds from the W. M. Keck Foundation (M.V. and F.P.R.); by Institute Sponsored Research funds from the Dana-Farber Cancer Institute Strategic Initiative (M.V. and CCSB); by NIH grant R01-HG001715 (M.V. and F.P.R.); by NIH grants U01-A1070499-01 and U56-CA113004 (A.-L.B.); by grant GOA12051401 from the University of Ghent and grant FWO-V G.0031.06 from the Fund for Scientific Research Flanders (J.T.); by a grant from the National Cancer Institute of Canada

Downloaded from www.sciencemag.org on October 2, 2008

(C.B.); and by NIH grant HG003224 (F.P.R.). I.L. is a postdoctoral fellow with the Fonds Wetenschappelijk Onderzoek–Vlanderen. M.V. is a "Chercheur Qualifié Honoraire" from the Fonds de la Recherche Scientifique (FRS-FNRS, French Community of Belgium). We thank members of our laboratories for helpful discussions and Agencourt Biosciences for sequencing assistance. All data sets can be downloaded from our Web site (http://interactome.dfci.harvard.edu/S_cerevisiae).

Supporting Online Material
www.sciencemag.org/cgi/content/full/1158684/DC1
SOM Text
Figs. S1 to S35
Tables S1 to S5
References

4 April 2008; accepted 1 August 2008
Published online 21 August 2008;
10.1126/science.1158684
Include this information when citing this paper.

Ceramide Biogenesis Is Required for Radiation-Induced Apoptosis in the Germ Line of *C. elegans*

Xinzhu Deng,[1] Xianglei Yin,[1] Richard Allan,[1] Diane D. Lu,[1] Carine W. Maurer,[2] Adriana Haimovitz-Friedman,[3] Zvi Fuks,[3] Shai Shaham,[2] Richard Kolesnick[1]*

Ceramide engagement in apoptotic pathways has been a topic of controversy. To address this controversy, we tested *loss-of-function (lf)* mutants of conserved genes of sphingolipid metabolism in *Caenorhabditis elegans*. Although somatic (developmental) apoptosis was unaffected, ionizing radiation–induced apoptosis of germ cells was obliterated upon inactivation of ceramide synthase and restored upon microinjection of long-chain natural ceramide. Radiation-induced increase in the concentration of ceramide localized to mitochondria and was required for BH3-domain protein EGL-1–mediated displacement of CED-4 (an APAF-1–like protein) from the CED-9 (a Bcl-2 family member)/CED-4 complex, an obligate step in activation of the CED-3 caspase. These studies define CEP-1 (the worm homolog of the tumor suppressor p53)–mediated accumulation of EGL-1 and ceramide synthase–mediated generation of ceramide through parallel pathways that integrate at mitochondrial membranes to regulate stress-induced apoptosis.

Although studies that use genetic deficiency in ceramide production support it as essential for apoptosis in diverse models (*1*), many have questioned whether ceramide functions as a bona fide transducer of apoptotic signals (*2*). One reason for skepticism is that, despite delineation of a number of ceramide-activated proteins, no single protein has been identified as mediator of ceramide-induced apoptosis. Recent studies have suggested an alternate mode of ceramide action, based on its capacity to self-associate and locally rearrange membrane bilayers into ceramide-rich macrodomains (1 to 5 μm in diameter), which are sites of protein concentration and oligomerization (*3*). Ceramide may thus mediate apoptosis through its ability to reconfigure membranes, coordinating protein complexation at critical junctures of signaling cascades.

To establish the role of ceramide definitively, we used a model of radiation-induced apoptosis in *Caenorhabditis elegans* germ cells (*4*). Germline stem cells, located at the distal gonad tip, divide incessantly throughout adult life, with daughter cells arresting in meiotic prophase. Upon exiting prophase, germ cells become sensitive to radiation-induced apoptosis, detected morphologically just proximal to the bend of the gonadal arm (*5*). This apoptotic pathway is antagonized by the ABL-1 tyrosine kinase, requiring sequentially the cell cycle checkpoint genes *rad-5*, *hus-1*, and *mrt-2*; the *C. elegans* p53 homolog *cep-1*; and the genes making up the conserved apoptotic machinery, the caspase *ced-3*, the apoptotic protease activating factor 1–like protein *ced-4*, the Bcl-2 protein *ced-9*, and the BH3-domain protein *egl-1*. This pathway differs from apoptotic somatic cell death, which is not subject to upstream checkpoint regulation via the CEP-1 pathway (*5*, *6*).

We identified conserved genes that regulate *C. elegans* sphingolipid intermediary metabolism and tested deletion alleles (Table 1 and table S1). Screening for mutants resistant to radiation-induced germ cell apoptosis revealed apoptosis suppression in only deletion mutants of *hyl-1* and *lagr-1*, two of the three ceramide synthase (CS) genes (Fig. 1A). CS gene products regulate de novo ceramide biosynthesis, acylating sphinganine to form dihydroceramide that is subsequently converted to ceramide by a desaturase (*7*). CSs contain six to seven putative transmembrane domains and a Lag1p motif [which confers enzyme activity (*8*)], regions conserved in the *C. elegans* orthologs. The deleted CS sequences in *hyl-1(ok976)* and *lagr-1(gk327)* result in frameshifts that disrupt the Lag1p motifs (fig. S1A). We detected a ~1.6-kb *hyl-1* transcript in wild-type (WT) worms and a smaller ~1.35-kb transcript in *hyl-1(ok976)*, whereas we observed a ~1.4-kb *lagr-1* transcript in WT worms and a ~1.25-kb transcript in *lagr-1(gk327)* (fig. S1B). In contrast, a deletion mutant of the third *C. elegans* CS (*9*, *10*), *hyl-2(ok1766)*, lacking a 1626-base pair fragment of the *hyl-2* gene locus that eliminates exons 2 to 5 corresponding to 74% of the coding sequence, displayed no defect in germ cell death (fig. S1C).

In N2 WT strain young adults, apoptotic germ cells gradually increased in abundance with age from a baseline of 0.7 ± 0.1 to 1.8 ± 0.2 corpses per distal gonad arm over 48 hours. Exposure to a 120-gray (Gy) ionizing radiation dose increased germ cell apoptosis to 5.2 ± 0.3 cells 36 to 48 hours after treatment. In contrast, in *hyl-1 (ok976)* and *lagr-1(gk327)* animals, age-dependent and radiation-induced germ cell apoptosis were nearly abolished (Fig. 1A). Similar effects were observed in the *lagr-1(gk327);hyl-1(ok976)* double mutant (Fig. 1B). The rate of germ cell corpse removal was unaffected in CS mutants, excluding the possibility that defective corpse engulfment elevated corpse numbers (table S2). In contrast, *loss-of-function (lf)* mutations of *hyl-1* or *lagr-1* did not affect developmental somatic cell death, nor did the *lf hyl-2(ok1766)* mutation (table S3). These studies indicate a requirement for two *C. elegans* CS genes for radiation-induced germline apoptosis.

To confirm ceramide as critical for germline apoptosis, we injected C_{16}-ceramide into gonads of young adult WT worms. C_{16}-ceramide is the predominant ceramide species in apoptosis induction by diverse stresses in multiple organisms (*11*) and in low abundance in *C. elegans* (*12*, *13*). C_{16}-ceramide microinjection resulted in time- and dose-dependent increases in germ cell apoptosis (Fig. 1C), with a median effective dose of ~0.05 μM gonadal ceramide. Peak effect occurred at ~0.1 μM gonadal ceramide at 36 hours (6.6 ± 0.8 versus 1.5 ± 0.4 cell corpses per distal gonad arm, $P < 0.0001$), qualitatively and quantitatively mimicking the 120-Gy effect in WT worms. In contrast, C_{16}-dihydroceramide, which differs from C_{16}-ceramide in a trans double bond at sphingoid base position four to five, was without effect (0.71 ± 0.28 cell corpses per distal gonad arm at ~1 μM), indicating specificity for ceramide in apoptosis induction. Furthermore, C_{16}-ceramide microinjection into *lagr-1(gk327);hyl-1(ok976)* animals (~1 μM gonadal ceramide) resulted in a 5.7-fold increase in germ cell apoptosis (from 0.60 ± 0.17 to 3.43 ± 0.88, $P < 0.0001$) (Fig. 1D). Note that the baseline level of apoptosis in *lagr-1(gk327);hyl-1(ok976)* was less than one-half that in WT worms. Moreover, ~0.005 μM gonadal ceramide, a concentration without impact on germ cell apoptosis, completely restored radiation (120 Gy)–induced apoptosis, an effect inhibitable in a *lf ced-3* background (Fig. 1E). C_{16}-ceramide's ability to bypass the genetic defect and restore the radiation-response pheno-

[1]Laboratory of Signal Transduction, Memorial Sloan-Kettering Cancer Center (MSKCC), New York, NY 10021, USA. [2]Laboratory of Developmental Genetics, Rockefeller University, New York, NY, 10021, USA. [3]Department of Radiation Oncology, Memorial Sloan-Kettering Cancer Center, New York, NY 10021, USA.

*To whom correspondence should be addressed. E-mail: r-kolesnick@ski.mskcc.org

Downloaded from www.sciencemag.org on October 2, 2008

EXTENDED PDF FORMAT
SPONSORED BY
usb
Products from Affymetrix
www.usbweb.com

Ceramide Biogenesis Is Required for Radiation-Induced Apoptosis in the Germ Line of C. elegans

Xinzhu Deng, *et al.*

Science **322**, 110 (2008);
DOI: 10.1126/science.1158111

The following resources related to this article are available online at www.sciencemag.org (this information is current as of October 2, 2008):

Updated information and services, including high-resolution figures, can be found in the online version of this article at:
http://www.sciencemag.org/cgi/content/full/322/5898/110

Supporting Online Material can be found at:
http://www.sciencemag.org/cgi/content/full/322/5898/110/DC1

This article **cites 19 articles**, 7 of which can be accessed for free:
http://www.sciencemag.org/cgi/content/full/322/5898/110#otherarticles

Information about obtaining **reprints** of this article or about obtaining **permission to reproduce this article** in whole or in part can be found at:
http://www.sciencemag.org/about/permissions.dtl

Downloaded from www.sciencemag.org on October 2, 2008

Science (print ISSN 0036-8075; online ISSN 1095-9203) is published weekly, except the last week in December, by the American Association for the Advancement of Science, 1200 New York Avenue NW, Washington, DC 20005. Copyright 2008 by the American Association for the Advancement of Science; all rights reserved. The title *Science* is a registered trademark of AAAS.